Graphene-Enabled, High-Performance Composites for Energy Storage and Energy Saving

---

A Dissertation

of

University of Virginia

In Partial Fulfillment of the

Requirements for the Degree

Of Doctor of Philosophy in **Mechanical & Aerospace Engineering**

By

Yunya Zhang

December 2019

APPROVAL SHEET

The dissertation is submitted in partial fulfillment of the requirements for the degree of

Doctor of Philosophy

Yunya Zhang, Author

This dissertation has been read and approved by the examining Committee:

Xiaodong Li, Advisor

Baoxing Xu, Committee Chair

Keivan Esfarjani, Committee Member

Sean R. Agnew, Committee Member

Gary Koenig, Committee Member

Accepted for the School of Engineering and Applied Science:

Craig H. Benson, Dean

School of Engineering and Applied Science

October 2019

Abstract

Booming populations and the emphasis on sustainability have put enormous pressure on energy storage and energy saving, which make us to rethink the exploitation of clean energy resources and the improvement of energy usage efficiency. Graphene is expected to hold the key to high-performance energy storage devices and novel, energy-saving materials. As a single layer of carbon atoms, the strong sp^2 bonds and the free-standing π bonds render graphene unique and incredible mechanical, electronic, and thermal properties. However, after a decade of extensive study, how to effectively use graphene and its potential remains a challenge. The agglomeration, degradation, and side reactions may largely deteriorate the properties of graphene, leading to minor, even negative effects on final product performance. In this dissertation, graphene was employed in both Li-S batteries and metal matrix composites, aiming to develop effective and efficient approaches of using graphene in electrochemical energy storage and energy-saving materials. Specifically, in Chapter 2, graphene was incorporated with porous carbon derived from two common biowastes, banana peel and paper cardboard. The hierarchical pores in these two biomass-derived carbon frameworks and the outstanding conductivity of graphene enhanced the performance of Li-S batteries. In Chapter 3, it was unveiled that Li-S batteries failed due to the growth of mossy Li, which originated from imperfections on the solid-electrolyte interface (SEI). Accordingly, a stronger artificial SEI was built by combining alpha-lipoic acid (ALA), a low-cost dietary supplement, with graphene oxide, which effectively prevented the growth of Li whiskers. In Chapter 4 and Chapter 5, graphene was added to Al and Ni powders, separately, for the fabrication of metal matrix composites with a nacre-like microstructure. Interfacial reactions between graphene and both metals were strategically leveraged to mimic the microscale architectures of nacre. The fabricated Al/Al_2O_3/graphene composite and Ni/NiC_3 composite displayed a joint improvement in a range of mechanical properties. The studies provide new inspirations for the development of high-performance, low-cost Li-S batteries and high-strength, high-toughness metal matrix composites, demonstrating that graphene can drastically change energy storage and energy saving if used smartly and effectively.

Key Words

Graphene, biomass, porous carbon, lithium sulfur battery, mossy lithium, bioinspired, nacre, metal matrix composite

Table of Content

Acknowledgements

I would like to express my sincere gratitude to my advisor Professor Xiaodong Li, for advising me through my years of Ph.D. study, for supporting me to pursue various scientific opportunities, for encouraging me to always aim high and do things patiently. His energy, enthusiasm and strong mentality always encourage me to do better. Without his guidance and constant supervision, it would be impossible for me to complete this dissertation. I am truly grateful for these valuable years, which certainly will benefit my career and life in the long run. I would also like to thank other committee members, Prof. Baoxing Xu, Prof. Sean Agnew, Prof. Keivan Esfarjani, and Prof. Gary Koenig, for their valuable time and guidance.

I would like to thank all the members of the Li group who have created such a diverse, welcoming and supportive atmosphere. To Zan, Ningning, Michael, Jamison, Clifton, Jiajun, Ruoxi, Yuchen, *et al.*, thanks for the help from all of you through my Ph.D. study. Wherever I will be in the future, UVa will be my life-long memory. I also would like to thank all my friends at UVa, Fulin Wang, Hongxi Luo, Naiming Liu, Chao Liu, Serena Luo, Bin Wang *et al.* for your accompanying, which makes my Ph.D. life so memorable.

I would like to acknowledge the financial support from the National Science Foundation (NSF) CMMI-1418696, CMMI-1537021, and CMMI-1728042, which necessarily make this dissertation study possible.

Lastly, I would like to express my deepest gratitude to my parents and family, thanks for raising me and supporting me to pursue my career. Here, I give my special thanks to my wife, Jing Liu, whose companion, support, and encouragement keep me proceeding in the difficult and sometimes frustrating scientific research.

List of Figures

Fig. 1-1 Li-S battery and graphene. Li-S battery suffers three major challenges: insulation of sulfur, solubility of polysulfides, and large volume fluctuation. Graphene and its derivatives are a potential solution for these problems. Graphene and graphene oxide (GO) are mechanically robust and flexible, so they can buffer the large volume change. High specific area and functional groups are able to encapsulate and immobilize polysulfides, thereby reducing shuttle effects. The high conductivity of graphene and reduced GO (rGO), as well as their constructed porous structures lay the foundation for outstanding electron and ion transferability, enabling higher utilization of active material. Graphene and its derivatives also have the potential for further development, such as doping, functionalization, and compositing with other materials, including metal components, carbonaceous materials, and conductive polymers. Images reproduced from ref. [49], [50], [51], [52], [53], [54].

Fig. 1-2 Interactions between sulfur and graphene/GO. a. Graphene and GO are able to encapsulate sulfur particles, thereby enhancing electron transfer, entrapping the dissolved polysulfides, and buffering the volume change [62]. b. Both graphene and element sulfur have symmetrical, non-polar structure [63]. c. The wettability between graphene and sulfur is outstanding [63]. d. Sulfur can bond with the functional groups on GO, leading to a stronger chemical interaction [65]. e. XPS spectra illustrate that C-S and O-S bonds formed after sulfur infiltration [66]. f. Oxygen functional groups have no major influence on the adsorption of S_8 but strongly effect the adsorption of polysulfides. Hydroxyl functions have the strongest interaction with Li_2S_4 and carboxyl functional groups have the strongest interaction with Li_2S_8 [67].

Fig. 1-3 Graphene and its derivatives for battery components other than cathode. a. Graphene/carbon black cathode interlayer anchored on polysulfides [90]. b. Graphene as both current collector and cathode interlayer [107]. c. Graphene wrapped Li_xM (M= Si, Sn, or Al) nanoparticle anode, showing an outstanding resistance to air and water [110].

Fig. 1-4 Graphene/metal composites. a. Mechanical performance of graphene/AA6061 composites fabricated by ball milling [127]. b,c. Graphene/Al composites fabricated by semi-powder metallurgy [131]. d,e. Graphene/Ni composites fabricated by molecular-level mixing [134].

Fig. 1-5 Graphene/dislocation interactions [140]. a. Graphene/Cu composite fabricated by CVD. Scale bar, 200 nm. b. Close-up inspection of metal–graphene interface. Scale bar, 5 nm. c. TEM image of a Cu–graphene nanopillar with 125-nm repeat layer spacing at a low magnification after deformation. Scale bar, 100 nm. d. TEM image of a Cu–graphene nanopillar after deformation that shows a higher density of dislocations above the graphene interface. Scale bar, 50 nm. e. Schematic figure illustrating the blocking of dislocation propagation at the metal–graphene interface.

Fig. 1-6 Microstructure of nacre. a. The laminated, brick-and-mortar structure of nacre [149]. b. The biopolymer strands formed between aragonite platelets [150]. c. Crack propagation of nacre under tension [154].

Fig. 2-1 Activation of ABP. a. Banana production in 2011. b. A piece of freeze dried banana peel. c. A piece of ABP. d. FTIR spectrum of ABP. e. Raman spectrum of ABP.

Fig. 2-2 Microstructure of ABP. a. 3D XCT image of ABP (the height of the examined ABP rectangle is 2 mm). b. The compact porous structure.

Fig. 2-3 Microstructure of ABP/Ni/graphene composite. a. SEM image of the $Ni(NO_3)_2$ treated ABP, showing the cellular porous structure. b. Close-up view of the $Ni(NO_3)_2$ treated ABP, showing co-existence of nanopores and Ni nanoparticles on the cell walls. c. TEM image of the $Ni(NO_3)_2$ treated ABP, showing the Ni nanoparticles wrapped with multilayered graphene. d. SAED patterns of the $Ni(NO_3)_2$ treated ABP, indicating the co-existence of crystalline carbon, amorphous carbon, and crystalline Ni. e. HRTEM image of a Ni nanoparticle wrapped with multilayered graphene. f. HRTEM image and FFT pattern of the multilayered graphene.

Fig. 2-4 Microstructure of ABP/Ni/graphene/S composite electrode. a. SEM image of ABP/Ni/graphene/S. b. Element map of carbon. c. Element map of nickel. d. Element map of sulfur. e. TEM image of ABP/Ni/graphene/S. f. SAED pattern of (a). g. HRTEM image of ABP/Ni/graphene/S. h. FFT patterns of areas ①, ②, ③, and ④ in (c), showing that the Ni nanoparticles, sulfur nanosphere crystals, multilayered graphene crystal and amorphous carbon jointly construct the ABP/Ni/graphene/S composite.

Fig. 2-5 Electrochemical performance of Li-ABP/Ni/graphene/S battery. a. Charge/discharge curve of Li-ABP/Ni/graphene/S battery. b. Charge/discharge curves of Li-ABP/Ni/graphene/S battery at different rates. c. Cycle ability of Li-ABP/Ni/graphene/S battery with reference to Li-ABP/S battery. d. Cycling performance of Li-ABP/Ni/graphene/S battery. e. Nyquist plot of Li-ABP/Ni/graphene/S battery under fully charging state before and after 200 cycles (inset: the Li-ABP/Ni/graphene/S battery can enlighten multiple LEDs).

Fig. 2-6 Activation and microstructure of recycled paper. a. Picture of a hardboard roll (a package of a calendar). b. SEM image of the recycled paper (inset: recycled paper stripe). c. SEM image of APC (inset: APC stripe). d. XRD of recycled paper, APC, APC/graphene composite. e. Raman spectra of APC and APC/graphene composite.

Fig. 2-7 Compositing graphene oxide with recycled paper via a capillary absorption method. a. Pictures showing compositing graphene oxide with the recycled paper by capillary force. b. The corresponding liquid height vs. time chart. c. The dried recycled paper/graphene oxide composite with different location noted as ①②③④. d. Corresponding SEM images at location ①②③④, showing that graphene oxide homogeneously covered on paper fibers irrelevant to the location.

anode. e. SEM image of the Li anode after 620 cycles, displaying crusts and big holes. f. Cross-section of Li anode after 620 cycles.

Fig. 3-1 Photographs of lithium anode after different amounts of cycles.

Fig. 3-2 Microstructural evolution of lithium anode from the beginning to the 600th cycle. a. SEM top-view images. Mossy Li gradually covered the electrode surface while a crust formed after repeated stripping/depositing. Large holes formed at areas without the crust coverage b. Cross-sectional SEM images of lithium electrodes. The dense crust blocked the reaction pathway for the lithium underneath, showing thicker underlying lithium.

Fig. 3-3 Chemical components of lithium electrodes with the proceeding of cycling. a. Typical XRD spectrum of lithium electrode after repeated stripping/depositing. b. The intensity of $Li_2S(220)$ peaks and the intensity ratio between $Li_2S(220)$ peaks and Li(110) peaks at different cycles. c. FTIR spectrum of lithium anode after 600 cycles. d. EDS element maps of the Li anode surface under SEM.

Fig. 3-4 Mechanical properties of lithium electrodes with the proceeding of cycling. a. An indentation on the pristine lithium. b. Typical load/displacement curve of nanoindentation. c. Evolution of surface modulus and hardness of lithium electrodes.

Fig. 3-5 Impedances of Li-S batteries with the proceeding of cycling. a. Typical EIS spectrum of the Li-S batteries, showing two semicircles in the high and intermediate frequency regime, and a straight line in the low frequency regime (inset is the equivalent circuit). b. Statistical results of resistances in EIS spectra of Li-S batteries at different cycles.

Fig. 3-6 Schematic diagram of the evolution of lithium anode during cycling in Li-S batteries. Upon cycling, the lithium electrode surface is etched to a rough morphology with coexisting pits and flat stages. Mossy Li whiskers grow from the bottom of the pits and gradually cover the entire electrode surface. Li_2S deposits, as well as sulfur, SEI flotsams, and dead Li, aggregate on the anode surface. The growth of mossy Li repeatedly compresses the passive sediments, forming a dense crust which blocks charge transfer for the lithium underneath. The uncovered part, on the other hand, is etched preferentially, leading to penetrating holes.

Fig. 3-7 Stripping of lithium anode in the first discharge. a. Discharge profile of the Li-S battery with microstructural images at different discharging time. b. AFM height profile of the edge of a square after 30 sec discharge. c. Depth distribution along the yellow line in (b), showing 195 nm collapse at the square edge. d. Close-up SEM image. e. EDS oxygen map. f. EDS sulfur map.

Fig. 3-8 SEI on the Li anode surface. a. AFM height profile of the edge of a square after 10 min self-discharge. b. Corresponding surface modulus map, showing a lower modulus on the square edge. c. Corresponding adhesion map, showing a clear boundary along the edge. d. Orientation of squares on the lithium electrode surface. e. Schematic diagram of SEI growth on the lithium electrode.

Fig. 3-9 Inhomogeneous formation of mossy Li in the first charge. a. Charge profile of the Li-S battery with microstructural images at different charging time, showing that mossy Li whiskers grew from the bottom of the pits. b. Cross-sectional SEM image of the lithium anode in the Li-S battery after the first charge process. c. A scratch on the lithium surface. d. Mossy Li whiskers grew from the bottom of the scratch instead of the flat banks after charging. e. A lithium anode in a Li‖Cu battery after the first plating process, showing mossy Li grew from etched pits.

Fig. 3-10 As-assumption mechanism of mossy Li growth. a. A fluid mechanics simulation of a constant flow over a pit in a flat surface with a Reynolds number of 3. The Flow at the bottom of the pit keeps steady. b. SEM image of a lithium anode after the second discharge. Mossy Li whiskers were etched preferentially. c. Cross section of a Lithium anode after the second discharge, showing residual hollowed SEI.

Fig. 3-11 Electrochemical properties of Li/APC-APC/graphene/S battery. a. Cycling capability of the Li/APC-APC/graphene/S battery at 0.96 C (inset: Li/APC-APC/graphene/S configuration). b. CV curves of the battery at first three cycles, and 120th and 121st cycles. c. EIS spectra of the battery before cycling, at 120th cycle, and after failure.

Fig. 3-12 Microstructure and schematic illustration of Li/APC anode. a. Top-down SEM image of the Li/APC anode after 1000 cycles, showing a flat surface without crusts, mossy Li, and dendrites. b. Cross-sectional SEM image of the Li/APC anode after 1000 cycles. c. Close-up observation of the APC interlayer, showing that electroactive materials filled out the gaps between paper fibers. d. Schematic illustration of Li anode with and without APC interlayer.

Fig. 3-13 The mechanism of converting ALA to a strong artificial SEI.

Fig. 3-14 The separator coated with ALA/GO. a. AFM height profile of the separator coated with ALA/GO. Inset is using capillary force to coat ALA/GO on the separator. b. AFM phase diagram of the separator coated with ALA/GO. c. XPS spectra of pure separator and separator coated with ALA/GO.

Fig. 3-15 Li anode surface morphology after five discharge/charge cycles. a. Untreated Li. b. Li with pure ALA. c. Li with ALA/GO.

Fig. 3-16 Electrochemical performance of the Li-S battery with ALA/GO. a. CV curves of the first three cycles. b. EIS spectrum before cycling. c. EIS spectrum after three cycles. d. Charge/discharge curves of Li-S batteries with ALA/GO. e. Cyclic performance of the Li-S battery with ALA/GO.

Fig. 4-7 Mechanical properties of graphene/Al_2O_3/Al composite and reference samples. a. Comparative tensile test curves. b. DIC analysis of the elastic deformation. c. High-load indentation on the cross-section of graphene/Al_2O_3/Al composite. d. Comparative bar chart of hardness, tensile strength, Young's modulus, and fracture toughness.

Fig. 4-8 Nanoindentation tests on graphene/Al_2O_3/Al composite, pure aluminum and Al/graphene mix samples. a. Graphene/Al_2O_3/Al composite. b. Schematic illustration explaining the modulus oscillation. c. Pure aluminum. d. Al/graphene mix.

Fig. 4-9 Graphene/Al_2O_3/Al composite after high temperature heating. a. A piece of graphene/Al_2O_3/Al composite was able to maintain the shape after heating at 750 ℃, while a piece of pure aluminum could not. b. After high temperature treatment, the laminated structure was preserved in graphene/Al_2O_3/Al composite and nanoasperities became thicker.

Fig. 4-10 XRD spectrum of graphene/Al_2O_3/Al composite after ion polishing.

Fig. 4-11 Determine the volume fraction and distribution of Al_2O_3 nanoparticles by convergent beam diffraction and TEM dark field image. a. Convergent beam diffraction at [023] direction. b. Corresponding dark field image (red cycles indicate the locations for CBD). c. Schematic diagram of the TEM sample.

Fig. 4-12 Determine the volume fraction and distribution of Al_2O_3 nanoparticles by FIB and 3D image reconstruction. a. Graphene/Al_2O_3/Al composite before FIB cutting. b. Graphene/Al_2O_3/Al composite after FIB cutting. c. ICE image. d. ICE image after processing, highlighting Al_2O_3 nanoparticles. e. 3D reconstruction Al_2O_3 nanoparticles. f. 3D reconstruction image after tilting, showing laminated morphology. g. Close-up inspection of one area.

Fig. 4-13 Grain structures of graphene/Al_2O_3/Al composite and Al powder metallurgy sample. a. graphene/Al_2O_3/Al composite. b. Al powder metallurgy sample.

Fig. 4-14 *In-situ* three-point bending test on the graphene/Al_2O_3/Al composite inside SEM. a. SEM images of the crack under various degrees of sample deflection. (Yellow arrows indicate the progression of bending and white arrows indicate the primary crack propagation direction). b. The crack propagation of graphene/Al_2O_3/Al composite sample exhibited a confluence of multiple toughening mechanisms. The primary crack was detoured into a serpentine morphology. Along with the primary crack, several large secondary cracks were stimulated and propagated parallel to the lamellae. The tip of the primary crack was blunt with large radius of curvature. The border of the primary crack displayed zig-zag shape with several small secondary cracks. Metal bridges formed behind the crack tip. c. The crack propagation of a graphene/Al mix sample (without PVA surface treatment and freeze-dry casting).

Fig. 5-1 Graphene sheets produced by shear mixing. a. TEM image of the graphene from shear mixing. b. SAED pattern of the graphene sheet. c. HRTEM image of the graphene sheet, showing intact crystal structure.

Fig. 5-2 Ni/graphene powders after shear mixing and freeze drying. a. SEM image of Ni/graphene powders, showing no noticeable aggregation of graphene sheets. b. Without shear mixing, graphene sheets were loosely wrapped on Ni particles. c. Without freeze drying, graphene agglomerated, forming graphite particles. d. TEM image of the surface of a Ni/graphene powder, showing that few layered graphene closely coated around the Ni particle. e. *In situ* heating observation of a Ni/graphene powder. Graphene gradually dissolved into Ni with increasing temperature.

Fig. 5-3 Ni powders with different concentrations of graphene after sintering. a. Ni/2 wt.% graphene. b. Ni. c. Ni/4 wt.% graphene. d. Ni/6 wt.% graphene.

Fig. 5-4 Microstructure of the graphene-enabled Ni/Ni_3C composite. a. SEM image of cold rolled Ni/Ni_3C composite, showing brick-and-mortar structures. b. Fracture surface of

Ni/Ni_3C composite, showing laminated structure constructed by elongated dimples. c. Low magnification TEM image, showing large second phase particle embedded in the Ni matrix. d. After cold rolling, Ni grains were deformed into long stripes with the thickness ranging from 100-300 nm. e. Close-up observation of the Ni/Ni_3C boundary. f. HRTEM image of the interface between Ni and a second phase particle, revealing a transition zone.

Fig. 5-5 XRD and EDS spectra of Ni/Ni_3C composite and Ni produced by powder metallurgy. a. Comprehensive XRD spectrum of Ni/Ni_3C composite. b. XRD spectra of Ni/Ni_3C composite and Ni produced by powder metallurgy from 40 ° to 50 °. c. EDS spectra of Ni_3C and Ni matrix in Ni/Ni_3C composite.

Fig. 5-6 Crystal structure of Ni_3C. a. Ni_3C crystal on [-110] plane. b. HRTEM image of the [-110] plane of Ni_3C particle, showing identical atomic arrangement as in the (a). c. FFT pattern of the [-110] plane. d. Schematic illustration of the formation of Ni/Ni_3C composite with brick-and-mortar structure.

Fig. 5-7 Mechanical properties of graphene-enabled Ni/Ni_3C composite with brick-and-mortar structure. a. Tensile stress-strain curves of Ni, Ni produced by powder metallurgy, and Ni/Ni_3C composite (inset is the size of tensile specimen). b. Comparative bar chart of mechanical properties of Ni and Ni/Ni_3C composite. c. Elongation vs. yield strength plot showing that the as-fabricated Ni/Ni_3C composite had an outstanding combination between strength and ductility (mechanical properties of nacre-like composites were derived from ref. [11-27, 29-34]).

Fig. 5-8 Stiffening mechanism of graphene derived Ni/Ni_3C composite with brick-and-mortar structure. a. Nanoindentation load-displacement curves of Ni and Ni_3C platelet. b. Hardness map derived from nanoindentation tests. c. Reduced modulus map derived from nanoindentation tests.

Fig. 5-9 Finite element simulation of the Ni/Ni_3C composite under tension. a. 3D FEA model of Ni/Ni_3C composite. b. 2D close-up view of the FEA model.

Fig. 5-10 Strengthening mechanisms of Ni matrix in Ni/Ni_3C composite. a. Nanoindentations on Ni in Ni/Ni_3C composite and Ni produced by powder metallurgy. b. TEM inspection of Ni/Ni_3C composite after 80 % reduction in thickness in cold rolling. c. TEM inspection of Ni produced by powder metallurgy after 80 % reduction in thickness in cold rolling. d. APT map of Ni and C atom distribution. f. APT map of C atom distribution.

Fig. 5-11 *In situ* tensile test of graphene-derived Ni/Ni_3C composite. a. *In situ* tensile test with DIC strain map. b. Close-up observation of the crack initiation at the artificial notch.

Fig. 5-12 *In situ* three-point bending test of graphene-derived Ni/Ni_3C composite. a. *In situ* three-point bending test under SEM. b. Close-up inspection of the crack propagation of three-point bending Ni/Ni_3C sample before chemical etching. c. After chemical etching.

List of Tables

Chapter 1 Introduction

1.1 Graphene – Potential and Challenge

Graphene is a single layer of carbon atoms [1]. It was first discovered in the early 21st century by A.K. Geim and K.S. Novoselov, and has been considered as a typical multi-functional, super material [2]. The strong sp^2 bonds enable graphene an ultrahigh stiffness of 1 TPa and an ultrahigh strength of 130 GPa [3]. The free-standing π bonds endow graphene outstanding electronic and thermal conductivity [4,5]. The one-atom-thick feature also makes graphene transparent and flexible, as well as a high theoretical specific surface area up to 2630 m^2/g [6]. Recently, it was found that by overlapping two layers of graphene to a certain degree, electrons can transfer without resistance, forming superconductors [7]. The most important derivative of graphene is graphene oxide, on which a variety of oxygen-containing functional groups are attached [8]. The functional groups enable graphene oxide unique properties, including outstanding dispersing ability in polar/nonpolar liquid, optical nonlinearity, and ion absorptivity [9]. Graphene and graphene oxide have already shown huge impacts on different fields, such as electronic devices, energy storage, composites, water purifying, and so on [10–13].

However, after years of intensive research, the commercialization of practical graphene products is still challenging. One roadblock is the synthesis of graphene [14]. Large, intact graphene sheets are usually fabricated by chemical vapor deposition (CVD) [15], which requires strict environmental control and sophisticated instruments, leading to the high cost and low productivity. Small graphene and graphene oxide nanoflakes can be synthesized by mechanical exfoliation [16] and Hummer's method [17–20], respectively, at kilogram level. These nanoflakes, although cheaper and more accessible, are often defective and contaminated [14]. In addition to the synthesis, how to effectively and efficiently utilize graphene remains unresolved. Large and intact graphene sheets are mainly used in transistors and conductive films. Graphene and graphene oxide nanoflakes are often used in energy storage and composites [14]. However, the defects and agglomeration of graphene nanoflakes largely deteriorate the properties of graphene [21–23], leading to inferior performance. Therefore, the potential of graphene has not been fully exploited; it is critical to explore new methods and new concepts to utilize graphene and its derivatives. In this dissertation, Li-S batteries and metal matrix composites are used for proof-of-concept studies of employing graphene in energy storage and energy-saving structures.

1.2 Graphene in Li-S batteries

1.2.1 Li-S battery – the successor of Li-ion batteries

Lithium-ion (Li-ion) battery has revolutionized human society in the past two decades. The "rocking chair" reaction mechanism renders Li-ion batteries outstanding stability and power density [24]. Unfortunately, currently commercialized cathode and anode materials for Li-ion batteries are plagued with low theoretical capacity ($LiCoO_2$ with a capacity of 270 mAh/g and $LiPFeO_4$ with a capacity of 170 mAh/g). The most advanced Li-ion batteries are approaching their maximum potential [25–27]. Clearly, Li-ion batteries cannot fulfill the urgent needs for large-scale grids and electric vehicles which require long time operation and/or high performance/weight ratio [28–30]. To overcome the aforementioned bottlenecks, efforts have been made to enhance the electrochemical performance of Li-ion battery system by replacing graphite anode with Si or Sn [31,32], developing new cathode materials [33], and exploring better electrolytes [34]. On the other hand, people have turned their attention to new battery systems with different reaction mechanisms [29,35].

Among all the candidates under the "beyond Li-ion battery" arena, lithium sulfur (Li-S) battery has attracted extensive attention and is considered as one of the most promising successors for Li-ion battery [36–38]. When sulfur couples with lithium metal anode, a complete conversion between sulfur and its lithiated product Li_2S delivers an ultra-high capacity of 1650 mAh/g, which is 6 times higher than $LiCoO_2$. Considering the average voltage of 2.2 V vs. Li/Li+, the theoretical energy density of Li-S reaches 2600 Wh/kg [39–41]. A fully packed Li-S battery is expected to deliver an specific energy of 400 to 600 Wh/kg, two times higher than the most advanced Li-ion batteries [37,42,43]. Li-S battery system also carries additional assets, such as low cost and environmentally friendly.

However, Li-S battery suffers several problems that severely hamper its commercialization (Fig. 1-1). Firstly, both sulfur and Li_2S are insulating, leading to the low utilization of active materials. Secondly, intermediates between sulfur and Li_2S (Li_2S_8, Li_2S_6, and Li_2S_4) are highly soluble in organic electrolyte, causing “shuttle effect” which deteriorates both anode and cathode [44,45]. Thirdly, the conversion between sulfur and Li_2S results in over 70 % volume change, inducing cracks and pulverization in the cathode. To address the aforementioned challenges, an accessible and effective approach is to incorporate sulfur or Li_2S with a scaffold constructed with conductive materials such as conductive polymers, carbon materials, and metal compounds. A qualified scaffold should have an intimate connection with sulfur, possess porous architecture to enhance sulfur loading and encapsulate polysulfides, and be flexible to buffer volume fluctuation [46–48].

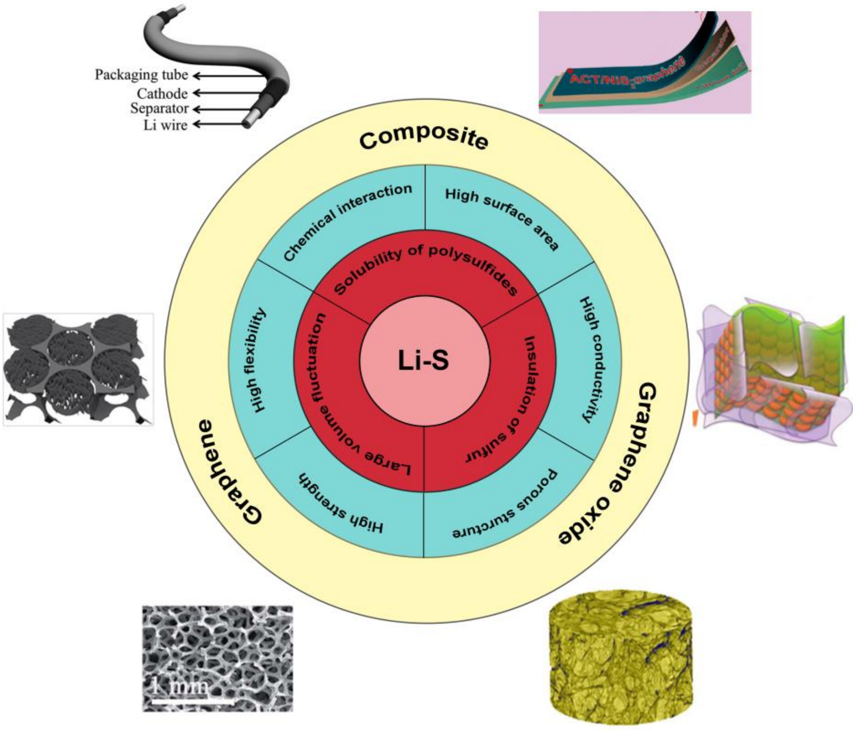

Fig. 1-1 Li-S battery and graphene. Li-S battery suffers three major challenges: insulation of sulfur, solubility of polysulfides, and large volume fluctuation. Graphene and its derivatives are a potential solution for these problems. Graphene and graphene oxide (GO) are mechanically robust and flexible, so they can buffer the large volume change. High specific area and functional groups are able to encapsulate and immobilize polysulfides, thereby reducing shuttle effects. The high conductivity of graphene and reduced GO (rGO), as well as their constructed porous structures lay the foundation for outstanding electron and ion transferability, enabling higher utilization of active material. Graphene and its derivatives also have the potential for further development, such as

doping, functionalization, and compositing with other materials, including metal components, carbonaceous materials, and conductive polymers. Images reproduced from ref. [49], [50], [51], [52], [53], [54].

Intriguingly, graphene and graphene oxide (GO) are gifted unique properties which are especially beneficial for Li-S batteries (Fig. 1-1). Graphene is prestigious for its exceptional conductivity [5], which can effectively facilitate the electron transfer for insulating sulfur/Li_2S. Graphene's outstanding mechanical robustness and flexibility [3] are able to buffer the large volume fluctuation during charge/discharge and facilitate the fabrication of flexible devices [55]. Its ultra-high specific area (2630 m^2/g) [6] empowers graphene-constructed scaffolds with superlative porous architecture for sulfur loading and redox. GO sheets, on the other hand, are often attached with numerous functional groups which tend to chemically interact with polysulfides, offering a strong entrapping ability [56–58]. In addition to their intrinsic properties, graphene and its derivatives can be functionalized or doped with functional groups or heteroatoms, further enhancing their polysulfide immobilizing ability. Moreover, graphene and GO are highly compatible with many engineering materials such as metal components, carbon materials, and conductive polymers. Graphene and its derivatives have been heavily employed to enhance the electrochemical performance of Li-S batteries [59–61] and hold promises in removing the roadblocks (the inevitable anode degradation and the actual low energy density) on the way of commercialization of Li-S batteries [37].

1.2.2 Graphene composites for Li-S battery cathodes

Sulfur/polysulfides can interact with graphene and its derivatives physically and chemically. The physical interaction stems from the geometrical feature and molecular structure of graphene. Macroscopically, graphene and its derivatives are flexible 2D materials which are able to encapsulate sulfur particles (Fig. 1-2a) [62]. Such configuration facilitates the electron transfer between insulating sulfur and electrolyte, entraps the dissolved lithium polysulfides, and buffers the large volume change between sulfur and Li_2S, thereby enhancing active material utilization, mitigating shuttle effect, and protecting the cathode from fracture and pulverization. Microscopically, graphene has a hexagonal honeycomb crystal structure with carbon-carbon sp^2 bonds connecting each atom and π/π^* bonds orientating out of the plane (Fig. 1-2b) [63]. Such highly symmetric bonding configuration leads to the non-polar nature of graphene. Intriguingly, element sulfur S_8 has a double layered, octagonal structure, which is also symmetric and non-polar. The non-polar/non-polar configuration results in strong van der Waals' interaction and superior wettability between graphene and melted element sulfur, leading to an extremely small contact angle (Fig. 1-2c) [63]. The outstanding wettability facilitates infiltration of sulfur into the scaffolds constructed with graphene and its derivatives. However, the hexagonal structure lacks out-of-plane interactions as such van der Waals' force is the only interaction route between graphene and sulfur/lithium polysulfides [64]. The weak interaction often results in poor immobilization of polysulfides. Comparing with perfect graphene, defective graphene exhibits stronger van der Waals' force with sulfur [64]. Cathode performance can be enhanced by introducing defects in graphene, such as vacants, heteroatoms, and edges on graphene sheets.

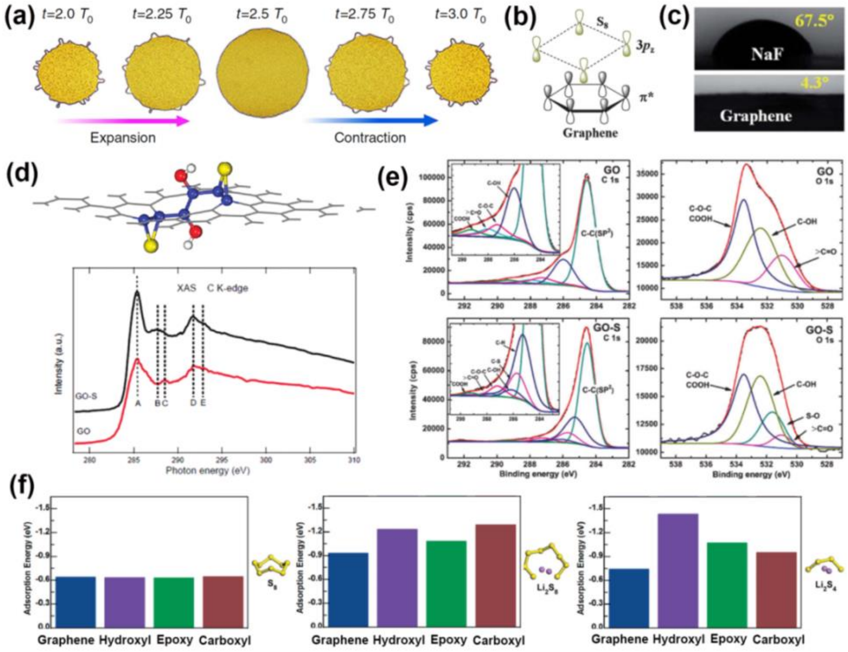

Fig. 1-2 Interactions between sulfur and graphene/GO. a. Graphene and GO are able to encapsulate sulfur particles, thereby enhancing electron transfer, entrapping the dissolved polysulfides, and buffering the volume change [62]. b. Both graphene and element sulfur have symmetrical, non-polar structure [63]. c. The wettability between graphene and sulfur is

outstanding [63]. d. Sulfur can bond with the functional groups on GO, leading to a stronger chemical interaction [65]. e. XPS spectra illustrate that C-S and O-S bonds formed after sulfur infiltration [66]. f. Oxygen functional groups have no major influence on the adsorption of S_8 but strongly effect the adsorption of polysulfides. Hydroxyl functions have the strongest interaction with Li_2S_4 and carboxyl functional groups have the strongest interaction with Li_2S_8 [67].

The chemical interaction mainly results from the functional groups attached to graphene sheets. GO, which is also called graphitic acid, is usually prepared by Hummer's method [17–20], in which strong oxidizing agents (H_2SO_4, HNO_3, $KMnO_4$, H_3PO_4) are used to forcibly insert between graphene layers in graphite and break the van der Waals' bonds. Because of such violent method, comparing with graphene, GO is highly defective, containing a large amount of chemical (functional groups) and structural (vacants and voids) defects [58]. In addition to carbonyl (C=O) and oxygen atoms (=O), epoxy, hydroxyl (-OH), carboxyl (-COOH), and phenol were also found on the graphene sheets [58]. The functional groups, mainly hydrogen containing groups such as hydroxyl and carboxyl, can be entirely or partially removed by thermal or chemical reductions. The reduced product, which is the so-called reduced GO (rGO), shows relatively higher conductivity, more mechanical robustness, and even higher defectiveness than GO [57]. The functional groups and defects, although deteriorate the conductivity and mechanical properties of graphene, render GO several unique properties. Firstly, GO is hydrophilic and hence dispersible in water and other solvents, such as liquid methanol, ethanol, and acetone. The hydrophilic nature not only reduces the tendency of restacking and aggregation, but also can be used for fabricating hierarchically porous structures. Secondly, sulfur can be incorporated with GO via multiple liquid methods, increasing sulfur loading and promoting homogenization. Finally, the most important advantage of GO for Li-S batteries is that the functional groups enable strong chemical interactions with lithium polysulfides, effectively entrapping and immobilizing them and largely reducing the shuttle effect. Soft X-ray absorption spectroscopy (XAS) inspection revealed that both epoxy and hydroxyl groups interacted with sulfur (Fig. 1-2d) [65]. X-ray photoelectron spectroscopy (XPS) discovered C-S and O-S bonds in a GO/S cathode (Fig. 1-2e) [66], suggesting that sulfur was chemically bonded to the GO. The incorporation of sulfur with GO demonstrated only a weak influence on the electronic structure of carbon but a considerable impact on the density of the occupied O 2p configurations, indicating that sulfur mainly reacted with the functional groups other than the carbon atoms [66]. Density functional theory (DFT) calculations [52] revealed that substantial binding occurred between the oxygen-containing groups and sulfur/polysulfides, especially S_3 anions. Wasalathilake *et al.* [67] further investigated interactions between sulfur, polysulfides, and graphene. Oxygen functional groups have no major influence on the adsorption of S_8 but strongly affect the adsorption of polysulfides. Hydroxyl functions have the strongest interaction with Li_2S_4 and carboxyl functional groups have the strongest interaction with Li_2S_8 (Fig. 1-2f).

Both physical and chemical interactions can be further enhanced by reforming and/or redeveloping graphene and GO. Rational design of graphene scaffold architectures can enhance the physical encapsulation. Various methods, such as hydrothermal annealing, CVD, templating, and acid/alkane etching, were employed to construct hierarchically porous structures on graphene/GO substrates. The micropores, with a pore size smaller than 2 nm, are able to affect the kinetics of S_8 dissolution process [68] and restrain the diffusion of polysulfide chain [69,70]. The van der Waals' force has a significant increase of adsorption strength as the pore size decreases from 1 nm to 0.75 nm, thereby improving the cyclic stability of Li-S batteries [67]. The mesopores (pore sizes ranging from 2 to 50 nm) have strong physical absorption of sulfur and polysulfides, increasing the utilization of active materials and improving specific capacity [48,71,72]. The macropores (pore sizes larger than 50 nm), on the other hand, have little influence on polysulfide confinement, but can improve sulfur loading, buffer volume change, and enhance electrolyte accessibility [73–75]. Two major approaches are often used to improve the chemical interactions: doping and functionalization. Many heteroatoms such as N [76,77], S [78], P [79], I [80], and B [81], were doped or co-doped onto graphene and its derivatives. The doped heteroatoms are able to form bonds with sulfur and polysulfides, doubling or even tripling the bonding energy [37,82]. Functional groups such as catecholamine [83], amino [42,84], phenyl sulfonate [85], oleylamine [68], and sulfhydryl [86] were implanted into graphene sheets to improve the bonding energy between graphene/GO and lithium polysulfides. The functionalization is often conducted in liquid under mild conditions, making the fabrication of functionalized graphene sheets efficient and low-cost.

1.2.3 Graphene composites for Li-S battery current collectors, interlayers, and anodes

Instead of cathode, graphene, GO/rGO, and their composites have been exploited in other components of Li-S batteries. To improve sulfur utilization and eliminate shuttle effect, a bifunctional cathode interlayer was put forward in the Li-S battery system [87,88]. A qualified cathode interlayer should be light-weight, robust, flexible and have a strong interaction with polysulfides, which are typical features of graphene and its derivatives. rGO was first used to build cathode interlayers, rendering high specific capacity and cyclic ability (Fig. 1-3a) [89,90]. Oxides, sulfides, and nitrides, such as TiO_2 [91], MnO_2 [92], MoS_2 [93], and BN [94], have been composited with graphene for the cathode interlayers. Because of the strong interaction between metal oxides and polysulfides, the battery with TiO_2/graphene interlayer showed a low capacity degradation rate of 0.01% and 0.018% per cycle, measured over 1000 cycles at 2 and 3 C, respectively [91]. A prototype supramolecular material, cucurbituril (CB), was then integrated with graphene, forming an interlayer. As an efficient lithium polysulfides capsule for Li-S batteries, CB has a large atomic fraction of binding sites, effectively reducing shuttle effect [95]. The interlayer, however, was a "dead weight" for the battery since it did not participate in the chemical reactions. Therefore, it is critical to reducing the volume fraction of the interlayer component. An ultra-thin interlayer with less than 100 nm in thickness and <1% in volume compared with the cathode was recently synthesized by mixing naphthalimide-functionalized poly(amidoamine) (PAMAM) G4 dendrimer (Naph-Den) and mildly oxidized graphene oxide (mGO). The amide-containing dendrimer molecules interacted actively with polysulfides, leading to an outstanding capacity retention rate (0.008 % capacity decay per cycle) [96].

The separator is a critical component of a battery system. A superior separator for Li-S batteries should not only have a good ionic conductivity, but also suppress the migration of polysulfides during cycling. Since traditional separators are unable to meet such requirements, new separators fabricated by graphene composites have been developed [97–106]. When being used as a separator, GO exhibited a premselective mechanism. The oxygen electronegative atoms modified GO to a polar plane, which allowed the transition of positively charged species (Li^+) while rejecting the transportation of negatively charged species (S_n^{2-}) due to the electrostatic interactions [97]. To further promote such mechanism, $Li_4Ti_5O_{12}$ (LTO) [100] and MOF [102] were separately composited with rGO via vacuum-filtration. The LTO nanospheres had a high chemical affinity with polysulfides and an excellent ionic conductivity; the MOF particles endowed a feasible ion transfer pathway while blocking the dissolute polysulfides; the graphene layers cemented the particles, serving as a physical barrier for polysulfides. Batteries with the LTO/rGO or MOF/rGO separators exhibited ultralow capacity decay rate. A twinborn TiO_2–TiN heterostructure was recently composited with GO for Li-S battery separators. The merits of highly adsorptive TiO_2 with conducting TiN was well combined and achieved smooth trapping–diffusion–conversion of lithium polysulfides across the interface [105].

Graphene and its derivatives also have the potential to be used in current collectors, electrolytes, and anodes. A graphene constructed current collector enabled outstanding lifespan and rate ability because it was able to entrap polysulfides and improve the battery conductivity (Fig. 1-3b) [107]. The rGO electrolyte additives have been proven to enhance ionic and electronic conductivities while reducing the lithium ion diffusion length and buffering the stress/strain in all-solid batteries, promoting the cyclic stability and lifespan [108,109]. Graphene/GO was found to stabilize Li anode [110]. The anode constructed with graphene wrapped Li_xM (M= Si, Sn, or Al) nanoparticles exhibited an outstanding resistance to air and water (Fig. 1-3c). When coupling with sulfur as the cathode, the full cell demonstrated an excellent cycling stability at 0.5 C and maintained a capacity of 858 mAh/g after 110 cycles with a coulombic efficiency of 99.5 % [110]. The SEI-coated graphene (SCG) framework, on the other hand, effectively prevented the growth of dendrites [111].

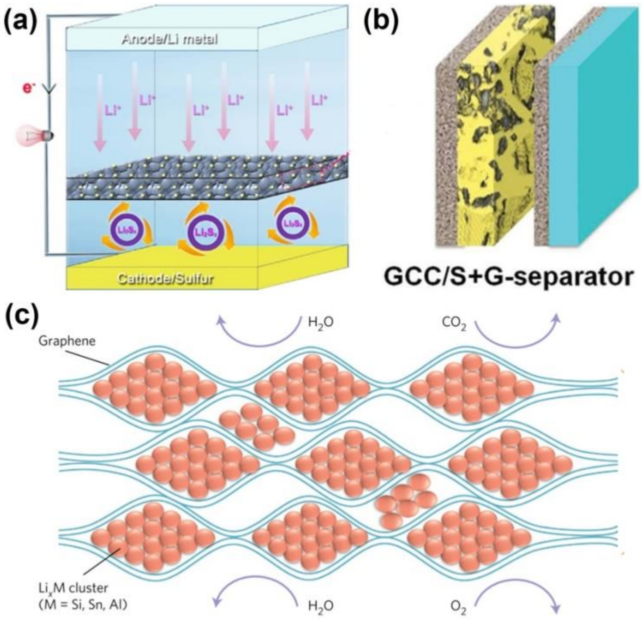

Fig. 1-3 Graphene and its derivatives for battery components other than cathode. a. Graphene/carbon black cathode interlayer anchored on polysulfides [90]. b. Graphene as both current collector and cathode interlayer [107]. c. Graphene wrapped Li_xM (M= Si, Sn, or Al) nanoparticle anode, showing an outstanding resistance to air and water [110].

1.3 Graphene in metal matrix composites

1.3.1 Graphene/metal composites

In addition to exploiting renewable energy resources and employing environmentally friendly energy storage, another critical approach to reduce energy consumption and improve energy usage efficiency is to develop energy-saving structural materials. Future energy-saving structural materials need to be lightweight, stiff, strong, and tough. They are also required to be able to work in harsh environments, such as high temperature, high corrosive or high radiative environment. However, single-phase materials are difficult to simultaneously fulfill these requirements. A rational strategy is to combine different materials and take advantage of their unique advantages, forming polymer-based, metal-based, and ceramic-based composites. These composites, if well fabricated, can exhibit superior properties. Among all the composites, metal matrix composites have an incomparable advantage of high-toughness and have been intensively studied for decades [112]. Different reinforcing agents, such as Al_2O_3 [113–115], SiC [116,117], B_4C [118,119], and carbon nanotube [120] *et al*. are attempted. The effects of size [119,121], distribution [122,123], shape [124], and surface properties [116] of the reinforcing particles on the mechanical performance have been extensively studied. Although a variety of methods have been employed, it is still challenging to achieve homogeneous dispersion and strong interfacial bonding of the reinforcers.

The ultra-high elastic modulus and strength, as well as the unique 2D morphology, make graphene an ideal reinforcer for metal matrix composites. If 10 wt. % of monolayer graphene flakes can be homogeneously dispersed in the Al matrix, theoretically, an over 200 % improvement of stiffness and an over 500 % enhancement of strength can be achieved. Considering the low density of graphene (2.2 g/cm^3), the reinforcing efficiency of graphene can be incredible. Because of these reasons, graphene-enabled Al, Ni, Ti, Mg, and Cu composites have attracted extensive attentions [125,126]. Ball milling was widely used to mix graphene flakes with metal powders to enhance the dispersion uniformity [127–130]. Pérez-Bustamante *et al.* [127] fabricated Al/graphene composites by ball milling and sintering. They found that longer ball milling time can improve strength due to better homogeneity and stronger bonding (Fig. 1-4a). Semi powder metallurgy, which mixes graphene or graphene oxide (GO) sheets with metal powders in liquid, was found to be more effective in dispersing reinforcements and enhancing graphene/metal bonding [131–133]. Wang *et al.* [131] treated Al powders by PVA, creating a hydrophilic layer on the Al surface, which facilitated the adhesion of GO flakes. After reduction and sintering, the Al/rGO composite exhibited a tensile strength of 249 MPa with 13% elongation, which was a 62% improvement in tensile strength compared to that of unreinforced Al (154 MPa) (Fig. 1-4b and c). Li *et al.* [133] hypothesized that the Al powder surface would be ionized to Al^{3+} upon contacting with water. The positively charged surface interacted with negatively charged GO sheets, leading to a homogeneous coating. When 0.3 % GO was composited with Al, the sintered composites exhibited an 18 % and 17% increase in elastic modulus and hardness, respectively, over unreinforced Al. Several new methods such as plasma sintering, molecular-level mixing [134], electrochemical deposition [135], electrostatic adsorption [136], and chemical adsorption [137] were recently exploited. Zhao [134] fabricated rGO/Ni powders by molecular-level mixing (MLM). Specifically, GO was mixed with $NiCl_2.6H_2O$ and reduced by Ar/H_2. The rGO/Ni powders were then sintered by spark plasma sintering (SPS). The obtained graphene/Ni composites exhibited a notable enhancement of yield strength and ultimate tensile strength (Fig. 1-4d and e). After high temperature sintering, severe plastic deformation, such as high-ratio differential speed rolling [130], hot extrusion [131], solid-state stirring [138], hot isostatic pressing [129], and uniaxial compression [136], was employed to densify the composite with the goal to improve material strength and graphene sheets dispersion. Chen *et al.* [138] combined liquid state ultrasonic processing and solid-state stirring to achieve a homogeneous dispersion of graphene nanoplatelets in Mg matrix composites. The graphene nanoplatelets exhibited a close bonding with Mg, leading to high strengthening efficiency.

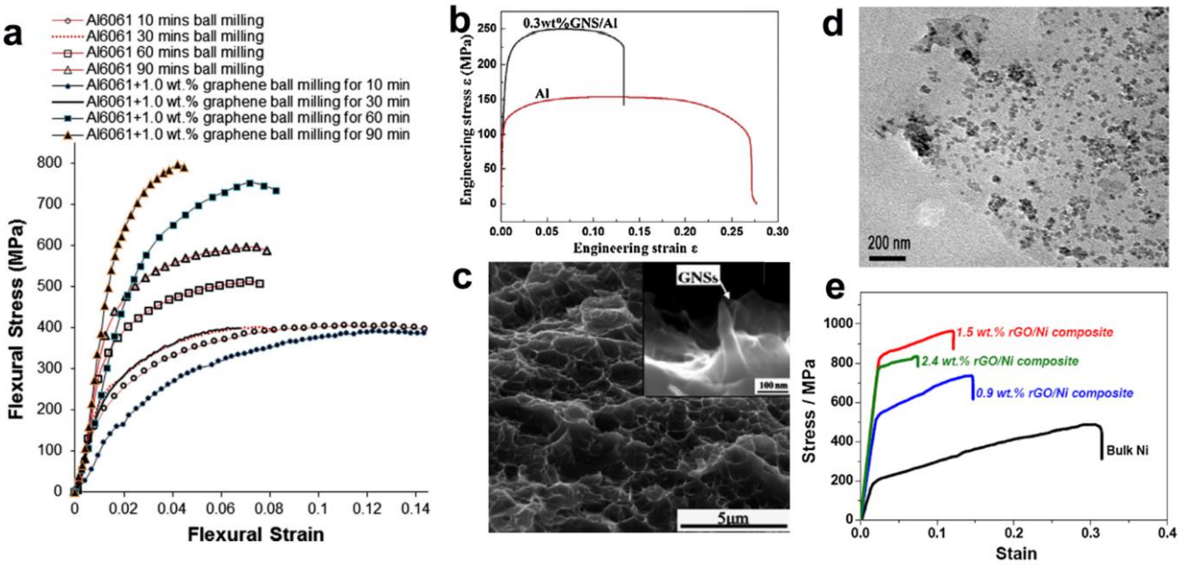

Fig. 1-4 Graphene/metal composites. a. Mechanical performance of graphene/AA6061 composites fabricated by ball milling [127]. b,c. Graphene/Al composites fabricated by semi-powder metallurgy [131]. d,e. Graphene/Ni composites fabricated by molecular-level mixing [134].

Along with the diverse methods of fabricating graphene/metal composites is the highly fluctuate mechanical performance. In some studies, graphene showed superior enhancement to the metal matrix [131,133,136]; in other studies, graphene exhibited minor and even negative effects on the mechanical properties [128,139]. To build better graphene-enabled metal matrix composites, it is important to understand the strengthening mechanisms of graphene in metals. Kim *et al.* [140] deposited single or double-layered graphene sheets fabricated by CVD on Cu and Ni substrates, forming nanolayered composites (Fig. 1-5a and b). The graphene/metal composites exhibited high strength in the nanopillar compression tests. Microstructural characterization revealed that graphene blocked the propagation of dislocations across the metal–graphene interface (Fig. 1-5c and d). MD simulation unveiled that the graphene sheet can pin the dislocation core because the formation of a surface edge structure at the graphene/metal interface is not favored due to the high bending stiffness of the graphene (Fig. 1-5e). This pioneering study experimentally and theoretically demonstrated that monolayer graphene can strengthen metals [140]. Another strengthening mechanism is graphene-enabled grain refinement. Several studies reported that the grain size was reduced after adding graphene [141–143]. Such grain refinement may be due to the heterogeneous nucleation induced by graphene or graphite. Some studies also demonstrated that graphene may reinforce metal matrix composites via filler strengthening [139,141,144], like carbon fiber reinforced composites. However, considering the small size of graphene nanoflakes and the fact that graphene may not fully stretch or not alligned in the metal matrix, it is questionable whether the load can effectively transfer to graphene.

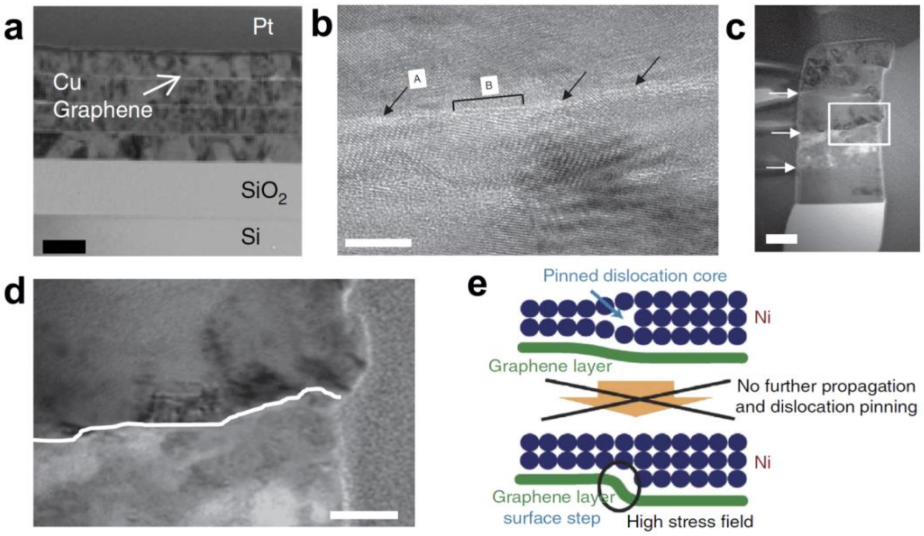

Fig. 1-5 Graphene/dislocation interactions [140]. a. Graphene/Cu composite fabricated by CVD. Scale bar, 200 nm. b. Close-up inspection of metal–graphene interface. Scale bar, 5 nm. c. TEM image of a Cu–graphene nanopillar with 125-nm repeat layer spacing at a low magnification after deformation. Scale bar, 100 nm. d. TEM image of a Cu–graphene nanopillar after deformation that shows a higher density of dislocations above the graphene interface. Scale bar, 50 nm. e. Schematic figure illustrating the blocking of dislocation propagation at the metal–graphene interface.

Therefore, although extensive studies have been carried out, graphene-enabled metal matrix composites are still at the initial stage. Fundamentally, the strengthening mechanisms of graphene are still unclear. How do the dislocations interact with graphene? How do the graphene flakes deform with the matrix? How does the load transfer to graphene? Practically, considering the amazing mechanical properties of graphene, the mechanical performance of synthesized graphene/metal composites are much lower than the expectation. Three factors likely hindered the development of metal/graphene composites. The first one is the agglomeration of graphene. Due to their high surface energy, graphene sheets have a strong tendency to restack during mixing. However, comparing with the strong sp^2 bond, the Van der Waals bond between graphene layers is weak. Therefore, agglomerated graphene (graphite) may not strengthen the metal matrix. The second factor is the degradation of graphene. As proven by experiments and numerical simulations, defects can severely deteriorate the mechanical properties of graphene. However, the mix, sinter, and deformation during the fabrication of metal matrix composite inevitably induce defects into graphene flakes. In some studies, graphene oxide was used, which is highly defective and may have even worse mechanical properties than metal matrix, like Ni and Ti. The last issue is the reactions between metals and graphene. Unlike stable ceramic particles, such as Al_2O_3, SiC, and B_4C, graphene is reactive to some metals. Previous studies reported the formation of carbides, such as Al_3C_4 and Ni_3C [127,128,145], in graphene metal matrix composites. It is uncertain how the carbides influence the mechanical performance of the composites.

1.3.2 Bioinspired high-toughness composites

A joint enhancement of strength and toughness is a vital requirement for next generation structural materials. Unfortunately, this pursuit often falls into a compromise between hardness versus ductility [146]. Moreover, in most engineering materials, once fracture is initiated, cracks propagate rapidly without any shielding behind the crack tip [147]. The wisdom of Nature negates this conflict by constructing materials with a hierarchical architecture, all while utilizing only limited materials and nontoxic processes [148]. A common example is nacre (mother-of-pearl). As one of the most well-known natural armors, nacre is endowed by a laminiated, brick-and-mortar structure composited with aragonite (a mineral form of $CaCO_3$) platelets and biopolymer [149]. Acting as the major load-bearers, aragonite platelets (the bricks) with 5-10 μm in length and 0.5 μm in thickness are constructed by nanocrystals (Fig. 1-6a) [149]. The biopolymer (the mortar) with only several nanometers in thickness closely binds the aragonite platelets together (Fig. 1-6b) [150]. Such a complex structure enables multiple extrinsic toughening mechanisms at different length-scales, leading to an outstanding combination of strength and toughness that is hardly seen in engineered materials. The layer-by-layer architecture redirects the crack growth into a tortuous path, effectively consuming fracture energy via extending the crack length and reducing stress concentration (Fig. 1-6c) [151]. In addition, mineral bridges prevent the crack opening [152] while bio-polymer layers dissipate fracture energy [153]. In the meantime, surface nanoasperities interlock the aragonite platelets, preventing large-scale delamination [154].

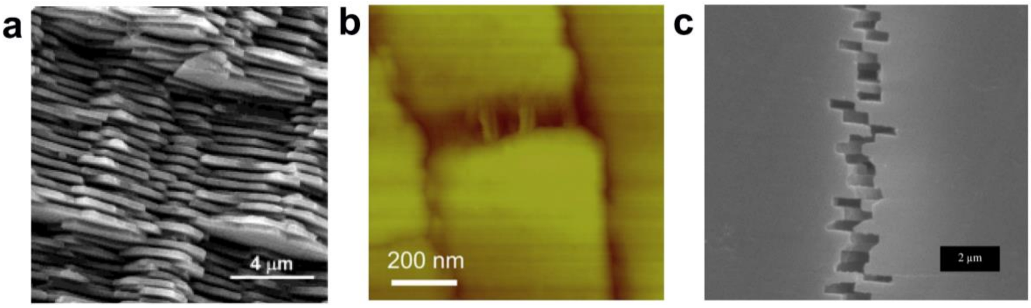

Fig. 1-6 Microstructure of nacre. a. The laminated, brick-and-mortar structure of nacre [149]. b. The biopolymer strands formed between aragonite platelets [150]. c. Crack propagation of nacre under tension [154].

While entirely mimicking the reinforcing multitude of these scale levels is difficult, the hierarchical architecture may hold the key of suppressing the dilemma between strength and toughness, and therefore, many researchers have gained inspiration from these bio-designs for new composite materials. Similar to nacre, ceramic composites with additional soft phases like polymers or metals have shown that brittle ceramic materials can be converted into tough materials [155–162]. Bioinspired polymer composites with added hard ceramic platelets exhibited high strength, outperforming most engineering polymers, while retaining ductility [163–167]. These studies are nothing short of remarkable; the toughness of such composites was magnitudes higher than the simple mixture of constituents. However, the intrinsically low ductility of ceramics and low strength of polymers limit the overall potential mechanical performance. Moreover, weak bonding between hard phases and soft phases may also lead to interface delamination. Therefore, it can be expected that cloning nacre's architecture with stronger constituents such as metals in engineered composites is a more promising yet more challenging task. Freeze-casting has been widely used to construct laminated ceramic composites [155–157]; polymer crosslinking, on the other hand, is the primary route to fabricate layer-by-layer architectured polymer-based composites [164,165]; compressing sintering, powder processing, electrochemical deposition and laser sintering have been employed to synthesize nacre-like metal-based composites [12,13,135,141,168]. The soft phases (polymers and metals) with a volume fraction ranging from 5 % to 40 % in the nacre-like ceramic composites effectively improved the ductility of the composites, with a tradeoff of reduction in the characteristically high strength of ceramics. The hard phase (mainly ceramic flakes) in nacre-like polymer-based composites prohibited the decoiling of polymer chains, which notably enhanced the strength of the polymer matrixes. In the nacre-like metal-based composites, the volume fraction of metal matrix, which is normally considered as the soft phase, is often over 70 %. Hard phases with platelet-like morphology, such as graphene, ceramics, and intermetallic compounds, were homogeneously dispersed in the metal matrixes, jointly improving of strength and toughness.

1.4 Research plan and objectives

According to the above literature review, graphene exhibits a great potential in energy storage and metal matrix composites. However, most of the graphene-based or graphene-enabled products are still at the concept level. In addition to the difficulties in mass graphene production and preservation, how to effectively use graphene remains challenging. This dissertation aims to explore effective and efficient ways to utilize graphene in Li-S batteries and metal matrix composites. Considering the cost and effectiveness, it is hypothesized that graphene/porous carbon composite is a better solution for high-performance Li-S cathodes. The porous carbon can provide a low-cost, conductive framework for electroactive materials while graphene can encapsulate and immobilize dissolved polysulfides, leading to a synergetic enhancement for the electrochemical performance. Moreover, the malfunction of Li anode is also a roadblock of Li-S batteries but the failure mechanisms are not clear yet. Graphene-enabled composites are expected to prevent the side reactions on the Li anode. Finally, the strengthening effects of graphene in metal matrix composites are, to a large extent, uncertain. Although intact graphene has extremely high modulus and strength, the agglomeration, deterioration, and side reactions of graphene are difficult to avoid during mixing, sintering, and deformation, which would largely decrease the final reinforcing efficiency. We can take advantage of graphene's 2D morphology instead of the intrinsic high modulus and strength in the fabrication of graphene-enabled metal matrix composites. Graphene sheet can wrap around metal powders and react with metals, forming second phase particles with superior homogeneity. Three research tasks are designed according to the above three hypotheses.

Task 1 Synthesizing graphene/porous carbon composites for high-performance Li-S battery cathodes (Chapter 2)

Biomass materials will be converted into conductive carbon while reserving their porous structure. Subsequently, graphene will be incorporated with the biomass-derived porous carbon via feasible chemical/physical methods, forming graphene/porous carbon composites. The graphene/porous carbon composites will be assembled with the lithium anode, separator, and electrolyte, forming Li-S coin batteries. The electrochemical performance of the Li-S batteries will be characterized. The objective of the research task is to fabricate high-performance Li-S battery cathodes with graphene/porous carbon composites.

Task 2 Unveiling Li anode degradation mechanisms in Li-S batteries and designing graphene composites to prevent the Li degradation (Chapter 3)

The failure mechanism of Li anode in Li-S batteries will be investigated by observing cycled Li-S batteries. The Li-S batteries will be discharged/charged for different periods to observe the stripping/plating of the Li surface. Methods of preventing the Li anode degradation and enhancing Li-S battery performance will be developed. Graphene-enabled composites will be employed to construct porous interlayers and/or stronger solid-electrolyte interfaces (SEIs). The objective of this research task is to unveil the Li-S battery failure induced by Li anode malfunction and develop graphene composites to prevent the malfunction of Li anode.

Task 3 Constructing graphene-enabled metal matrix composites with nacre-like microstructure (Chapter 4 and Chapter 5)

Homogeneously dispersing graphene and compositing graphene with metal powders without agglomeration are two keys to fabricated graphene reinforced composites. Methods that can prevent the restacking of graphene flakes, such as surface activation by surfactant and/or freeze-drying, will be developed. Subsequently, the graphene/metal powders will be sintered to fabricate graphene/metal composites with nacre-like, laminated microstructure. Al and Ni will be chosen as metal matrix materials because of their high ductility and wide applications. Finally, the stiffening, strengthening, and toughening mechanisms of graphene/metal composites will be studied. The objective of the research task is to achieve simultaneously high strength and high toughness in graphene/metal composites.

References

[1] K. S. Novoselov, D. Jiang, F. Schedin, T. J. Booth, V. V. Khotkevich, S. V. Morozov, and A. K. Geim, Two-dimensional atomic crystals, Proc. Natl. Acad. Sci. 102 (2005) 10451-10453.

[2] A.K. Geim, K.S. Novoselov, The rise of graphene, Nat. Mater. 6 (2007) 183-191.

[3] C. Lee, X. Wei, J.W. Kysar, J. Hone, Measurement of the elastic properties and intrinsic strength of monolayer graphene, Science 321 (2008) 385-388.

[4] Y.W. Tan, Y. Zhang, K. Bolotin, Y. Zhao, S. Adam, E. H. Hwang, S. Das Sarma, H. L. Stormer, and P. Kim, Measurement of scattering rate and minimum conductivity in

graphene, Phys. Rev. Lett. 99 (2007) 246803.

[5] A. A. Balandin, S. Ghosh, W. Bao, I. Calizo, D. Teweldebrhan, F. Miao, C. N. Lau, Superior thermal conductivity of single-layer graphene 2008, Nano Lett. 8 (2008) 902-907.

[6] F. Bonaccorso, L. Colombo, G. Yu, M. Stoller, V. Tozzini, A.C. Ferrari, R.S. Ruoff, V. Pellegrini, Graphene, related two-dimensional crystals, and hybrid systems for energy conversion and storage, Science 347 (2015) 1246501.

[7] Y. Cao, V. Fatemi, S. Fang, K. Watanabe, T. Taniguchi, E. Kaxiras, P. Jarillo-Herrero, Unconventional superconductivity in magic-angle graphene superlattices, Nature 556 (2018) 43-50.

[8] D.R. Dreyer, S. Park, C.W. Bielawski, R.S. Ruoff, The chemistry of graphene oxide, Chem. Soc. Rev. 39 (2010) 228-240.

[9] D. Chen, H. Feng, J. Li, Graphene oxide : preparation, functionalization, and electrochemical applications, Chem. Rev. 112 (2012) 6027-6035.

[10] A.K. Geim, Graphene : status and prospects, Science 324 (2009) 1530–1534.

[11] Y. Zhang, Z. Gao, N. Song, J. He, X. Li, Graphene and its derivatives in lithium-sulfur batteries, Mater. Today Energy 9 (2018) 319–335.

[12] Y. Zhang, X. Li, Bio-inspired, graphene/Al_2O_3 doubly reinforced aluminum composites with high strength and toughness, Nano Lett. 17 (2017) 6907-6915.

[13] Y. Zhang, F.M. Heim, J.L. Bartlett, N. Song, D. Isheim, X. Li, Bioinspired , graphene-enabled Ni composites with high strength and toughness, Sci. Adv. 5 (2019) eaav5577.

[14] L. Lin, H. Peng, Z. Liu, Synthesis challenges for graphene industry, Nat. Mater. 18 (2019) 520-524.

[15] Y. Zhang, L. Zhang, C. Zhou, Review of chemical vapor deposition of graphene and related applications, Acc. Chem. Res. 46 (2013) 2329-2339.

[16] K.R. Paton, E. Varrla, C. Backes, R.J. Smith, U. Khan, A. O'Neill, C. Boland, M. Lotya, O.M. Istrate, P. King, T. Higgins, S. Barwich, P. May, P. Puczkarski, I. Ahmed, M. Moebius, H. Pettersson, E. Long, J. Coelho, S.E. O'Brien, E.K. McGuire, B.M. Sanchez, G.S. Duesberg, N. McEvoy, T.J. Pennycook, C. Downing, A. Crossley, V. Nicolosi, J.N. Coleman, Scalable production of large quantities of defect-free few-

layer graphene by shear exfoliation in liquids, Nat. Mater. 13 (2014) 624-630.

[17] W.S. Hummers Jr, R.E. Offeman, Preparation of graphitic oxide, J. Am. Chem. Soc. 80 (1958) 1339.

[18] S. Stankovich, R.D. Piner, S.T. Nguyen, R.S. Ruoff, Synthesis and exfoliation of isocyanate-treated graphene oxide nanoplatelets, Carbon 44 (2006) 3342-3347.

[19] D.A. Dikin, S. Stankovich, E.J. Zimney, R.D. Piner, G.H.B. Dommett, G. Evmenenko, S.T. Nguyen, R.S. Ruoff, Preparation and characterization of graphene oxide paper, Nature 448 (2007) 457-460.

[20] D.C. Marcano, D.V. Kosynkin, J.M. Berlin, A. Sinitskii, Z. Sun, A. Slesarev, L.B. Alemany, W. Lu, J.M. Tour, Improved synthesis of graphene oxide, ACS Nano 4 (2010) 4806-4814.

[21] A. Shekhawat, R.O. Ritchie, Toughness and strength of nanocrystalline graphene, Nat. Commun. 7 (2016) 10546.

[22] S. Vinod, C.S. Tiwary, L.D. Machado, S. Ozden, J. Cho, P. Shaw, R. Vajtai, D.S. Galvao, P.M. Ajayan, Strain rate dependent shear plasticity in graphite oxide, Nano Lett. 16 (2016) 1127-1131.

[23] J.H. Chen, W.G. Cullen, C. Jang, M.S. Fuhrer, E.D. Williams, Defect scattering in graphene, Phys. Rev. Lett. 102 (2009) 236805.

[24] A. Yoshino, The birth of the lithium-ion battery, Angew. Chem. Int. Ed. 51 (2012) 5798-5800.

[25] J.B. Goodenough, Y. Kim, Challenges for rechargeable batteries, J. Power Sources. 196 (2011) 6688-6694.

[26] J.B. Goodenough, Y. Kim, Challenges for rechargeable Li batteries, Chem. Mater. 22 (2010) 587-603.

[27] V. Etacheri, R. Marom, R. Elazari, G. Salitra, D. Aurbach, Challenges in the development of advanced Li-ion batteries: a review, Energy Environ. Sci. 4 (2011) 3243-3262.

[28] B. Dunn, H. Kamath, J.M. Tarascon, Electrical energy storage for the grid: a battery of choices, Science 334 (2011) 928-935.

[29] M.M. Thackeray, C. Wolverton, E.D. Isaacs, Electrical energy storage for

transportation-approaching the limits of, and going beyond, lithium-ion batteries, Energy Environ. Sci. 5 (2012) 7854-7863

[30] L. Lu, X. Han, J. Li, J. Hua, M. Ouyang, A review on the key issues for lithium-ion battery management in electric vehicles, J. Power Sources 226 (2013) 272-288.

[31] L.F Cui, Y. Yang, C.M. Hsu, Y. Cui, Carbon - silicon core - shell nanowires as high capacity electrode for lithium ion batteries 2009, Nano Lett. 9 (2009) 3370-3374.

[32] G. Derrien, J. Hassoun, S. Panero, B. Scrosati, Nanostructured Sn-C composite as an advanced anode material in high-performance lithium-ion batteries, Adv. Mater. 19 (2007) 2336-2340.

[33] P. Poizot, S. Laruelle, S. Grugeon, L. Dupont, J.M. Tarascon, Nano-sized transition-metal oxides as negative-electrode materials for lithium-ion batteries, Nature 407 (2000) 496-499.

[34] S.S. Zhang, A review on electrolyte additives for lithium-ion batteries, J. Power Sources 162 (2006) 1379–1394.

[35] R. Van Noorden, The rechargeable revolution: a better battery, Nature 507 (2014) 26-28.

[36] P.G. Bruce, S.A. Freunberger, L.J. Hardwick, J.M. Tarascon, Li–O2 and Li–S batteries with high energy storage, Nat. Mater. 11 (2011) 19-29.

[37] Q. Pang, X. Liang, C.Y. Kwok, L.F. Nazar, Advances in lithium–sulfur batteries based on multifunctional cathodes and electrolytes, Nat. Energy 1 (2016) 16132.

[38] S. Urbonaite, T. Poux, P. Novák, Progress towards commercially viable Li-S battery cells, Adv. Energy Mater. 5 (2015) 1500118.

[39] S.E. Cheon, K.S. Ko, J.H. Cho, S.W. Kim, E.Y. Chin, H.T. Kim, Rechargeable lithium sulfur battery I. structural change of sulfur cathode during discharge and charge, J. Electrochem. Soc. 150 (2003) A796-A799.

[40] S.E. Cheon, K.S. Ko, J.H. Cho, S.W. Kim, E.Y. Chin, H.-T. Kim, Rechargeable lithium sulfur battery II. rate capability and cycle characteristics, J. Electrochem. Soc. 150 (2003) A800-A805.

[41] M. Wild, L. O'Neill, T. Zhang, R. Purkayastha, G. Minton, M. Marinescu, G.J. Offer, Lithium sulfur batteries, a mechanistic review, Energy Environ. Sci. 8 (2015) 3477-

3494.

[42] Z. Li, J.T. Zhang, Y.M. Chen, J. Li, X.W.(David) Lou, Pie-like electrode design for high-energy density lithium–sulfur batteries, Nat. Commun. 6 (2015) 8850.

[43] D. Lin, Y. Liu, Y. Cui, Reviving the lithium metal anode for high-energy batteries, Nat. Nanotechnol. 12 (2017) 194–206.

[44] P.P.R.M.L. Harks, C.B. Robledo, T.W. Verhallen, P.H.L. Notten, F.M. Mulder, The significance of elemental sulfur dissolution in liquid electrolyte lithium sulfur batteries, Adv. Energy Mater. 7 (2017) 1601635.

[45] Y.V. Mikhaylik, J.R. Akridge, Polysulfide shuttle study in the Li/S battery system, J. Electrochem. Soc. 151 (2004) A1969-A1976.

[46] A. Manthiram, S.H. Chung, C. Zu, Lithium-sulfur batteries: progress and prospects, Adv. Mater. 27 (2015) 1980–2006.

[47] M.A. Pope, I.A. Aksay, Structural design of cathodes for Li-S batteries, Adv. Energy Mater. 5 (2015) 1500124.

[48] X. Ji, K.T. Lee, L.F. Nazar, A highly ordered nanostructured carbon-sulphur cathode for lithium-sulphur batteries, Nat. Mater. 8 (2009) 500–506.

[49] J. Cao, C. Chen, Q. Zhao, N. Zhang, Q. Lu, X. Wang, Z. Niu, J. Chen, A flexible nanostructured paper of a reduced graphene oxide-sulfur composite for high-performance lithium-sulfur batteries with unconventional configurations, Adv. Mater. 28 (2016) 9629–9636.

[50] Z. Gao, N. Song, Y. Zhang, X. Li, Cotton-textile-enabled, flexible lithium-ion batteries with enhanced capacity and extended lifespan, Nano Lett. 15 (2015) 8194-8203.

[51] N. Li, M. Zheng, H. Lu, Z. Hu, C. Shen, X. Chang, G. Ji, J. Cao, Y. Shi, High-rate lithium–sulfur batteries promoted by reduced graphene oxide coating, Chem. Commun. 48 (2012) 4106-4108.

[52] G. Zhou, L.C. Yin, D.W. Wang, L. Li, S. Pei, I.R. Gentle, F. Li, H.M. Cheng, Fibrous hybrid of graphene and sulfur nanocrystals for high-performance lithium-sulfur batteries, ACS Nano 7 (2013) 5367-5375.

[53] K. Xi, P.R. Kidambi, R. Chen, C. Gao, X. Peng, C. Ducati, S. Hofmann, R.V. Kumar, Binder free three-dimensional sulphur/few-layer graphene foam cathode with

enhanced high-rate capability for rechargeable lithium sulphur batteries, Nanoscale 6 (2014) 5746-5753.

[54] G. Hu, C. Xu, Z. Sun, S. Wang, H.M. Cheng, F. Li, W. Ren, 3D Graphene-Foam-Reduced-Graphene-Oxide Hybrid Nested Hierarchical Networks for High-Performance Li-S Batteries, Adv. Mater. 28 (2016) 1603–1609.

[55] H.J. Peng, J.Q. Huang, Q. Zhang, A review of flexible lithium–sulfur and analogous alkali metal-chalcogen rechargeable batteries, Chem. Soc. Rev. 46 (2017) 5237–5288.

[56] K. Haubner, J. Murawski, P. Olk, L.M. Eng, C. Ziegler, B. Adolphi, E. Jaehne, The route to functional graphene oxide, ChemPhysChem. 11 (2010) 2131–2139.

[57] Y. Zhu, S. Murali, W. Cai, X. Li, J.W. Suk, J.R. Potts, R.S. Ruoff, Graphene and graphene oxide: synthesis, properties, and applications, Adv. Mater. 22 (2010) 3906-3924.

[58] W. Gao, The Chemistry of graphene oxide, in: Graphene Oxide, Springer International Publishing, Cham, (2015) 61-95.

[59] M. Yu, R. Li, M. Wu, G. Shi, Graphene materials for lithium-sulfur batteries, Energy Storage Mater. 1 (2015) 51-73.

[60] L. Ji, P. Meduri, V. Agubra, X. Xiao, M. Alcoutlabi, Graphene-based nanocomposites for energy storage, Adv. Energy Mater. 6 (2016) 1502159.

[61] S. Wu, R. Ge, M. Lu, R. Xu, Z. Zhang, Graphene-based nano-materials for lithium-sulfur battery and sodium-ion battery, Nano Energy 15 (2015) 379-405.

[62] Y. Zhao, J. Feng, X. Liu, F. Wang, L. Wang, C. Shi, L. Huang, X. Feng, X. Chen, L. Xu, M. Yan, Q. Zhang, X. Bai, H. Wu, L. Mai, Self-adaptive strain-relaxation optimization for high-energy lithium storage material through crumpling of graphene, Nat. Commun. 5 (2014) 4565.

[63] T. Lin, Y. Tang, Y. Wang, H. Bi, Z. Liu, F. Huang, X. Xie, M. Jiang, Scotch-tape-like exfoliation of graphite assisted with elemental sulfur and graphene-sulfur composites for high-performance lithium-sulfur batteries, Energy Environ. Sci. 6 (2013) 1283-1290.

[64] Q. Zhang, Y. Wang, Z.W. Seh, Z. Fu, R. Zhang, Y. Cui, Understanding the anchoring effect of two-dimensional layered materials for lithium-sulfur batteries, Nano Lett. 15

(2015) 3780-3786.

[65] L. Ji, M. Rao, H. Zheng, L. Zhang, Y. Li, W. Duan, J. Guo, E.J. Cairns, Y. Zhang, Graphene oxide as a sulfur immobilizer in high performance lithium/sulfur cells, J. Am. Chem. Soc. 133 (2011) 18522-18525.

[66] L. Zhang, L. Ji, P.A. Glans, Y. Zhang, J. Zhu, J. Guo, Electronic structure and chemical bonding of a graphene oxide-sulfur nanocomposite for use in superior performance lithium-sulfur cells, Phys. Chem. Chem. Phys. 14 (2012) 13670-13675.

[67] K.C. Wasalathilake, M. Roknuzzaman, K. (Ken) Ostrikov, G.A. Ayoko, C. Yan, Interaction between functionalized graphene and sulfur compounds in a lithium-sulfur battery-a density functional theory investigation, RSC Adv. 8 (2018) 2271-2279.

[68] J. Park, E.T. Kim, C. Kim, J. Pyun, H.S. Jang, J. Shin, J.W. Choi, K. Char, Y.E. Sung, The importance of confined sulfur nanodomains and adjoining electron conductive pathways in subreaction regimes of Li-S batteries, Adv. Energy Mater. 7 (2017) 1700074.

[69] K. Xi, S. Cao, X. Peng, C. Ducati, R. Vasant Kumar, A.K. Cheetham, Carbon with hierarchical pores from carbonized metal-organic frameworks for lithium sulphur batteries, Chem. Commun. 49 (2013) 2192-2194.

[70] R. Chen, T. Zhao, T. Tian, S. Cao, P.R. Coxon, K. Xi, D. Fairen-Jimenez, R. Vasant Kumar, A.K. Cheetham, Graphene-wrapped sulfur/metal organic framework-derived microporous carbon composite for lithium sulfur batteries, APL Mater. 2 (2014) 124109.

[71] H.J. Peng, J. Liang, L. Zhu, J.Q. Huang, X.B. Cheng, X.F Guo, W. Ding, W. Zhu, Q. Zhang, Catalytic self-limited assembly at hard templates: a mesoscale approach to graphene nanoshells for lithium-sulfur batteries, ACS Nano 8 (2014) 11280-11289.

[72] G. Li, J. Sun, W. Hou, S. Jiang, Y. Huang, J. Geng, Three-dimensional porous carbon composites containing high sulfur nanoparticle content for high-performance lithium–sulfur batteries, Nat. Commun. 7 (2016) 10601.

[73] G. Zhou, L. Li, C. Ma, S. Wang, Y. Shi, N. Koratkar, W. Ren, F. Li, H.M. Cheng, A graphene foam electrode with high sulfur loading for flexible and high energy Li-S batteries, Nano Energy 11 (2015) 356-365.

[74] Y. Zhang, Z. Gao, N. Song, X. Li, High-performance supercapacitors and batteries derived from activated banana-peel with porous structures, Electrochim. Acta 222 (2016) 1257-1266.

[75] R. Raccichini, A. Varzi, S. Passerini, B. Scrosati, The role of graphene for electrochemical energy storage, Nat. Mater. 14 (2014) 271-279.

[76] J. Song, T. Xu, M.L. Gordin, P. Zhu, D. Lv, Y.B. Jiang, Y. Chen, Y. Duan, D. Wang, Nitrogen-doped mesoporous carbon promoted chemical adsorption of sulfur and fabrication of high-areal-capacity sulfur cathode with exceptional cycling stability for lithium-sulfur batteries, Adv. Funct. Mater. 24 (2014) 1243-1250.

[77] J. Song, Z. Yu, M.L. Gordin, D. Wang, Advanced sulfur cathode enabled by highly crumpled nitrogen-doped graphene sheets for high-energy-density lithium-sulfur batteries, Nano Lett. 16 (2016) 864-870.

[78] Z. Ma, S. Dou, A. Shen, L. Tao, L. Dai, S. Wang, Sulfur-doped graphene derived from cycled lithium-sulfur batteries as a metal-free electrocatalyst for the oxygen reduction reaction , Angew. Chem. 54 (2015) 1888-1892.

[79] H. Wu, L. Xia, J. Ren, Q. Zheng, C. Xu, D. Lin, A high-efficiency N/P co-doped graphene/CNT@porous carbon hybrid matrix as cathode host for high performance lithium-sulfur batteries, J. Mater. Chem. A 5 (2017) 20458-20472.

[80] Z. Xiao, Z. Yang, L. Zhang, H. Pan, R. Wang, Sandwich-Type NbS_2@S@I-doped graphene for high-sulfur-loaded, ultrahigh-rate, and long-life lithium-sulfur batteries, ACS Nano 11 (2017) 8488-8498.

[81] M.R. Kaiser, Z. Ma, X. Wang, F. Han, T. Gao, X. Fan, J.Z. Wang, H.K. Liu, S. Dou, C. Wang, Reverse microemulsion synthesis of sulfur/graphene composite for lithium/sulfur batteries, ACS Nano 11 (2017) 9048-9056.

[82] G. Zhou, E. Paek, G.S. Hwang, A. Manthiram, Long-life Li/polysulphide batteries with high sulphur loading enabled by lightweight three-dimensional nitrogen/sulphur-codoped graphene sponge, Nat. Commun. 6 (2015) 7760.

[83] S.A. Ahad, P.R. Kumar, J.H. Kim, D.J. Kim, P. Ragupathy, D.K. Kim, Catecholamine-functionalized reduced graphene oxide: a scalable carbon host for stable cycling in lithium–sulfur batteries, Electrochim. Acta 246 (2017) 451-458.

[84] Z. Wang, Y. Dong, H. Li, Z. Zhao, H. B. Wu, C. Hao, S. Liu, J. Qiu, X.W. (David) Lou, Enhancing lithium–sulphur battery performance by strongly binding the discharge products on amino-functionalized reduced graphene oxide, Nat. Commun. 5 (2014) 5002.

[85] L. Zhou, X. Lin, T. Huang, A. Yu, Binder-free phenyl sulfonated graphene/sulfur electrodes with excellent cyclability for lithium sulfur batteries, J. Mater. Chem. A 2 (2014) 5117-5123.

[86] N. Xu, T. Qian, X. Liu, J. Liu, Y. Chen, C. Yan, Greatly suppressed shuttle effect for improved lithium sulfur battery performance through short chain intermediates, Nano Lett. 17 (2017) 538-543.

[87] Y.S. Su, A. Manthiram, Lithium-sulphur batteries with a microporous carbon paper as a bifunctional interlayer, Nat. Commun. 3 (2012) 1166.

[88] Y.S. Su, A. Manthiram, A new approach to improve cycle performance of rechargeable lithium-sulfur batteries by inserting a free-standing MWCNT interlayer, Chem. Commun. 48 (2012) 8817-8819.

[89] X. Wang, Z. Wang, L. Chen, Reduced graphene oxide film as a shuttle-inhibiting interlayer in a lithium-sulfur battery, J. Power Sources 242 (2013) 65–69.

[90] L.B. Xing, K. Xi, Q. Li, Z. Su, C. Lai, X. Zhao, R. Vasant Kumar, Nitrogen , sulfur-codoped graphene sponge as electroactive carbon interlayer for high-energy and -power lithium-sulfur batteries, J. Power Sources 303 (2016) 22–28.

[91] Z. Xiao, Z. Yang, L. Wang, H. Nie, M. Zhong, Q. Lai, X. Xu, L. Zhang, A lightweight TiO 2/graphene interlayer, applied as a highly effective polysulfide absorbent for fast, long-life lithium-sulfur batteries, Adv. Mater. 27 (2015) 2891-2898.

[92] X. Liang, C. Hart, Q. Pang, A. Garsuch, T. Weiss, L.F. Nazar, A highly efficient polysulfide mediator for lithium-sulfur batteries, Nat. Commun. 6 (2015) 5682.

[93] P. Guo, D. Liu, Z. Liu, X. Shang, Q. Liu, D. He, Dual functional MoS2/graphene interlayer as an efficient polysulfide barrier for advanced lithium-sulfur batteries, Electrochim. Acta 256 (2017) 28-36.

[94] Y. Fan, Z. Yang, W. Hua, D. Liu, T. Tao, M.M. Rahman, W. Lei, S. Huang, Y. Chen, Functionalized boron nitride nanosheets/graphene interlayer for fast and long-life

lithium-sulfur batteries, Adv. Energy Mater. 7 (2017) 1602380.

[95] J. Xie, H.J. Peng, J.Q. Huang, W.T. Xu, X. Chen, Q. Zhang, A supramolecular capsule for reversible polysulfide storage/delivery in lithium-sulfur batteries, Angew. Chem. 56 (2017) 16223-16227.

[96] W. Liu, J. Jiang, K.R. Yang, Y. Mi, P. Kumaravadivel, Y. Zhong, Q. Fan, Z. Weng, Z. Wu, J.J. Cha, H. Zhou, V.S. Batista, G.W. Brudvig, H. Wang, Ultrathin dendrimr-graphene oxide composite film for stable cycling lithium-sulfur batteries, Proc. Natl. Acad. Sci. 114 (2017) 3578-3583.

[97] J.Q. Huang, T.Z. Zhuang, Q. Zhang, H.J. Peng, C.M. Chen, F. Wei, Permselective graphene oxide membrane for highly stable and anti-self-discharge lithium-sulfur batteries, ACS Nano 9 (2015) 3002-3011.

[98] P. Zhu, J. Zang, J. Zhu, Y. Lu, C. Chen, M. Jiang, C. Yan, M. Dirican, R.K. Selvan, D. Kim, X. Zhang, Effect of reduced graphene oxide reduction degree on the performance of polysulfide rejection in lithium-sulfur batteries, Carbon 126 (2018) 594–600.

[99] H.J. Peng, D.W. Wang, J.Q. Huang, X.B. Cheng, Z. Yuan, F. Wei, Q. Zhang, Janus separator of polypropylene-supported cellular graphene framework for sulfur cathodes with high utilization in lithium-sulfur batteries, Adv. Sci. 3 (2015) 1500268.

[100] Y. Zhao, M. Liu, W. Lv, Y.B. He, C. Wang, Q. Yun, B. Li, F. Kang, Q.H. Yang, Dense coating of $Li_4Ti_5O_{12}$ and graphene mixture on the separator to produce long cycle life of lithium-sulfur battery, Nano Energy 30 (2016) 1-8.

[101] J. Zhu, C. Chen, Y. Lu, J. Zang, M. Jiang, D. Kim, X. Zhang, Highly porous polyacrylonitrile/graphene oxide membrane separator exhibiting excellent anti-self-discharge feature for high-performance lithium-sulfur batteries, Carbon 101 (2016) 272-280.

[102] S. Bai, X. Liu, K. Zhu, S. Wu, H. Zhou, Metal-organic framework-based separator for lithium-sulfur batteries, Nat. Energy 1 (2016) 16094.

[103] P.Y. Zhai, H.J. Peng, X.B. Cheng, L. Zhu, J.Q. Huang, W. Zhu, Q. Zhang, Scaled-up fabrication of porous-graphene-modified separators for high-capacity lithium-sulfur batteries, Energy Storage Mater. 7 (2017) 56-63.

[104] J. Li, S. Ma, L. Cheng, Q. Wu, Egg yolk-derived three-dimensional porous carbon for

stable electrochemical supercapacitors, Mater. Lett. 139 (2015) 429-432.

[105] T. Zhou, W. Lv, J. Li, G. Zhou, Y. Zhao, S. Fan, B. Liu, B. Li, F. Kang, Q.H. Yang, Twinborn TiO_2-TiN heterostructures enabling smooth trapping-diffusion-conversion of polysulfides towards ultralong life lithium-sulfur batteries, Energy Environ. Sci. 10 (2017) 1694-1703.

[106] T.Z. Zhuang, J.Q. Huang, H.J. Peng, L.Y. He, X.B. Cheng, C.M. Chen, Q. Zhang, Rational integration of polypropylene/graphene oxide/nafion as ternary-layered separator to retard the shuttle of polysulfides for lithium-sulfur batteries, Small 12 (2016) 381-389.

[107] G. Zhou, S. Pei, L. Li, D.W. Wang, S. Wang, K. Huang, L.C. Yin, F. Li, H.M. Cheng, A graphene-pure-sulfur sandwich structure for ultrafast, long-life lithium-sulfur batteries, Adv. Mater. 26 (2014) 625–631.

[108] Y. Zhang, Y. Zhao, Z. Bakenov, A novel lithium/sulfur battery based on sulfur/graphene nanosheet composite cathode and gel polymer electrolyte, Nanoscale Res. Lett. 9 (2014) 137.

[109] X. Yao, N. Huang, F. Han, Q. Zhang, H. Wan, J.P. Mwizerwa, C. Wang, X. Xu, High-performance all-solid-state lithium-sulfur batteries enabled by amorphous sulfur-coated reduced graphene oxide cathodes, Adv. Energy Mater. 7 (2017) 1602923.

[110] J. Zhao, G. Zhou, K. Yan, J. Xie, Y. Li, L. Liao, Y. Jin, K. Liu, P.C. Hsu, J. Wang, H.M. Cheng, Y. Cui, Air-stable and freestanding lithium alloy/graphene foil as an alternative to lithium metal anodes, Nat. Nanotechnol. 12 (2017) 993-999.

[111] X.B. Cheng, H.J. Peng, J.Q. Huang, R. Zhang, C.Z. Zhao, Q. Zhang, Dual-phase lithium metal anode containing a polysulfide-induced solid electrolyte interphase and nanostructured graphene framework for lithium-sulfur batteries, ACS Nano 9 (2015) 6373-6382.

[112] K.K. Chawla, Composite materials (3rd edition), Springer, (2006).

[113] S.A. Sajjadi, H.R. Ezatpour, H. Beygi, Microstructure and mechanical properties of Al-Al_2O_3 micro and nano composites fabricated by stir casting, Mater. Sci. Eng. A 528 (2011) 8765-8771.

[114] B.F. Schultz, J.B. Ferguson, P.K. Rohatgi, Microstructure and hardness of Al_2O_3

nanoparticle reinforced Al-Mg composites fabricated by reactive wetting and stir mixing, Mater. Sci. Eng. A 530 (2011) 87–97.

[115] M.K. Akbari, H.R. Baharvandi, O. Mirzaee, Nano-sized aluminum oxide reinforced commercial casting A356 alloy matrix : evaluation of hardness, wear resistance and compressive strength focusing on particle distribution in aluminum matrix, Compos. Part B 52 (2013) 262-268.

[116] K.M. Shorowordi, T. Laoui, A.S.M.A. Haseeb, J.P. Celis, L. Froyen, Microstructure and interface characteristics of B_4C , SiC and Al_2O_3 reinforced Al matrix composites : a comparative study, J. Mater. Process. Technol. 142 (2003) 738-743.

[117] A. Dolatkhah, P. Golbabaei, M.K.B. Givi, F. Molaiekiya, Investigating effects of process parameters on microstructural and mechanical properties of Al5052/SiC metal matrix composite fabricated via friction stir processing, Mater. Des. 37 (2012) 458-464.

[118] F. Toptan, A. Kilicarslan, A. Karaaslan, M. Cigdem, I. Kerti, Processing and microstructural characterisation of AA 1070 and AA 6063 matrix B_4C_P reinforced composites, Mater. Des. 31 (2010) S87-S91.

[119] X.G. Chen, M. da Silva, P. Gougeon, L. St-georges, Microstructure and mechanical properties of friction stir welded AA6063-B_4C metal matrix composites, Mater. Sci. Eng. A 518 (2009) 174-184.

[120] S.R. Bakshi, D. Lahiri, A. Agarwal, Carbon nanotube reinforced metal matrix composites-a review, Int. Mater. Rev. 55 (2010) 41-46.

[121] L.H. Dai, Z. Ling, Y.L. Bai, Size-dependent inelastic behavior of particle-reinforced metal-matrix composites, Compos. Sci. Technol. 61 (2001) 1057-1063.

[122] J. Hashim, L. Looney, M.S.J. Hashmi, Particle distribution in cast metal matrix composites-Part I, J. Mater. Process. Technol. 123 (2002) 251-257.

[123] J. Hashim, L. Looney, M.S.J. Hashmi, Particle distribution in cast metal matrix composites-Part II, J. Mater. Process. Technol. 123 (2002) 258-263.

[124] Y. Li, K.T. Ramesh, Influence of particle volume fraction, shape, and aspect ratio on the behavior of particle-reinforced metal-matrix composites at high rates of strain, Acta Mater. 46 (1998) 5633–5646.

[125] Z. Hu, G. Tong, D. Lin, C. Chen, H. Guo, J. Xu, L. Zhou, Graphene-reinforced metal

matrix nanocomposites-a review, Mater. Sci. Technol. 32 (2016) 930-953.

[126] A. Nieto, A. Bisht, D. Lahiri, C. Zhang, A. Agarwal, Graphene reinforced metal and ceramic matrix composites : a review, Int. Mater. Rev. 62 (2017) 241-302.

[127] R. Pérez-Bustamante, D. Bolaños-Morales, J. Bonilla-Martínez, I. Estrada-Guel, R. Martínez-Sánchez, Microstructural and hardness behavior of graphene-nanoplatelets/aluminum composites synthesized by mechanical alloying, J. Alloys Compd. 615 (2014) S578-S582.

[128] S.F. Bartolucci, J. Paras, M.A. Rafiee, J. Rafiee, S. Lee, D. Kapoor, N. Koratkar, Graphene-aluminum nanocomposites, Mater. Sci. Eng. A 528 (2011) 7933-7937.

[129] S.J. Yan, S.L. Dai, X.Y. Zhang, C. Yang, Q.H. Hong, J.Z. Chen, Z.M. Lin, Investigating aluminum alloy reinforced by graphene nanoflakes, Mater. Sci. Eng. A 612 (2014) 440-444.

[130] W.J. Kim, T.J. Lee, S.H. Han, Multi-layer graphene/copper composites: preparation using high-ratio differential speed rolling, microstructure and mechanical properties, Carbon 69 (2014) 55-65.

[131] J. Wang, Z. Li, G. Fan, H. Pan, Z. Chen, D. Zhang, Reinforcement with graphene nanosheets in aluminum matrix composites, Scr. Mater. 66 (2012) 594-597.

[132] M. Rashad, F. Pan, A. Tang, M. Asif, Effect of graphene nanoplatelets addition on mechanical properties of pure aluminum using a semi-powder method, Prog. Nat. Sci. Mater. Int. 24 (2014) 101-108.

[133] Z. Li, G. Fan, Z. Tan, Q. Guo, D. Xiong, Y. Su, Z. Li, D. Zhang, Uniform dispersion of graphene oxide in aluminum powder by direct electrostatic adsorption for fabrication of graphene/aluminum composites, Nanotechnology 25 (2014) 325601.

[134] C. Zhao, Enhanced strength in reduced graphene oxide/nickel composites prepared by molecular-level mixing for structural applications, Appl. Phys. A Mater. Sci. Process. 118 (2015) 409-416.

[135] Z. Ren, N. Meng, K. Shehzad, Y. Xu, S. Qu, B. Yu, J.K. Luo, Mechanical properties of nickel-graphene composites synthesized by electrochemical deposition, Nanotechnology 26 (2015) 065706.

[136] Z. Li, Q. Guo, Z. Li, G. Fan, D.B. Xiong, Y. Su, J. Zhang, D. Zhang, Enhanced

mechanical properties of graphene (reduced graphene oxide)/aluminum composites with a bioinspired nanolaminated structure, Nano Lett. 15 (2015) 8077-8083.

[137] Z.Y. Zhao, R.G. Guan, X.H. Guan, Z.X. Feng, H. Chen, Y. Chen, Microstructures and properties of graphene-Cu/Al composite prepared by a novel process through clad forming and improving wettability with copper, Adv. Eng. Mater. 17 (2015) 663-668.

[138] L.Y. Chen, H. Konishi, A. Fehrenbacher, C. Ma, J.Q. Xu, H. Choi, H.F. Xu, F.E. Pfefferkorn, X.C. Li, Novel nanoprocessing route for bulk graphene nanoplatelets reinforced metal matrix nanocomposites, Scr. Mater. 67 (2012) 29-32.

[139] M. Rashad, F. Pan, A. Tang, M. Asif, Effect of graphene nanoplatelets addition on mechanical properties of pure aluminum using a semi-powder method, Prog. Nat. Sci. Mater. Int. 24 (2014) 101-108.

[140] Y. Kim, J. Lee, M.S. Yeom, J.W. Shin, H. Kim, Y. Cui, J.W. Kysar, J. Hone, Y. Jung, S. Jeon, S.M. Han, Strengthening effect of single-atomic-layer graphene in metal-graphene nanolayered composites, Nat. Commun. 4 (2013) 2114.

[141] Z. Hu, G. Tong, D. Lin, Q. Nian, J. Shao, Y. Hu, M. Saeib, S. Jin, G.J. Cheng, Laser sintered graphene nickel nanocomposites, J. Mater. Process. Technol. 231 (2016) 143-150.

[142] T. Borkar, H. Mohseni, J. Hwang, T.W. Scharf, J.S. Tiley, S.H. Hong, R. Banerjee, Excellent strength-ductility combination in nickel-graphite nanoplatelet (GNP/Ni) nanocomposites, J. Alloys Compd. 646 (2015) 135-144.

[143] L. Zhao, H. Lu, Z. Gao, Microstructure and mechanical properties of Al/graphene composite produced by high-pressure torsion, Adv. Energy Mater. 17 (2015) 976-981.

[144] M. Rashad, F. Pan, M. Asif, A. Tang, Powder metallurgy of Mg-1%Al-1%Sn alloy reinforced with low content of graphene nanoplatelets (GNPs), J. Ind. Eng. Chem. 20 (2014) 4250-4255.

[145] P. Shao, W. Yang, Q. Zhang, Q. Meng, X. Tan, Z. Xiu, J. Qiao, Z. Yu, G. Wu, Microstructure and tensile properties of 5083 Al matrix composites reinforced with graphene oxide and graphene nanoplates prepared by pressure in fi ltration method, Compos. Part A Appl. Sci. Manuf. 109 (2018) 151-162.

[146] R.O. Ritchie, The conflicts between strength and toughness, Nat. Mater. 10 (2011)

817-822.

[147] M.E. Launey, R.O. Ritchie, On the fracture toughness of advanced materials, Adv. Mater. 25 (2009) 2103-2110.

[148] U.G.K. Wegst, H. Bai, E. Saiz, A.P. Tomsia, R.O. Ritchie, Bioinspired structural materials, Nat. Mater. 14 (2015) 23-36.

[149] X. Li, W.C. Chang, Y.J. Chao, R. Wang, M. Chang, Nanoscale structural and mechanical characterization of a natural nanocomposite material: the shell of red abalone, Nano Lett. 4 (2004) 613-617.

[150] Z.H. Xu, Y. Yang, Z. Huang, X. Li, Elastic modulus of biopolymer matrix in nacre measured using coupled atomic force microscopy bending and inverse finite element techniques, Mater. Sci. Eng. C 31 (2011) 1852-1856.

[151] F. Barthelat, H.D. Espinosa, An experimental investigation of deformation and fracture of nacre-mother of pearl, Exp. Mech. 47 (2007) 311-324.

[152] A.Y.M. Lin, P.Y. Chen, M.A. Meyers, The growth of nacre in the abalone shell, Acta Biomater. 4 (2008) 131-138.

[153] Z. Huang, Z. Pan, H. Li, Q. Wei, X. Li, Hidden energy dissipation mechanism in nacre, J. Mater. Res. 29 (2014) 1573-1578.

[154] A.Y.M. Lin, M.A. Meyers, Interfacial shear strength in abalone nacre, J. Mech. Behav. Biomed. Mater. 2 (2009) 607-612.

[155] M.E. Launey, E. Munch, D.H. Alsem, H.B. Barth, E. Saiz, A.P. Tomsia, R.O. Ritchie, Designing highly toughened hybrid composites through nature-inspired hierarchical complexity, Acta Mater. 57 (2009) 2919-2932.

[156] E. Munch, M.E. Launey, D.H. Alsem, E. Saiz, A.P. Tomsia, R.O. Ritchie, Tough, bio-inspired hybrid materials, Science 322 (2008) 1516-1520.

[157] F. Bouville, E. Maire, S. Meille, B. Van De Moortèle, A.J. Stevenson, S. Deville, Strong, tough and stiff bioinspired ceramics from brittle constituents, Nat. Mater. 13 (2014) 508-514.

[158] M. Grossman, F. Bouville, F. Erni, K. Masania, R. Libanori, A.R. Studart, Mineral Nano-Interconnectivity Stiffens and Toughens Nacre-like Composite Materials, Adv. Mater. 29 (2017) 1605039.

[159] R.P. Wilkerson, B. Gludovatz, J. Watts, A.P. Tomsia, G.E. Hilmas, R.O. Ritchie, A novel approach to developing biomimetic ("nacre-like") metal-compliant-phase (nickel–alumina) ceramics through coextrusion, Adv. Mater. 28 (2016) 10061-10067.

[160] H. Bai, F. Walsh, B. Gludovatz, B. Delattre, C. Huang, Y. Chen, A.P. Tomsia, R.O. Ritchie, Bioinspired hydroxyapatite/poly(methyl methacrylate) composite with a nacre-mimetic architecture by a bidirectional freezing method, Adv. Mater. 28 (2016) 50-56.

[161] A. Dreyer, A. Feld, A. Kornowski, E.D. Yilmaz, H. Noei, A. Meyer, T. Krekeler, C. Jiao, A. Stierle, V. Abetz, H. Weller, G.A. Schneider, Organically linked iron oxide nanoparticle supercrystals with exceptional isotropic mechanical properties, Nat. Mater. 15 (2016) 522-528.

[162] M.E. Launey, E. Munch, D.H. Alsem, E. Saiz, A.P. Tomsia, R.O. Ritchie, A novel biomimetic approach to the design of high-performance ceramic-metal composites, J. R. Soc. Interface 7 (2010) 741-753.

[163] L.J. Bonderer, A.R. Studart, L.J. Gauckler, Bioinspired design and assembly of platelet reinforced polymer films, Science 319 (2008) 1069-1073.

[164] S. Seo, D.W. Lee, J.S. Ahn, K. Cunha, E. Filippidi, S.W. Ju, E. Shin, B.-S. Kim, Z.A. Levine, R.D. Lins, J.N. Israelachvili, J.H. Waite, M.T. Valentine, J.E. Shea, B.K. Ahn, Significant performance enhancement of polymer resins by bioinspired dynamic bonding, Adv. Mater. 29 (2017) 1703026.

[165] W. Cui, M. Li, J. Liu, B. Wang, C. Zhang, L. Jiang, Q. Cheng, A strong integrated strength and toughness artificial nacre based on dopamine cross-linked graphene oxide, ACS Nano 8 (2014) 9511-9517.

[166] J. M. Malho, P. Laaksonen, A. Walther, O. Ikkala, M. B. Linder, Facile method for stiff, tough, and strong nanocomposites by direct exfoliation of multilayered graphene into native nanocellulose matrix, Biomacromolecules 13 (2012) 1093-1099.

[167] J. Wang, J. Qiao, J. Wang, Y. Zhu, L. Jiang, Bioinspired hierarchical alumina–graphene oxide–poly(vinyl alcohol) artificial nacre with optimized strength and toughness, ACS Appl. Mater. Interfaces 17 (2015) 9281-9286.

[168] M. Cao, D.B. Xiong, Z. Tan, G. Ji, B. Amin-Ahmadi, Q. Guo, G. Fan, C. Guo, Z. Li,

D. Zhang, Aligning graphene in bulk copper: Nacre-inspired nanolaminated architecture coupled with in-situ processing for enhanced mechanical properties and high electrical conductivity, Carbon 117 (2017) 65-74.

Chapter 2 Graphene/Biomass Derived Carbon Composites for High-Performance Li-S batteries

2.1 Background and motivation

With ever-increasing global energy consumption and the depletion of fossil fuels, finding a sustainable and clean energy source has become an important scientific and technological challenge facing humanity today [1]. The intermittent nature of sustainable energy sources as well as the emerging always-on portable devices and electric vehicles urgently need stable energy storage systems with high capacity and long lifespan. Batteries have been proven to be the most effective electrochemical energy conversion and storage devices. As the most widely used battery system, lithium-ion (Li-ion) batteries have served our daily life and changed the world extensively in the past two decades. Top-of-the-line Li-ion batteries can deliver an energy density of ~200 Wh kg^{-1}. However, the potential of Li-ion battery system is approaching its limit and unable to fulfill diverse requirements [2–4]. Among all possible candidates, lithium sulfur (Li-S) battery chemistry is considered to be one of the most promising next-generation, high energy density battery chemistries. A Li-S battery has a lithium metal anode and a sulfur-containing composite cathode. The overall chemistry during discharge of the Li-S battery, with complete conversion of the sulfur, is $2Li + S \rightarrow Li_2S$. The theoretical gravimetric capacity of this reaction is 1675 mAh g^{-1}, and with the expected average voltage during discharge, the maximum energy density can be 2600 mWh g^{-1} [5–7]. It is anticipated that a fully packed Li-S battery is able to achieve a specific energy of 400 to 600 Wh kg^{-1}, which is 2-3 times higher than that of commercial Li-ion batteries [8,9]. Li-S batteries will be competitive where weight and energy capacity are both critical design criteria, such as in electric cars or aerospace applications. Unfortunately, Li-S batteries still suffer from a number of challenges which severely hinder the practical application and commercialization of Li-S batteries. On the cathode side, the insulating nature of sulfur (a resistance of $\sim 5 \times 10^{-18}$ S cm^{-1}) and the solubility of lithium polysulfides (Li_2S_x (x = 8, 6, 5, and 4)) lead to low utilization of active materials, quick capacitance decay, and short cyclic performance [10–12]. An effective and widely acknowledged approach to solving the aforementioned challenges is to composite sulfur with carbonaceous materials, such as activated carbon [13–15], graphite [16,17], acetylene black [18,19], carbon nanotube [20,21], carbon spheres [22,23], and graphene [9,24]. Such sulfur/carbon composites often exhibit remarkable mechanical robustness, excellent chemical stability, outstanding electric conductivity, and superior electrolyte accessibility. Considering the bonding nature of polysulfides (polar), reduced graphene oxide with polar functional groups has been widely adopted to enhance the surface redox chemistry, remarkably improving the overall performance of Li-S batteries [25–37]. On the anode side, it is well recognized that unavoidable Li degradation such as the formation of dendrites, mossy Li, and passive sediments not only deteriorates the battery performance, but also imposes safety issues [38,39].

In addition to pursuing superior electrochemical performance, the cost of battery cannot be ignored. The bulk cost of lithium-ion batteries is ~\$350 per kWh, which is far beyond the target price of practical electric vehicle applications (~\$100 per kWh) [6]. Although sulfur is low-cost, constructing carbonaceous sulfur carriers with delicate nanostructures is costly [40]. For instance, current method (Hummer’s method) for graphene oxide fabrication involves long time processes and expensive chemicals, making it economic inefficiency [41,42]. Meanwhile, we should also turn our attention to the environment issues. Graphite is widely utilized as an electrode material in batteries, but it is a limited natural resource. Fabrication of nanostructured carbonaceous materials (such as graphene oxide and carbon nanotubes) needs to use toxic precursors and chemicals, which may deteriorate the environment even more. To ensure the sustainability of battery development, various bio-mass materials have been adopted for battery applications [43], such as cotton [14,15], banana peel [44], and paper [45–47]. However, Li-S batteries derived from recycled bio-mass materials often suffer quick capacity fading and short lifespan due to unavoidable anode degradation and poor lithium polysulfide absorbability [45,46]. Can we simultaneously reduce the cost, minimize the environmental damage, and maximize the electrochemical properties for sulfur carriers? A wisdom solution is to composite low-cost, environmental friendly bio-mass derived carbon scaffold derived with a small amount of high-performance, nanostructured carbonaceous materials.

Here, we report two innovative solutions to capitalize on currently overlooked resources to produce high-performance lithium-sulfur (Li-S) batteries from banana peel and recycled paper. First, a piece of banana peel was freeze dried to preserve the natural porous structure. The following-up high temperature annealing process converted the freeze dried banana peel into activated banana peel (ABP). The hierarchically porous architecture of the ABP scaffold improved the accessibility of electrolyte and electroactive materials while retaining its conductivity and mechanical robustness, making the ABP an superior carbon framework for free-standing electrodes. Nano sized pores were created by annealing the $Ni(NO_3)_2$ solution-treated ABP. Such nanoporous architecture effectively improved the utilization of sulfur and electrochemical performance of the as-assembled lithium-sulfur (Li-S) batteries. The synergetic effects between the hierarchically porous carbon scaffolds and the active materials enabled the superior electrochemical performance and utilization of active materials (sulfur) for Li-S battery applications. Considering the unparalleled economic and social benefits of recycling waste banana peels, banana-peel derived porous carbon electrodes can pave the way to next-generation, low-cost energy storage devices. In another work, capillarity was utilized creatively to wrap graphene oxide sheets onto paper fibers. The following-up high temperature annealing simultaneously reduced graphene oxide into graphene and converted the paper into activated carbon, forming activated paper carbon/reduced graphene (APC/graphene) scaffold. Sulfur was then impregnated into the scaffold by a two-step heat treatment to form an APC/graphene/S electrode. The obtained APC/graphene/S composite was used as a free-standing cathode for constructing a Li-S battery without using binders and current collectors. The paper-derived graphene Li-S battery exhibited outstanding lifespan of 620 cycles and excellent capacity retention rate of 60.5%. This recycled paper-derived Li-S battery configuration is low-cost and scalable for environmentally benign energy storage devices.

2.2 Experimental methods

Activation of banana peels

Banana peels were punched to 15 mm diameter round pieces and frozen in a freezer before degradation without further treatment. The frozen pieces were then lyophilized in a freeze dryer for 3 h. Next, the freeze-dried pieces were inserted into a horizontal tube furnace and heated at 900 ℃ for 1 h with continuous argon gas flow to convert the banana peel pieces into activated carbon. After carbonization, banana peel pieces shrank about 15 % in size. The activated banana peel (ABP) pieces were washed with distilled water several times and subsequently dried at 75 ℃ for 2 h.

Fabrication of ABP/Ni/graphene/S electrodes

For the fabrication of lithium-sulfur batteries, round ABP pieces were immersed into 0.3 M $Ni(NO_3)_2$ solution and then dried at 70 ℃ for 2 h. The $Ni(NO_3)_2$ treated pieces were heated at 1000 ℃ with the protection of inert gas to create nanopores and graphene wrapped Ni nanoparticles on the cell walls of ABP. Sulfur was deposited onto the ABP/Ni/graphene by heating the sulfur-loaded ABP/Ni/graphene at 155 ℃ for 12 h and then at 200 ℃ for 2 h in a sealed Teflon-lined stainless steel autoclave.

Preparation of graphene oxide solution

Graphene oxide solution was prepared using Hummers method [41,42]. Specifically, 3 g of graphite powders with 99.9 % purity were added into 200 mL of 98 % H_2SO_4 at 10 ℃ while being stirred vigorously. Subsequently, within 30 min 30 g of $KMnO_4$ was gradually added into the slurry and stirred at 10 ℃ for 2 h. The reaction continued at 40 ℃ for 12 h. Next, 200 mL of distilled water was added to the reacting product to enable the reaction to continue at 70 ℃ for 2 h. 36 mL of 20% H_2O_2 was then added into the product to react with the remaining $KMnO_4$, turning the slurry to golden brown. The slurry was centrifugally separated several times at 5000 rpm to remove the acid, and finally ultra-sonicated to obtain the graphene oxide solution of high quality.

Fabrication of APC/graphene/S electrodes

Recycled paper strips were peeled from hardboard panels or rolls and then cut into pieces with length of 7 cm and width of 1.5 cm. The stripes were rinsed by dilute water and ethanol three times before dried at 60 ℃ for 12 h. One end of the strip (about 5 mm) was then placed into the graphene oxide solution with a concentrate of 2 mg mL^{-1} for 2 h. Graphene oxide sheets were absorbed onto the paper fibers by capillary force. After absorption, the top part and the bottom part of the strip were cut. To minimize the cost of raw materials, graphene oxide attached on the bottom part was washed out by dilute water for reuse and the top part dry recycled paper can be dipped into graphene oxide solution with the same method. The middle part with capillary-absorbed graphene oxide sheets was dried at 60 ℃ for 2 h and then heated at 1000 ℃ for 1 h in a tube furnace with continuous argon gas flow to convert the recycled paper/graphene oxide composite into APC/graphene composite. The APC/graphene strip was then punched into small plates with the diameter of 13 mm (the same size of lithium plates). Sulfur powders were loaded onto the APC/graphene plates and heat treated at 155 ℃ for 12 h and at 200 ℃ for 2 h to impregnate sulfur into the composite, forming APC/graphene/S hybrids, which will be used as cathodes directly. As a reference sample, a paper strip was entirely dipped into graphene oxide solution for 1 min and then taken out and dried. The obtained recycled paper/dipped-graphene oxide stripe was annealed at 1000 ℃ for 1 h with the protection of Argon and noted as APC/dipped-graphene composite.

Assembly of coin Li-S batteries

The electrolyte was produced by dissolving 1 mol/L LiTFSI and 0.4 mol/L $LiNO_3$ in an organic solvent of dimethoxyethane (DME) + 1,3-dioxolane (DOL) at a 1:1 volume ratio. The electrolyte/sulfur ratio was 15:1. Lithium metal was used as anode and Celgard 2400 film as separator. The CR2032 coin cells were assembled with a MTI MSK-110 crimping machine in an argon-filled glove box (M. Braun, Germany) with oxygen and water contents below 0.1 and 0.1 ppm, respectively. After the assembled batteries failed in the recycling tests, the coin batteries were disassembled manually and the cathode and anodes were taken out and immediately merged into DME to remove residual electrolyte and sulfur, all in an argon-filled glove box. The cycled APC/graphene electrodes were then taken out and rinsed by acetone and dilute water for several times. The rinsed APC/graphene pieces were then dried at 70 ℃ for 12 h before conducting the surface area measurement.

Materials and structural characterization

The as-prepared ABP, APC, and elecrodes were characterized by X-ray diffraction (XRD, a PANalytical X'Pert Pro Multi-Purpose Diffractometer (MPD) equipped with Cu K_{α} radiation (λ = 0.15406 nm)), scanning electron microscopy (SEM, FEI Quanta 650 with EDS detector), transmission electron microscopy (TEM, JEOL 2000FX), high resolution transmission electron microscopy (HRTEM, FEI Titan), scanning TEM (STEM, FEI Titan), atomic force microscopy (AFM, Bruker Dimension Icon), Raman spectroscopy (Renishaw inVia Raman microscope at the wave length of 514 nm), Fourier-transform infrared spectroscopy (FTIR, Nicolet iS5 IR spectrometer), and Time-of-Flight Secondary Ion Mass Spectrometer (TOF-SIMS). The specific area and pore size of APC and electrodes were measured using a Quantachrom Autososrb iQ nitrogen adsorption-desorption analyzer and measured with the Brunauer–Emmett–Teller (BET) theory. Data points ranged from 0.01 to 0.9 P/P0 were used to calculate the pore size distribution based on BJH theory.

Electrochemical characterization

A LAND CT2003A battery test instrument was used to perform galvanostatic charge/discharge measurements. The cyclic voltammetry (CV) and electrochemical impedance spectroscopy (EIS) tests in the frequency range from 100 kHz to 0.005 Hz with an AC perturbation of 5 mV were carried out using a CHI 660E electrochemical workstation.

2.3 High-performance Li-S batteries derived from activated banana-peel with porous structures

2.3.1 Activation of banana peels

A banana from Guatemala was used as the raw material without further treatment. Considering the mass production of bananas and waste banana peels (Fig. 2-1a), recycling surplus and abandoned banana peels is economically and socially significant. After the freeze-drying process, the banana peel pieces preserved their original architectures but were dehydrated (Fig. 2-1b). The subsequent heating process at 900 ℃ for 1 h with continuous argon gas flow converted the banana peel pieces into activated carbon with dark black color (Fig. 2-1c). Comparing with the freeze dried banana peel pieces, activated banana peel (ABP) pieces shrank about 15%. The density of ABP ranges from 0.08 g cm^{-3} to 0.13 g cm^{-3}, depending on the raw materials. The ABP from mature bananas often exhibits slightly higher densities, which may be ascribed to a higher concentration of sugar and more extensive dehydration. Therefore, round pieces have a weight about 0.04 g (0.036-0.045g). The electrical resistance of the ABP was measured (by multimeter) to be 17.7 Ω. Statistically, the sheet resistance of ABP ranges from 7.5-16.5 Ω sq^{-1}. There were no obvious peaks beyond 1500 cm^{-1} in the Fourier transform infrared spectroscopy (FTIR) spectrum of ABP (Fig. 2-1d). Several peaks located in between 600 to 1500 cm^{-1} were attributed to C-H, C-N, and C-O bonds, indicating ABP is not pure carbon but also contains other elements like H, O and N. This result is constant with other researches about activated banana peels [48–52]. ABP's Raman spectrum exhibited a broad G bond at ~1580 cm^{-1} and D bond at 1350 cm^{-1} (Fig. 2-1e). The G band and D band are assigned to the hexagonal carbon plane and crystal defects or imperfections, respectively. The ratio of the relative intensity of these two bands (I_D/I_G) is proportional to the number of defect sites in the graphite carbon. Different from the sharp G bonds and low I_D/I_G values of graphite and graphene, the obvious broad D bonds and high I_D/I_G values of ABP pointed towards the amorphous carbon with relative low graphitization.

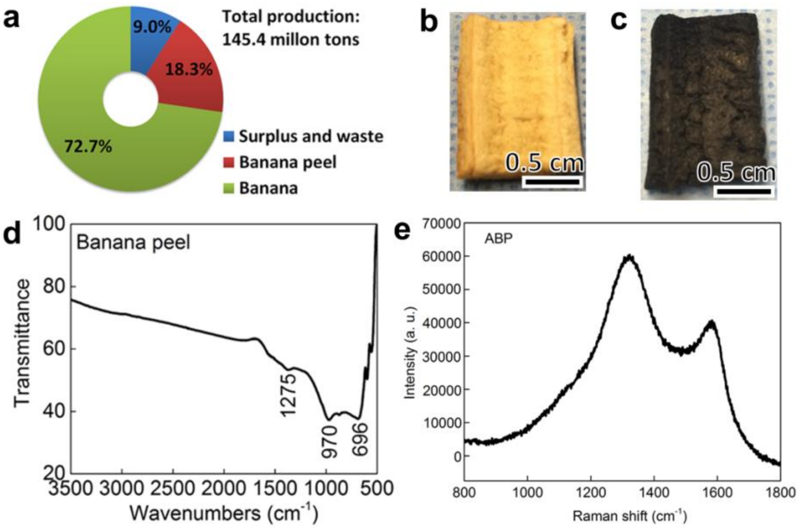

Fig. 2-1 Activation of ABP. a. Banana production in 2011. b. A piece of freeze dried banana peel. c. A piece of ABP. d. FTIR spectrum of ABP. e. Raman spectrum of ABP.

The reconstructed three dimensional X-ray computed tomography (XCT) image (Fig. 2-2a) and low magnification scanning electron microscope (SEM) image (Fig. 2-2b) of ABP exhibited an incompact and porous architecture. The compact pores with a size of about 20 μm may originate from the outer epidermal cells of the peel. Such porous structural configuration is expected to improve the performance of energy storage devices because the loosely interconnected pores are able to enhance the accessibility of electrolyte and active material whereas the compact layer can retain the conductivity and mechanical robustness. The porous structure of this ABP resulted in a large Brunauer−Emmet−Teller (BET) [53] surface area of 194 m^2 g^{-1} and low density (0.094 g cm^{-3}). The obtained BET surface area is higher than the carbonized banana fiber (36 m^2 g^{-1}) [48], banana peel (14.5-33 m^2 g^{-1}) [50], and zinc nitrite treated banana peel (131 m^2 g^{-1}) [49] because banana peels were freeze dried before dehydration and degradation so that the original porous structure was reversed. Without freeze-drying ABP architectures would collapse during activation, leading to a structure without definite shape and a low specific surface area of 31 m^2 g^{-1}, which is close to the reported directly pyrolytic banana fiber and banana peel [48,50]. To study the structural variation of bananas from different locations, three other bananas from Costa Rica, Colombia, and Ecuador were inspected by SEM. Banana peels from various locations exhibited almost identical porous microstructure with minor differences, which are negligible when being used as electrodes. Therefore, banana peel is naturally porous with high specific surface area and interconnected microstructure even without further chemical treatment.

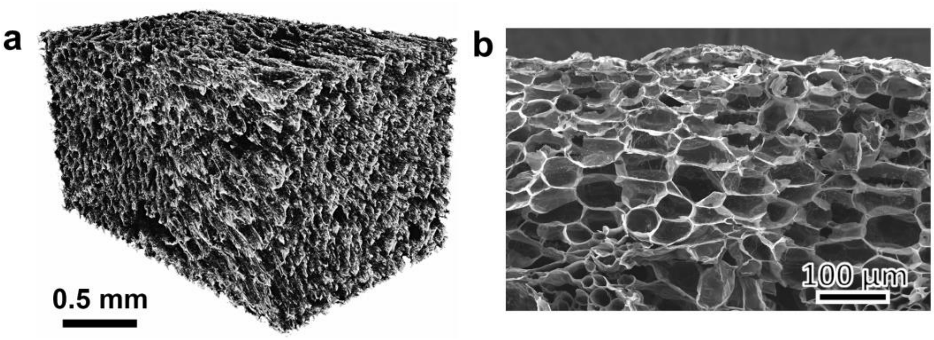

Fig. 2-2 Microstructure of ABP. a. 3D XCT image of ABP (the height of the examined ABP rectangle is 2 mm). b. The compact porous structure.

2.3.2 Fabrication of Li-S battery cathodes from ABP

Sulfur powders were first loaded onto a piece of ABP. The sulfur loaded ABP was then annealed at 155 ℃ for 12 h and at 200 ℃ for 2 h to infiltrate sulfur into the pores of ABP and coat a sulfur layer on the ABP surface without agglomeration. The sulfur loading was measured to be ~2.3 mg cm^{-2}. This is ascribed to the hierarchically porous structure in ABP that enhanced sulfur loading. The ABP/S (as the cathode) was assembled with lithium (as the anode) into a Li-S battery. This Li-ABP/S battery achieved a specific capacity of 1205 mAh g^{-1} in the first discharge. In the second cycle, however, the capacity dropped abruptly down to ~600 mAh g^{-1}. After 50 cycles, the capacity stabilized at ~450 mAh g^{-1}.

To overcome the fast capacity decay and the low utilization of sulfur, we created nanosized pores and deposited Ni nanoparticles simultaneously on the cell walls of ABP via a simple, low cost chemical route using $Ni(NO_3)_2$ solution. The $Ni(NO_3)_2$ treated ABP decomposed into the following products during the heat treatment at 1000 ℃ [54]:

$$Ni(NO_3)_2 \cdot 2H_2O \rightarrow Ni(NO_3)(OH)_2 \cdot H_2O + NO_2 \quad (1)$$

$$Ni(NO_3)(OH)_{1.5}O_{0.25} \cdot H_2O \rightarrow 0.5Ni_2O_3 + HNO_3 + 1.25H_2O \quad (2)$$

$$3Ni_2O_3 \rightarrow 2Ni_3O_4 + 0.5O_2 \quad (3)$$

$$Ni_3O_4 \rightarrow 3NiO + 0.5O_2 \quad (4)$$

$NiO + C \rightarrow Ni + CO$ (5)

$NiO + CO \rightarrow Ni + CO_2$ (6)

Among the decomposed products, the corrosive HNO_3 vapors etched the ABP surface, creating nanoporous structure with an average pore size of 30 nm while the original cell structure remained (Fig. 2-3a, b). A close-up inspection of the $Ni(NO_3)_2$ treated ABP revealed that Ni nanoparticles were embedded in nano carbon rings (Fig. 2-3c). In addition to Ni and amorphous C, the SAED pattern validated the existence of C crystal (Fig. 2-3d). High resolution TEM (HRTEM) image shows that Ni nanoparticles were wrapped with multilayered graphene, forming Ni/graphene core/shell structure (Fig. 2-3e, f). At high temperature, the C atoms from ABP dissolved into Ni. When the sample cooled down to room temperature, the C atoms precipitated out and segregated on the Ni nanoparticle surface, forming multilayered graphene shell [55,56]. This ABP/Ni/graphene composite demonstrated an improved conductivity with a sheet resistance of 7.4 Ω sq^{-1}. The conductivity improvement can be ascribed to the graphene-wrapped-Ni-nanoparticles because nickel and graphene are both excellent conductors. The ABP/Ni/graphene has a specific area of 474 m^2 g^{-1}, 2.5 times larger than ABP (194 m^2 g^{-1}). The Barrett-Joyner-Halenda (BJH) pore size distribution showed that most of the pores in the ABP/Ni/graphene were less than 40 nm, in good agreement with the SEM observation (Fig. 2-3b). Thusly, the ABP/Ni/graphene hybrid with order arranged nanopores and Ni/graphene core/shell nanoparticles is expected to overcome the quick capacity decay and improve the specific capacity of Li-S batteries.

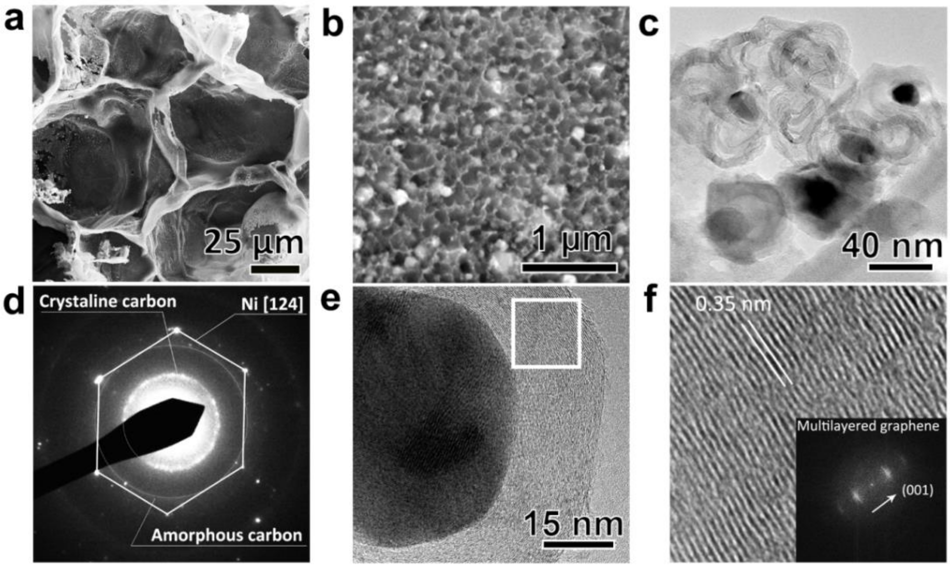

Fig. 2-3 Microstructure of ABP/Ni/graphene composite. a. SEM image of the $Ni(NO_3)_2$ treated ABP, showing the cellular porous structure. b. Close-up view of the $Ni(NO_3)_2$ treated ABP, showing co-existence of nanopores and Ni nanoparticles on the cell walls. c. TEM image of the $Ni(NO_3)_2$ treated ABP, showing the Ni nanoparticles wrapped with multilayered graphene. d. SAED patterns of the $Ni(NO_3)_2$ treated ABP, indicating the co-existence of crystalline carbon, amorphous carbon, and crystalline Ni. e. HRTEM image of a Ni nanoparticle wrapped with multilayered graphene. f. HRTEM image and FFT pattern of the multilayered graphene.

Next, we used the ABP/Ni/graphene composite to load sulfur. Sulfur was homogeneously anchored on the ABP/Ni/graphene scaffold with the sulfur loading of 5.3 mg cm^{-2}, which is approximately two times higher than that of the untreated ABP (2.3 mg cm^{-2}). The enhancement of sulfur loading can be ascribed to the nanopores in the composite, which offer more sites for sulfur storage. The BET surface area decrease drastically to 23 m^2 g^{-1}, indicating S filled the pores on the ABP walls, which was also proved by SEM image and EDS maps in Fig. 2-4a to 2-4d. Low magnification TEM image (Fig. 2-4e) exhibited that sulfur filled into carbon rings in Fig. 2-3c. The corresponding SAED pattern validated the existence of sulfur polycrystals (Fig. 2-4f). The close-up HRTEM inspection (Fig. 2-4g) unveiled that the Ni nanoparticles were coated with multilayered graphene (inner shell) and polycrystalline sulfur (outer shell). The outer sulfur shell contained nanosphere S crystals with the size of 5 nm embedded in the amorphous C (Fig. 2-4g). The corresponding FFT patterns (Fig. 2-4h) confirmed that Ni nanoparticles, sulfur nanosphere crystals, multilayered graphene crystal and amorphous carbon jointly construct the ABP/Ni/graphene/S composite. The close contact between S, graphene, Ni and ABP in cellulose architecture is expected to increase conductivity and facilitate ion diffusion and electron transfer, therefore jointly enhancing the electrochemical performance of Li-ABP/Ni/graphene/S batteries.

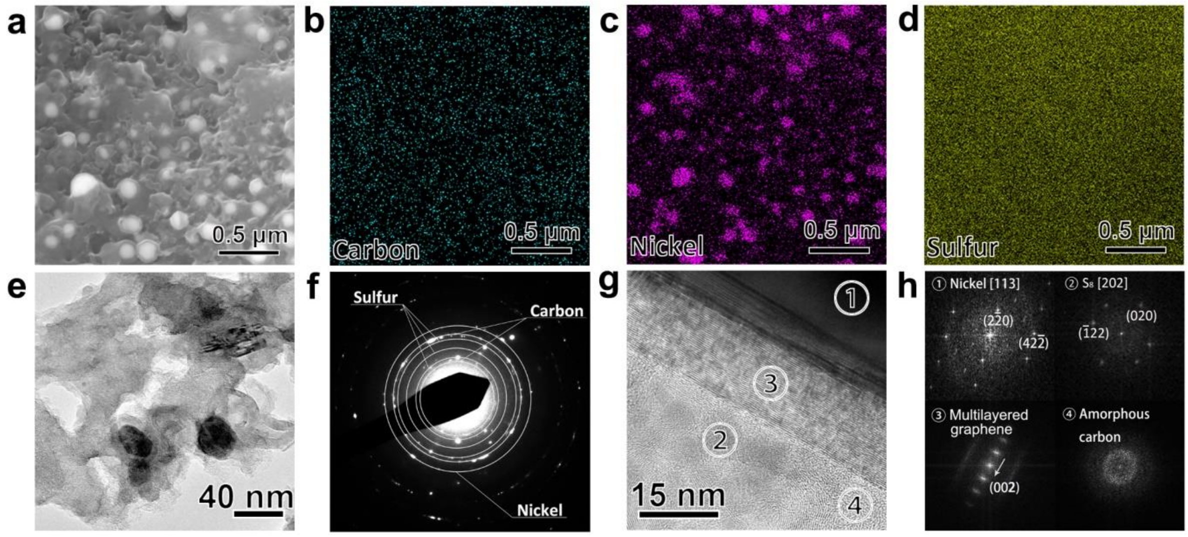

Fig. 2-4 Microstructure of ABP/Ni/graphene/S composite electrode. a. SEM image of ABP/Ni/graphene/S. b. Element map of carbon. c. Element map of nickel. d. Element map of sulfur. e. TEM image of ABP/Ni/graphene/S. f. SAED pattern of (a). g. HRTEM image of ABP/Ni/graphene/S. h. FFT patterns of areas ①, ②, ③, and ④ in (c), showing that the Ni nanoparticles, sulfur nanosphere crystals, multilayered graphene crystal and amorphous carbon jointly construct the ABP/Ni/graphene/S composite.

2.3.3 Electrochemical performance of ABP derived Li-S batteries

The most exciting development was the successful assembly of the ABP/Ni/graphene/S (as the cathode) and lithium (as the anode) into a high-performance Li-S battery. Fig. 2-5a shows the typical charge/discharge curve of the Li-ABP/Ni/graphene/S battery. Four stages appear to exist during discharge process (Stage I to IV in Fig. 2-5a), which can be respectively ascribed to the formation of $S_3^{\bullet-}$ radical anion (Stage I: plateau at 2.3 V), the formation of high-order polysufides from $S_3^{\bullet-}$ (Stage II: dip between 2.3 – 2.1 V), the transformation between S_4^{2-} and S^{2-} (Stage III: plateau at 2.1 V), and the formation of solid Li_2S (Stage IV: dip between 2.1 – 1.5 V) [57]. The charge process can be grouped into 3 stages (Stage V to VII in Fig. 2-5a). The first stage of charge process (Stage V) represents the conversion from solid Li_2S to soluble low-order polysulfide (S_2^{2-}). The plateau at 2.3-2.4 V (Stage VI) can be ascribed to the transformation between low-order polysulfide (S_2^{2-} or

S_4^{2-}) to high-order polysulfides (S_8^{2-} or S_6^{2-}) [53]. The last step of charge process (Stage VII in Fig. 2-5a) is a quick ascendance of voltage from 2.4 V to 2.8 V, indicating the transformation of high-order polysulfides back to solid sulfur. It is noteworthy that the last stage (Stage IV) of the discharge process and the first stage of the charge process (Stage V) both exhibited gentle slopes, rather than an abrupt dip or sudden jump which were often reported in Li-S batteries. The gentle slopes in Stages IV and V are ascribed to the 3D hierarchically porous structure of ABP, in which the sulfur stored in the pores slowed down capacity decay.

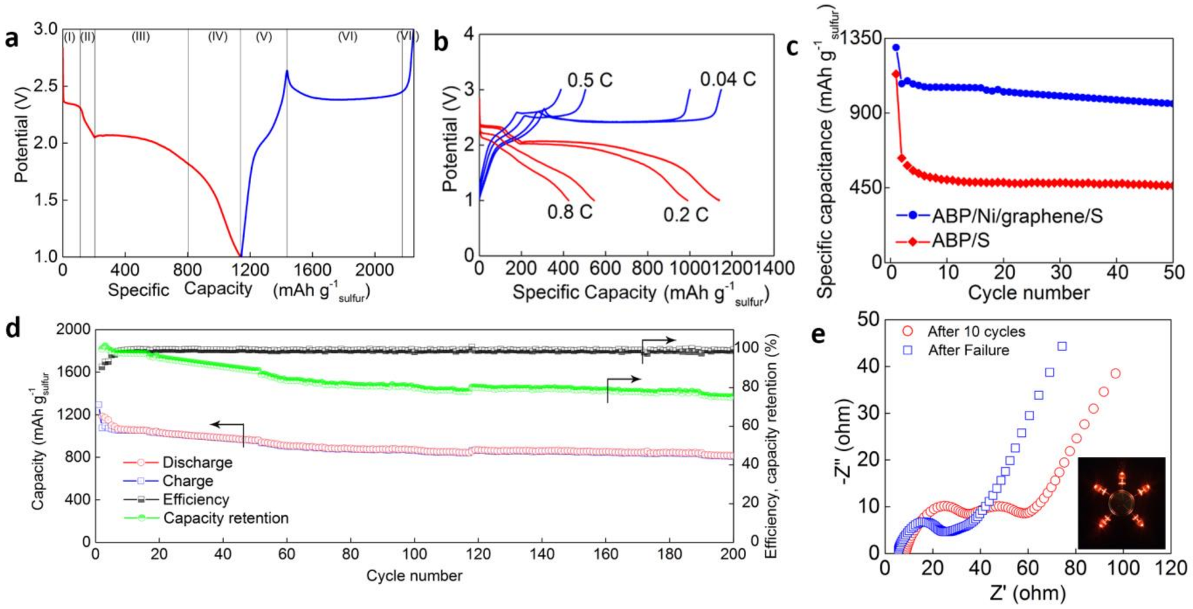

Fig. 2-5 Electrochemical performance of Li-ABP/Ni/graphene/S battery. a. Charge/discharge curve of Li-ABP/Ni/graphene/S battery. b. Charge/discharge curves of Li-ABP/Ni/graphene/S battery at different rates. c. Cycle ability of Li-ABP/Ni/graphene/S battery with reference to Li-ABP/S battery. d. Cycling performance of Li-ABP/Ni/graphene/S battery. e. Nyquist plot of Li-ABP/Ni/graphene/S battery under fully charging state before and after 200 cycles (inset: the Li-ABP/Ni/graphene/S battery can enlighten multiple LEDs).

It is especially recognized that the Li-ABP/Ni/graphene/S battery exhibited good rate ability (Fig. 2-5b). At a relatively low rate of 0.04 C its specific capacity achieved 1183.5 mAh g^{-1}. When the charge/discharge rate was raised up to 0.8 C its specific capacity was still kept above 400 mAh g^{-1}. However, further pushing up the rate led to distorted charge/discharge curves. The plateau at 2.0 V in the discharge curve (Stage I) reduced down to 1.8 V whereas the plateau at 2.2 V in the charge curve (Stage VI) raised up to 2.3 V. Such distortion can be ascribed to the insufficient electrochemical reactions and high internal resistance, jointly leading to a higher over-potential but lower capacity in the high current density regime. Cycling life and coulombic efficiency are two critical factors for evaluating the practical applications of a battery. the first discharge process at 0.2 C delivered a high capacity of 1260.3 mAh g^{-1}. Unlike the Li-ABP/S battery, the assembled Li-ABP/Ni/graphene/S battery did not show abrupt capacity decay in the second cycle, suggesting better capacity retention (Fig. 2-5c). The superior capacity retention is ascribed to the synergetic effects of Ni nanoparticles, graphene, and nanopores in cellulose architecture. In the Li-S battery, the stable $S_3^{\bullet-}$ radical anions play a key role because they are very active and can transfer into the electrolyte [8,57,58]. Other high order polysulfides (S_8^{2-}, S_6^{2-}, and S_4^{2-}) are either passive phases or semisolids [57], which can easily accumulate on the surface of the cathode, blocking the pathway between the electrode, active material, and electrolyte. The micro/nanopores in ABP/Ni/graphene/S cathode were able to encapsulate and immobilize sulfur chains [10], ensuring the local chemical environment suitable for more stable $S_3^{\bullet-}$ radical anions [58] as well as avoiding the shuttle effect. Encouragingly, the Li-ABP/Ni/graphene/S battery exhibited eminent cyclic performance with a recovery of capacity of 832.4 mAh g^{-1} at 0.2 C after 200 cycles. With the exception of the first few cycles, the ABP/Ni/S-based Li-S battery exhibited excellent coulombic efficiency of almost 100 % even after 200 cycles (Fig. 2-5d), indicating outstanding coulombic efficiency.

EIS measurements were also carried out to further investigate the electrochemical performance of the assembled Li-ABP/Ni/graphene/S battery. As shown in Fig. 6e, at the early stage of cycling (10th cycle), two semicircles appeared in the high frequency regime. The first one at the relatively higher frequency resulted from the deposition of a passive film on the surface of electrodes, the other one at the intermediate frequency arose from the migration of lithium ions through the solid-electrolyte-interphase (SEI) film. The straight line in the low frequency regime was the result of the Li ion diffusion [59]. The intercept of x axis was used to find out the charge transfer resistance, which is closely related to the resistance of interfaces. After failure, the second semicircle disappeared, indicating the broken of SEI film (Fig. 2-5e) [60]. It is highly possible that large Li dendrites penetrated the SEI. The fracture of the SEI film in turn accelerated the growth of Li dendrites, resulting in the failure of the battery. The reduced charge transfer resistance and the semicircle at the high frequency regime can be attributed to the rearrangement of insulate sulfur to more electroactive locations and the closer contact between the cathode, separator, and anode as cycling preceded. This banana-peel derived battery is able to enlighten multiple LEDs (see the inset in Fig. 2-5e). It is noteworthy that the hierarchically porous architecture contributed remarkably to the exceptional electrochemical performance of the Li-ABP/Ni/graphene/S battery. The porous foam-like structure accommodated the volume change during the transformation between sulfur and polysulfides, suppressed the formation of passive films which might impede the electrochemical reactions, mitigated dissolution of polysulfides via trapping and encapsulating multi-atom sulfur chains, and shortened the pathway of ion transfer. Moreover, the highly conductive Ni/graphene core/shell nanoparticles further facilitated ion transport and electron transfer, while the graphene shell blocked the possible reactions between nickel and sulfur, reducing internal resistance and enhance coulombic efficiency. Considering economic and social benefits of recycling banana peels, such low cost biomass-based activated porous carbon holds an unprecedented promise for energy storage application.

2.4 Capillarity composited recycled paper/graphene scaffold for lithium-sulfur batteries with enhanced capacity and extended lifespan

2.4.1 Activation and microstructure of activated paper carbon

Recycled paper pieces were peeled from a hardboard roll (a package of a calendar) (Fig. 2-6a) and cut into long, rectangular stripes (Fig. 2-6a inset). Scanning electron microscope (SEM) inspection for the pristine recycled paper unveiled interweaving fibers with sparse particles (Fig. 2-6b). In the X-ray diffraction (XRD) spectrum, two broad peaks centered at 15 ° and 22 ° represented cellulose, two sharp peaks at 24 ° and 29 ° can be ascribed to $CaCO_3$ and a small peak at 12 ° indicated the existence of SiO_2 (Fig. 2-6d). $CaCO_3$ and SiO_2 are common reinforcing agents in paper production. The high temperature annealing converted the paper stripes into activated paper carbon (APC) with dark black color (see Fig.

2-6c inset). SEM inspection (Fig. 2-6c) revealed that the APC inherited paper's microstructure but the fibers shrunk about 20 %. Close-up observation of an APC fiber showed micron-sized crinkles on the fiber. XRD (Fig. 2-6d) showed that the cellulose peaks from the pristine paper were replaced a broad but weak peak centering at 26 °, indicating that the pristine cellulosic wood fibers were successfully converted into low graphitized carbon. Based on the intensity of the XRD peaks and SEM observation, the impurity content in APC should be lower than 5 %. Raman spectroscopy (Fig. 2-6e) inspection identified a broad G bond at ~1580 cm^{-1} and D bond at 1350 cm^{-1} in the APC. The G peak reflects crystal disorder of carbon while the D peak corresponds to an ideal graphitic lattice. The intensity ratio of D band and G band (I_D/I_G) is an indicator of graphitization [61]. The high intensity of D band together with the I_D/I_G of 0.85 agrees well with the XRD result. The as-prepared APC showed a large Brunauer−Emmet−Teller (BET) [53] surface area of 201.53 m^2 g^{-1}, indicating a readily porous structure which is expected to enhance electrolyte accessibility and buffer the volume change during electrochemical reactions. The electrical resistance of the APC alone was measured to be 11.67 Ω cm^{-2}.

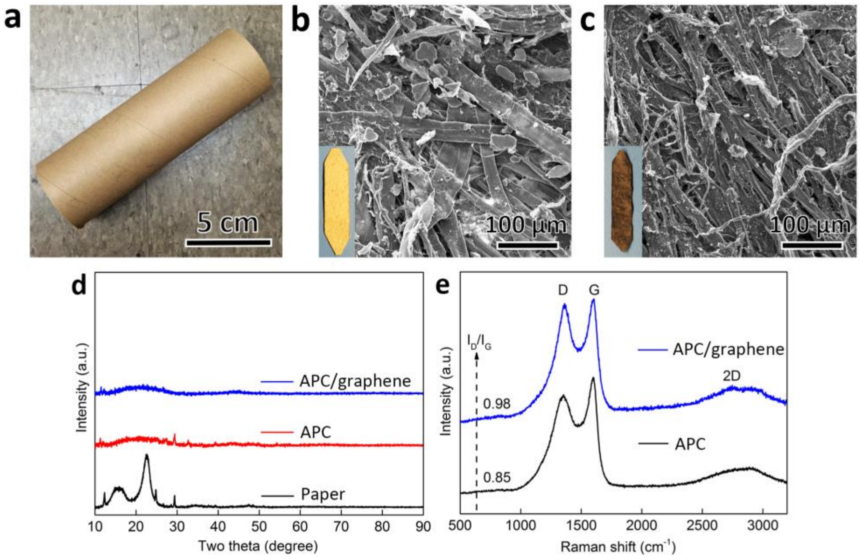

Fig. 2-6 Activation and microstructure of recycled paper. a. Picture of a hardboard roll (a package of a calendar). b. SEM image of the recycled paper (inset: recycled paper stripe). c. SEM image of APC (inset: APC stripe). d. XRD of recycled paper, APC, APC/graphene composite. e. Raman spectra of APC and APC/graphene composite.

2.4.2 Fabrication of APC/graphene/S electrodes

Graphene oxide is dispersible in water and highly compatible to other scaffolds because of its hydrophilic and flexible nature. In this study, graphene oxide was creatively composited with paper fibers via capillary absorption (Fig. 2-7a and b). This capillary adsorption method is completely chemical-free and highly scalable. It is able to coat porous materials with a homogeneous graphene oxide layer at lowest waste (Fig. 2-7c and d). In the present study with 2 mg mL^{-1} graphene oxide solution, the weight percentage of graphene oxide on recycled paper constantly ranged from 10 to 12 wt. %, indicating outstanding repeatability and stability of this method. High temperature annealing can largely recover the strength and conductivity of graphene oxide sheets without eliminating the functional groups. The remaining functional groups on the reduced graphene oxide are able to immobilized and entrap lithium polysulfides, effectively mitigating shuttle effect in the Li-S battery system [25-37].

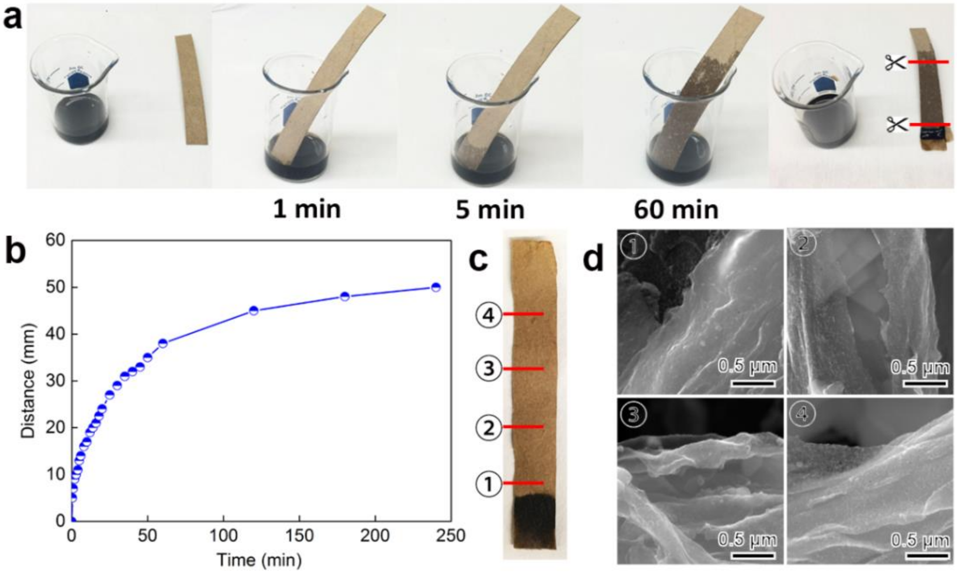

Fig. 2-7 Compositing graphene oxide with recycled paper via a capillary absorption method. a. Pictures showing compositing graphene oxide with the recycled paper by capillary force. b. The corresponding liquid height vs. time chart. c. The dried recycled paper/graphene oxide composite with different location noted as ①②③④. d. Corresponding SEM images at location ①②③④, showing that graphene oxide homogeneously covered on paper fibers irrelevant to the location.

The obtained recycled paper/graphene oxide stripes were annealed at 1000 ^{o}C for 1 h, forming activated paper carbon/reduced graphene oxide (APC/graphene) composite. A remarkable change in the surface morphology of APC occurred after compositing with graphene sheets. Except for the pristine crinkles (Fig. 2-8a), nano-sized winkles with tortuous bulges formed on the APC/graphene composite surface (Fig. 2-8b). The APC/graphene composite exhibited a certain degree of flexibility and was able to maintain structural integrity (see the inset of Fig. 2-8b). Transmission electron microscopy (TEM) observation further revealed that multilayered graphene was homogeneously wrapped on the APC fiber with cavities and pores in between (Fig. 2-8c and d). XRD spectrum of APC/graphene composite exhibited almost identical morphology as the APC (Fig. 2-6c). Raman spectroscopy inspection of the APC/graphene composite showed a more notable 2D peak, the second order of the D peak at ~2680 cm^{-1}, and higher I_D/I_G ratio, indicating that the graphene coated on the APC retained the defects from graphene oxide (Fig. 2-6d). Apart from higher BET specific surface area (272.19 m^2 g^{-1}) than the APC (201.53 m^2 g^{-1}), the APC/graphene composite exhibited a notable hysteresis loop in the isothermal curve and improved BJH pore surface area of 115.64 m^2 g^{-1}, 120% higher than the APC (52.47 m^2 g^{-1}), indicating that mesopores were created by applying the graphene films. The higher pore volume of APC/graphene is expected to improve sulfur loading and shorten ion transfer path. Since graphene is an excellent conductor, the resistance of APC/graphene composite reduced down to 9.16 Ω cm^{-2}, 21.4 % lower than APC (11.67 Ω cm^{-2}). In contrast, the APC/dipped-graphene composite (recycled paper dipped into graphene oxide solution and then annealed at 1000 ^{o}C for 1 h) was covered by a thick reduced graphene film and no nano-sized winkles were found. The BET surface area of this reference sample dropped abruptly down to 94.10 m^2 g^{-1} with a very low BJH pore surface area of 15.28 m^2 g^{-1}; the thick graphene layer blocked the pristine pores of APC.

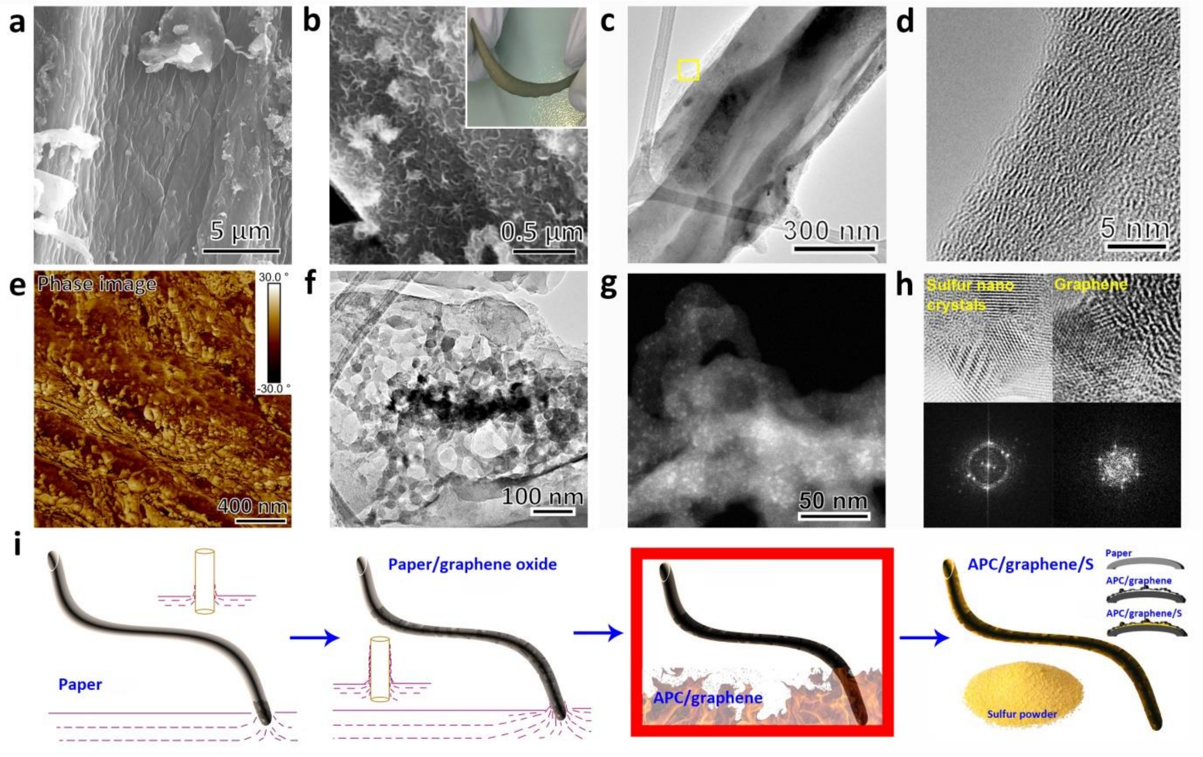

Fig. 2-8 Microstructure of APC/graphene and APC/graphene/S composites. a. SEM image of APC. b. SEM image of APC/graphene composite, showing nano sized winkles on the surface (inset: flexibility of the APC/graphene composite). c. TEM image of graphene wrapped APC fiber, showing similar morphology to the SEM image. d. HRTEM image of a bulge in the graphene film, showing clear multilayered graphene structure. e. AFM phase image. Sulfur appears in the form of nano particles with sizes ranging from several nano meters to tens of nano meters. f. TEM image of graphene film with S. g. HAADF STEM image of graphene film with S. h. HRTEM and FFT patterns of S nano particles and graphene. i. Schematic diagram of fabricating the recycled paper based cathode material.

To prepare an APC/graphene/S electrode, sulfur powders were first loaded onto the APC/graphene scaffold. The sulfur loaded APC/graphene was then annealed at 155 ℃ for 12 h to infiltrate sulfur into the pores of APC/graphene scaffold and then at 200 ℃ for 2 h to evaporate extra sulfur on the surface. After the two-step infiltration, sulfur was homogeneously coated on the APC/graphene scaffold without agglomeration. Close-up observation of the APC/graphene/S composite under atomic force microscope (AFM) unveiled that nanometer-sized sulfur particles were well bonded onto individual APC/graphene fibers (Fig. 2-8e). TEM observation shows that sulfur infiltrated into the nano bugles of graphene film (Fig. 2-8f). The high angle annular dark field (HAADF) Z-contrast scanning TEM image uncovered that sulfur nanoparticles were wrapped by graphene films (Fig. 2-8g), which was further validated by higher resolution TEM (HRTEM) observation and corresponding fast Fourier transform (FFT) patterns (Fig. 2-8h). The sulfur loading in the APC/graphene was measured to be 3.6 mg cm^{-2}, 50 % of the electrode weight, more than three times higher than the sulfur loading of pure APC (1.07 mg cm^{-2}, 23 % of the electrode weight). The sulfur loading of APC/dipped-graphene composite was measured to be 1.8 mg cm^{-2}, but was only 20 % of the electrode weight. This is because the thick graphene layer increased the weight of carbon scaffold and blocked the sulfur infiltration into the pores of APC.

Since APC and APC/graphene processed similar microstructure and specific area, the graphene film should have played a critical role in the enhancement of sulfur loading. Conductivity, mechanical properties, and element distribution of the electrodes were measured to uncover the mechanism. After sulfur infiltration, the resistance of APC/S composite increased from 11.7 to 22.1 Ω cm^{-2} whereas that of APC/graphene/S composite maintained at 9.27 Ω cm^{-2}. The surface modulus and hardness of APC/S composite were measured to be respectively 0.73 GPa and 0.16 GPa, lower than the modulus (1.5 GPa) and hardness (0.55 GPa) of APC/graphene/S composite (Fig. 2-9a) (measured by AFM with a diamond indenter tip). Secondary ion mass spectrometry (SIMS) revealed high carbon concentration on the surface of APC/graphene/S and sulfur beneath the surface (Fig. 2-9b), indicating the surface of the composite is covered with carbon. These measurements confirmed that sulfur was capsuled by the graphene film, which not only provided more pores for sulfur storage and protected sulfur from vaporizing, but also can entrap dissolved polysulfides in the following reactions.

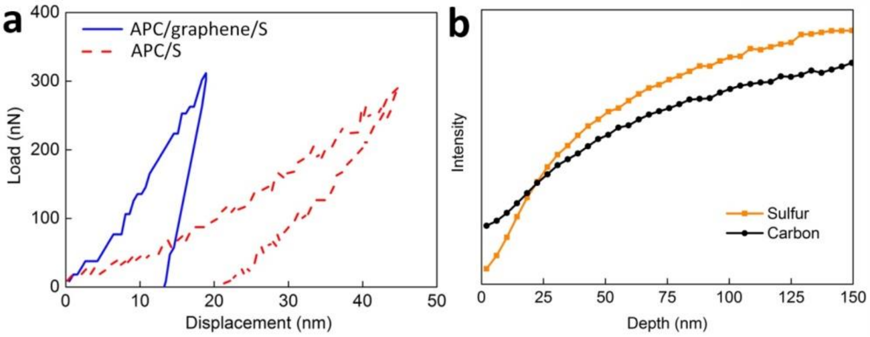

Fig. 2-9. Mechanical properties and SIMS depth profile of APC/graphene/S composite. a. Load-displacement curves of APC/S and APC/graphene/S composites measured by AFM with a diamond tip. b. SIMS depth profile of APC/graphene/S composite, showing higher carbon concentration on the surface.

Armed with the above systematic studies we are able to summarize the formation mechanism of the APC/graphene/S cathode (Fig. 2-8i). Theoretically, when a dry porous medium (e.g. paper) is brought into contact with liquid, it will absorb the liquid at a rate which decreases over time because of surface tension build-up. The cumulative wetted length h of absorbed liquid after a time period of t is:

$$h = \frac{s}{f}\sqrt{t} \qquad (1)$$

where f is the porosity of the medium and s is the sorptivity of the medium. The s/f ratio of the recycled paper strip was measured to be 4.91±0.019 $\mathrm{mm\,min^{-1/2}}$ by fitting the obtained time/height curve (Fig. 2-7b**)**. In this study, hydrophilic graphene oxide flakes were homogeneously dispersed in water and adhered on the paper fibers by capillarity. After drying, a uniform graphene oxide coating was deposited on the fibers (Fig. 2-7c and d). This bottom-up self-assembly method assures homogeneous dispersion and minimum graphene oxide consumption at the same time. This capillary absorption method has been successfully grafted to other porous bio-mass materials, such as activated cotton textile (ACT) and activated banana peel (ABP), and should find more applications in different porous media. The recycled paper/graphene oxide stripes were then converted to APC/graphene by high temperature activation. During the high temperature annealing, the paper fibers shrunk about 20 % which was much larger than the negative thermal expansion of graphene oxide [62]. To accommodate the 20% size reduction, graphene film contracted geometrically, leading to the wrinkle-like morphology with nano sized bulges. Upon the following-up sulfur infiltration, sulfur exhibited the highest fluidity at 155 ℃ [20] and infiltrated into the cavities between APC fibers. Moreover, melted sulfur has remarkable wettability with graphene because of the similar ring-like structure, which promoted sulfur permeating under the graphene film. Further heating at 200 ℃ vaporized agglomerated sulfur on the APC/graphene surface, whereas the sulfur beneath the graphene was preserved, leading to high sulfur loading. The formed C/S/C sandwich configuration can facilitate ion and electron transfer and to confine lithium polysulfides [63,64]. It is noteworthy that sulfur was not only encapsulated by the graphene film, but also chemically bonded with it. Such strong interactions are expected to enhance the immobilization of polysulfides, promoting the electrochemical performance of Li-S batteries.

2.4.3 Electrochemical performance of Li-S batteries with APC/graphene/S cathodes

The most exciting development was the successful assembly of the APC/graphene/S (as the cathode) and lithium (as the anode) into a high-performance Li-S battery. Surprisingly, the assembled Li-APC/graphene/S battery operated 620 cycles at 0.96 C rate (1 C rate means the current density is 1670 mA g^{-1}_{sulfur}; the corresponding areal current density of 0.96 C is 4.2 mA cm^{-3}). It exhibited a discharge capacity of 1083.1 mAh g^{-1} in the first cycle and that of 754.2 mAh g^{-1} in the last cycle, which equates to a 60.5% retention rate or a 0.05% decrease for each cycle (Fig. 2-10a). The longevity and outstanding capacity retention rate of the Li-APC/graphene/S battery stem from a synergic contribution of multiple features. The APC exhibited rich porosity and high surface area, which accommodated volume fluctuation and enhanced sulfur loading. The graphene film with nano sized bugles wrapped on the APC fibers, improving conductivity and facilitating ion/electron transfer. Besides, the graphene film encapsulated dissolved polysurfides and prevented the shuttling effect because of the C/S/C sandwiched structure and the functional groups on the graphene surface which bonded with lithium polysulfuide chains. A notable activation happened after first several cycles. Such behavior may be ascribed to the following three aspects: (1) sulfur encapsulated in the graphene film released gradually to the electrolyte; (2) the dissolved polysulfides permeated through the graphene coating, increasing sulfur utilization [36]; and (3) reversible formation/dissolution of SEI-like product on the surface assisted in ion exchange and created more electroactive sites for electrochemical reactions [65]. In the first 250 cycles, coulombic efficiency remained at nearly 100 %. In subsequent cycles, the coulombic efficiency decreased slowly. However, even at the 620th cycle, the coulombic efficiency still remained at 92.1%. The decrease of coulombic efficiency derived from the inevitable nonhomogeneous strapping/plating of Li anode, leading to continuous consumption of $LiNO_3$, which is considered to be able to reduce the shuttling effect. For comparison, both APC/dipped-graphene/S and APC/S composites were used as reference cathode materials to assemble Li-S batteries. The cycling performance of Li-APC/dipped-graphene/S battery (Fig. 2-10b**)** exhibited an abrupt capacity fading in first several cycles and failed at 312th cycle with the capacity retention rate of 34.6 %. The poor electrochemical performance of this battery is attributed to the low specific area, thusly decreasing the utilization of active materials. Moreover, excessive graphene from the dipping process filled pores of APC fibers and constrained the volume change during cycling, leading to earlier failure of the battery. For the Li-APC/S battery (Fig. 2-10c), the capacity decreased rapidly and subsequently cycled at a low capacity (around 300 mAh g^{-1}) and failed at 474th cycle with the capacity retention rate of 25 %. The absence of graphene encapsulation and functional group bonding in the Li-APC/S battery resulted in its quick capacity fading. However, the APC electrode had a readily porous structure which accommodated the volume change during cycling, leading to a longer lifespan than the Li-APC/dipped-graphene/S battery. Considering the heavier weight of APC/dipped-graphene/S electrode and the extra cost of graphene, the Li-APC/S battery actually outperformed the Li-APC/dipped-graphene/S battery, suggesting that the excessive abuse of graphene may even undercut the performance of batteries. Worth mentioning is that a relative high concentration of $LiNO_3$ (0.4 mol L^{-1}) was used in the electrolyte, which is believed to be able to effectively reduce the shuttle effect and stabilize the lithium anode. However, Li-APC/S and Li-APC/dipped-graphene/S battery exhibited quick capacity decay even with $LiNO_3$ additive, indicating that the graphene layer formed by capillary absorption method can entrap lithium polysulfides physically and chemically, resulting in superior performance of Li-APC/graphene/S battery.

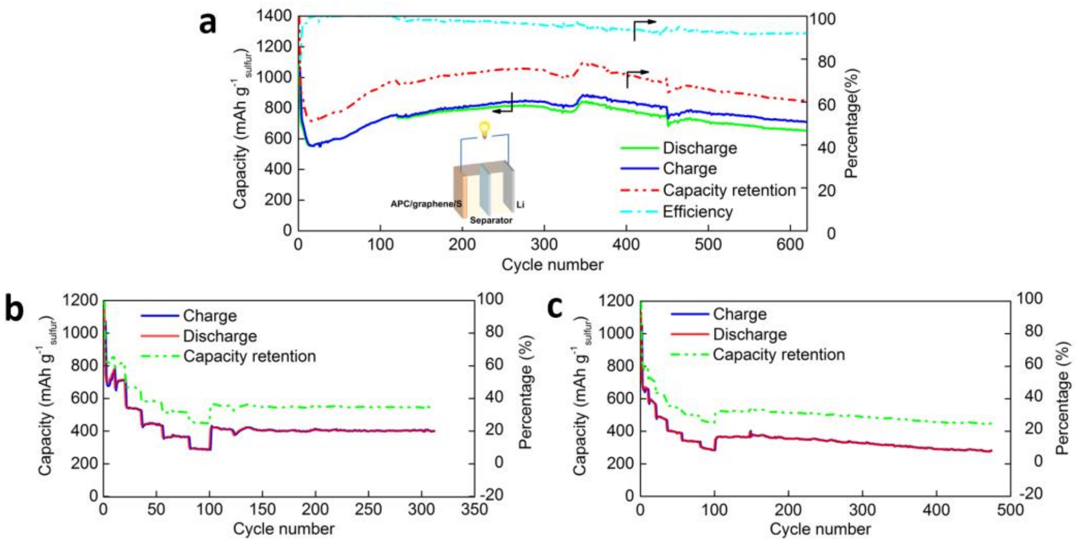

Fig. 2-10 Cyclic performance of Li-APC/graphene/S, Li-APC/dipped-graphene/S and Li-APC/S batteries. a. Li-APC/graphene/S battery. b. Li-APC/dipped-graphene/S battery. c. Li-APC/S battery.

Fig. 2-11a shows the typical charge/discharge curve of the Li-APC/graphene/S battery which can be divided into seven stages. Four stages appear to exist during discharge process (Stage I to IV in Fig. 2-11a), which can be respectively ascribed to the formation of high order polysulfides (S_8^{2-}, S_6^{2-}) (Stage I: plateau at 2.3 V), the formation of S_4^{2-} from high order polysulfides (Stage II: dip between 2.3 – 2.1 V), the transformation between S_4^{2-} and S^{2-} (Stage III: plateau at 2.1 V), and the formation of solid Li_2S (Stage IV: dip between 2.1 – 1.5 V) [58,66]. The charge process can be grouped into 3 stages (Stage V to VII in Fig. 2-11a), which are attributed to the conversion from solid Li_2S to soluble low-order polysulfide (S_2^{2-}) (Stage V), the transformation between low-order polysulfide (S_2^{2-}) to high-order polysulfides (S_8^{2-} or S_6^{2-}) (Stage VI), and the transformation of high-order polysulfides back to solid sulfur (Stage VII), respectively [67]. Fig. 2-11n shows CV profiles for the Li-APC/graphene/S battery at the scan rate of 0.001 mV s^{-1} in the voltage range of 1.5 to 2.8 V vs Li/Li^+. During cathodic scans, two reduction peaks at 1.9 V and 2.3 V correspond to two discharge plateaus in the charge/discharge curve (Fig. 2-11a). In the subsequent anodic scans, the board oxidation peak around 2.5 V represents the complete transformation from LiS_2 to S_8, corresponding to the large charge plateau in the charge curve in Fig. 2-11a. The discharge/charge curve and CV curved displayed typical Li-S system features without distortion or extra reactions, implying that impurities (small amount of SiO_2 and $CaCO_3$) remaining in the APC had no effect on the battery performance.

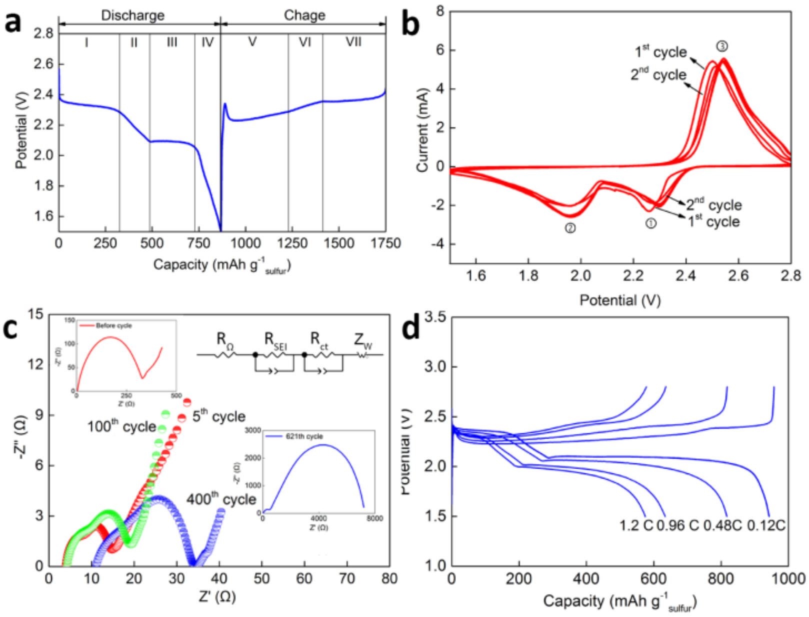

Fig. 2-11 Electrochemical performance of the Li-APC/graphene/S battery. a. Typical charge/discharge curve of the Li-APC/graphene/S battery. b. CV curves of the first five cycles. c. EIS curves before cycling, at 5th cycle, 100th cycle, 400th cycle, and after battery's failure (inset is the fitting model of the EIS curve). d. Rate performance of the Li-APC/graphene/S battery.

EIS tests were carried out to further investigate the Li-APC/graphene/S battery performance (Fig. 2-11c). Before cycling, the EIS spectrum exhibited a large internal resistance because of the unconducive nature of sulfur and the impurity of lithium surface. However, after the fifth cycle the internal resistance reduced dramatically and two semicircles formed at the high frequency regime and intermediate frequency regime. The semicircle at the high frequency regime stems from the impedance of ions passing through the SEI on the anode surface, which can be represented as a resistor and a capacitor in parallel in the equivalent circuit (see Fig. 2-11c inset). The resistance part was calculated from the diameter of the semicircle and is marked as R_{SEI}. Another semicircle in the intermediate frequency regime indicates the impedance of the charge transfer between the electrodes and electrolyte, which is ascribed to the passive deposits on the surface of the electrodes. Similarly, it can be represented as a combination of a resistor and capacitor in the equivalent circuit and the resistance part is noted as R_{ct}. The intercept between the EIS curve and the Z' axis is the equivalent series resistance, which is noted as R_{Ω} and is equal to a resistance in the equivalent circuit. The straight line at the low frequency regime is the so called "Warburg impedance" which derives from an ion diffusion limited process in the electrolyte and is denoted as Z_w [59]. Upon continuous cycling, the total resistance increased moderately; the charge transfer resistance (R_{ct}) increased to 10 Ω only while the charge-transfer resistance to 22 Ω after 400 cycles, indicating that the APC/graphene/S electrode was stable after long time operation. However, when the battery failed, the R_{ct} increased rapidly, leading to circular breaking of the battery. Apart from long life span, the Li-APC/graphene/S battery also exhibited outstanding rate ability (Fig. 2-11c). A battery which stabilized after 80 cycles showed a reversible capacity from 960 mAh g^{-1} to 600 mAh g^{-1} when the discharge rate increased 10 times from 0.12 C to 1.2 C, which was equivalent to 60 % capacity retention rate. Pushing up the rate led to distorted charge/discharge curves. The plateau at 2.0 V in the discharge curve reduced down to 1.8 V whereas the plateau at 2.2 V in the charge curve rose up to 2.4 V. Such distortion can be ascribed to a higher over-potential due to the insufficient electrochemical reactions. Even so, the discharge curves still displayed obvious two-stage morphology in the high current density regime while the polarization remained small even when the scan rate was raised 10 times up, indicating eminent stability of the assembled battery. The specific capacity of the battery completely recovered after the current density reduced from 1.2 C down to 0.48 C, further supporting the conclusion. The outstanding rate capacity can be ascribed to the graphene film, which enhanced the electron transfer and captured polysulfide chains via chemical bonds even at high charge/discharge current.

2.4.4 Failure mechanisms of Li-S batteries with APC/graphene/S cathodes

Since a life span of 620 cycles with the capacity retention rate of 60.5% is indeed outstanding for a Li-S battery, we performed post failure tests on both cathode and anode in an attempt to uncover the failure mechanisms for the battery. SEM inspection unveiled that the cathode material preserved original porous structure of APC after 620 discharge/charge cycles (Fig. 2-12a). EDS element maps of C, S, and O showed that the deposit on APC surface was a mixture of electrolyte and polysulfides. Close-up SEM inspection revealed that graphene coating broke into fragments whereas APC surface cracked (Fig. 2-12b). TEM observation showed that numerous nano sized cracks formed throughout the entire fiber (Fig. 2-12c). Therefore, the stress from the volume fluctuation during discharge/charge cycling accumulated on the surface of the APC fiber, leading to the formation of cracks. The continuous electrochemical reactions may occur on the newly exposed interfaces, promoting the propagation of the cracks. These cracks, on one hand, increased the cathode's specific area to 357 $m^2 g^{-1}$, but had almost no contribution to the pore volume; on the other hand, they impeded the electron transfer, leading to larger charge transfer resistance. The mechanical property of the APC/graphene/S electrode before and after cycling (620 cycles) was measured by AFM with a diamond indenter tip. The cycled APC/graphene/S cathode exhibited much lower elastic modulus (0.745 GPa) and hardness (0.095 GPa) compared to an uncycled cathode which had an elastic modulus of 1.724 GPa and hardness 0.547 GPa. The electrochemical reactions indeed deteriorated the structure and mechanical properties of the cathode, but not to the degree of catastrophic failure.

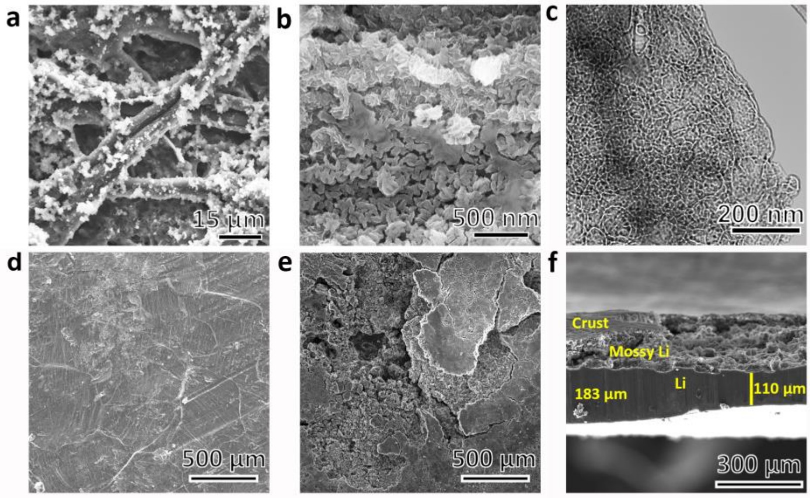

Fig. 2-12 Microstructure of APC/graphene/S cathode and Li anode after 620 cycles. a. SEM image of APC/graphene/S electrode after 620 cycles. The structure of APC was preserved. b. Close-up observation of a fiber showing nano sized cracks on the surface. c. TEM image of a cycled APC, showing nano sized cracks. d. SEM image of the pristine Li anode. e. SEM image of the Li anode after 620 cycles, displaying crusts and big holes. f. Cross-section of Li anode after 620 cycles.

We then performed microstructural and mechanical characterization on the cycled anode with the goal to elucidate the root cause of failure. Compared with the original lithium plate with a flat surface and parallel grooves from machine work (Fig. 2-12d), after 620 cycles, the cycled plate exhibited a rough surface with large pores and pits coupled with facet crusts (Fig. 2-12e). Cross-sectional SEM inspection revealed that the cycled Li anode had three layers (Fig. 2-12f). The crust was on the top surface, Li was at the bottom, and mossy Li was sandwiched in between. Since mossy Li and corrosion pits are frequently observed in Li anodes, the question is: what was the crust? The pristine Li plate exhibited an average modulus of 4.4 GPa whereas the crust displayed a much lower modulus of 1.3 GPa, suggesting the curst was a different material from Li. EDS element analysis showed that the crust had a high concentration of sulfur and oxygen, indicating that the crust was a thick sediment layer consisting of both SEI and polysulfides. Dendrites formed on the lithium metal electrode during repeated depositing and stripping. These tree-like crystals may break off, forming isolated micro-aggregates wrapped by thick SEI. Moreover, SEI remained on the anode surface after mossy Li whiskers being etched, forming SEI flotsams. In addition, unsolvable lithium polysulfides slowly segregated on the surface of electrodes. The aforementioned sediments aggregated on the Li surface, forming a passive layer and thus blocking ion transfer and electrochemical reactions. This conclusion was also supported by the cross-sectional SEM observation (Fig. 2-12f) showing that the Li anode was thicker at the places covered by the passive layer. In the Li-APC/graphene/S battery, a decrease of coulombic efficiency was observed after 250 cycles (Fig. 2-10a) whereas a rise in the charge transfer resistance started at the 400th cycle (Fig. 2-11c), jointly indicating that $LiNO_3$ was gradually consumed and passive sediments had covered the reaction area. After battery failure, the internal resistance from the semicircle at intermediate frequency regime became almost infinite (Fig. 2-11c) and the anode surface formed flat crust, suggesting the formed passive layer had covered all electroactive sites and blocked the redox chemistry. Since the APC/graphene/S cathode retained its structural integrity even after 620 cycles, the failure of the Li-APC/graphene/S battery can be ascribed to the malfunction of Li anode.

2.5 Conclusions

In summary, banana peels have been successfully converted into hierarchically porous activated carbon scaffolds for energy storage applications. Annealing $Ni(NO_3)_2$ treated ABP created nanopores and graphene wrapped Ni nanoparticles simultaneously on the cell walls of ABP. The hierarchically porous ABP/Ni/graphene architecture accommodated the volume change during the charge/discharge cycling, suppressed the formation of passive layer, mitigated dissolution of polysulfides via trapping and encapsulating multi-atom sulfur chains, and shortened the pathway of ion transfer. Moreover, the highly conductive Ni nanoparticles and graphene further enhanced electron transfer, ensuring low internal resistance and high coulombic efficiency. The banana-peel derived Li-S batteries present a new promise for the design and fabrication of high performance energy storage devices while reducing material waste. In another work, recycled paper was creatively composited with graphene oxide sheets by capillary method. The obtained recycled paper/graphene oxide hybrid was annealed at 1000 ℃ to convert to APC/graphene scaffold. Since the shrinkage of APC was larger than graphene, the graphene film on the APC contracted geometrically, forming wrinkle-like morphology with nanometer-sized tortuous bulges. Sulfur powders were then loaded onto the scaffold by a two-step heat treatment. The graphene film encapsulated sulfur nano particles, increasing the sulfur loading and electrode’s conductivity as well as preventing the vaporization of sulfur. The APC/graphene/S composite was used as a free-standing cathode to construct Li-S batteries, which exhibited superior life span of 620 cycles, excellent capacity retention rate of 60.5%, and outstanding rate ability (60 % retention when scan rate increased from 0.12 C to 1.2 C). The porous APC/graphene/S architecture accommodated the volume change induced by the transformation between sulfur and polysulfides. The graphene film entrapped and encapsulated polysulfides and facilitated electron/ion transfer. After 620 cycles, APC/graphene/S cathode deteriorated but not to the degree of catastrophic failure. However, the Li anode malfunctioned because mossy Li and passive sediments blocked redox chemistry. The novel Li-S battery configuration provides new insight into the design and fabrication of sustainable, high performance energy storage devices.

References

[1] C. McGlade, P. Ekins, The geographical distribution of fossil fuels unused when limiting global warming to 2 ℃, Nature 517 (2015) 187-190.

[2] M.S. Whittingham, Lithium batteries and cathode materials, Chem. Rev. 104 (2004) 4271–4301.

[3] J.B. Goodenough, Y. Kim, Challenges for rechargeable batteries, J. Power Sources 196 (2011) 6688–6694.

[4] P.G. Bruce, B. Scrosati, J.M. Tarascon, Nanomaterials for rechargeable lithium batteries, Angew. Chem. Int. Ed. Engl. 47 (2008) 2930-2946.

[5] S.E. Cheon, K.S. Ko, J.H. Cho, S.W. Kim, E.Y. Chin, H.T. Kim, Rechargeable lithium sulfur battery I. structural change of sulfur cathode during discharge and charge, J. Electrochem. Soc. 150 (2003) A796-A799.

[6] S.E. Cheon, K.S. Ko, J.H. Cho, S.W. Kim, E.Y. Chin, H.T. Kim, Rechargeable Lithium Sulfur Battery II. Rate Capability and Cycle Characteristics, J. Electrochem. Soc. 150 (2003) A800–A805.

[7] P.G. Bruce, S.A. Freunberger, L.J. Hardwick, J.M. Tarascon, Li-O2 and Li-S batteries with high energy storage, Nat. Mater. 11 (2012) 19-29.

[8] M. Wild, L. O’Neill, T. Zhang, R. Purkayastha, G. Minton, M. Marinescu, G.J. Offer, Lithium sulfur batteries, a mechanistic review, Energy Environ. Sci. 6 (2015) 3477-3494.

[9] G. Hu, C. Xu, Z. Sun, S. Wang, H.M. Cheng, F. Li, W. Ren, 3D graphene-foam-reduced-graphene-oxide hybrid nested hierarchical networks for high-performance Li-S batteries, Adv. Mater. 28 (2015) 1603-1609.

[10] Y. V. Mikhaylik, J.R. Akridge, Polysulfide shuttle study in the Li/S battery system, J. Electrochem. Soc. 151 (2004) A1969-A1974.

[11] A. Manthiram, S.H. Chung, C. Zu, Lithium-sulfur batteries: progress and prospects, Adv. Mater. 27 (2015) 1980–2006.

[12] J.J. Hu, G.R. Li, X.P. Gao, Current status, problems and chal-lenges in lithium-sulfur batteries, J. Inorg. Mater. 28, 1181–1186 (2013).

[13] L. Bao, X. Li, Towards textile energy storage from cotton T-shirts, Adv. Mater. 24

(2012) 3246-3252.

[14] Z. Gao, N. Song, Y. Zhang, X. Li, Cotton-textile-enabled, flexible lithium-ion batteries with enhanced capacity and extended lifespan, Nano Lett. 15 (2015) 8194-8203.

[15] Z. Gao, C. Bumgardner, N. Song, Y. Zhang, J. Li, X. Li, Cotton-textile-enabled flexible self-sustaining power packs via roll-to-roll fabrication, Nat. Comm. 7 (2016) 11586

[16] S. Li, M. Xie, J. Liu, H. Wang, H. Yan, Layer structured sulfur/expanded graphite composite as cathode for lithium battery, Electrochem, Solid-State Lett. 14 (2011) A105-A107.

[17] Y. Fu, C. Zu, A. Manthiram, In situ-formed Li_2S in lithiated graphite electrodes for lithium-sulfur batteries, J. Am. Chem. Soc. 135 (2013) 18044-18047.

[18] X. Ji, K.T. Lee, L.F. Nazar, A highly ordered nanostructured carbon-sulphur cathode for lithium-sulphur batteries, Nat. Mater. 8 (2009) 500–506.

[19] B. Zhang, C. Lai, Z. Zhou, X.P. Gao, Preparation and electrochemical properties of sulfur-acetylene black composites as cathode materials, Electrochim. Acta 54 (2009) 3708–3713.

[20] J. Guo, Y. Xu, C. Wang, Sulfur-impregnated disordered carbon nanotubes cathode for lithium-sulfur batteries, Nano Lett. 11 (2011) 4288-4294.

[21] L. Ji, M. Rao, S. Aloni, L. Wang, E.J. Cairns, Y. Zhang, Porous carbon nanofiber-sulfur composite electrodes for lithium/sulfur cells, Energy Environ. Sci. 4 (2011) 5053–5059.

[22] N. Jayaprakash, J. Shen, S.S. Moganty, A. Corona, L.A. Archer, Porous hollow carbon@sulfur composites for high-power lithium-sulfur batteries, Angew. Chemie - Int. Ed. 50 (2011) 5904-5908.

[23] D.S. Jung, T.H. Hwang, J.H. Lee, H.Y. Koo, R.A. Shakoor, R. Kahraman, Y.N. Jo, M.S. Park, J.W. Choi, Hierarchical porous carbon by ultrasonic spray pyrolysis yields stable cycling in lithium-sulfur battery, Nano Lett. 14 (2014) 4418-4425.

[24] M.S. Park, J.S. Yu, K.J. Kim, G. Jeong, J.H. Kim, Y.N. Jo, U. Hwang, S. Kang, T. Woo, Y.J. Kim, One-step synthesis of a sulfur-impregnated graphene cathode for lithium-sulfur batteries, Phys. Chem. Chem. Phys. 14 (2012) 6796–6804.

[25] L. Zhu, H.J. Peng, J. Liang, J.Q. Huang, C.M. Chen, X. Guo, W. Zhu, P. Li, Q. Zhang, Interconnected carbon nanotube/graphene nanosphere scaffolds as free-standing paper electrode for high-rate and ultra-stable lithium-sulfur batteries, Nano Energy. 11 (2015) 746–755.

[26] H. Wang, Y. Yang, Y. Liang, J.T. Robinson, Y. Li, A. Jackson, Y. Cui, H. Dai, Graphene-wrapped sulfur particles as a rechargeable lithium-sulfur battery cathode material with high capacity and cycling stability, Nano Lett. 11 (2011) 2644-2647.

[27] L.S. Cells, L. Ji, M. Rao, H. Zheng, L. Zhang, O.Y. Li, W. Duan, Graphene oxide as a sulfur immobilizer in high performance lithium/sulfur cells, J. Am. Chem. Soc. 133 (2011) 18522-18525.

[28] L. Zhang, L. Ji, P.A. Glans, Y. Zhang, J. Zhu, J. Guo, Electronic structure and chemical bonding of a graphene oxide-sulfur nanocomposite for use in superior performance lithium-sulfur cells, Phys. Chem. Chem. Phys. 14 (2012) 13670-13675.

[29] S. Evers, L.F. Nazar, Graphene-enveloped sulfur in a one pot reaction: a cathode with good coulombic efficiency and high practical sulfur content, Chem Commun. 48 (2012) 1233-1235.

[30] C. Wang, X. Wang, Y. Wang, J. Chen, H. Zhou, Y. Huang, Macroporous free-standing nano-sulfur/reduced graphene oxide paper as stable cathode for lithium-sulfur battery, Nano Energy 11 (2015) 678-686.

[31] N. Li, M. Zheng, H. Lu, Z. Hu, C. Shen, X. Chang, G. Ji, J. Cao, Y. Shi, High-rate lithium–sulfur batteries promoted by reduced graphene oxide coating, Chem. Commun. 48 (2012) 4106.

[32] C. Xu, Y. Wu, X. Zhao, X. Wang, G. Du, J. Zhang, J. Tu, Sulfur/three-dimensional graphene composite for high performance lithium-sulfur batteries, J. Power Sources 275 (2015) 22-25.

[33] L. Zhou, X. Lin, T. Huang, A. Yu, Binder-free phenyl sulfonated graphene/sulfur electrodes with excellent cyclability for lithium sulfur batteries, J. Mater. Chem. A 2 (2014) 5117-5123.

[34] S. Lu, Y. Chen, X. Wu, Z. Wang, Y. Li, Three-dimensional sulfur/graphene multifunctional hybrid sponges for lithium-sulfur batteries with large areal mass

loading, Sci. Rep. 4 (2014) 4629.

[35] X. Huang, B. Sun, K. Li, S. Chen, G. Wang, Mesoporous graphene paper immobilised sulfur as a flexible electrode for lithium-sulfur batteries, J. Mater. Chem. A 1 (2013) 13484-13489.

[36] X. Wang, Z. Wang, L. Chen, Reduced graphene oxide film as a shuttle-inhibiting interlayer in a lithium-sulfur battery, J. Power Sources 242 (2013) 65–69.

[37] C. Zu, A. Manthiram, Hydroxylated graphene-sulfur nanocomposites for high-rate lithium-sulfur batteries, Adv. Energy Mater. 3 (2013) 1008-1012.

[38] A. Rosenman, E. Markevich, G. Salitra, D. Aurbach, A. Garsuch, F.F. Chesneau, Review on Li-sulfur battery systems: an nitegral perspective, Adv. Energy Mater. 5 (2015) 1500212.

[39] R. Cao, W. Xu, D. Lv, J. Xiao, J.G. Zhang, Anodes for rechargeablelithium-sulfur batteries. Adv. Energy Mater. 5 (2015) 1402237.

[40] A.S. Aricò, P. Bruce, B. Scrosati, J.M. Tarascon, W. van Schalkwijk, Nanostructured materials for advanced energy conversion and storage devices, Nat. Mater. 4 (2005) 366–377.

[41] H.S. William, R.E. Offeman, Preparation of graphitic oxide, J. Am. Chem. Soc. 80 (1958) 1339.

[42] D.C. Marcano, D. V. Kosynkin, J.M. Berlin, A. Sinitskii, Z. Sun, A. Slesarev, L.B. Alemany, W. Lu, J.M. Tour, Improved synthesis of graphene oxide, ACS Nano 4 (2010) 4806-4814.

[43] Z. Gao, Y. Zhang, N. Song, X. Li, Biomass-derived renewable carbon materials for electrochemical energy storage, Mater. Res. Lett. 5 (2017) 69-88.

[44] Y. Zhang, Z. Gao, N. Song, X. Li, High-performance supercapacitors and batteries derived from activated banana-peel with porous structures, Electrochim. Acta 222 (2016) 1257-1266.

[45] K. Zhang, Q. Li, L. Zhang, J. Fang, J. Li, F. Qin, Z. Zhang, Y. Lai, From filter paper to carbon paper and toward Li-S battery interlayer, Mater. Lett. 121 (2014) 198-201.

[46] S.H. Chung, A. Manthiram, A hierarchical carbonized paper with controllable thickness as a modulable interlayer system for high performance Li-S batteries, Chem.

Commun. 50 (2014) 4184-4187.

[47] L. Zhang, P. Zhu, F. Zhou, W. Zeng, H. Su, G. Li, J. Gao, R. Sun, C. Wong, Flexible asymmetrical solid-state supercapacitors based on laboratory filter paper, ACS Nano 10 (2016) 1273-1282.

[48] V. Subramanian, C. Luo, A.M. Stephan, K.S. Nahm, S. Thomas, B. Wei, Supercapacitors from activated carbon derived from banana fibers, J. Phys. Chem. C 111 (2007) 7527-7531.

[49] Y. Lv, L. Gan, M. Liu, W. Xiong, Z. Xu, D. Zhu, D.S. Wright, A self-template synthesis of hierarchical porous carbon foams based on banana peel for supercapacitor electrodes, J. Power Sources 209 (2012) 152-157.

[50] L. Wang, X. Li, J. Ma, Q. Wu, X. Duan, Non-activated , N , S-co-doped Biochar Derived from Banana with Superior Capacitive Properties, Sustainable Energy 2 (2014) 39-43.

[51] E.M. Lotfabad, J. Ding, K. Cui, A. Kohandehghan, W.P. Kalisvaart, M. Hazelton, D. Mitlin, High-density sodium and lithium ion battery anodes from banana peels, ACS Nano 8 (2014) 7115-7129.

[52] B. Liu, L. Zhang, P. Qi, M. Zhu, G. Wang, Y. Ma, X. Guo, H. Chen, B. Zhang, Z. Zhao, B. Dai, F. Yu, Nitrogen-doped banana peel-derived porous carbon foam as binder-free electrode for supercapacitors, Nanomaterials 6 (2016) 18.

[53] S. Brunauer, P.H. Emmett, E. Teller, Adsorption of gases in multimolecular layers, J. Am. Chem. Soc. 60 (1938) 309-319.

[54] W. Brockner, C. Ehrhardt, M. Gjikaj, Thermal decomposition of nickel nitrate hexahydrate, $Ni(NO_3)_2$ $6H_2O$, in comparison to $Co(NO_3)_2$ $6H_2O$ and $Ca(NO_3)_2$ $4H_2O$, Thermochim. Acta 456 (2007) 64-68.

[55] K.S. Kim, Y. Zhao, H. Jang, S.Y. Lee, J.M. Kim, K.S. Kim, J.H. Ahn, P. Kim, J.Y. Choi, B.H. Hong, Large-scale pattern growth of graphene films for stretchable transparent electrodes, Nature 457 (2009) 706-710.

[56] A.N. Obraztsov, E.A. Obraztsova, A.V. Tyurnina, A.A. Zolotukhin, Chemical vapor deposition of thin graphite films of nanometer thickness, Carbon 45 (2007) 2017-2021.

[57] Q. Wang, J. Zheng, E. Walter, H. Pan, D. Lv, P. Zuo, H. Chen, Z.D. Deng, B.Y. Liaw,

X. Yu, X. Yang, J.G. Zhang, J. Liu, J. Xiao, Direct observation of sulfur radicals as reaction media in lithium sulfur batteries, J. Electrochem. Soc. 162 (2015) A474-A478.

[58] M.A. Lowe, J. Gao, H.D. Abruña, Mechanistic insights into operational lithium-sulfur batteries by in situ X-ray diffraction and absorption spectroscopy, RSC Adv. 4 (2014) 2046-2069

[59] N.J. Dudney, Addition of a thin-film inorganic solid electrolyte (Lipon) as a protective film in lithium batteries with a liquid electrolyte, J. Power Sources 89 (2000) 176-179.

[60] X. Liang, Z. Wen, Y. Liu, M. Wu, J. Jin, H. Zhang, X. Wu, Improved cycling performances of lithium sulfur batteries with $LiNO_3$-modified electrolyte, J. Power Sources 196 (2011) 9839-9843.

[61] A.C. Ferrari, J.C. Meyer, V. Scardaci, C. Casiraghi, M. Lazzeri, F. Mauri, S. Piscanec, D. Jiang, K.S. Novoselov, S. Roth, A.K. Geim, Raman spectrum of graphene and graphene layers, Phys. Rev. Lett. 97 (2006) 187401.

[62] D.A. Dikin, S. Stankovich, E.J. Zimney, R.D. Piner, G.H.B. Dommett, G. Evmenenko, S.T. Nguyen, R.S. Ruoff, Preparation and characterization of graphene oxide paper, Nature 448 (2007) 457-460.

[63] J.Z. Wang, L. Lu, M. Choucair, J.A. Stride, X. Xu, H.K. Liu, Sulfur-graphene composite for rechargeable lithium batteries, J. Power Sources 196 (2011) 7030-7034.

[64] G. Zhou, S. Pei, L. Li, D.W. Wang, S. Wang, K. Huang, L.C. Yin, F. Li, H.M. Cheng, A graphene-pure-sulfur sandwich structure for ultrafast, long-life lithium-sulfur batteries, Adv. Mater. 26 (2014) 625-631.

[65] A. Ponrouch, P.L. Taberna, P. Simon, M.R. Palacín, On the origin of the extra capacity at low potential in materials for Li batteries reacting through conversion reaction, Electrochim. Acta 61 (2012) 13-18.

[66] D. Moy, A. Manivannan, S.R. Narayanan, Direct measurement of polysulfide shuttle current: a window into understanding the performance of lithium-sulfur cells, J. Electrochem. Soc. 162 (2015) A1-A7.

[67] A. Kawase, S. Shirai, Y. Yamoto, R. Arakawa, T. Takata, Electrochemical reactions of lithium-sulfur batteries: an analytical study using the organic conversion technique, Phys. Chem. Chem. Phys. 16 (2014) 9344-9350.

Chapter 3 Mossy Li Induced Li-S Battery Failure Mechanisms and Prevention

3.1 Background and motivation

An effective and widely-accepted approach to reduce engine-out pollutants and fossil fuel dependency is to replace traditional internal combustion engine vehicles with electric driven counterparts [1]. However, there is currently a critical hindrance in electric car designs that eminently hurts their competitiveness in the automobile industry: the ponderous and range-limited batteries. Thus, in order to promote widespread consumer acceptance, next generation energy storage devices must have a significantly higher energy density and longer lifespan than current systems. A highly competitive successor within this scope is the lithium sulfur (Li-S) battery [2]. When lithium metal is coupled with abundant and nontoxic sulfur, the complete conversion between sulfur and lithium sulfide (Li_2S) is able to deliver an ultrahigh theoretical energy density of 2600 Wh kg^{-1} [3]. It is anticipated that a fully packed Li-S battery can reach a practical energy density of 600-700 Wh kg^{-1}, three times higher than top-of-the-line lithium ion batteries [4]. The first roadblock in the commercialization of Li-S batteries is the sulfur cathode, which is plagued by severe technological problems. The insulating nature of sulfur (conductivity of sulfur is $\sim 5\times10^{-18}$ S cm^{-1} at room temperature) [5], solubility of intermediate products (lithium polysulfides Li_2S_x (x=4, 6, 8)) [6–8], and the over 70 % volume fluctuation of active material during repeated cycling [9,10], lead to rapid capacity decay, irreversible active material loss, and pulverization of the cathode. To overcome these obstacles, hierarchically porous carbon materials are used as sulfur carriers, which effectively bypass the insulating nature of sulfur, adjust the large volume fluctuation, and encapsulate polysulfides via physical attraction [11–15]. Surface chemistry was then leveraged to band polysulfides chemically using functional groups and/or heteroatoms, effectively entrapping them within the cathode area and reducing the shuttle effect [16–21]. Currently, although sulfur loading and sulfur utilization still require optimization, the lifespan of the Li-S battery has been successfully increased from hundreds to thousands of cycles [21–23], making the degradation of the lithium anode no longer negligible. Hence, just like other lithium metal batteries [24], the lithium anode is becoming an equally critical roadblock for the practical production of Li-S batteries.

Although lithium metal has long been considered as an ideal anode material because of its high theoretical specific capacity (3860 mAh g^{-1}), low electrochemical potential (-3.04 V versus standard hydrogen electrode), and low density (0.59 g cm^{-3}) [25], viable lithium metal secondary batteries have remained impractical for decades because of the highly active and unstable nature of the lithium electrode. It is proved by postmortem and in-situ observations [26,27] that when the lithium metal electrode is exposed to an organic liquid electrolyte, lithium metal tends to exhibit inhomogeneous stripping/plating, forming dendritic, mossy, or granular Li crystals depending on various conditions [28]. Large dendrites were considered the most harmful because they not only continuously consume active materials and electrolyte, but also may penetrate the separator, short circuit the battery, and cause catastrophic safety issues such as burning or even exploding [29]. To overcome the uncontrolled growth of dendrites, five approaches have been employed: building a stable and strong solid electrolyte interlayer (SEI) by tuning electrolyte solvents and additives [30–35], replacing the liquid electrolyte with a solid state electrolyte [36–41], inserting a conformal interlayer between the lithium anode and the separator, which works as an artificial SEI [23,42–44], engineering smart separators to prevent the penetration of dendrites [45], and designing 3D electrode frameworks with novel architectures [46,47]. These achievements are nothing but remarkable. Since current Li-S batteries are often operated within an intermediate voltage window (1.5-2.8 V) at a relatively low current density (normally lower than 2 C rate), failures derived from large dendrites in Li-S system have been almost eliminated when using optimized cathode materials and electrolytes. An immediate question is posed to the Li-S community: if the C/S cathode is robust, the electrolyte is sufficient, and no large dendrites form, can the Li-S battery last forever? With the answer of a certain “no”, it is critical to unearth other factors that may result in anode malfunction. Mossy Li has long been observed in Li-S batteries and it is often considered much less harmful than large dendrites. It was assumed that the electrolyte was slowly consumed in the porous structure of mossy Li, leading to the final malfunction. However, the mechanisms of how the mossy Li interacting with the sulfur cathode and inducing failure in long lifespan Li-S batteries remains unclear. More importantly, no final conclusion of the formation mechanism of the mossy Li has been drawn, making the efforts of preventing mossy Li growth a trial-and-error scenario.

Here, a thorough study of the lithium electrode from the beginning to the 600th cycle was carried out to unveil the mossy Li induced lithium degradation in long lifespan Li-S batteries. With continued cycling, mossy Li whiskers repeatedly grew and decomposed, remaining SEI residue as well as dead Li on the anode surface. The remaining SEI flotsams and dead Li, combined with deposited sulfur and Li_2S, accumulated on the lithium surface and were subsequently pushed by the growth of mossy Li, forming a dense and thick crust, which blocked charge transfer underneath and induced aggravated local etching, leading to the ultimate failure of the battery. Further analysis shows that, upon discharging, the lithium surface collapsed in a mosaic morphology and developed irregularly shaped pits. Kinked lithium whiskers (mossy Li) grew preferentially from the bottom of these pits instead of protuberances during charging. This finding is contradictory to previous studies; hence an alternative controlling factor of lithium stripping/plating, namely the flow of the electrolyte, was put forward to explain the mechanism of mossy Li growth. Although specific to Li-S, these findings are anticipated to assist the development of all other lithium batteries. Accordingly, two approaches were designed to prevent the growth of mossy Li. In the first approach, a porous APC interlayer was inserted between separator and Li anode to redistribute Li ions and confine the flow of electrolyte. In the second approach, alpha-lipoic acid (ALA) and GO were used to form a stronger SEI to prevent the Li whiskers growth.

3.2 Experimental methods

Fabrication of APC/graphene/S electrodes

To ensure the long lifespan of Li-S batteries, the cathode was fabricated according to ref. [23]. Specifically, recycled paper strips were peeled from hardboard panels or rolls. Graphene oxide suspension was prepared via Hummer’s method. Obtained hardboard strips absorbed graphene oxide solution by capillary forces and were subsequently heated at

1000 ℃ for 1 h in a tube furnace with continuous argon gas flow to convert the recycled paper/graphene oxide hybrid into activated paper carbon/reduced graphene composite (APC/graphene). Round pieces with a diameter of 13 mm were then punched from the APC/graphene stripes. Sulfur powders were loaded onto the APC/graphene plates and heat-treated at 155 ℃ for 12 h, followed by heating to 200 ℃ for 2 h to impregnate sulfur into the composite and form APC/graphene/S hybrids. The sulfur loading of each plate was controlled at 2.8-3.2 mg/cm^2. The APC/graphene/S cathode can adjust the volume fluctuation and encapsulate polysulfides, leading to a long lifespan for assembled Li-S batteries.

Assembly and disassembly of coin Li-S batteries.

The electrolyte was produced by dissolving 1 mol/L LiTFSI and 0.5 mol/L $LiNO_3$ in an organic solvent of dimethoxyethane (DME) + 1,3-dioxolane (DOL) at a 1:1 volume ratio. The electrolyte/sulfur ratio was strictly controlled as 15:1 μL mg^{-1} to rule out the effects from variations in the electrolyte amount. Lithium metal pieces with a diameter of 13 mm were purchased from MTI corp. The lithium pieces were rinsed by DME before being used as anodes. Celgard 2400 film was used as separators. The CR2032 coin cells were assembled with a MTI MSK-110 crimping machine in an argon-filled glove box (M. Braun, Germany) with oxygen and water contents below 0.1 and 0.1 ppm, respectively. The pressure for each battery during assembling was controlled at 1500 psi to avoid any influence of variations in the applied pressure. After the assembled batteries discharged/charged for different amounts of cycles, the coin batteries were disassembled manually and the lithium anodes were taken out and immediately merged into DME to remove any residual electrolyte and polysulfides; disassembly was conducted in an argon-filled glove box. After three rinses by DME, the lithium anodes were carefully sealed in air-tight sample bags. For the measurement and calculation of average Columbic efficiency, lithium plates were assembled with conformal copper foils under the same conditions with the same amount of electrolyte.

Fabrication of ALA/GO coated separators

ALA was treated by tetrabutyl ammonium hydroxide solution, forming ALA tetrabutyl ammonium salt, which was a light yellow and viscous liquid. The ALA tetrabutyl ammonium salt was dissolved into water and mixed with GO suspension. The ALA/GO suspension was homogeneously coated on the separator via capillary force before drying at 100 ℃ under vacuum. The ALA/GO coated separators were assembled with sulfur cathodes and Li anodes in coin cells.

Materials and structural characterization

The microstructures of lithium electrodes were characterized by scanning electron microscopy (SEM, FEI Quanta 650 with EDS detector) and atomic force microscopy (AFM, Bruker Dimension Icon). Lithium samples were transferred into the SEM chamber without exposure to air, and the AFM was sealed in an argon filled glove box with oxygen and water contents below 1 and 1 ppm, respectively. X-ray diffraction (XRD, PANalytical X'Pert Pro Multi-Purpose Diffractometer (MPD) equipped with Cu K_α radiation (λ = 0.15406 nm)) and Fourier-transform infrared spectroscopy (FTIR, Nicolet iS5 IR spectrometer) were used to characterize the chemical phases. To avoid the oxidization of lithium, the lithium pieces were sealed by thin polymer films under argon protection. Nanoindentation tests were carried out under AFM by a diamond tip with a maximum load of 750 nN.

Electrochemical characterization

A LAND CT2003A battery test instrument was used to perform galvanostatic charge/discharge measurements. All Li-S batteries were operated within a voltage window of 1.5-2.8 V and a current density of 0.75 mA cm^{-2} (the area of the cathode and anode plates was 1.33 cm^2, hence the current of charge/discharge for all batteries was 1 mA). Electrochemical impedance spectroscopy (EIS) tests in the frequency range from 100 kHz to 0.005 Hz with an AC perturbation of 5 mV were carried out using a CHI 660E electrochemical workstation. Batteries for EIS tests are at a fully charged state with voltage around 2.4 V.

Numerical simulation

2D flow simulations were performed in Flowsquare 4.0 software for a simplified case of channel flow over a half-hemisphere pore. In all of these simulations the fluid density was set to 1.353 g mL^{-1}, the dynamic viscosity was set to 2.3E-3 kg m^{-1} s^{-1}, the initial pressure was set to atmospheric conditions at 101 KPa, and for numeric stability the characteristic length of the channel or distance between the upper and lower plate, was set to 0.025 m. To alter the magnitude of the Re, the flow velocity was changed accordingly from 2.00E-4 to 20.00 m s^{-1}.

3.3 New insights into mossy Li induced anode degradation and its formation mechanism in Li-S batteries

3.3.1 Mossy Li induced Li-S battery failure

Lithium plates with a diameter of 13 mm were assembled with activated paper carbon/graphene/sulfur (APC/graphene/S) cathodes, as in the previous study [23]. 1 mol L^{-1} LiTFSI and 0.5 mol L^{-1} $LiNO_3$ in an organic solvent of dimethoxyethane (DME) + 1,3-dioxolane (DOL) at a 1:1 volume ratio was used as electrolyte. The electrolyte/sulfur ratio was strictly controlled as 15:1 µL mg^{-1}. The assembled Li-S batteries were operated at 1 mA, corresponding to a current density of 0.75 mA cm^{-2}, in a voltage window ranging from 1.5 V to 2.8 V for varied amounts of discharge/charge cycles. The discharge capacity of the battery at the 5th cycle was about 2.23 mAh and decayed to 1.57 mAh by the 600th cycle. The average discharge capacity of 600 cycles was 1.82 mAh, indicative of a 0.47 mg lithium usage per cycle. Lithium anodes after 1, 10, 100, 300, and 600 cycles were taken out from the coin batteries and rinsed three times by DME prior to examination. The electrode surface displayed evident morphological changes after repeated stripping/depositing (Fig. 3-1). The flat surface with parallel grooves from machine work on the pristine lithium was replaced by rough and inhomogeneous deposits after only 10 discharge/charge cycles. After 100 cycles, the metallic luster of the lithium metal disappeared entirely and the surface was covered with a layer of grey colored sediments. The grey layer became thicker after 300 cycles and cracked or peeled at the 600th cycle.

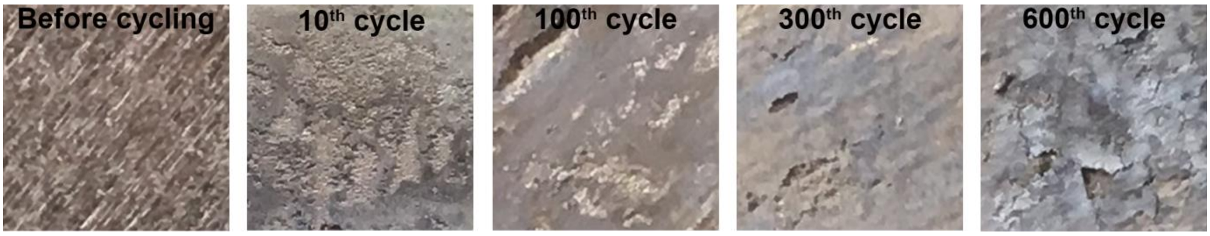

Fig. 3-1 Photographs of lithium anode after different amounts of cycles.

To unveil the morphological changes, the top surface and cross section of the lithium electrodes were observed under SEM and are displayed in Fig. 3-2. The top view offered a clear visualization of the microstructural evolution of the lithium anodes (Fig. 3-2a). Features of the original lithium surface were entirely changed even after one discharge/charge cycle. Instead of large dendrites, mossy Li grew from pits and gradually dominated the entire surface with the continued cycling. No mossy Li whiskers pointed vertically nor exhibited the potential to penetrate the separator; on the contrary, flat planes were formed, which implied that the growth was likely impeded by the separator and the cathode, indicating that the weak and kinked mossy Li was not strong enough to break the commercial separator and short the battery. Sediments accumulated between the lithium whiskers and evolved into a crust which partially covered the mossy Li layer after 300 cycles. After 600 cycles (the last two images in Fig. 3-2a), the surface of the lithium anode appeared to be highly uneven. The bulky and dense crust, with cracks and peelings, covered most of the anode while the lithium metal was locally etched at locations without the crust covering (the last image in Fig. 3-2a), indicating that the chemical reactions on the anode surface were not macroscopically homogeneous after the crust had formed. In cross sectional images (Fig. 3-2b), it is obvious that both the etching of the lithium surface and the growth of mossy Li were non-uniform. After the first cycle, the lithium surface was etched into an uneven profile featuring interlaced pits and flat regions with frequency on the order of tens of microns. Mossy Li was found to grow from the pits, which was in a good agreement with findings in ref. [26]. With increased cycles, the thickness of the lithium metal decreased evenly for the first 100 cycles, but this uniform reduction stopped after the lithium was covered by the compact crust; lithium was much thicker under the coverage of the crust (the last two images of Fig. 3-2b). Together with the results observed in the top-view images (Fig. 3-2a), it is rational to postulate that the crust blocked the reaction pathway for the lithium underneath. It is noteworthy that no evidence of large dendrites can be found either in photographs (Fig. 3-1) or SEM images (Fig. 3-2) from the beginning to the 600th cycle, and the mossy Li was proven unlikely to break the separator. Therefore, the crust induced by the mossy Li growth is determined to be responsible for the battery failure.

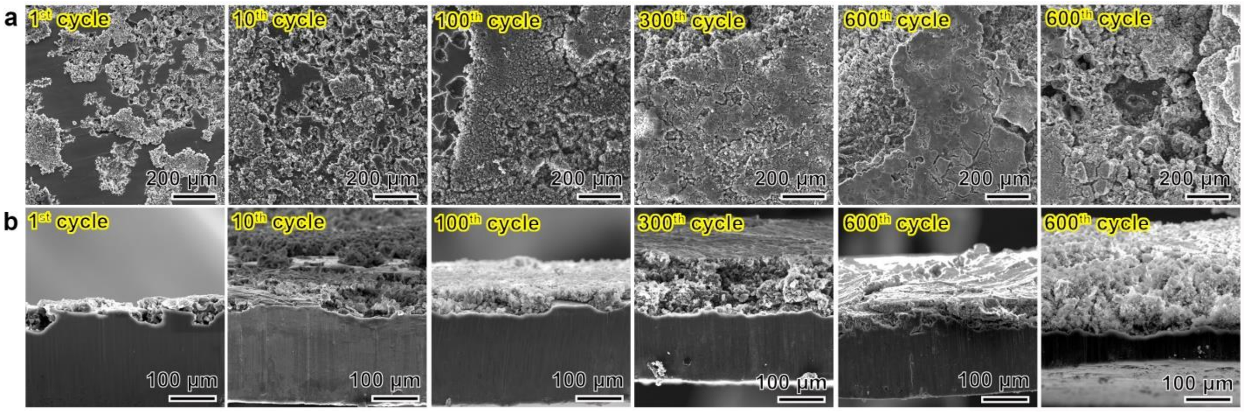

Fig. 3-2 Microstructural evolution of lithium anode from the beginning to the 600th cycle. a. SEM top-view images. Mossy Li gradually covered the electrode surface while a crust formed after repeated stripping/depositing. Large holes formed at areas without the crust coverage b. Cross-sectional SEM images of lithium electrodes. The dense crust blocked the reaction pathway for the lithium underneath, showing thicker underlying lithium.

Naturally, a question must be posed: what is the crust? X-ray diffraction (XRD), energy-dispersive X-ray spectroscopy (EDS), and Fourier-transform infrared spectroscopy (FTIR) tests were carried out to characterize the chemical phases of the cycled lithium electrodes. After being rinsed by DME, only S, Li, and Li_2S can be distinguished in the XRD spectrum (Fig. 3-3a) because the two end products are insoluble in the organic solvent and have a well-defined crystal structures. The intensity of the Li_2S(220) peak and the ratio between the intensity of the Li_2S(220) peak and the Li(110) peak at different cycles are quantified and plotted in Fig. 3-3b. With the proceeding of cycling, the intensity of the Li_2S peaks increased continuously, as the intensity ratio between Li_2S(220) peaks and Li(110) peaks. This result indicated that the concentration of Li_2S increased on the electrode surface continuously. Other than Li_2S, the element sulfur was also found in XRD spectrum. Therefore, although the APC/graphene scaffold was proven to be capable of entrapping polysulfides and weaken shuttling, the dissolved lithium polysulfide chains may still travel through the separator and aggregate on the anode surface. The shuttled lithium polysfulides reacted with lithium and formed insoluble Li_2S and sulfur. EDS and FTIR were then used to verify the amorphous components of the crust. There are five evident peaks in the FTIR spectrum (Fig. 3-3c). The very sharp peak at the wavelength of 3676 cm^{-1} can be ascribed to –OH, which may derive from the degradation of metal lithium. The large peak at 1400 cm^{-1} indicates the existence of $–CF_3$ and the peak at about 1000 cm^{-1} represents C–O in ester. Another sharp peak at 866 cm^{-1} represents the –CH in a loop structure, indicative of C–O–C. A broad peak appeared at 3343 cm^{-1} peak in the FTIR spectrum indicated –NH, which possibly stemmed from the $LiNO_3$ additive. In the EDS element analysis, oxygen, fluorine, nitrogen, and carbon were concentrated in the crust (Fig. 3-3d). These observations are consistent with the previous studies about the SEI in the same electrolyte system [46–48]. Therefore, the amorphous SEI residual is one of the major components of the crust. According to the in situ observation of the lithium whiskers [27], hollow SEI shells, which contain elements from the electrolyte and additives, such as oxygen, fluorine, nitrogen, and carbon, remained on the electrode surface after the whiskers were etched away. Another possible component in the crust is dead Li, which is a disassociated Li particle that cannot participate in the electrochemical reactions. Thusly, since insoluble Li_2S, sulfur, SEI flotsams, and dead Li particles are all irreversible products, they accumulated on the electrode surface and jointly formed the crust.

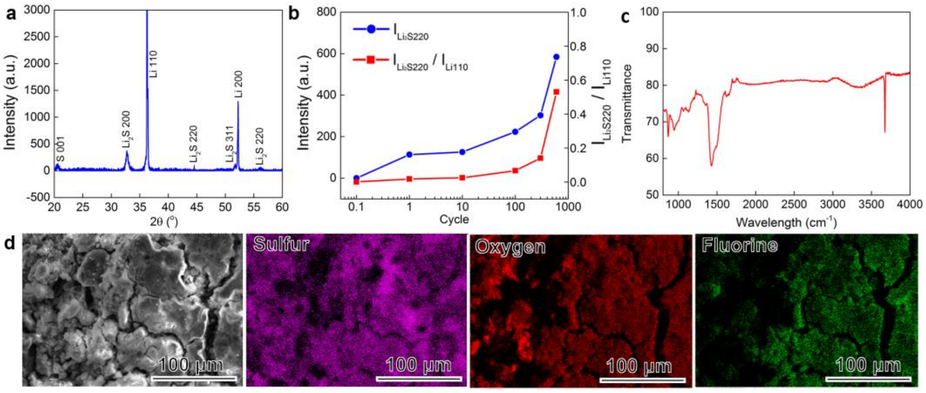

Fig. 3-3 Chemical components of lithium electrodes with the proceeding of cycling. a. Typical XRD spectrum of lithium electrode after repeated stripping/depositing. b. The intensity of $Li_2S(220)$ peaks and the intensity ratio between $Li_2S(220)$ peaks and Li(110) peaks at different cycles. c. FTIR

spectrum of lithium anode after 600 cycles. d. EDS element maps of the Li anode surface under SEM.

We then proceeded to answer the next question: how did the crust form? Surface morphology and mechanical properties were characterized to address this question. SEM top-view images in Fig. 3-2 displayed a loose-to-dense morphological evolution of the lithium anode surface. A diamond Berkovich tip was used to conduct nanoindentation tests on the electrode surface. The shape function of the tip was carefully calibrated by a standard fused silica sample. A typical load/displacement curve is shown in Fig. 3-4b and the indentation on pristine lithium is shown in Fig. 3-4a. The modulus can be calculated from the slope of the unloading curve and the hardness is derived from the maximum load and the area of the indentation, which is related to the depth and the shape function [49]. The cleaned lithium plate exhibited a modulus of 4.87 GPa, which is very close to the standard elastic modulus of lithium. The modulus (on the mossy Li) decreased to 2.04 GPa after the first cycle and dropped to 0.88 GPa (on the mossy Li) after 10 cycles (Fig. 3-3c). The large decrease of surface modulus can be ascribed to the loosely stacked deposits. After the 10th cycle, the surface modulus gradually increased to 2.11 GPa by the 600th cycle. The surface mechanical test is a powerful complement to microstructural observations and verified that insoluble deposits on the anode surface were gradually densified into a compact, hard coating layer. Based on the microstructural and mechanical observations, it can be concluded that the crust layer is derived from the large volume expansion of mossy Li. The thickness of the original lithium plate was 200 μm. After 100 cycles, the total thickness of the anode exhibited in Fig. 3-2b was 246 μm, corresponding to a 23% increase compared with the pristine lithium plate. Moreover, the thickness of the lithium metal was 192 μm while the thickness of mossy Li was 54 μm, indicating that a 575% volume expansion occurred when the lithium was replaced by mossy Li. After 300 cycles, the thickness of the anode increased to 254 μm, which was comprised of 139 μm of lithium metal and 115 μm of mossy Li. The volume expansion induced by mossy Li was reduced to 88%, indicating that the growth of mossy Li was constrained, inevitably inducing pressure on the top of the anode surface. Passive sediments, including SEI flotsams, dead Li, Li_2S, and sulfur, were continuously produced after stripping and were repeatedly pushed against the separator by the growth of mossy Li during the following depositing, making porous deposits, into an eventual dense crust. Since mossy Li was found in both coin and punched Li-S cells and the volume expansion derived from mossy Li is enormous, we deem that the formation of such curst is inevitable if electrode materials and electrolyte are sufficient.

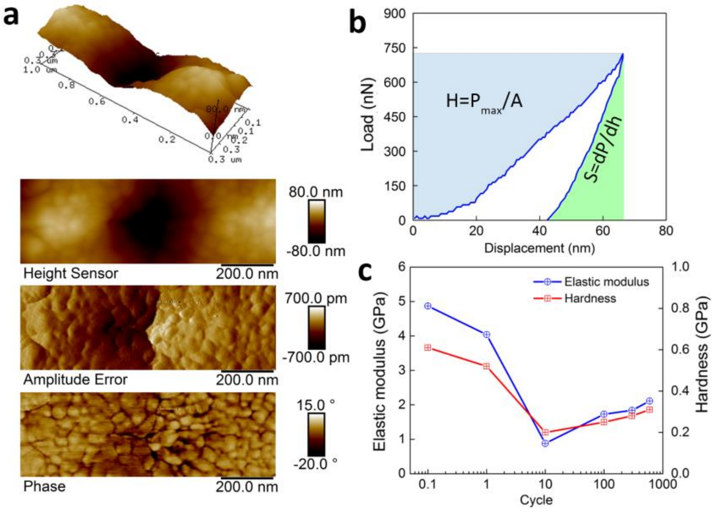

Fig. 3-4 Mechanical properties of lithium electrodes with the proceeding of cycling. a. An indentation on the pristine lithium. b. Typical load/displacement curve of nanoindentation. c. Evolution of surface modulus and hardness of lithium electrodes.

The last remaining question is therefore: how does the crust ultimately lead to the malfunction of the lithium electrode? To address this question, electrochemical impedance spectroscopy (EIS) tests were conducted to verify the influence of the crust on the electrochemical properties of the batteries. A typical EIS spectrum of the Li-S battery is shown in Fig. 3-5a. The intercept between the EIS curve and the *Z'* axis is the equivalent series resistance, which stems from the electrolyte resistance, the intrinsic resistance of the active material, and the interfacial contact resistance between electrodes and current collectors. This part is noted as R_{Ω} and is equal to a resistance in the equivalent circuit (Fig. 3-5b inset). The semicircle at the high frequency regime stems from the impedance of ions passing through the SEI on the anode surface, which can be represented as a resistor and a capacitor in parallel in the equivalent circuit. The resistance part is calculated from the diameter of the semicircle and is marked as R_{SEI}. Another semicircle in the intermediate frequency regime indicates the impedance of the charge transfer between the electrodes and electrolyte, which is mainly influenced by the passive deposits on the surface of the electrodes. Similarly, it can be represented as a combination of a resistor and capacitor in the equivalent circuit and the resistance part is noted as R_{ct}. The straight line at the low frequency regime is the so called "Warburg impedance" which derives from an ion diffusion limited process in the electrolyte and is denoted as Z_w [50]. R_Ω was kept at a relatively low value for hundreds of cycles and then increased only to 57 Ω at the 600th cycle (Fig. 3-5b). In contrast, R_{SEI} was 391 Ω before cycling because of the oxides on the lithium surface. After several cycles, R_{SEI} decreased drastically to 4 Ω with the formation of a stable SEI [15]. R_{SEI} started rising after 300 cycles, most likely due to the reduced electroactive locations [23]. Unlike R_{SEI}, R_{ct} started low but increased vigorously after 300 cycles. At the 600th cycle, the R_{ct} trended towards infinite (6693 Ω), indicating that the electron and ion transfer was severely hindered. Thusly, it is highly possible that the crust blocked the charge transfer, leading to a complete malfunction of the lithium anode.

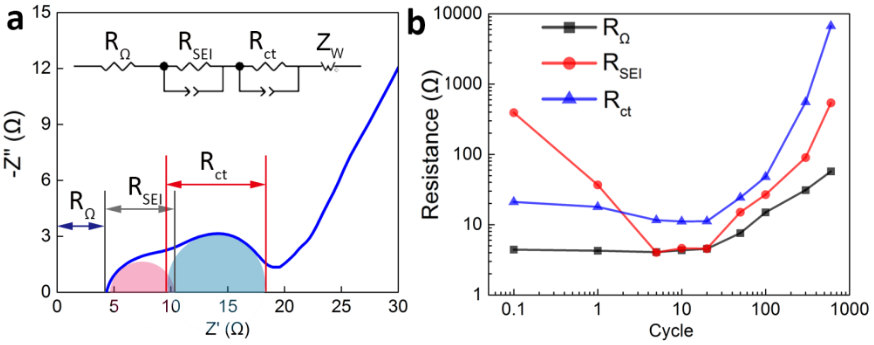

Fig. 3-5 Impedances of Li-S batteries with the proceeding of cycling. a. Typical EIS spectrum of the Li-S batteries, showing two semicircles in the high and intermediate frequency regime, and a straight line in the low frequency regime (inset is the equivalent circuit). b. Statistical results of resistances in EIS spectra of Li-S batteries at different cycles.

Armed with the aforementioned findings, we can schematically conclude the mechanisms behind mossy Li induced failure of the lithium anode in the long lifespan Li-S batteries. As illustrated in Fig. 3-6, upon cycling, the lithium electrode surface is etched to a rough morphology with coexisting pits and flat regions. Mossy Li whiskers grow from the bottom of the pits and gradually cover the entire electrode surface. A large volume expansion occurs when the lithium metal is replaced by mossy Li. Passive deposits, including Li_2S, sulfur, SEI flotsams, and dead Li, are aggregated at the anode surface and pushed by mossy Li against the separator and cathode. The continuously increasing deposits are repeatedly pressed together during cyclic stripping/depositing, forming a dense crust that blocks the charge transfer to the underlying lithium. Regions where no compact crust existed are etched preferentially, leading to penetrating holes as shown in the last image of Fig. 3-2a. When the small amount of bare lithium within the etching hole is depleted, while all other surfaces are covered by the passive crust, the lithium anode fails. Therefore, even if a Li-S battery possesses a robust cathode, a sufficient electrolyte, and a strong separator to prevent the growth of large dendrites, while being operated in a moderate voltage window with a low current density, the battery will still fail after prolonged cycling due to the mossy Li induced anode malfunction.

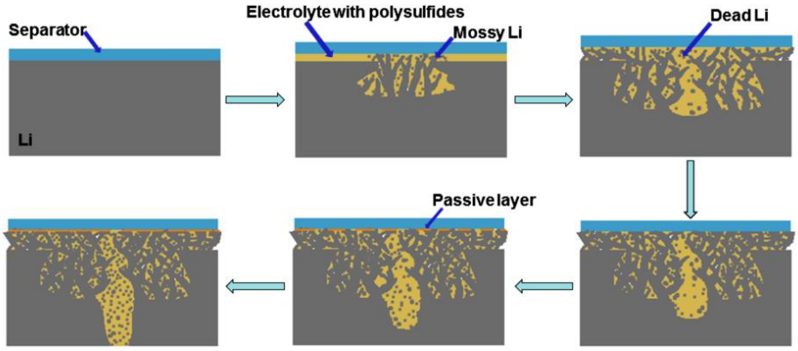

Fig. 3-6 Schematic diagram of the evolution of lithium anode during cycling in Li-S batteries. Upon cycling, the lithium electrode surface is etched to a rough morphology with coexisting pits and flat stages. Mossy Li whiskers grow from the bottom of the pits and gradually cover the entire electrode surface. Li_2S deposits, as well as sulfur, SEI flotsams, and dead Li, aggregate on the anode surface. The growth of mossy Li repeatedly compresses the passive sediments, forming a dense crust which blocks charge transfer for the lithium underneath. The uncovered part, on the other hand, is etched preferentially, leading to penetrating holes.

To unveil the influence of the sulfur cathode on the lifespan of the lithium anode, the coulombic efficiency of lithium metal stripping/plating under the same conditions was measured and calculated by two approaches according to ref. [51]. Lithium plates were assembled with conformal copper foils and operated in the same amount of electrolyte. For the first method, as shown in the measured voltage versus time plot, a given amount of lithium metal was electroplated at a current density of 0.75 mA cm^{-2} onto the copper substrate which had no lithium in its initial state (represented by the amount of charge passed in the external circuit, Q_P), followed by stripping lithium metal from the copper substrate to a cut-off voltage of 1 V which signified that all the removable lithium had been stripped from the surface of the substrate (represented by the amount of charge passed in the external circuit, Q_s). The average coulombic efficiency over n cycles can be calculated by:

$$CE_{avg} = \frac{1}{n}\sum\frac{Q_S}{Q_P} \qquad (1)$$

The average coulombic efficiency of the battery in the first 100 cycles (including stabilization process) was 97.15%, indicative of a theoretical lifespan of 1945 cycles, more than three times higher than the battery with a sulfur cathode. Since the first method ignored the reaction between lithium and copper, which may cause a lower coulombic efficiency, another method was applied to measure the average coulombic efficiency more accurately. Specifically, the copper foil was preconditioned via a single plating/stripping cycle at a high capacity of 5 mAh (3.8 mAh cm^{-2}) before the lithium reservoir (Q_T) was deposited on the copper foil. Subsequently, the battery was cycled at 1 mAh (0.75 mAh cm^{-2}) for 49 cycles. Finally, the lithium on the copper foil was then fully stripped to 1 V. The average coulombic efficiency can be calculated by:

$$CE_{avg} = \frac{nQ_c+Q_S}{nQ_c+Q_T} \qquad (2)$$

where n is the cycle number, Q_c is the cycling capacity, Q_s is the final stripping discharge capacity. The calculated average coulombic efficiency is 99.57%. In comparison, the average coulombic efficiency of the Li-S battery in the first 50 cycles was 98.72% while that in the last 50 cycles (after the crust formed) was only 91.94%. The estimated cycle life (N) of the used lithium anode can be calculated by:

$$N = \frac{Q_T}{(1-CE_{avg})Q_c} \qquad (3)$$

When N is 300, the required lithium reservoir (Q_T) is 1.94 mAh cm^{-2}, which equates to only 4.65 μm of lithium usage much lower than the actual situation. The measurement and calculation of the average coulombic efficiency indicated that with sufficient electrolyte and without the sulfur cathode, the lithium anode can operate for a much longer duration.

However, the shuttled polysulfides reacted with lithium, forming passive sulfur and Li_2S on the electrode surface, which severely promoted the formation of the crust and accelerated the malfunction of the anode.

Further conclusions can be derived from these newly revealed mechanisms. Firstly, if the formation of the crust can be prevented, the lifespan of the battery can be largely extended. This postulation has been proven in our previous study that a porous interlayer between separator and Li anode was able to suppress the formation of the crust and the assembled Li-S battery experienced an extension in lifespan of over 400 cycles. Secondly, an excessive 300% of lithium was considered to be necessary to compensate for the irreversible consumption of active materials due to the repeated formation of SEI. However, results in the present study indicate that less than 10% of the lithium participated in the reaction after the passive crust had formed. Therefore, an increase of 800% in lithium is most likely needed to sustain the long life-span for a Li-S battery in a liquid electrolyte. Finally, we cannot fully isolate lithium from the cathode and the electrolyte in the Li-S battery system. The lithium polysulfides entrapment ability of the cathode and the lithium polysulfides solubility in the electrolyte are also closely related to the malfunction of the lithium anode.

3.3.2 The growth mechanisms of mossy Li

Further analyzing the concluded failure mechanism of the lithium electrode, the inhomogeneous stripping/depositing of mossy Li is in fact the fundamental cause of the anode failure. Mossy Li is the primary source of SEI flotsams and dead Li; simultaneously the formation of the crust is derived from the large volume expansion of mossy Li. Thus, it would be rewarding if we could decipher the mechanism of stripping/depositing of mossy Li whiskers. Fig. 3-7a shows the discharge profile of the Li-S battery, showing a typical two-plateau morphology. The first plateau at 2.3 V can be ascribed to the formation of high order polysulfides (S_8^{2-}, S_6^{2-}), the dip between 2.3 – 2.1 V represents the formation of S_4^{2-} from high order polysulfides, the plateau at 2.1 V indicates transformation between S_4^{2-} and S^{2-}, and the dip between 2.1 – 1.5 V derives from the formation of solid Li_2S. Unlike the conversion between sulfur and lithium sulfide, which has a definite sequence, the stripping of the lithium anode exhibited a continuous process (Fig. 3-7a insets). Pristine lithium displayed a flat and smooth surface profile in high magnification SEM images, but after 30 seconds of discharge, numerous orderly aligned squares appeared on the lithium surface. It is worth mentioning that the lithium electrodes in batteries which self-discharged (a battery spontaneously discharges without extra current) over a day also exhibited similar surface morphology, suggesting that the squares are the initiation sites of the lithium stripping. Close-up observation of one square edge demonstrated a depth variance of hundreds of nanometers (Fig. 3-7b and c). Additionally, EDS element mapping uncovered a higher concentration of oxygen on the square edges (Fig. 3-7d to f), jointly indicating that the etching of the lithium started at the edge of the squares. Tortuous cracks then propagated along the squares after 2 minutes of discharging. The cracks coalesced and stimulated a large scale collapse, forming several micron sized pits. These small pits further grew into larger, irregularly shaped pits and homogeneously dispersed on the electrode surface without notable preference at the end of the discharge process. This finding is in fact inconsistent with a commonly held belief that stripping is prone to occur at defects (grain boundaries or pores) or surface protuberances (grooves or bumps) on lithium because of a higher potential and/or larger inner stress gradient. These processes happened concurrently, i.e. new squares appeared simultaneously as large pits were forming.

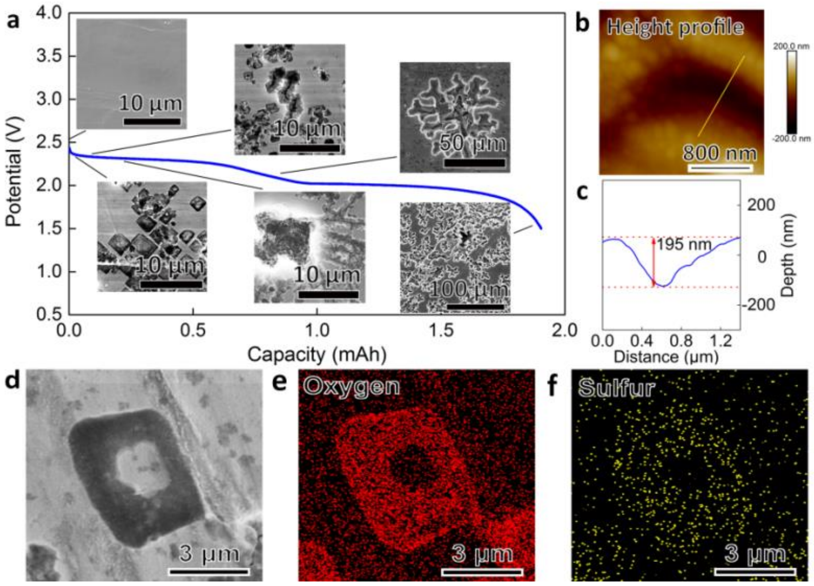

Fig. 3-7 Stripping of lithium anode in the first discharge. a. Discharge profile of the Li-S battery with microstructural images at different discharging time. b. AFM height profile of the edge of a square after 30 sec discharge. c. Depth distribution along the yellow line in (b), showing 195 nm collapse at the square edge. d. Close-up SEM image. e. EDS oxygen map. f. EDS sulfur map.

As the initiation sites of the stripping, these squares have attracted attention. To unveil the identity of the squares, a battery was assembled, self-discharged for 10 minutes, and disassembled. The lithium electrode surface exhibited a weak square profile under AFM (Fig. 3-8a). In the surface modulus map (Fig. 3-8b), the square edges displayed a decreased modulus (0.4-0.8 GPa) compared with other areas (2.3-2.6 GPa), while a clear boundary was exhibited in the adhesion map (Fig. 3-8c). Another noticeable fact is that the squares aligned in one direction in a certain region while aligning in another orientation in a different region (Fig. 3-8d). At the boundary of the two regions, there was an obvious transition of square orientation (Fig. 3-8d). It has long been proven that although the SEI is considered a thin film, which uniformly covered the lithium surface, the SEI in fact has a polycrystalline structure and is comprised of multiple chemical phases [52]. The thickness, structure, chemical phases, and functions of the SEI on lithium metal were studied experimentally and numerically, but the grain structure of the SEI has not yet been researched systematically. Based on the results, we postulate that the squares were in fact grains of the SEI formed under the operating conditions (electrolyte, temperature, current density, *etc.*). Similar to the chemical vapor deposition (CVD) or physical vapor deposition (PVD) processes, the orientation of these grains is determined by the orientation of the underlying lithium matrix. Therefore, as schematically illustrated in Fig. 3-8e, the electrolyte reacted with the lithium upon contact and nucleated the SEI; the nuclei grew in an orientation related to the Li matrix until the electrode surface was covered. During discharge, the boundary of the SEI offered an etching pathway, leading to more drastic chemical reactions. The hypothesis was consistent with the experimental findings in Fig. 3-8, which showed that after the square edge collapsed, etching tended to develop toward the center of the square. The SEI that formed on the exposed lithium surface was thinner and less stable, resulting in more severe etching. The inhomogeneous stripping was thusly self-amplified by this ripple effect, forming big, irregularly shaped pits through the electrode surface. Therefore, the stripping of lithium tends to happen at the defects of SEI rather than at defects on the lithium. The size of a single SEI grain is small (less than 10 µm), leading to the homogeneous dispersion of pits macroscopically. If a stronger SEI with larger grain size can be obtained, it is anticipated that the etching of the Li anode would be more homogeneous. This postulation has been proven by Cui *et al.* [53] who built a stronger SEI by adding lithium polysulfides into the electrolyte, leading to more uniform etching and deposition.

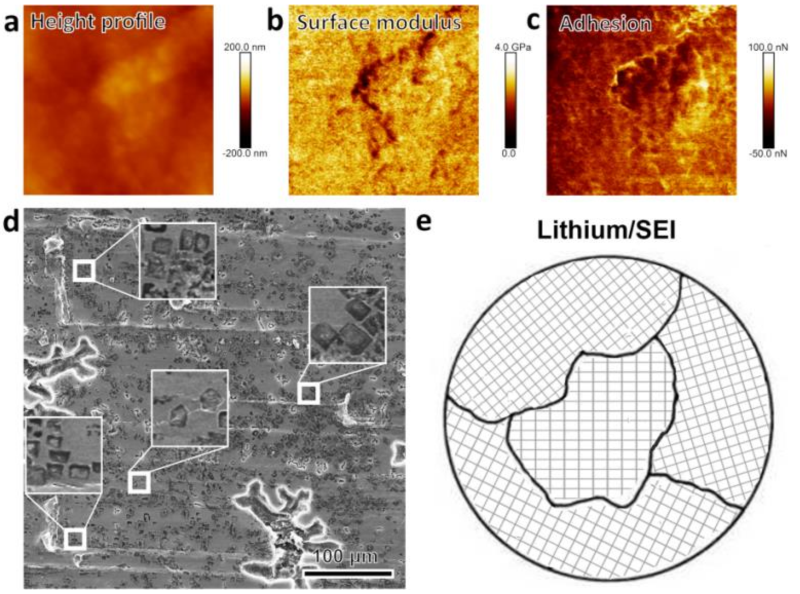

Fig. 3-8 SEI on the Li anode surface. a. AFM height profile of the edge of a square after 10 min self-discharge. b. Corresponding surface modulus map, showing a lower modulus on the square edge. c. Corresponding adhesion map, showing a clear boundary along the edge. d. Orientation of squares on the lithium electrode surface. e. Schematic diagram of SEI growth on the lithium electrode.

In the following charge (Fig. 3-9a), mossy Li seeds sprouted in the etched pits after 1 min. The seeds then grew into thin and torturous mossy Li whiskers and then the number of whiskers increased after 5 min and 20 min charging. Whiskers swelled into thick mossy Li dendrites with continued charging. At the end of the charge process, mossy Li islands were formed and were inhomogeneously dispersed on the anode surface. Li *et al.* [27] provided a complete observation of the growth of Li whiskers in the liquid electrolyte by in-situ TEM method. Specifically, spherical lithium nuclei emerged at the surface and acted as “fumaroles”, boosting the growth of whiskers. Kinks formed when the SEI became thicker and separated the whisker into several segments, leading to the tortuous morphology. An interesting phenomenon, which has not received much attention, is that mossy Li only grew from the pits while no whiskers could be found on the flat regions (Fig. 3-9a insets and Fig. 3-9b). In order to validate this result, a scratch with width of 20 μm was made on the lithium anode (Fig. 3-9c). After deposition, whiskers only grew from the bottom of the scratch (Fig. 3-9d). In the batteries without sulfur cathodes (Li‖Cu batteries used for average coulombic efficiency measurement), mossy Li still grew from etched pits (Fig. 3-9e). This result is contrary to a commonly held belief concerning Li dendrite growth, which was considered to be stimulated by protuberances on the surface because of a higher current density on sharp points [54]. Such deviation can be ascribed to the different growth mechanisms of mossy Li whiskers and large lithium dendrites. The growth of mossy Li whiskers is controlled by the competition between SEI formation and lithium nucleation, leading to a root growth mechanism. However, the growth of large dendrites is limited by the lithium ion diffusion in the electrolyte, because of which the lithium grows from the top in lithium dendrites. Thusly, the lithium dendrites are more sensitive to the protuberance on the surface. However, the difference in growth mechanisms still cannot explain why mossy Li grew from the bottom of these pits. Tarascon *et al.* [26] observed a similar phenomenon in a Li-C battery with liquid electrolyte but they did not explain the mechanism. Chen *et al.* [55] achieved the controlled deposition of a lithium anode in a liquid electrolyte system by patterning orderly arranged holes on the electrode surface. They found that the whiskers grew from the bottom of the holes and explained that the bottom of the pits corresponded to the tip of electrolyte protuberances, which may also promote electron and ion aggregation and stimulate whisker growth. In the present study, the etched pits exhibited irregular shapes with inhomogeneous curvature distributions at the bottom. Technically, the intensity of the electric field is inversely proportional to the radius of the curvature of the cavity, but it seems that the whiskers tend to grow on the flat bottom of the pits rather than at the bottom with a smaller radius of curvature (Fig. 3-9a and b). Interestingly, no such mossy Li aggregation can be found in Li-S batteries with solid-state electrolyte [18], indicating that this uncontrolled growth of mossy Li is related to the liquid nature of the electrolyte.

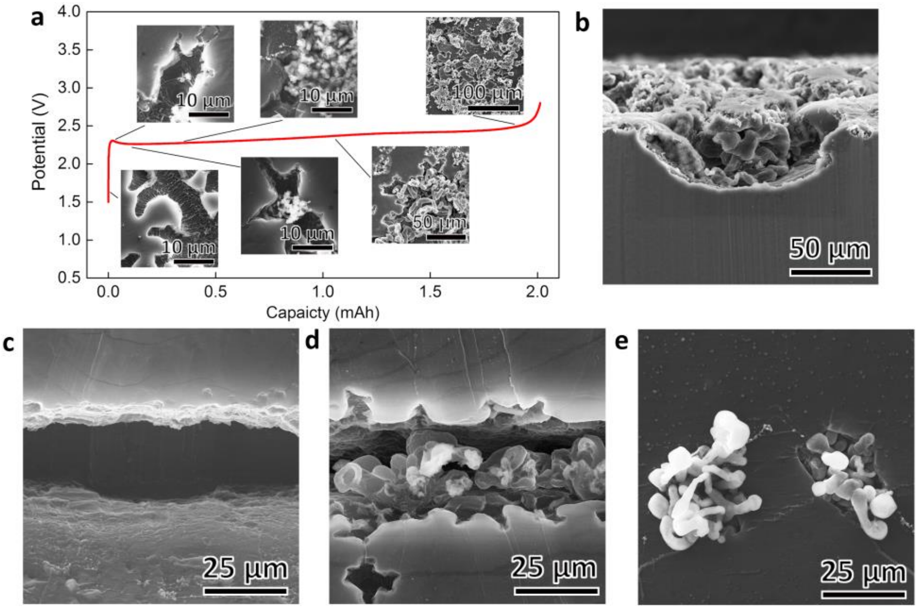

Fig. 3-9 Inhomogeneous formation of mossy Li in the first charge and stripping of lithium anode at the second discharge process. a. Charge profile of the Li-S battery with microstructural images at different charging time, showing that mossy Li whiskers grew from the bottom of the pits. b. Cross-sectional SEM image of the lithium anode in the Li-S battery after the first charge process. c. A scratch on the lithium surface. d. Mossy Li whiskers grew from the bottom of the scratch instead of the flat banks after charging. e. A lithium anode in a Li‖Cu battery after the first plating process, showing mossy Li grew from etched pits.

To explain this observation, we assessed another factor that may influence the inhomogeneous deposition of lithium anode in liquid electrolytes: the flow of fluids. The inner environment of an assembled battery with liquid electrolyte is far beyond stagnant. Liquid electrolyte flows at a small scale and can be introduced by heat-induced convection, Marangoni convection, electro-osmotic/electrocapillary forces, dielectro-phoretic electric field induced membrane bending, *etc*. Moreover, the surface of the lithium anode is etched away during discharging, leaving an interstitial space between the electrode and separator for liquid flow. A series of computational fluid dynamics (CFD) simulations were carried out on a proportionally amplified model (see supporting information for details of the CFD simulation) (Fig. 3-10a). The flow would travel across the existing pit without disturbing the liquid at the bottom. No matter how the effective Reynolds number changes, whether convection happens above the pit, or if the flow is discontinuous and intermittent, the liquid at the bottom of the pit stays relatively stagnant. The undisturbed environment at the bottom of the pit protects the delicate nuclei of whiskers and provides optimal sites for sustained mossy Li growth. In contrast, a large velocity gradient exists above the flat regions, exerting shear stresses on surface perturbations and breaking delicate whisker sprouts. It can be assumed that if there are no pits on the electrode surface, mossy Li whiskers will be broken by the flow before they grow, leaving short granular nuclei on the electrode surface and leading to homogeneous deposition. This postulate is proven by the fact that a homogeneous deposition can be obtained on a polished surface [26]. Thusly, although exploring the growth mechanism of lithium dendrites or mossy Li has profound significance, it is necessary to discuss the stripping and deposition jointly in real Li metal battery systems because the inhomogeneous stripping indeed induced the inhomogeneous growth of mossy Li. The fluids flow factor is able to compensate explanations for other phenomena. For instance, gel electrolyte can effectively improve the homogeneity of the lithium deposition in lithium metal batteries. Since the mechanical properties of gel electrolytes are similar to or even weaker than the commercial separator, it is irrational to ascribe the homogenous lithium deposition to the mechanical confinement. Another possible reason is that liquid flow is largely limited by the long-chain polymer, ensuring a stable environment above the lithium anode surface and, thereby, the homogeneous deposition.

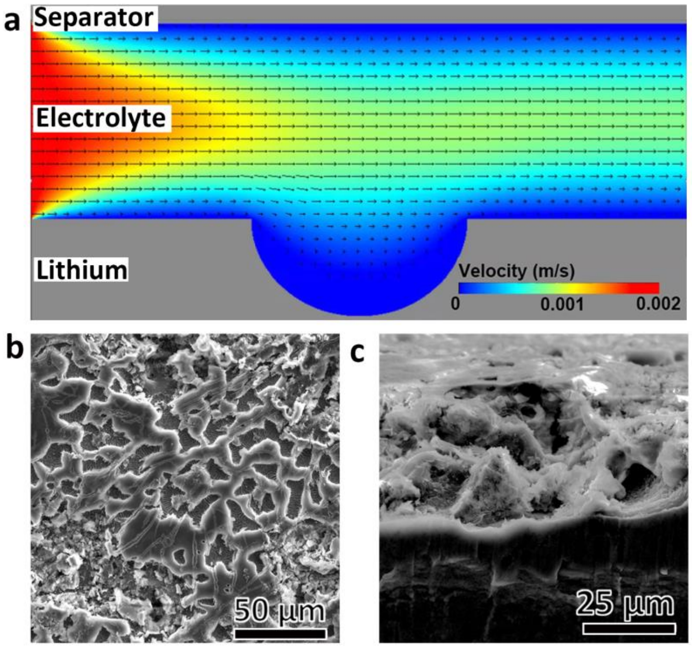

Fig. 3-10 As-assumption mechanism of mossy Li growth. a. A fluid mechanics simulation of a constant flow over a pit in a flat surface with a Reynolds number of 3. The Flow at the bottom of the pit keeps steady. b. SEM image of a lithium anode after the second discharge. Mossy Li

whiskers were etched preferentially. c. Cross section of a Lithium anode after the second discharge, showing residual hollowed SEI.

After the following discharge (the second discharge), the mossy Li whiskers were etched preferentially (Fig. 3-10b). This is because the SEI on the whiskers is thinner than those in the flat regions and the geometry of the whiskers makes them more active due to a higher surface/volume ratio. The whiskers were hollowed out and the SEI that surrounded them remained on the electrode surface, forming porous deposits (Fig. 3-10c). These porous and loose deposits, together with dead Li, will aggregate and densify after repeated stripping/depositing, jointly forming a dense crust as shown in Fig. 3-2. This finding further proved that mossy Li promoted the aggregation of passive sediments and the malfunction of the anode. Moreover, it is obvious that more flat regions were etched after the second discharge, indicating the irreversible consumption of lithium, which can be ascribed to the formation of dead Li and SEI. Therefore, unlike the "sudden death" induced by large dendrites, the malfunction derived from mossy Li in long life-span Li-S batteries is an incremental procedure that is closely related to the inhomogeneous stripping and the uncontrolled depositing of lithium. Numerous pits formed after discharging because of imperfections in the SEI. The bottom of the pits experienced a relatively steady environment, promoting the growth of mossy Li whiskers. The mossy Li whiskers were etched preferentially because of their higher surface/volume ratio and thinner SEI, leaving hollowed SEI fathoms and dead Li particles on the anode surface. These mossy Li induced passive sediments, together with deposited Li_2S, were densified into a compact crust, which blocked reaction pathways and lead to the anode failure.

3.4 The prevention of mossy Li induced battery failure

3.4.1 Porous carbon interlayer

Armed with an in-depth understanding of the failure mechanism of the Li-S batteries, we strive to push up the lifespan beyond 620 cycles. To prevent the formation of mossy Li and passive crust, we propose an additional interlayer consisting of porous APC to be placed between the separator and the anode. The porous APC interlayer is expected to eliminate the formation of passive sediments and mossy Li by promoting the homogeneous deposition of Li metal, which will lead to the overall enhancement of the stability and durability of the battery (Fig. 3-11a inset). Encouragingly, this conductive porous interlayer stretched the battery's lifespan from 620 to over 1000 cycles at 0.96 C rate (Fig. 3-11a). At the 1000th cycle, the battery still delivered a capacity of 527 mAh g^{-1} with a capacity retention rate of 52.3%. The specific capacity decreased in the first several cycles and then increased gradually. At the 250th cycle, the capacity decreased gradually until the 1000th cycle. We postulate that sulfur on the electrode surface dissolved into the electrolyte quickly, leading to the sudden drop in capacity in the first several cycles. The encapsulated sulfur then released and participated in the electrochemical reaction, pushing up the specific capacity. At about the 250th cycle, no more extra sulfur encapsulated in the graphene film can compensate the natural capacity decay from electrolyte consumption and electrode degradation, leading to the capacity turning point. At the 1000th cycle, the coulombic efficiency slowly decreased to 99.2%, suggesting that the APC interlayer indeed effectively reduced the consumption of $LiNO_3$. The elongated lifespan, coupling with the smooth capacity decay after activation, in turn validated the outstanding stability of the APC/graphene/S cathode. No distortion was found in the CV curves of the 1st, 2nd, 3rd, and 120th and 121st cycles (Fig. 3-11b), indicating that the APC interlayer did not deform the stability of the Li-S battery system. The EIS spectrum of the Li/APC-APC/graphene/S battery before cycling exhibited a large internal resistance, which can be ascribed to the insulating nature of sulfur. After failure, a near 45 ° straight line was observed from the intermediate frequency to the low frequency and a small semicircle formed at the high frequency regime, suggesting that the battery had low ion diffusion resistance and equivalent series resistance even after failure (Fig. 3-11c).

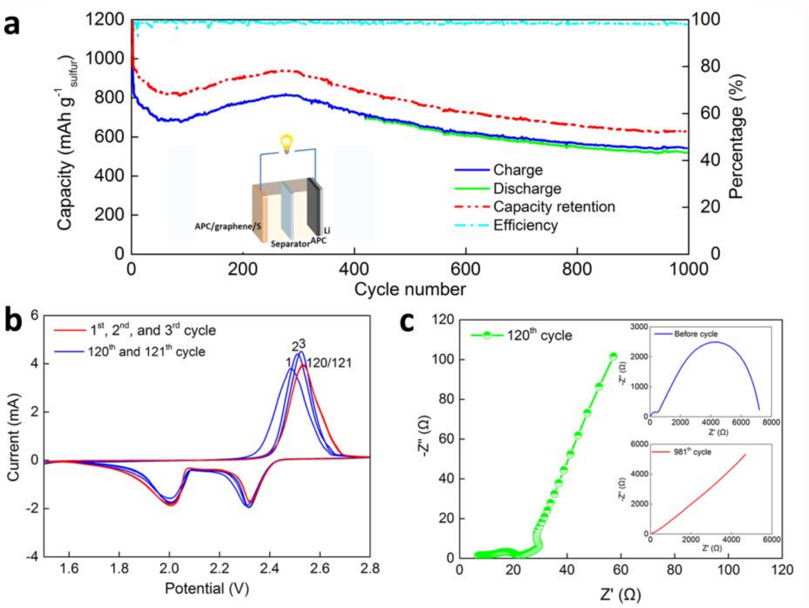

Fig. 3-11 Electrochemical properties of Li/APC-APC/graphene/S battery. a. Cycling capability of the Li/APC-APC/graphene/S battery at 0.96 C (inset: Li/APC-APC/graphene/S configuration). b. CV curves of the battery at first three cycles, and 120th and 121st cycles. c. EIS spectra of the battery before cycling, at 120th cycle, and after failure.

Intriguingly, the APC interlayer prevented the formation of septarian crusts, big holes, dendrites, and mossy Li (Fig. 3-12a). The APC interlayer eliminated the mossy Li layer and the thickness of Li anode beneath the APC interlayer was more homogeneous (Fig. 3-12b). the ACP acted as the Li/ACP anode and the original Li metal as the current collector. The close-up observation of the APC interlayer uncovered that the Li was embedded into gaps between APC fibers, no dendrites or mossy Li formed (Fig. 3-12c). Clearly the porous conductive interlayer redistributed Li ions, preventing the formation of Li dendrites and mossy Li. More importantly, the APC interlayer served as an artificial SEI to suppress the repeated formation of SEI, preventing the formation of passive sediments and facilitating the ion and electron transfer (Fig. 3-12d). The APC interlayer battery configuration protected the Li anode from unfavorable reactions, remarkably increasing the battery's lifespan. However, since the porous interlayer did not improve the active material utilization or enhance the electrochemical reactions, the extra mass from the interlayer would decrease the energy density of the whole cell about 20 %. Therefore, a balance between energy density and lifespan should be considered in real-life applications.

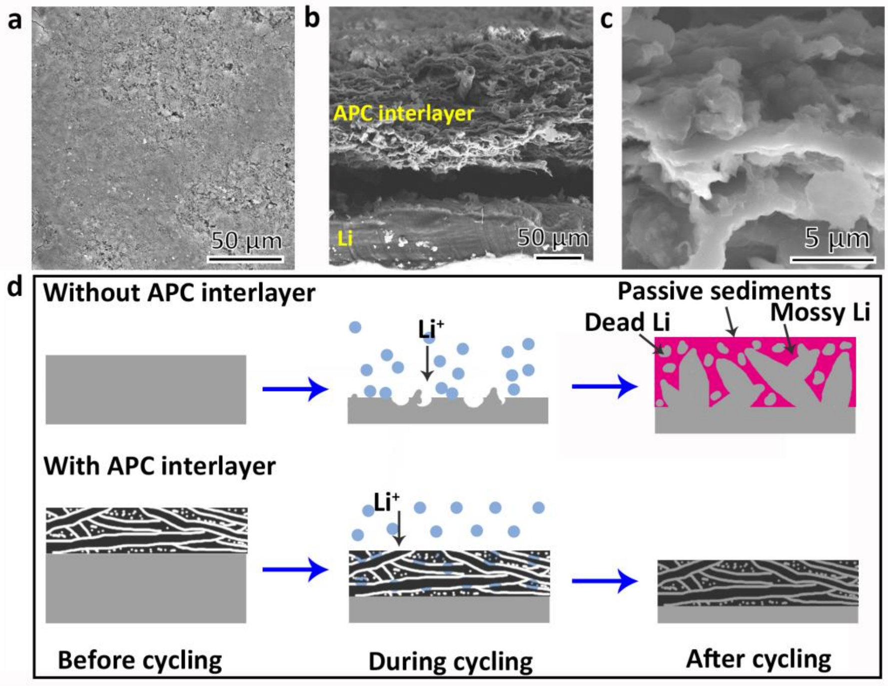

Fig. 3-12 Microstructure and schematic illustration of Li/APC anode. a. Top-down SEM image of the Li/APC anode after 1000 cycles, showing a flat surface without crusts, mossy Li, and dendrites. b. Cross-sectional SEM image of the Li/APC anode after 1000 cycles. c. Close-up observation of the APC interlayer, showing that electroactive materials filled out the gaps between paper fibers. d. Schematic illustration of Li anode with and without APC interlayer.

3.4.2 ALA/graphene composite as artificial SEI

ALA is a naturally existing small molecule and is used as an inexpensive dietary supplement. ALA has a bifunctional molecular structure with a self-polymerizable disulfide bond and an ion exchangeable carboxylate group. The material can be prepared to be ion-conductive and mechanically strong. The unique self-healing properties of ALA [56] will further enhance safety and durability. Ion transport properties of ALA can be enhanced via chemical functionalization. In this study, graphene oxide (GO) was blended with ALA as an additional route to enhance ionic conductivity and mechanical/thermal stability (Fig. 3-13). It is expected that the S-S bonds will open and reconnect during charging and discharging, forming a stable SEI on the Li anode and a uniform layer at the cathode-electrolyte interface on the sulfur-containing cathode, which simultaneously prevent polysulfide shuttling and Li dendrite formation.

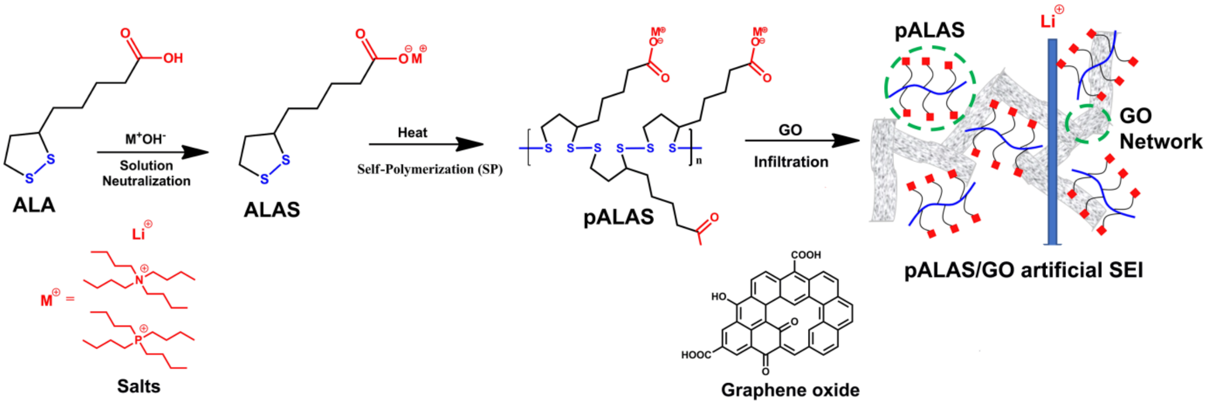

Fig. 3-13 The mechanism of converting ALA to a strong artificial SEI.

ALA can dissolve into organic solvents, including DOL and DME, but it is insoluble in water. Therefore, pure ALA is unable to be used in Li-S batteries due to the instability in the electrolyte. To avoid the dissolution of ALA, the ALA was treated by a tetrabutylammonium hydroxide solution. The tetrabutylammonium replaced the hydrogen during neutralization, forming ALA tetrabutylammonium salt, which is a viscous liquid with a light yellow color. The viscosity of ALA tetrabutylammonium salt is sensitive to the temperature. When the temperature is higher than 70 ℃, the viscosity decreases drastically. After adding graphene oxide, the viscosity and thermal stability were largely increased due to the strong interactions between ALA and the functional groups on graphene oxide sheets. To add ALA/GO into the Li-S battery systems, ALA/GO suspension was homogeneously coated on the separator via capillary force (Fig. 3-14a inset). After drying, ALA/GO formed small islands that were homogeneously dispersed on the separator (Fig. 3-14 a and b). XPS spectrum (Fig. 3-14c) unveiled that the separator coated with ALA/GO had notable oxygen peaks and sulfur peaks.

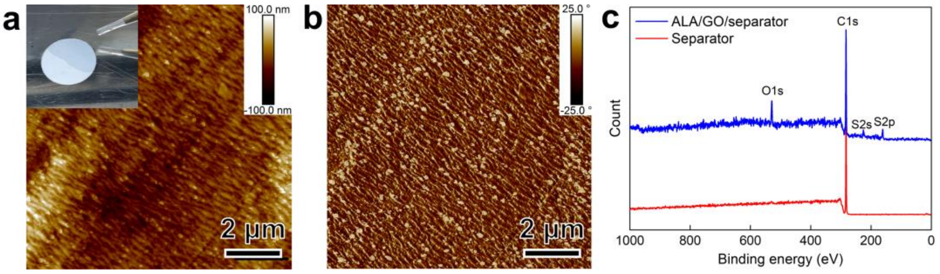

Fig. 3-14 The separator coated with ALA/GO. a. AFM height profile of the separator coated with ALA/GO. Inset is using capillary force to coat ALA/GO on the separator. b. AFM phase diagram of

the separator coated with ALA/GO. c. XPS spectra of pure separator and separator coated with ALA/GO.

Intriguingly, ALA/GO effectively prevented the growth of Li dendrites and whiskers of Li anodes in Li-S batteries. After five discharge/charge cycles at 0.5 mA, mossy Li sprouted from the etched holes (Fig. 3-15a), which was consistent with the results shown in Fig. 3-2. When the separator coated with pure ALA tetrabutylammonium salt was used, mossy Li whiskers still grew but ALA fibers were wrapped around the mossy Li (Fig. 3-15b). This result indicates that ALA can form an artificial SEI on the Li anode surface, but pure ALA tends to polymerize into fibular morphology which could not prevent the growth of mossy Li. In the Li-S battery which ALA/GO coated separator was used, the growth of mossy Li was effectively prevented by the formed polymer film (Fig. 3-15c). Therefore, the ALA/GO islands in Fig. 3-14a and b decomposed and polymerized on the Li anode surface during discharging, forming artificial SEI. GO sheets enhanced the mechanical robustness of ALA-based SEI due to the strong interactions and acted as templates for ALA polymerization, converting the fibular morphology to thin film, which is more effective for the prevention of mossy Li growth.

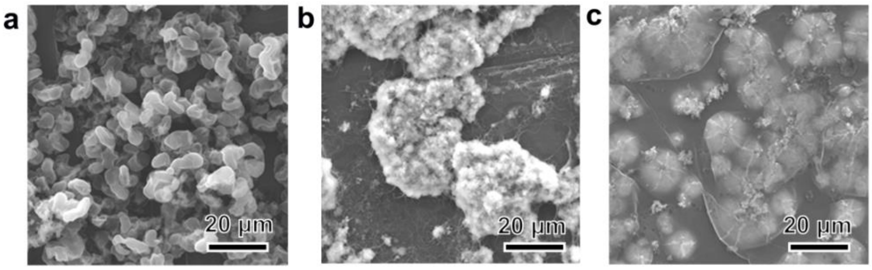

Fig. 3-15 Li anode surface morphology after five discharge/charge cycles. a. Untreated Li. b. Li with pure ALA. c. Li with ALA/GO.

The ALA/GO additive had a notable influence on the electrochemical performance of the as-assembled Li-S battery. The CV curve of the first cycle was highly unstable and largely deviated from standard Li-S batteries (Fig. 3-16a), indicating that ALA/GO decomposed from the separator between 2.5 to 3 V. In the second cycle, the CV curve started displaying Li-S chemical features with minor deviation, which was two small peaks between 2.5 to 3 V.

The CV curves of the third and fourth cycles were identical to that of a typical Li-S battery, i.e. two cathodic peaks and one anodic peak, indicating the formation of stable SEI. Therefore, the ALA/GO on the separator experienced a decomposition/polymerization at the first one or two cycles. It is possible that the S-S bonds opened up during discharging. Subsequently, the decomposed small molecules polymerized on electrodes in charging. A shred of evidence is that before cycling, the battery exhibited large internal impendence (Fig. 3-16b); after 5 cycles, the internal impendence reduced drastically, indicative of a stable SEI formed after the first cycle (Fig. 3-16c). The charge/discharge curves of the first two cycles were unstable (Fig. 3-16d). Unlike our previous Li-S batteries, the battery with ALA/GO did not show the huge drop of specific capacity in the second cycle (Fig. 3-16e), implying the enhanced SEI may also prevent the shuttle effect. The battery cycled over 150 cycles and has almost no capacity decay comparing with the first cycle (Fig. 3-16e). Clearly, the ALA/GO enabled SEI is promising for simultaneously reducing Li dendrite growth and S shuttle effect.

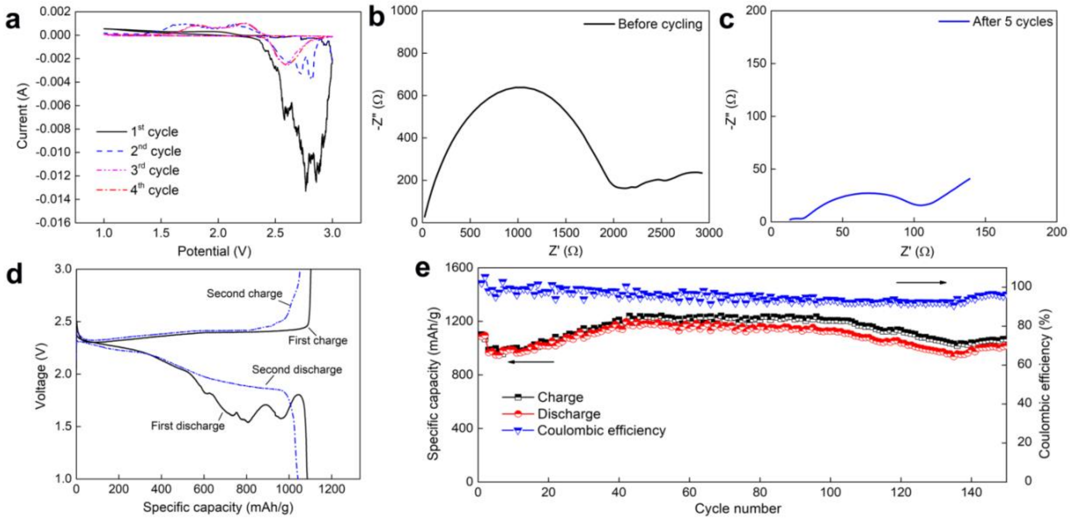

Fig. 3-16 Electrochemical performance of the Li-S battery with ALA/GO. a. CV curves of the first four cycles. b. EIS spectrum before cycling. c. EIS spectrum after five cycles. d. Charge/discharge curves of Li-S batteries with ALA/GO. e. Cyclic performance of the Li-S battery with ALA/GO.

3.5 Conclusions

In summary, mossy Li induced anode failure in Li-S battery system was studied. Stripping/plating of mossy Li whiskers continuously produced SEI flotsams and dead Li particles on the anode surface. These passive deposits, together with sulfur and Li_2S, were repeatedly compressed by the growth of mossy Li, densifying into a compact crust. The formed passive crust blocked the charge transfer pathway for the lithium underneath, while additionally inducing severe local etching on the lithium. When lithium was depleted within the etching hole, as the rest of the surface was covered by the passive crust, the lithium anode failed. Therefore, the malfunction of the lithium anode is inevitable after repeated stripping/depositing even with sufficient electrolyte and active materials. The formation mechanism of mossy Li was then studied. When the lithium came in contact with the electrolyte, the SEI formed into square grains on the lithium surface, with the orientation being determined by the orientation of the underlying lithium crystals. Upon discharging, the boundaries of the SEI grains created a pathway for etching, leading to collapse along the squares and the formation of irregularly shaped pits. Thusly, the inhomogeneous etching of the lithium surface is more influenced by the defects on the SEI rather than the lithium, indicating that a stronger SEI can facilitate the uniformity of stripping. In the following charge process, mossy Li whiskers grew from the bottom of the pits instead of at protuberances on the anode surface. In this regard, the flow of fluids within the battery was used to explain this phenomenon. The flow above the pits only weakly interacted with the fluid at the bottom of the pits, offering a near stagnant environment for the preferential growth of mossy Li. Therefore, the formation of mossy Li is closely related to the inhomogeneous etching of the anode surface; when studying lithium plating in practical batteries, the stripping process cannot be ignored. Although the Li-S battery system was analyzed in the present study, the findings and proposed mechanisms are expected to improve the understanding of the failure mechanisms in other long life-span Li metal based batteries. To overcome the growth of mossy Li, two methods were employed. A porous conductive APC interlayer was placed between the Li anode and separator to redistribute Li ions, promoting the homogeneous deposition of Li during electrochemical reactions. The interlayer effectively suppressed the formation of mossy Li and passive sediments, extending the Li-S battery's life span up to 1000 cycles with a capacitance retention rate of 52.3 % and eminent coulombic efficiency. Another method is to construct stronger SEI on the Li anode surface. ALA, a common food supplement, was combined with GO and coated on the separator. Upon discharging, the ALA/GO decomposed from the separator and polymerized on the electrode surface, forming an artificial SEI. The stronger SEI effectively prevented the growth of mossy Li, leading to high specific capacitance and low capacity decay. The ALA/GO additive for stronger SEI is promising for overcoming the challenges of Li dendrite growth and S shuttling.

References

[1] J.B. Goodenough, Y. Kim, Challenges for rechargeable batteries, J. Power Sources 196 (2011) 6688-6694.

[2] R. Van Noorden, The rechargeable revolution: a better battery, Nature 507 (2014) 26-28.

[3] P.G. Bruce, S.A. Freunberger, L.J. Hardwick, J.M. Tarascon, Li-O_2 and Li–S batteries with high energy storage, Nat. Mater. 11 (2012) 19-29.

[4] S. Urbonaite, T. Poux, P. Novák, Progress towards commercially viable Li-S battery cells, Adv. Energy Mater. 5 (2015) 1500118.

[5] P.P.R.M.L. Harks, C.B. Robledo, T.W. Verhallen, P.H.L. Notten, F.M. Mulder, The significance of elemental sulfur dissolution in liquid electrolyte lithium sulfur batteries, Adv. Energy Mater. 7 (2017) 1601635.

[6] Y. V. Mikhaylik, J.R. Akridge, Polysulfide shuttle study in the Li/S battery system, J. Electrochem. Soc. 151 (2004) A1969.

[7] X. Wang, Z. Wang, L. Chen, Reduced graphene oxide film as a shuttle-inhibiting interlayer in a lithium-sulfur battery, J. Power Sources. 242 (2013) 65-69.

[8] G. Hu, C. Xu, Z. Sun, S. Wang, H.M. Cheng, F. Li, W. Ren, 3D graphene-foam-reduced-graphene-oxide hybrid nested hierarchical networks for high-performance Li-S batteries, Adv. Mater. 28 (2016) 1603-1609.

[9] Y. Yang, G. Zheng, Y. Cui, Nanostructured sulfur cathodes, Chem. Soc. Rev. 42 (2013) 3018-3032.

[10] M.A. Pope, I.A. Aksay, Structural design of cathodes for Li-S batteries, Adv. Energy Mater. 5 (2015) 1500124.

[11] H. Wang, Y. Yang, Y. Liang, J.T. Robinson, Y. Li, A. Jackson, Y. Cui, H. Dai, Graphene-wrapped sulfur particles as a rechargeable lithium-sulfur battery cathode material with high capacity and cycling stability, Nano Lett. (2011) 2644-2647.

[12] X.Y. Zhao, J.P. Tu, Y. Lu, J.B. Cai, Y.J. Zhang, X.L. Wang, C.D. Gu, Graphene-coated mesoporous carbon/sulfur cathode with enhanced cycling stability, Electrochim. Acta 113 (2013) 256-262.

[13] C. Liang, N.J. Dudney, J.Y. Howe, Hierarchically structured sulfur/carbon nanocomposite material for high-energy lithium battery, Chem. Mater. 21 (2009) 4724-4730.

[14] X. Ji, K.T. Lee, L.F. Nazar, A highly ordered nanostructured carbon-sulphur cathode for lithium-sulphur batteries, Nat. Mater. 8 (2009) 500-506.

[15] Y. Zhang, Z. Gao, N. Song, X. Li, High-performance supercapacitors and batteries derived from activated banana-peel with porous structures, Electrochim. Acta 222 (2016) 1257-1266.

[16] Z.W. Seh, Q. Zhang, W. Li, G. Zheng, H. Yao, Y. Cui, Stable cycling of lithium sulfide cathodes through strong affinity with a bifunctional binder, Chem. Sci. 4 (2013) 3673-3677.

[17] H. Wu, G. Chan, J.W. Choi, I. Ryu, Y. Yao, M.T. Mcdowell, S.W. Lee, A. Jackson, Y. Yang, L. Hu, Y. Cui, Stable cycling of double-walled silicon nanotube battery anodes through solid-electrolyte interphase control, Nat. Nanotechnol. 7 (2012) 310-315.

[18] S. Xiong, K. Xie, Y. Diao, X. Hong, Characterization of the solid electrolyte interphase on lithium anode for preventing the shuttle mechanism in lithium-sulfur batteries, J. Power Sources 246 (2014) 840-845.

[19] H.J. Peng, T.Z. Hou, Q. Zhang, J.Q. Huang, X.B. Cheng, M.Q. Guo, Z. Yuan, L.Y. He, F. Wei, Strongly coupled interfaces between a heterogeneous carbon host and a sulfur-containing guest for highly stable lithium-sulfur batteries: mechanistic insight into capacity degradation, Adv. Mater. Interfaces. 1 (2014) 1400227.

[20] H. Chen, C. Wang, Y. Dai, S. Qiu, J. Yang, W. Lu, L. Chen, Rational design of cathode structure for high rate performance lithium-sulfur batteries, Nano Lett. 15 (2015) 5443-5448.

[21] X. Liang, Y. Rangom, C.Y. Kwok, Q. Pang, L.F. Nazar, Interwoven MXene nanosheet/carbon-nanotube composites as Li-S cathode hosts, Adv. Mater. 29 (2016) 1603040.

[22] T. Chen, B. Cheng, G. Zhu, R. Chen, Y. Hu, L. Ma, H. Lv, Y. Wang, J. Liang, Z. Tie, Z. Jin, J. Liu, Highly efficient retention of polysulfides in “sea urchin”-like carbon nanotube/nanopolyhedra superstructures as cathode material for ultralong-life lithium-sulfur batteries, Nano Lett. 17 (2016) 437-444.

[23] Y. Zhang, Z. Gao, X. Li, Capillarity composited recycled paper/graphene scaffold for lithium-sulfur batteries with enhanced capacity and extended lifespan, Small 13 (2017) 1701927.

[24] D. Lin, Y. Liu, Y. Cui, Reviving the lithium metal anode for high-energy batteries, Nat. Nanotechnol. 12 (2017) 194-206.

[25] W. Xu, J. Wang, F. Ding, X. Chen, E. Nasybulin, Y. Zhang, J.G. Zhang, Lithium metal anodes for rechargeable batteries, Energy Environ. Sci. 7 (2014) 513-537.

[26] L. Gireaud, S. Grugeon, S. Laruelle, B. Yrieix, J.M. Tarascon, Lithium metal stripping/plating mechanisms studies: a metallurgical approach, Electrochem. Commun. 8 (2006) 1639-1649.

[27] A. Kushima, K.P. So, C. Su, P. Bai, N. Kuriyama, T. Maebashi, Y. Fujiwara, M.Z. Bazant, J. Li, Liquid cell transmission electron microscopy observation of lithium metal growth/dissolution: root growth, dead lithium and lithium flotsams, Nano Energy 32 (2017) 271-279.

[28] Z. Li, J. Huang, B. Yann Liaw, V. Metzler, J. Zhang, A review of lithium deposition in lithium-ion and lithium metal secondary batteries, J. Power Sources 254 (2014) 168-182.

[29] M.D. Tikekar, S. Choudhury, Z. Tu, L.A. Archer, Design principles for electrolytes and interfaces for stable lithium-metal batteries, Nat. Energy 1 (2016) 16114.

[30] Y. Gofer, Y. Ein Ely, D. Aurbach, Surface chemistry of lithium in 1,3-dioxolane, Electrochim. Acta 37 (1992) 1897-1899.

[31] K.M. Abraham, Recent developments in secondary lithium battery technology, J. Power Sources 14 (1985) 179-191.

[32] N. Takami, T. Ohsaki, K. Inada, The impedance of lithium electrodes in LiPF6- based electrolytes, J. Electrochem. Soc. 139 (1992) 1849–1854.

[33] M. Cuisinier, P.E. Cabelguen, B.D. Adams, A. Garsuch, M. Balasubramanian, L.F. Nazar, Unique behaviour of nonsolvents for polysulphides in lithium-sulphur batteries, Energy Environ. Sci. 7 (2014) 2697.

[34] S.S. Zhang, Role of $LiNO_3$ in rechargeable lithium/sulfur battery, Electrochim. Acta 70 (2012) 344-348.

[35] A. Rosenman, R. Elazari, G. Salitra, E. Markevich, D. Aurbach, A. Garsuch, The effect of interactions and reduction products of $LiNO_3$, the Anti-Shuttle Agent, in Li-S Battery Systems, J. Electrochem. Soc. 162 (2015) A470-A473.

[36] J.B. Bates, N.J. Dudney, G.R. Gruzalski, R.A. Zuhr, A. Choudhury, C.F. Luck, J.D. Robertson, Electrical properties of amorphous lithium electrolyte thin films, Solid State Ion. 56 (1992) 647-654.

[37] M. Rao, X. Geng, X. Li, S. Hu, W. Li, Lithium-sulfur cell with combining carbon nanofibers-sulfur cathode and gel polymer electrolyte, J. Power Sources 212 (2012) 179-185.

[38] J. Jin, Z. Wen, X. Liang, Y. Cui, X. Wu, Gel polymer electrolyte with ionic liquid for high performance lithium sulfur battery, Solid State Ion. 225 (2012) 604-607.

[39] S.S. Zhang, D.T. Tran, How a gel polymer electrolyte affects performance of lithium/sulfur batteries, Electrochim. Acta 114 (2013) 296-302.

[40] Z. Lin, Z. Liu, W. Fu, N.J. Dudney, C. Liang, Lithium polysulfidophosphates: a family of lithium-conducting sulfur-rich compounds for lithium-sulfur batteries, Angew. Chemie - Int. Ed. 125 (2013) 7608-7611.

[41] S. Xin, Y. You, S. Wang, H.C. Gao, Y.X. Yin, Y.G. Guo, Solid-state lithium metal batteries promoted by nanotechnology: progress and prospects, ACS Energy Lett. 2 (2017) 1385-1394.

[42] Z. Tu, Y. Kambe, Y. Lu, L.A. Archer, Nanoporous polymer-ceramic composite electrolytes for lithium metal batteries, Adv. Energy Mater. 4 (2014) 1300654

[43] X.B. Cheng, T.Z. Hou, R. Zhang, H.J. Peng, C.Z. Zhao, J.Q. Huang, Q. Zhang, Dendrite-free lithium deposition induced by uniformly distributed lithium-ions for

efficient lithium metal batteries, Adv. Mater. 28 (2016) 2888-2895.

[44] W. Liu, W. Li, D. Zhuo, G. Zheng, Z. Lu, K. Liu, Y. Cui, Core–shell nanoparticle coating as an interfacial layer for dendrite-free lithium metal anodes, ACS Cent. Sci. 3 (2017) 135-140.

[45] K. Liu, D. Zhuo, H.W. Lee, W. Liu, D. Lin, Y. Lu, Y. Cui, Extending the life of lithium-based rechargeable batteries by reaction of lithium dendrites with a novel silica nanoparticle sandwiched separator, Adv. Mater. 3 (2016) 1603987.

[46] C.P. Yang, Y.X. Yin, S.F. Zhang, N.W. Li, Y.G. Guo, Accommodating lithium into 3D current collectors with a submicron skeleton towards long-life lithium metal anodes, Nat. Commun. 6 (2015) 8058.

[47] S.H. Wang, Y.X. Yin, T.T. Zuo, W. Dong, J.Y. Li, J.L. Shi, C.H. Zhang, N.W. Li, C.J. Li, Y.G. Guo, Stable Li metal anodes via regulating lithium plating/stripping in vertically aligned microchannels, Adv. Mater. 29 (2017) 1703729.

[48] S. Xiong, K. Xie, Y. Diao, X. Hong, On the role of polysulfides for a stable solid electrolyte interphase on the lithium anode cycled in lithium-sulfur batteries, J. Power Sources 236 (2013) 181-187.

[49] W.C. Oliver, G.M. Pharr, An improved technique for determining hardness and elastic modulus using load and displacement sensing indentation experiments, J. Mater. Res. 7 (1992) 1564-1583.

[50] N.J. Dudney, Addition of a thin-film inorganic solid electrolyte (Lipon) as a protective film in lithium batteries with a liquid electrolyte, J. Power Sources. 89 (2000) 176-179.

[51] B.D. Adams, J. Zheng, X. Ren, W. Xu, J.G. Zhang, Accurate determination of coulombic efficiency for lithium metal anodes and lithium metal batteries, Adv. Energy Mater. 8 (2017) 1702097.

[52] X.B. Cheng, R. Zhang, C.Z. Zhao, F. Wei, J.G. Zhang, Q. Zhang, A review of solid electrolyte interphases on lithium metal anode, Adv. Sci. 3 (2016) 1500213.

[53] W. Li, H. Yao, K. Yan, G. Zheng, Z. Liang, Y.M. Chiang, Y. Cui, The synergetic effect of lithium polysulfide and lithium nitrate to prevent lithium dendrite growth., Nat. Commun. 6 (2015) 7436.

[54] F. Ding, W. Xu, G.L. Graff, J. Zhang, M.L. Sushko, X. Chen, Y. Shao, M.H.

Engelhard, Z. Nie, J. Xiao, X. Liu, P. V. Sushko, J. Liu, J.G. Zhang, Dendrite-free lithium deposition via self-healing electrostatic shield mechanism, J. Am. Chem. Soc. 135 (2013) 4450-4456.

[55] Y. Li, J. Jiao, J. Bi, X. Wang, Z. Wang, L. Chen, Controlled deposition of Li metal, Nano Energy 32 (2017) 241-246.

[56] Q. Zhang, C.Y. Shi, D.H. Qu, Y.T. Long, B.L. Feringa, H. Tian, Exploring a naturally tailored small molecule for stretchable, self-healing, and adhesive supramolecular polymers, Sci. Adv. 4 (2018) eaat8192.

Chapter 4 Graphene/Al_2O_3/Al Composites with High Strength and Toughness

4.1 Background and motivation

Up to now, it is still a challenge to develop engineering materials that exhibit greatly enhanced strength without increasing brittleness or fragility [1]. Fortunately, nature provides us with abundant and diverse inspirations which may simultaneously achieve high strength and high toughness [2]. Nacre, commonly referred to as nature's armor, is renowned for its unusual combination of strength and toughness [3]. Nature's "wisdom" in nacre resides in its structural design strategy - a hierarchical structure consisting of layered hard aragonite platelets in soft organic biopolymer matrix. The aragonite component is in a layered form and serves as the primary load bearer for strength [3,4]. The soft organic biopolymer layer in between the platelets plays a critical role in both load distribution and energy dissipation due to its unique deformation features [5–9]. The surface nanoasperities on aragonite platelets and mineral bridges between the platelets work to interlock the platelets and prevent single platelet motion [6,7]. However, this deceptively simple hard/soft/hard architecture demonstrated by nacre is actually exceptionally difficult to replicate with engineering materials and traditional manufacturing methods. Most efforts in mimicking nacre's architecture use a ceramic/polymer configuration [10–14]. Ritchie *et al.* [10] synthesized an aluminum oxide/polymethyl methacrylate (Al_2O_3/PMMA) lamellar composite which has similar structure to nacre. Yu *et al.* [14] fabricated a highly nacre-like calcium carbonate/polyacrylic acid ($CaCO_3$/PAA) composite via a mesoscale "assembly-and-mineralization" approach. Those composites have proven that laminated structure configuration can effectively enhance the toughness of brittle materials. However, an intrinsic limitation of using synergic polymers is the low strength, which may handicap the mechanical performance of the fabricated composites. Cloning nacre's architecture with a stronger substitute, such as aluminum, in engineered composites has proven to be a more challenging task.

Due to its ultra-high hardness and outstanding chemical stability, Al_2O_3 nanoparticles have long been considered as an ideal reinforcement to strengthen metallic materials [15]. However, Al_2O_3 nanoparticles tend to agglomerate in the matrix - one of the major roadblocks limiting their reinforcing effect and applications. Substantial efforts have been devoted to improve the dispersion of Al_2O_3 nanoparticles, such as hot rolling [16], friction stirring [17], and DC plasma process [18]. It has been recently recognized that orderly arranged Al_2O_3 nanoparticles in metallic matrix are beneficial for the joint enhancement of strength and toughness [19]. Another reinforcement is graphene, as a 2-D single layer atomic crystal with extremely high strength (130 GPa) and stiffness (1 TPa) [20,21], but relatively low toughness [22], is expected to serve as a perfect mechanical reinforcement for metal-based composites [23–32]. Ball milling was widely used to mix graphene flakes with metal powders to enhance the dispersion uniformity [23–27]. Semi powder metallurgy, which mixes graphene or graphene oxide (GO) sheets with metal powders in liquid, was found to be more effective in dispersing reinforcements and enhancing graphene/metal bonding [28–30]. Several new methods such as electrostatic adsorption [31] and chemical adsorption [32] were recently exploited. After high temperature sintering, severe plastic deformation, such as high-ratio differential speed rolling [27], hot extrusion [28], and uniaxial compression [33], was often adopted to densify the composite with the goal to improve material strength and align graphene sheets. However, considering the amazing mechanical properties of graphene, the synthesized graphene/metal composites are still lower than the expectation, likely due to three roadblocks hindering the development of metal/graphene composites: weak interfacial bonding between graphene and metals, aggregation of graphene, and degradation of graphene.

Here, we converted low cost, low purity aluminum flakes and graphene oxide sheets into a durable and noteworthy composite. Through a series of bottom-up assembling procedures, including semi powder metallurgy, ice-templating, sintering, and densification process, typical nacre features, such as a laminated structure, nanoasperities and mineral bridges, were effectively replicated. In particular, Al_2O_3 nanoparticles were introduced as a co-reinforcement with graphene to further strengthen the composite. Such a multireinforcement (graphene and Al_2O_3) strategy enabled a joint improvement in both strength and toughness in Al composites which have significant applications in lightweight structures, such as aircrafts and electric vehicles.

4.2 Experimental methods

Graphene oxide synthesis

All chemicals were purchased from Sigma-Aldrich Company without further purification. Graphene oxide (GO) was prepared through the Hummer method [34,35]. Specifically, 3 g of graphite powders with purity of 99.9 % were added into 200 mL H_2SO_4 while being stirred vigorously. Subsequently, within 30 min 30 g of $KMnO_4$ was gradually added into the slurry and stirred at 10 ℃ for 2 h. The reaction continued at 40 ℃ for 12 h. Next, 200 mL of distilled water was added to the reacting product to enable the reaction to continue at 70 ℃ for 2 h. 36 mL of 20% H_2O_2 was then added into the product to react with the remaining $KMnO_4$, turning the slurry to golden brown. The slurry was centrifugally separated several times at 5000 rpm for 2 h to remove the acid, and finally ultra-sonicated to obtain a graphene oxide solution of high quality.

Fabrication of graphene/Al_2O_3/Al composites

Low cost aluminum flakes with purity ≥ 91 % were used as raw materials (~100 μm in diameter and ~4 μm in thickness). The procedure of fabricating the composite is illustrated as follows and sketched in Fig. 4-1:

1. 10g of aluminum flakes were stirred in 50 mL of 3 wt. % polyvinyl alcohol (PVA) solution to coat a hydrophilic layer on their surface [28]. The obtained slurry was then rinsed several times with distilled water.
2. Surface treated aluminum flakes were mixed with 40 mL of 5 mg/mL GO suspension and stirred for 5 h to coat GO sheets on aluminum flakes until the brown GO suspension became clear, indicating that GO sheets were successfully coated onto aluminum flakes. The concentration of GO in the composite was 2 wt. %.
3. The obtained Al/GO hybrid flakes were filtered and then mixed with 5 % PVA solution which served as a binder and morphology regulator. After being frozen in a conventional

refrigerator freezer, the mix was then freeze dried for 24 h to form Al/GO foam with a height of 30 mm.

4. The Al/GO foam was afterwards thermally heated at 350 ℃ in an argon atmosphere to eliminate the PVA and partially reduce GO. Then the Al/graphene foam was further compressed under a load of 50 kN and subsequently sintered in an argon atmosphere at 655 ℃ for 2 h. Sintered samples were then cold rolled to 0.3 mm thin.

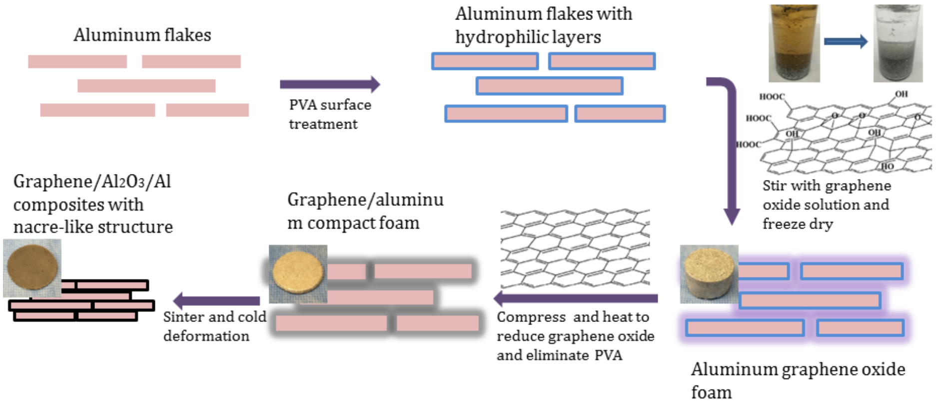

Fig. 4-1 Illustration of the fabrication process for graphene/Al_2O_3/Al composite.

For comparison, four control samples were fabricated. For the first control sample, a pure aluminum plate (99% purity) was purchased from ESPI Metal and cold rolled with the same thickness reduction/deformation rate as used for the graphene/Al_2O_3/Al composite plates. For the second control sample, aluminum flakes were surface treated with PVA, freeze dried, annealed, compressed, and sintered without adding GO. The sample was compressed and cold rolled with the same thickness reduction/deformation rate as used for the graphene/Al_2O_3/Al composite plates. The third control sample was fabricated using aluminum flakes without PVA surface treatment, that were then mixed with GO suspension directly and dried at 75 ℃ for 12 h and compressed and sintered without freeze drying, the as-obtained bulk material was cold rolled to 0.3 mm as well. For the last control sample, aluminum flakes were surface treated by PVA and shear mixed with graphite powders [36]. The as-obtained slurry was freeze-dried, sintered, and rolled by the same procedure as described in Fig. 4-1. In this study, we term the first control sample pure aluminum, the second as Al semi powder metallurgy, the third sample is denoted as graphene/Al mix, and the last control sample is called graphene/Al composite by shear mixing. Detailed processes and parameters are listed in Table 4-1.

Table 4-1 Sample notations and corresponding fabrication processes

Processes Notations	Surface treatment	Mixing	Freeze dry	Annealing	Compression	Sintering	Cold rolling
Graphene/Al_2O_3/ Al composite	PVA surface treatment	Stir with GO	24 h	350 °C 1 h	50 kN	655 °C 2h	80 % reduction
Pure aluminum							80 % reduction
Al semi powder metallurgy	PVA surface treatment		24 h		50 kN	655 °C 2h	80 % reduction
Al/graphene mix		Stir with GO		350 °C 1 h	50 kN	655 °C 2h	80 % reduction
Graphene/Al composite by shear mixing	PVA surface treatment	Shear mixing with graphite	24 h	350 °C 1 h	50 kN	655 °C 2h	80 % reduction

Material and mechanical characterization

Tensile testing was carried out on an INSTRON MicroTester 5848 with an extension speed of 0.6 mm/min. Strain was measured using the Vic-3D v7 digital image correlation sy stem from Correlated Solutions. Specimens for tensile tests were prepared according to ASTM standard E8. Hardness testing was performed using a Rockwell hardness tester with a peak indentation load of 30 N for 30 s holding. Loading-unloading nanoindentation tests were carried out using a MicroMaterials Vantage nanoindenter with a load increment of 0.1 mN each loading cycle. X-Ray patterns (XRD) were obtained using PANalytical X'Pert Pro MPD equipped with Cu Kα radiation (λ = 0.15406 nm). Raman spectra were detected with an inVia Raman microscope from Renishaw with 514 nm laser wavelength and 5% laser power. Microstructure of the specimens was characterized with a FEI Quanta 650 scanning electron microscope (SEM) with EDS detector, a JEOL 2000FX transmission electron microscope (TEM), a FEI TITAN G2 aberration corrected scanning TEM (STEM)/high resolution TEM (HRTEM). TEM specimens for cross sectional imaging were first cut using ultrathin microtome, and then ion milled. STEM samples with a thickness of 100 nm were prepared by focused ion beam (FIB). Nanoindentation tests were carried out using a nanoTest Vantage from Micro Materials. 100 cycles of partial loading-unloading from 15 to

25 mN with an increment of 0.1 mN were performed on the graphene/Al_2O_3/Al composite and four control samples. The nanoindenter was a diamond Berkovich tip whose shape function was carefully calibrated.

4.3 Microstructure and mechanical performance of nacre-like graphene/Al_2O_3/Al composites

4.3.1 Fabrication of nacre-like graphene/Al_2O_3/Al composites

Table 4-1 outlines the preparation procedures of graphene/Al_2O_3/Al composites and reference samples. Fig. 4-1 schematically demonstrates the preparation procedures for graphene/Al_2O_3/Al composites. Specifically, the graphene oxide (GO) suspension was prepared by the Hummers method. The functional groups on the GO sheets make them hydrophilic and hence dispersible in an aqueous solvent without aggregation, forming a brown aqueous suspension. Most as-obtained GO flakes were measured to be about 0.8 nm thick and highly flexible and transparent, indicative of high quality monolayered GO nanosheets. A solution of 3 wt. % polyvinyl acetate (PVA) was used to coat a hydrophilic layer on the surface of the Al flakes with the intention of enhancing the bonding between the aluminum flakes and GO sheets (Fig. 4-2) [28,37]. PVA can be frozen together with water in a freezer and vaporized at a temperature lower than 300 ℃. After the subsequent sintering and densification processes, graphene/Al_2O_3/Al composites were successfully fabricated.

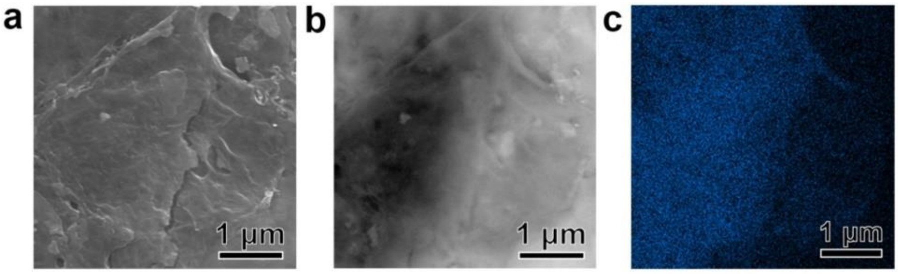

Fig. 4-2 The combination of aluminum flakes and reduced graphene oxide sheets. a. SEM image of Al flake after stirring with graphene oxide and heating at 350 °C. b. Corresponding backscattered electron image. c. EDS carbon map.

4.3.2 Microstructure of the nacre-like graphene/Al_2O_3/Al composites

Excitingly, a very well arranged layered structure was successfully built throughout the composite (Fig. 4-3a). Nanoasperities were observed on the aluminum flake surfaces and metallic bridges (indicated by the blue arrow in Fig. 4-3a) were found to connect layers together. Therefore, nacre's three identifying features (laminated structure, nanoasperities, and mineral bridges) were effectively emulated in the composite. Yu *et al.* [14] achieved a high resemblance to nacre in their $CaCO_3$/PAA composite, however, the biological features that are essential for high strength and toughness have never been realized in metal/ceramic composites. Interestingly, no other reference samples exhibited similar morphological features. The fracture surface of pure Al exhibited pyramid morphology, a typical fracture surface of ductile metals (Fig. 4-3b). The fracture surface of Al powder metallurgy sample (with PVA but without GO) showed small dimples, indicating that PVA induced impurities (Fig. 4-3c). The graphene/Al mix sample, which indicates graphene oxide directly mixed with Al powders without PVA treatment and freeze drying, had larger dimples and agglomerated particles (Fig. 4-3d). The graphene/Al composite, which was fabricated by shear mixing graphite powders with aluminum flakes [36], processed a laminated structure which was similar to Li's work (Fig. 4-3e) [33]. However, a key difference of this sample from the graphene/Al_2O_3/Al composite in Fig. 4-3a was the absence of nanoasperities. Thusly, the GO addition, PVA surface treatment, and ice-templating process are essential for successfully reproducing nacre-like lamellar structure.

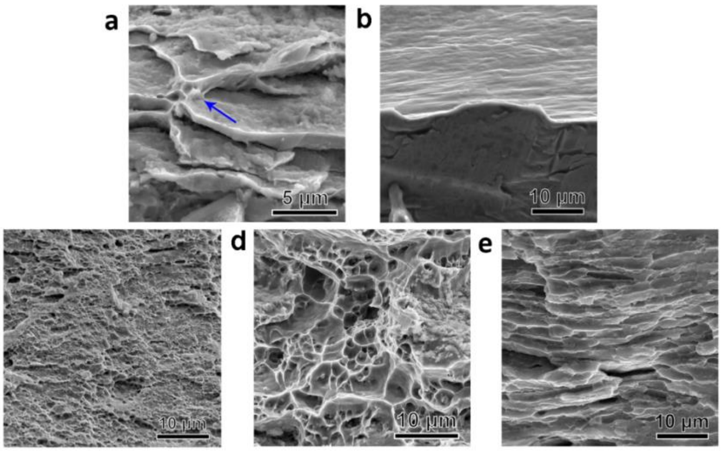

Fig. 4-3 Fracture surfaces of graphene/Al_2O_3/Al composite and reference samples. a. Graphene/Al_2O_3/Al composite. b. Pure Al. c. Al powder metallurgy. d. Al/graphene mix. e. Graphene/Al composite.

We then proceeded to answer the question: what were the nanoasperities/nanoparticles in the graphene/Al_2O_3/Al composite? Energy-dispersive X-ray spectroscopy (EDS) element maps of the polished graphene/Al_2O_3/Al composite cross section exhibited oxygen and aluminum alternating layers (Fig. 4-4a-c). The dark field transmission electron microscopy (TEM) cross-sectional image revealed that nanoparticle bands embedded between two aluminum layers (Fig. 4-4d). The close-up inspection on the interface area (Fig. 4-4e) validated that the nanoasperities were in fact numerous nanoscale particles with quasi-rectangular shape. Selected area electron diffraction (SAED) pattern of the nanoscale asperities uncovered that these particles were actually Al_2O_3 (Fig. 4-4f). The average thickness of aluminum layers and Al_2O_3 nanoparticle bands, calculated from scanning electron microscopy (SEM) and dark field TEM, were 1.05 μm and ~200 nm, respectively. Compared with the spontaneously formed amorphous Al_2O_3 in ref. [33], this Al_2O_3 nanoparticle band was much thicker and had well-defined crystalline structure. SEM images of the peeled graphene/Al_2O_3/Al composite surface showed rod-like Al_2O_3 nanoparticles (Fig. 4-4g), and the EDS element maps suggested that the surface was covered by a carbon layer. Conversely, graphene/Al composites fabricated by shear mixing method did not show any nanoasperities on the peeled surface (Fig. 4-4h).

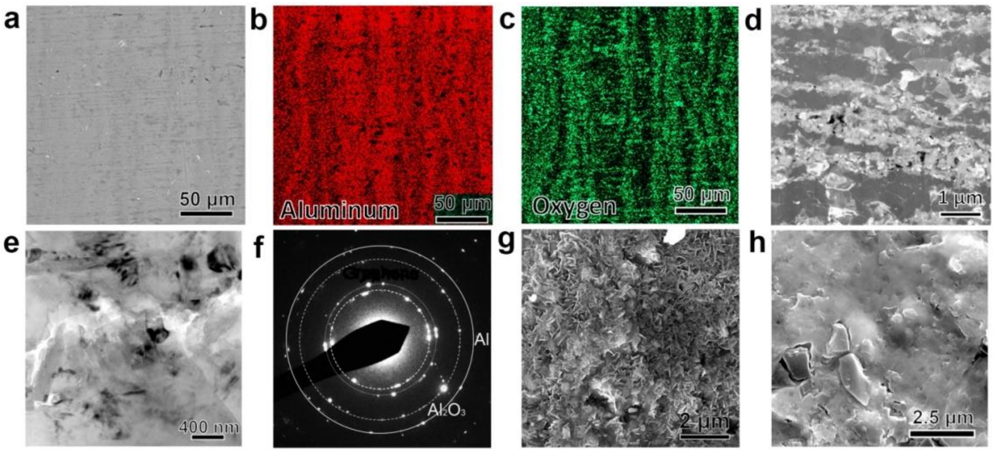

Fig. 4-4 Microstructure of graphene/Al_2O_3/Al composite. a. Backscattered electron image. b. Corresponding EDS aluminum map. c. EDS oxygen map. d. TEM dark field cross-sectional image of the graphene/Al_2O_3/Al composite sample, showing aluminum layers and nanoparticle bands. e. Close-up inspection on the interface area, showing nanoparticles with quasi-rectangular shape. f. The corresponding SAED pattern of (e). g. SEM image of a peeled graphene/Al_2O_3/Al composite

sample, showing rod-like nanoparticles. h. SEM image of a peeled graphene/Al composite by shear mixing, showing no nanoasperities on the surface.

An instant question arises: where was the graphene in the composite? To address this question, atomic resolution EDS scanning and high resolution TEM (HRTEM) inspection were performed. Low magnification scanning TEM (STEM) image and the corresponding EDS element map (Fig. 4-5a and b) demonstrated similar results to the SEM image and EDS maps in Fig. 4-4b and Fig. 4-4c: only lamellar interfaces were found to be rich in oxygen. A close-up observation of the interface area and atomic resolution EDS maps of aluminum, oxygen, carbon, and a combined element map are respectively shown in Fig. 4-5c-g. A carbon film with a thickness ranging from 5 to 13 nm was clearly embedded in the Al_2O_3 band, separating the aluminum lamellae and forming an Al/Al_2O_3/graphene sandwiched structure. The thickness of monolayer graphene was measured to be 0.38 nm, therefore this carbon film is equivalent to approximately 13 to 34 layers of 2D graphene. The HRTEM images (Fig. 4-5c) reliably validated that the carbon layer was multilayered graphene. Unlike the aluminum and Al_2O_3 crystals, which processed a nearly perfect lattice structure, the multilayered graphene displaced a discontinuous and tortuous pattern, indicative of the degradation of graphene. The HRTEM image and FFT pattern, coupled with SEAD pattern in Fig. 4-4a**,** also confirmed that the Al_2O_3 particles were α-Al_2O_3, which has a corundum structure and thermodynamically tends to grow along the close packed <0001> direction, leading to the rod-like morphology displayed in Fig. 4-4g. Unlike aluminum and oxygen that overlapped on a large scale (Fig. 4-5d and e), carbon was concentrated along the laminar interface, indicating that only a handful of Al/C components formed in this composite (differing from the findings of others [23,26]).

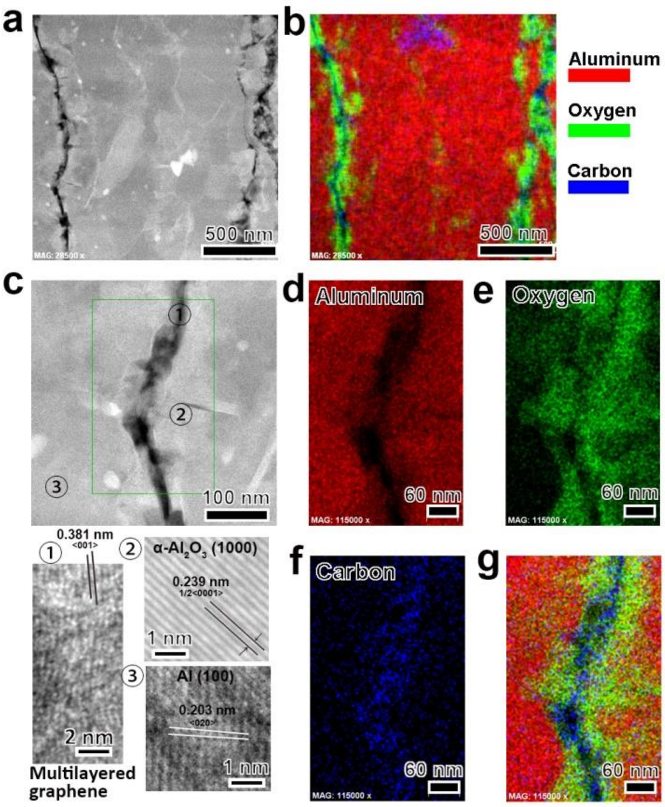

Fig. 4-5 STEM and atomic resolution EDS element maps of the graphene/Al_2O_3/Al composite. a. STEM image of graphene/Al_2O_3/Al composite. b. Corresponding EDS map of (a), indicating that the interfaces were rich in oxygen and carbon. c. Close-up STEM inspection of the interface with three HRTEM images, suggesting that multilayered graphene embedded in α-Al_2O_3 at the interface and beyond the interface was aluminum. d. EDS map of aluminum. e. EDS map of oxygen. f. EDS map of carbon. g. EDS overlapped map, showing that a layer of carbon separated the aluminum and Al_2O_3 nanoparticle layers.

As a laminated composite, the interfaces between layers are of special importance because weak interfacial connection may trigger interfacial delamination. Fig. 4-6 is the HRTEM images of graphene/Al_2O_3 and Al_2O_3/Al interfaces. A 2-3 nm thick amorphous interlayer was found to bond the graphene and the Al_2O_3 together (Fig. 4-6a). EDS mapping (Fig. 4-5d-g**)** unveiled that the amorphous layer contains Al, O, and C. A previous study [33] showed that an amorphous Al_2O_3 layer spontaneously forms on the Al surface. Moreover, since C was also found in the EDS map, we postulate that C atoms diffused into the amorphous layer during high-temperature annealing. No voids and defects were found at the graphene/Al_2O_3 interface, suggesting that a transition zone did link up the graphene and Al_2O_3, which can redistribute load, reducing interfacial delamination tendency. In contrast, a boundary layer was found between the Al_2O_3 and Al (Fig. 4-6b). Therefore, intimate interfacial layers did exist at both the graphene/Al_2O_3 and the Al_2O_3/Al interfaces.

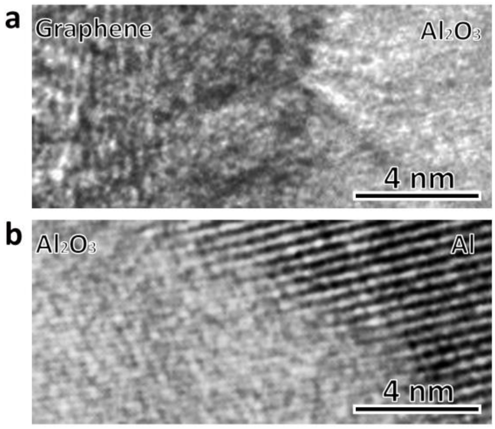

Fig. 4-6 HRTEM images of graphene/Al_2O_3 interface and Al_2O_3/Al interface. a. Graphene/Al_2O_3 interface. b. Al_2O_3/Al interface.

4.3.3 Mechanical properties of the graphene/Al_2O_3/Al composite and reference samples

The nacre-like graphene/Al_2O_3/Al composite exhibited superiority in mechanical properties compared to all other samples tested (Fig. 4-7). Tensile test samples were machined into a dog-bone shape according to the ASTM standard. Compared with the other three control samples, the tensile strength, yield strength, and Young's modulus of the graphene/Al_2O_3/Al composite sample were superior (Fig. 4-7a). Although the composite was not as ductile as pure aluminum, the tensile curve still exhibited a notable plastic deformation stage. To accurately identify the elastic modulus of the specimens, digital image correlation (DIC) analysis was used. It is a widely accepted practice in the experimental mechanics society that DIC analysis which focused on the initial, early stage of deformation is an effective method to identify the modulus. As shown in Fig. 4-7b, the elastic modulus derived from the DIC analysis was about 117 GPa. High-load indentation was then used to validate the elastic modulus. Indentations with the depth of about 3 μm were made (Fig. 4-7c), which can give us global modulus of the composite. The average elastic modulus calculated from the indentation unload curves was 118.5 GPa, consistent with the DIC results.

Quantitatively, for the five specimens showed in Fig. 4-7a, the graphene/Al_2O_3/Al composite exhibited 210% improvement in hardness, 223% increase in ultimate strength, 67% enhancement in Young's modulus, and 30% raise in toughness (area under the tensile test curve) compared with pure aluminum (Fig. 4-7d) (detailed numbers are listed in Table 4-2). A moderate increase in elastic modulus and strength of the graphene/Al mix sample (without PVA treatment and freeze dry) and Al semi powder metallurgy sample (without GO additive) was arisen from impurities and defects, which, in turn, also made these samples less ductile. Since pores and defects were also found in the graphene/Al_2O_3/Al composites, the laminated design is considered to be less defect-sensitive. The improvement of mechanical properties of the graphene/Al_2O_3/Al composite exceeds all other previous works [23–32]. The ultimate tensile strength is also comparable to that of AA6061-T6 alloy. For the nine tensile samples taken from three separately prepared batches of the graphene/Al_2O_3/Al composites, the ultimate strength ranged from 303 MPa to 332 MPa with a mean value of 313 MPa, with the final strain at fracture ranging from 2.4 % to 3.3 % with an average value of 2.8 %. Values of ultimate strength and strain are not linearly related; samples that have higher ultimate strengths may also be more ductile.

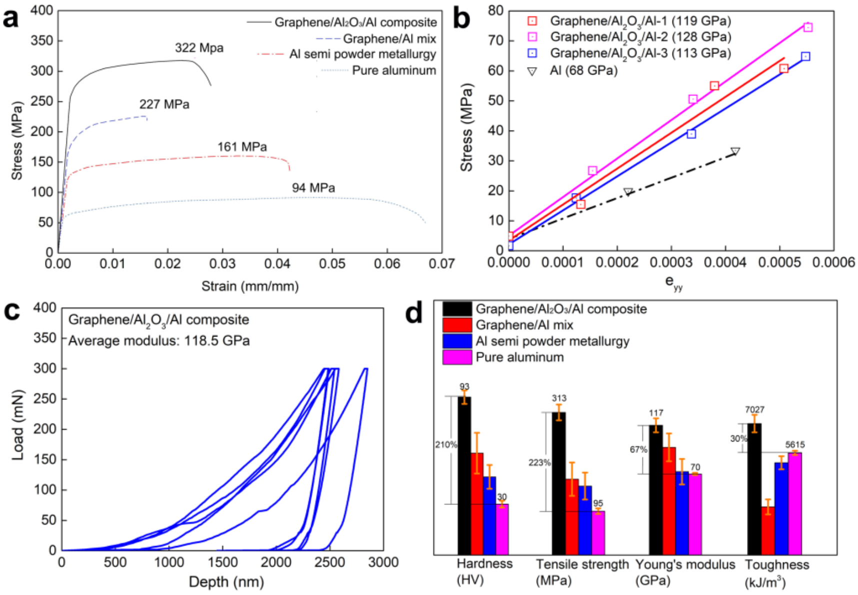

Fig. 4-7 Mechanical properties of graphene/Al_2O_3/Al composite and reference samples. a. Comparative tensile test curves. b. DIC analysis of the elastic deformation. c. High-load indentation on the cross-section of graphene/Al_2O_3/Al composite. d. Comparative bar chart of hardness, tensile strength, Young's modulus, and fracture toughness.

Table 4-2 Mechanical properties of graphene/Al_2O_3/Al composite and other three reference samples in Fig. 4-7d

Sample	Strength (MPa)	Hardness (HV)	Young's Modulus (GPa)	Toughness (kJ/m^3)
Graphene/Al_2O_3/Al composite	312.72	93	117.12	7027
Pure aluminum	94.75	30	69.87	5615
Al semi powder metallurgy	148.93	46	72.66	5075
Graphene/Al mix	163.76	60	93.53	3646

To probe the microscopic mechanical response of the graphene/Al_2O_3/Al composite, a series of loading-unloading nanoindentation tests with a load increment of 0.1 mN each loading cycle were carried out on the composite. Intriguingly, as the indenter was pushed down into the composite, the corresponding reduced modulus exhibited an orderly wave-like pattern (Fig. 4-8a), oscillating between a peak value of 93 GPa and a valley value of 73 GPa. Each indentation loading cycle corresponded to an approximately 800 nm indentation depth. The aluminum layer thickness was 1.05 μm. Thus it is highly likely that the indenter tip encountered one aluminum layer in one cycle and penetrated through the Al_2O_3/graphene/Al_2O_3 layer in the subsequent cycle, leading to an ordered oscillation of reduced modulus (Fig. 4-8b). The result further validated the hard-soft-hard laminated architecture in our composite. In contrast, pure aluminum sample exhibited a relatively constant modulus value ranging from 65 GPa to 70 GPa as a function of indentation depth (Fig. 4-8c). The Al/graphene mix sample, on the other hand, displayed a strong fluctuation of reduced modulus (Fig. 4-8d). At some locations, the sample showed a high modulus of over 90 GPa, indicative of inhomogeneous dispersion of Al_2O_3 clusters.

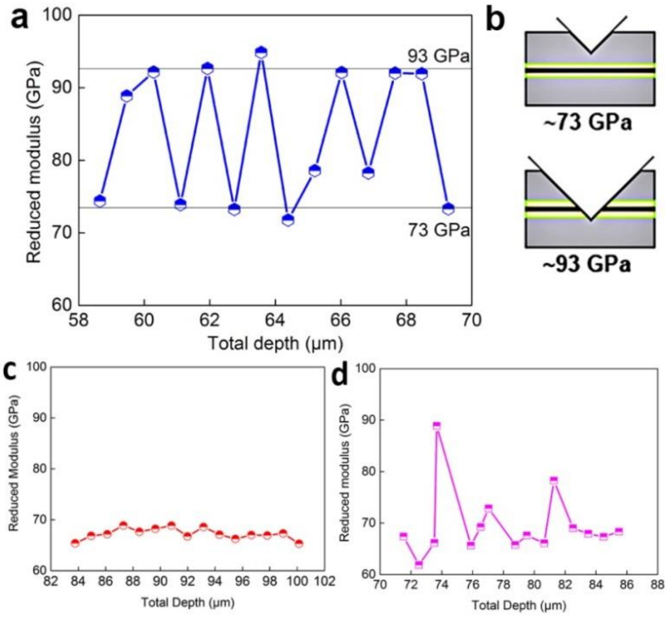

Fig. 4-8 Nanoindentation tests on graphene/Al_2O_3/Al composite, pure aluminum and Al/graphene mix samples. a. Graphene/Al_2O_3/Al composite. b. Schematic illustration explaining the modulus oscillation. c. Pure aluminum. d. Al/graphene mix.

The graphene/Al_2O_3/Al composite also exhibited a superior stability at high temperature compared with pure aluminum. A piece of graphene/Al_2O_3/Al composite and a piece of pure aluminum with the same dimensions were heated to 750 ℃ for 1 h (much higher than the melting point of aluminum, 660 ℃). The graphene/Al_2O_3/Al composite sheet remained the same as it was in terms of shape and size, whereas the pure aluminum piece was melted into an irregularly shaped bar (Fig. 4-9a). Further experiments showed that graphene/Al_2O_3/Al composites could maintain their size and shape up to temperatures on the order of 900 ℃. We hypothesize that this is due to the encapsulation of the aluminum flakes by Al_2O_3/graphene shells, which have much higher melting point than pure aluminum. During high temperature annealing these shells surrounded the aluminum core allowing the material to retain its shape and size even when the aluminum core melted. After the 750 ℃ heat treatment the graphene/Al_2O_3/Al composite remained in a lamellar structure, but the nanoscale asperities became thicker, coarser and less uniform (Fig. 4-9b) because GO release more oxygen-containing gases at higher temperature.

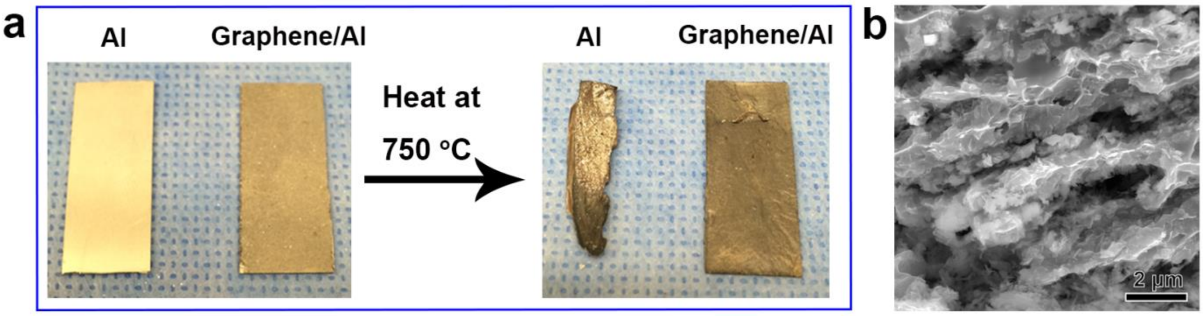

Fig. 4-9 Graphene/Al_2O_3/Al composite after high temperature heating. a. A piece of graphene/Al_2O_3/Al composite was able to maintain the shape after heating at 750 °C, while a piece of pure aluminum could not. b. After high temperature treatment, the laminated structure was preserved in graphene/Al_2O_3/Al composite and nanoasperities became thicker.

4.4 Stiffening, strengthening, and toughening mechanisms of graphene/Al_2O_3/Al composites

4.4.1 Volume fraction of Al_2O_3 nanoparticles

To study the stiffening and strengthening mechanisms of the graphene/Al_2O_3/Al composite, it is critical to determine the volume fraction of Al_2O_3 particles. Here, three methods were employed to determine the volume fraction. XRD quantitative analysis was first used. Fig. 4-10 is the XRD spectrum of the graphene/Al_2O_3/Al composite after mechanical and ion polishing, showing peaks of graphite, Al, and Al_2O_3. The general scattering cross section for Bragg scattering is proportional to N/V, where N is the number of cells contributing to the scattering and V is the unit cell volume. The scale factor S, which can be calculated by the Rietveld method [49], is then proportional to N/V. The volume fraction of one phase can then be calculated by the equation below:

$$v = \frac{(SV^2)_p}{\Sigma(SV^2)} \qquad (1)$$

According to the XRD spectrum in Fig. 4-10, the scale factor of Al was determined to be1 and that of Al_2O_3 was 0.015; the unit cell volume of Al is 66.42 Å^3 and that of Al_2O_3 is 255.49 Å^3. The volume fraction of Al_2O_3 was then calculated to be 18.3 %.

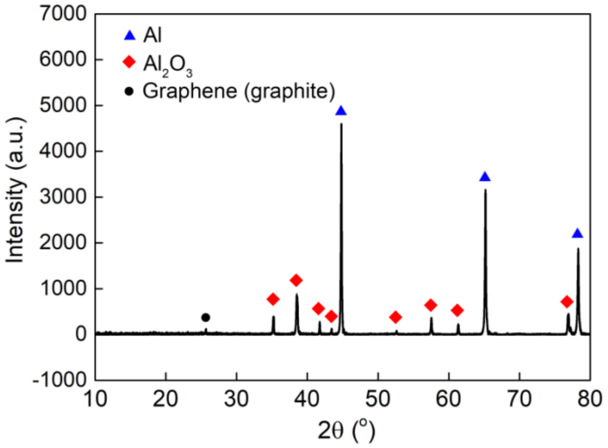

Fig. 4-10 XRD spectrum of graphene/Al_2O_3/Al composite after ion polishing.

In addition to the volume fraction, how the Al_2O_3 particles distribute has an eminent influence on the strengthening effect. TEM dark-field imaging with convergent beam diffraction (CBD) was used to simultaneously unveil the volume fraction and particle distribution. Fig. 4-11a is the [023] CBD pattern of an Al grain at location 1 in Fig. 4-11b. By analyzing the brightness distribution of the lines inside the pattern spots via HyperSpy, the thickness of location 1 was obtained, which to be 158 nm. The thickness of location 2 was 223 nm. If we assume that the Al_2O_3 particles were distributed vertically, the volume fraction of Al_2O_3 particles was calculated to be 31.4 % based on the areal fraction and the volume of the wedge from location 1 to location 2, much larger than that calculated from the XRD spectrum. The main reason for such deviation is that the TEM image is, in fact, a projection of a 3D volume on a 2D plane. As shown in Fig. 4-11c, the Al_2O_3 particles may be dispersive and not aligned vertically, giving the wrong areal fraction after projection. Therefore, this method could not give us an accurate volume fraction and distribution of Al_2O_3 particles.

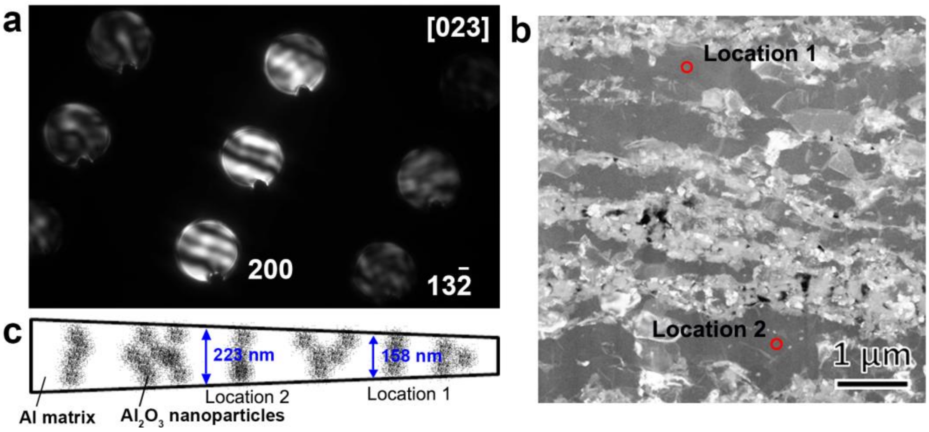

Fig. 4-11 Determine the volume fraction and distribution of Al_2O_3 nanoparticles by convergent beam diffraction and TEM dark field image. a. Convergent beam diffraction at [023] direction. b. Corresponding dark field image (red cycles indicate the locations for CBD). c. Schematic diagram of the TEM sample.

Focus ion beam (FIB) was then employed to unveil the volume fraction and particle distribution. As shown in Fig. 4-12 a and b, a piece of graphene/Al_2O_3/Al composite with a thickness of 4.5 μm was cut into 30 slices, corresponding to 150 nm per slice. Al_2O_3 nanoparticles with rod-like morphology were clearly seen on the ion beam-polished surface by the ion conversion and electron (ICE) detector (Fig. 4-12c). The morphology was similar to that of Fig. 4-4c. The ICE image was further processed, turning Al_2O_3 particles into white while the Al matrix into black (Fig. 4-12d). The bi-phase images were stacked together, forming a 3D Al_2O_3 particle distribution map (Fig. 4-12e). When rotating the 3D map to a certain degree, we can clearly find the layer-by-layer distribution of Al_2O_3 particles (Fig. 4-12f and g). The volume fraction of Al_2O_3 particles calculated from 3D reconstruction map was 24.8 % while that calculated from the average areal fraction of 30 slices was 16.1 %. Such difference mainly came from the image processing, in which assumed the thickness of Al_2O_3 particles was 150 nm. Therefore, the most accurate volume fraction should be the one calculated from the XRD spectrum while the FIB slices revealed the distribution of Al_2O_3 particles.

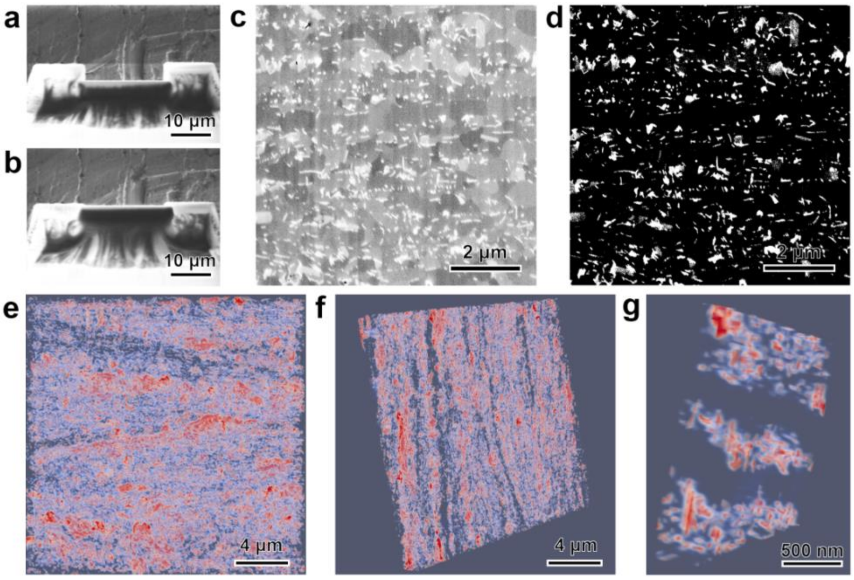

Fig. 4-12 Determine the volume fraction and distribution of Al_2O_3 nanoparticles by FIB and 3D image reconstruction. a. Graphene/Al_2O_3/Al composite before FIB cutting. b. Graphene/Al_2O_3/Al composite after FIB cutting. c. ICE image. d. ICE image after processing, highlighting Al_2O_3 nanoparticles. e. 3D reconstruction Al_2O_3 nanoparticles. f. 3D reconstruction image after tilting, showing laminated morphology. g. Close-up inspection of one area.

4.4.2 Stiffening and strengthening mechanisms

As shown in Fig. 4-7 and Table 4-2, the graphene/Al_2O_3/Al composite has a notable improvement in elastic modulus comparing with pure Al. From the TEM and XRD analyze, the residual graphene inside the Al matrix was sparse and defective. Therefore, we can assume that the enhancement of modulus solely came from Al_2O_3 particles. The upper limit of the enhanced elastic modulus can be calculated by the rule of mixtures below

$$E_{max} = E_1 \nu_1 + E_2 \nu_2 \qquad (2)$$

where E_1 is the modulus of pure Al, ν_1 is the volume fraction of Al matrix, E_2 is the modulus of Al_2O_3, which is assumed to be 400 GPa, and ν_2 is the volume fraction of Al_2O_3 particles, which was calculated to be 18.3 % from the XRD spectrum. Thusly, the upper limit of the elastic modulus was calculated to be 130.39 GPa.

If the Al_2O_3 particles were not aligned along the tensile direction, the enhancement of elastic modulus would largely decrease. The lower limit of the enhancement can be calculated by the equation below:

$$E_{min} = \left\{\frac{v_1}{E_1} + \frac{v_1}{E_2}\right\}^{-1} \quad (3)$$

the lower limit of elastic modulus was calculated to be 82.4 GPa. Therefore, the arithmetic mean value of the upper limit and the lower limit was 106.4 GPa. The experimental values from tensile tests along the rolling direction were 117 GPa (Fig. 4-7a), which were higher than the arithmetic mean value; on the other hand, the modulus revealed by nanoindentation perpendicular to the rolling direction was about 93 GP, lower than the arithmetic mean value and close to the lower limit (Fig. 4-8a). The possible reason is that based on the SEM and TEM observation (Fig. 4-4 and Fig.4-5), the Al_2O_3 particles were almost continuously aligned along the tensile direction. Therefore, the experimental values from tensile tests were closer to the upper limit of elastic modulus.

The superior mechanical performance of our graphene/Al_2O_3/Al composite stems from a synergic contribution of multiple features. Here, the graphene/Al_2O_3/Al composite exhibited higher yield strength than the Al powder metallurgy sample. Considering the defects and low concertation of rGO, the difference in the strength should mainly originate from Al_2O_3 nanoparticles. Bulk Al_2O_3 possesses an elastic modulus of 400 GPa and a strength of 3 GPa [38]. Such high strength makes dislocations difficult to cut through, enabling the Orowan mechanism [39] the most likely strengthening mechanism. When dislocations pass hard particles, the particles would pin the dislocations, leading to higher yield strength. The improved yield strength σ_{ys} can be calculated by the following two equations.

$$\tau_y = \frac{Gb}{l} \quad (4)$$

$$\sigma_{ys} = M\tau_y \quad (5)$$

where τ_y is the shear stress required to move dislocations, G is the shear modulus (25.5 GPa), b is Burger's vector (0.286 nm), l is the distance between two second phase particles, and M is Taylor's factor (3.06). Therefore, it is critical to determine the distance between Al_2O_3 nanoparticles. According to Fig. 4-12d, the distribution of Al_2O_3 nanoparticles was not homogeneous; they were closer along the rolling direction. To improve accuracy, 10 particles were picked in Fig. 4-12d and the distance of these particles to five of their adjacent particles were measured. The average value was calculated to be 224 nm. The enhancement due to Al_2O_3 nanoparticles was then calculated to be 101.45 MPa.

As harder second phase particles dispersed in the Al matrix, the Al_2O_3 nanoparticles should act as load bearers. However, we cannot apply the model of fiber-reinforced composites because of the small size. Therefore, a short-fiber model is used, in which the geometry of the second phase particles was considered. The yield strength of the composite can be calculated by the equation below.

$$\sigma_c = \sigma_f V_f \left(\frac{l}{2l_c}\right) + \sigma_m Vm \qquad (6)$$

where σ_f is the strength of second phase particles, V_f is the volume fraction of the second phase particles, l is the length of the particles, l_c is the critical length of the second phase particles, σ_m is the yield strength of the matrix, V_m is the volume fraction of matrix. When $l > l_c$, the second phase particles should break; when $l < l_c$, the failure should occur at the interface between the matrix and the second phase particle. Therefore, it is important to calculate the critical length.

When a composite is loaded, the matrix is deformed and the strain of the matrix transfers the load to reinforcement by means of shear stresses on the reinforcement–matrix interface. The shear forces on the interface parallel to the load direction are balanced with the normal forces on the fiber cross-sections normal to the load direction. If we assume the Al_2O_3 particles are bars with length (l) of 400 nm and diameter (d_f) of 100 nm, the load balance can be expressed by the equation below.

$$\tau_m(\pi d_f)dx = \left(\frac{\pi d_f^2}{4}\right) d\sigma_x \qquad (7)$$

where τ_m is the shear stress of the matrix and σ_x is the normal stress on the second phase particle. When the normal stress equals the strength of the second phase particles, the length of the particle should be the critical length. Therefore, the critical length (l_c) can be calculated by the equation below.

$$l_c = \frac{d_f \sigma_f}{4\tau_m} \qquad (8)$$

where σ_f is the tensile stress of the second phase particle. If we substitute this equation into the short fiber model, the yield strength of the composite can be calculated by the equation below.

$$\sigma_c = \tau_m V_f \left(\frac{2l}{d_f}\right) + \sigma_m Vm \qquad (9)$$

The yield strength improvement due to load transfer was calculated to be 102.48 MPa.

Another strengthening mechanism may be grain refining. The grain boundaries acted as pinning points to impede dislocation propagation. The relationship between grain size and strength can be demonstrated by Hall-Patch equation [40,41]:

$$\sigma_y = \sigma_0 + \frac{k_y}{\sqrt{d}} \qquad (10)$$

where σ_y is the yield strength, $\sigma_0$is a materials constant for the starting stress for dislocation movement, k_y is the strengthening coefficient, which is 200 MPa $\mu m^{1/2}$ [42], and d is the grain size. Therefore, the change of the yield strength due to the reduction of grain size should be:

$$\Delta\sigma_{gb} = \frac{k_y}{\sqrt{d_1}} - \frac{k_y}{\sqrt{d_2}} \qquad (11)$$

Fig. 4-13a is the close-up inspection of the graphene/Al_2O_3/Al composite under ICE detector, showing an average grain size of 291.92 nm (Fig. 4-13a). In contrast, the grain size of Al powder metallurgy sample (no GO) was larger, about 385.75 nm (Fig. 4-13b). Therefore, the strength enhancement from grain size refining was estimated to be 47.8 MPa. The Al_2O_3 nanoparticles were mostly distributed along grain boundaries, which may prohibit the migration of grain boundaries, leading to smaller grains. If we assume the strain hardening magnitudes of the graphene/Al_2O_3/Al composite and the Al powder metallurgy sample were the same, the yield strength enhancement due to Orowan mechanism and grain refining should be 149.25 MPa, close to the real improvement of 142 MPa. If we consider the load transfer and grain refining were the main strengthening mechanisms, the yield stress improvement of the composite was calculated to be 115.91 MPa, lower than the experimental result. In the real composites, some Al_2O_3 particles located within grains, pinning the dislocations and strengthening the composite via Orowan mechanism while some of the particles located on the grain boundaries, which enhanced the composite mainly due to load transfer. The final yield strength of the composites should be a confluent result of load transfer, Orowan mechanism, and grain refining.

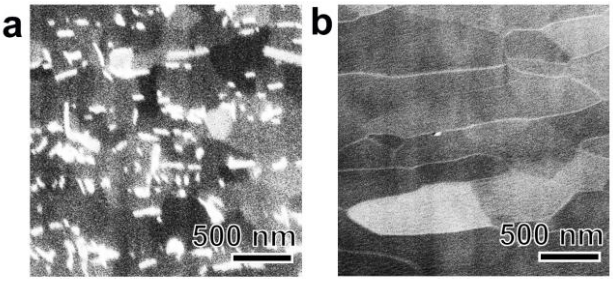

Fig. 4-13 Grain structures of graphene/Al_2O_3/Al composite and Al powder metallurgy sample. a. graphene/Al_2O_3/Al composite. b. Al powder metallurgy sample.

4.4.3 Toughening Mechanisms

We also cannot ignore the toughening mechanisms stemming from the laminated design. Ritchie and his co-workers [1,2] have worked extensively on the toughening mechanisms of layered biological structures and concluded that, unlike monolithic materials such as aluminum alloys, toughness in these materials often derived from extrinsic mechanisms (behind the crack tip, > 1μm) including crack deflection, bridging, crack tip blunting, and secondary cracks. Developed bio-inspired materials also showed similar toughening mechanisms [10,43,44]. To explore the fracture process of our graphene/Al_2O_3/Al composite, an *in situ* three-point bending test on the graphene/Al_2O_3/Al composite sample was carried out under SEM to observe the crack evolution (Fig. 4-14a). The crack propagation of the graphene/Al_2O_3/Al composite exhibited a confluence of multiple toughening mechanisms (Fig. 4-14b).

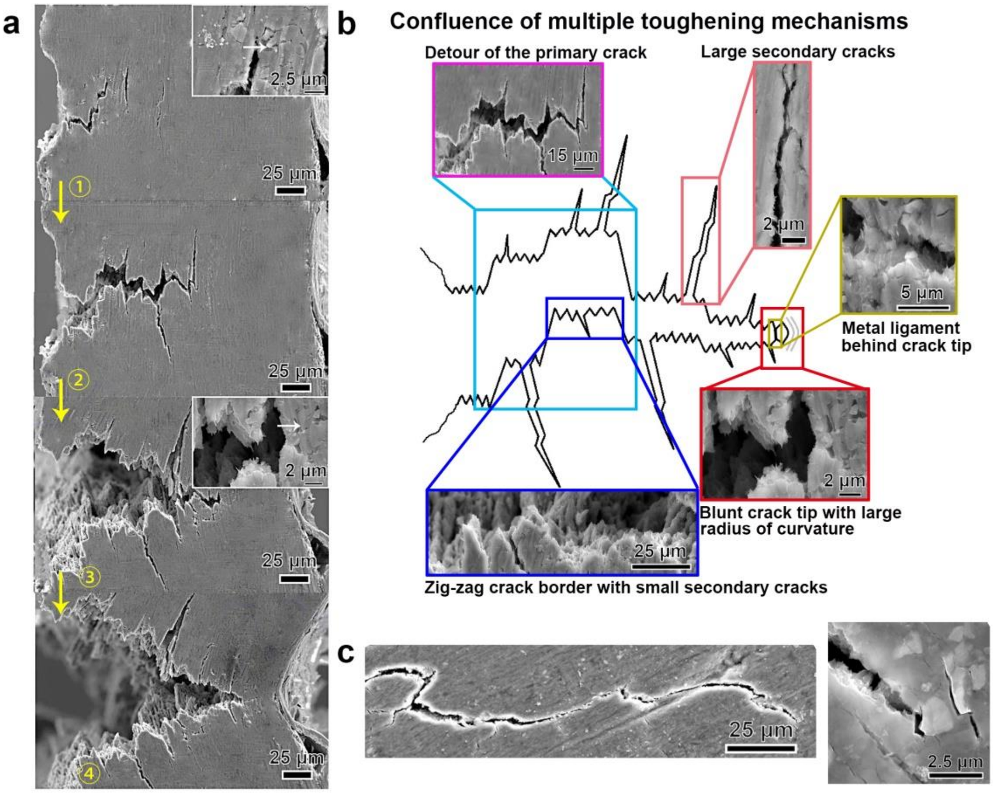

Fig. 4-14 *In-situ* three-point bending test on the graphene/Al_2O_3/Al composite inside SEM. a. SEM images of the crack under various degrees of sample deflection. (Yellow arrows indicate the progression of bending and white arrows indicate the primary crack propagation direction). b. The crack propagation of graphene/Al_2O_3/Al composite sample exhibited a confluence of multiple toughening mechanisms. The primary crack was detoured into a serpentine morphology. Along with the primary crack, several large secondary cracks were stimulated and propagated parallel to the lamellae. The tip of the primary crack was blunt with large radius of curvature. The border of the primary crack displayed zig-zag shape with several small secondary cracks. Metal bridges formed behind the crack tip. c. The crack propagation of a graphene/Al mix sample (without PVA surface treatment and freeze-dry casting).

The primary crack was detoured into a serpentine morphology instead of a straight fracture. Along with the primary crack, several large secondary cracks were stimulated and propagated parallel to the plate (perpendicular to the propagation of primary crack). Moreover, the edge of the primary crack displayed a zig-zag path with small secondary cracks. All of these mechanisms inherently elongated the crack length, leading to more energy required to propagate the crack, W_s [45]:

$$W_s = 2ab\gamma \qquad (12)$$

where a is the crack length, b is the out-of-plane thickness of the solid material, and γ is the sum of surface energy (γ_s) and energy related to plastic deformation (γ_p). The crack length in Fig. 4-13a② was measured carefully by pixels. The span between the crack tip and plate surface was measured to be 164.11 μm, but the total crack length was summed up to 512.89 μm. For comparison, an identical experiment was performed on a graphene/Al mix sample as in Fig. 4-14c (without PVA surface treatment and freeze dry) with the same size and shape. Fig. 4-14c shows the crack morphology of the graphene/Al mix sample with the same bending deflection as Fig. 4-13a①. Clearly, the crack propagated straight from one side of the plate to the other side without deflections. The span from the plate surface to the tip of the crack in this sample was 160.61 μm and the total length of the crack was 227.15 μm. Since both of the two samples comprised of aluminum and defective graphene, we postulate that the values of energy γ were almost the same. Substituting all the numbers into equation (1), the work required to propagate a crack for the laminated graphene/Al_2O_3/Al composite sample is 2.21 times higher than that of the graphene/Al mix sample. This result is consistent with the fracture toughness calculated from tensile test curves (Fig. 4-7a).

Apart from the deviation and elongation of the crack, Cook-Gordon toughening mechanism also takes effects in the composite [46]. When a composite processes soft layers (aluminum) embedded within hard layers (Al_2O_3/graphene/Al_2O_3), as the crack reaches a weak interface, the stress on the crack can easily break the interface, forming a perpendicular crack ahead of the crack tip. When these cracks merge, the crack tip radius of curvature will significantly increase, expelling stress concentration on the interfaces. Comparing the images of the crack tips for the two samples, the crack tip of the graphene/Al_2O_3/Al composite sample had a much larger radius of curvature (ρ) (1.47 μm) than that of graphene/Al mix sample (0.20 μm). This is because in the graphene/Al_2O_3/Al composite sample the aluminum layers are perpendicular to the crack propagation direction; hence the crack has to "breakdown" the aluminum layers. However, for the graphene/Al mix sample, the crack can easily propagate through defects, which originated from the non-homogeneously dispersed graphene and

Al_2O_3 particles. The radius of curvature is inversely related with the stress concentration on the crack tip [47]:

$$\sigma_{tip} = \sigma_a(1 + 2\sqrt{\frac{a}{\rho}}) \qquad (13)$$

Here, a is the pre-existing crack or void length. Thus, obviously, the stress concentration on the crack tip of the graphene/Al_2O_3/Al composite sample is much lower than that of the graphene/Al mix sample, which also explains why the crack in the graphene/Al mix sample propagated more quickly under the same degree of deformation.

Two other toughening mechanisms are the nanoasperities and the metal bridges. Delamination because of weak connections between different layers may cause quick fracturing in laminated materials. Close observation of the fracture surface of the graphene/Al_2O_3/Al composite sample showed rare evidence of “pulling out” between layers because the roughness provided by the nanoasperities interlocked the lamellae, preventing large-scale delamination. Additionally, metal bridges behind the crack tip impeded the opening of the crack, further preventing/delaying catastrophic fracture.

According to previous studies [38,48], the fracture toughness density of Al_2O_3 is about 255 kJ/m^3 and defective graphene is 223 kJ/m^3 (maximum). A simple superposition of these values with the fracture toughness of pure aluminum in Fig. 4-7 is 6133 kJ/m^3, which is 18 % lower than the fracture toughness of the graphene/Al_2O_3/Al composite. Thusly, via the cooperation of multiple phases and the unique features of the laminated structure, the laminated graphene/Al_2O_3/Al composite successfully reproduced the nature’s accomplishment in nacre, i.e. the toughness value exceeds its individual constituents and their simple mixture.

4.5 Conclusions

Summarily, a rational design strategy for nacre-like laminated graphene/Al_2O_3/Al composites was proposed in this contribution. During high-temperature sintering, oxygen on GO sheets reacted with Al, forming Al_2O_3 nanoparticles along with the interfaces. The

Al_2O_3 nanoparticles strengthened the composite by pining dislocations and refining grains. The nacre-like laminated structure toughened the composite via elongating crack length and blunt crack tip. Moreover, the Al_2O_3 nanoasperities and metal Al bridges together prevented large-scale delamination of the layers, further delaying catastrophic fracture. Compared with pure aluminum, the obtained composite exhibited a 210% improvement in hardness, a 223% increase in ultimate strength, a 67% enhancement in Young's modulus, and a 30% rise in toughness. The toughness value exceeded its individual constituents and their simple mixture. This smart manufacturing strategy which the oxygen-containing functional groups on GO and the high strength of metal oxides can be grafted to other metallic materials such as Mg, Ti, Cu, and Zn. The design principles create new opportunities for developing bio-inspired materials to achieve superior mechanical performance for applications in an extensive range of fields.

References

[1] R.O. Ritchie, The conflicts between strength and toughness, Nat. Mater. 10 (2011) 817-822.

[2] U.G.K. Wegst, H. Bai, E. Saiz, A.P. Tomsia, R.O. Ritchie, Bioinspired structural materials, Nat. Mater. 14 (2014) 23-36.

[3] G. Zhang, X. Li, Uncovering aragonite nanoparticle self-assembly in nacre-A natural armor, Cryst. Growth Des. 12 (2012) 4306-4310.

[4] X. Li, W.C. Chang, Y.J. Chao, R. Wang, M. Chang, Nanoscale structural and mechanical characterization of a natural nanocomposite material: the shell of red abalone, Nano Lett. 4 (2004) 613-617.

[5] Z.H. Xu, X. Li, Deformation strengthening of biopolymer in nacre, Adv. Funct. Mater. 21 (2011) 3883-3888.

[6] F. Song, X.H. Zhang, Y.L. Bai, Microstructure and Characteristics in the Organic Matrix Layers of Nacre, J. Mater. Res. 17 (2002) 1567-1570.

[7] J. Sun, B. Bhushan, Hierarchical structure and mechanical properties of nacre: a review, RSC Adv. 2 (2012) 7617-7632.

[8] R.Z. Wang, Z. Suo, a. G. Evans, N. Yao, I. a. Aksay, Deformation mechanisms in nacre, J. Mater. Res. 16 (2001) 2485-2493.

[9] Z. Huang, Z. Pan, H. Li, Q. Wei, X. Li, Hidden energy dissipation mechanism in nacre, J. Mater. Res. 29 (2014) 1573-1578.

[10] E. Munch1, M.E. Launey, D.H. Alsem, E. Saiz1, A.P. Tomsia1, R.O. Ritchie1, Tough, bio-inspired hybrid materials, Science 322 (2008) 1516-1520.

[11] J. Wang, Q. Cheng, Z. Tang, Layered nanocomposites inspired by the structure and mechanical properties of nacre, Chem. Soc. Rev. 41 (2012) 1111.

[12] P. Podsiadlo, A.K. Kaushik, E.M. Arruda, A.M. Waas, B.S. Shim, J. Xu, H. Nandivada, B.G. Pumplin, J. Lahann, A. Ramamoorthy, N.A Kotov, Ultrastrong and stiff layered polymer nanocomposites, Science 318 (2007) 80-83.

[13] A. Sellinger, P.M. Weiss, A. Nguyen, Y. Lu, R.A. Assink, W. Gong, C.J. Brinker, Continuous self-assembly of organic-inorganic nanocomposite coatings that mimic nacre, Nature 394 (1998) 256-260.

[14] L.B. Mao, H.L. Gao, H.B. Yao, L. Liu, H. Colfen, G. Liu, S.M. Chen, S.K. Li, Y.X. Yan, Y.Y. Liu, S.H. Yu, Synthetic nacre by predesigned matrix-directed mineralization, Science 354 (2016) 107-110.

[15] B.F. Quigley, G.J. Abbaschian, R. Wunderlin, R. Mehrabian, A method for fabrication of aluminum-alumina composites, Metall. Trans. A 13 (1982) 93-100.

[16] M. Zabihi, M.R. Toroghinejad, A. Shafyei, Application of powder metallurgy and hot rolling processes for manufacturing aluminum/alumina composite strips, Mater. Sci. Eng. A 560 (2013) 567-574.

[17] K.J. Hodder, H. Izadi, A.G. McDonald, A.P. Gerlich, Fabrication of aluminum-alumina metal matrix composites via cold gas dynamic spraying at low pressure followed by friction stir processing, Mater. Sci. Eng. A 556 (2012) 114-121.

[18] P.W. Wang, S. Sui, W. Wang, W. Durrer, Aluminum nitride and alumina composite film fabricated by DC plasma processes, Thin Solid Films 295 (1997) 142-146.

[19] R. Jamaati, M.R. Toroghinejad, Manufacturing of high-strength aluminum/alumina composite by accumulative roll bonding, Mater. Sci. Eng. A 527 (2010) 4146-4151.

[20] K.S. Novoselov, D. Jiang, F. Schedin, T.J. Booth, V.V. Khotkevich, S.V Morozov,

A.K. Geim, Two-dimensional atomic crystals, Proc. Natl. Acad. Sci. U.S.A. 102 (2005) 10451-10453.

[21] C. Lee, X. Wei, J.W. Kysar, J. Hone, Measurement of the elastic properties and intrinsic strength of monolayer graphene, Science 321 (2008) 385-388.

[22] P. Zhang, L. Ma, F. Fan, Z. Zeng, C. Peng, P.E. Loya, Z. Liu, Y. Gong, J. Zhang, X. Zhang, P.M. Ajayan, T. Zhu, J. Lou, Fracture toughness of graphene, Nat. Commun. 5 (2014) 3782.

[23] S.F. Bartolucci, J. Paras, M. a. Rafiee, J. Rafiee, S. Lee, D. Kapoor, N. Koratkar, Graphene-aluminum nanocomposites, Mater. Sci. Eng. A 528 (2011) 7933-7937.

[24] M. Bastwros, G.Y. Kim, C. Zhu, K. Zhang, S. Wang, X. Tang, X. Wang, Effect of ball milling on graphene reinforced Al6061 composite fabricated by semi-solid sintering, Compos. Part B Eng. 60 (2014) 111-118.

[25] S.J. Yan, S.L. Dai, X.Y. Zhang, C. Yang, Q.H. Hong, J.Z. Chen, Z.M. Lin, Investigating aluminum alloy reinforced by graphene nanoflakes, Mater. Sci. Eng. A 612 (2014) 440-444.

[26] R. Pérez-bustamante, D. Bolaños-morales, J. Bonilla-martínez, I. Estrada-guel, Microstructural and hardness behavior of graphene-nanoplatelets/aluminum composites synthesized by mechanical alloying, J. Alloys Compd. 615 (2014) S578-S582.

[27] W.J. Kim, T.J. Lee, S.H. Han, Multi-layer graphene/copper composites: preparation using high-ratio differential speed rolling, microstructure and mechanical properties, Carbon 69 (2014) 55-65.

[28] J. Wang, Z. Li, G. Fan, H. Pan, D. Zhang, Reinforcement with graphene nanosheets in aluminum matrix composites, Scr. Mater. 66 (2012) 594-597.

[29] M. Rashad, F. Pan, A. Tang, M. Asif, Effect of Graphene nanoplatelets addition on mechanical properties of pure aluminum using a semi-powder method, Prog. Nat. Sci. Mater. Int. 24 (2014) 101-108.

[30] M. Rashad, F. Pan, M. Asif, A. Tang, Powder metallurgy of Mg-1%Al-1%Sn alloy reinforced with low content of graphene nanoplatelets (GNPs), J. Ind. Eng. Chem. 20 (2014) 4250-4255.

[31] Z. Li, G. Fan, Z. Tan, Q. Guo, D. Xiong, Y. Su, Z. Li, D. Zhang, Uniform dispersion of graphene oxide in aluminum powder by direct electrostatic adsorption for fabrication of graphene/aluminum composites, Nanotechnology 25 (2014) 325601.

[32] Z.Y. Zhao, R.G. Guan, X.H. Guan, Z.X. Feng, H. Chen, Y. Chen, Microstructures and properties of graphene-Cu/Al composite prepared by a novel process through clad forming and improving wettability with copper, Adv. Eng. Mater. 17 (2015) 663-668.

[33] Z. Li, Q. Guo, Z. Li, G. Fan, D.B. Xiong, Y. Su, J. Zhang, D. Zhang, Enhanced mechanical properties of graphene (reduced graphene oxide)/aluminum composites with a bioinspired nanolaminated structure, Nano Lett. 15 (2015) 8077-8083.

[34] W.S. Hummers, R.E. Offeman, Preparation of graphitic oxide, J. Am. Chem. Soc. 80 (1958) 1339.

[35] S. Stankovich, R.D. Piner, S.T. Nguyen, R.S. Ruoff, Synthesis and exfoliation of isocyanate-treated graphene oxide nanoplatelets, Carbon 44 (2006) 3342-3347.

[36] K.R. Paton, E. Varrla, C. Backes, R.J. Smith, U. Khan, A. O'Neill, C. Boland, M. Lotya, O.M. Istrate, P. King, T. Higgins, S. Barwich, P. May, P. Puczkarski, I. Ahmed, M. Moebius, H. Pettersson, E. Long, J. Coelho, S.E. O'Brien, E.K. McGuire, B.M. Sanchez, G.S. Duesberg, N. McEvoy, T.J. Pennycook, C. Downing, A. Crossley, V. Nicolosi, J.N. Coleman, Scalable production of large quantities of defect-free few-layer graphene by shear exfoliation in liquids, Nat. Mater. 13 (2014) 624-630.

[37] C. Peko, B. Groth, I. Nettleship, The effect of polyvinyl alcohol on the microstructure and permeability of freeze-cast alumina, J. Am. Ceram. Soc. 93 (2010) 115-120.

[38] P. Auerkari, Mechanical and physical properties of engineering alumina ceramics, Tech. Res. Cent. Finl. 1792 (1996) 26.

[39] M.C. Breslin, J. Ringnalda, L. Xu, M. Fuller, J. Seeger, G.S. Daehn, T. Otani, H.L. Fraser, Processing, microstructure, and properties of co-continuous alumina-aluminum composites, Mater. Sci. Eng. A 195 (1995) 113-119.

[40] E.O. Hall, the Deformation and ageing of mild steel: III discussion of results, Proc. Phys. Soc. London Sect. B 64 (1951) 747-753.

[41] R.W. Armstrong, Hall–petch description of nanopolycrystalline Cu, Ni and Al strength levels and strain rate sensitivities, Philos. Mag. 96 (2016) 3097-3108.

[42] C.Y. Yu, P.W. Kao, C.P. Chang, Transition of tensile deformation behaviors in ultrafine-grained aluminum, Acta Mater. 53 (2005) 4019-4028.

[43] F. Bouville, E. Maire, S. Meille, B. Van De Moortèle, A.J. Stevenson, S. Deville, Strong, tough and stiff bioinspired ceramics from brittle constituents, Nat. Mater. 13 (2014) 508-514.

[44] A.R. Studart, Bioinspired ceramics: turning brittleness into toughness, Nat. Mater. 13 (2014) 433-435.

[45] H. Zhou, T. Fan, D. Zhang, Biotemplated materials for sustainable energy and environment: current status and challenges, ChemSusChem. 4 (2011) 1344-1387.

[46] J. Cook, J.E. Gordon, C.C. Evans, D.M. Marsh, A mechanism for the control of crack propagation in all-brittle systems, Proc. R. Soc. A Math. Phys. Eng. Sci. 282 (1964) 508-520.

[47] P.Y. Chen, J. McKittrick, M.A. Meyers, Biological materials: functional adaptations and bioinspired designs, Prog. Mater. Sci. 57 (2012) 1492-1704.

[48] J.W. Suk, R.D. Piner, J. An, R.S. Ruoff, Mechanical properties of monolayer graphene oxide, ACS Nano 4 (2010) 6557-6564.

[49] H.M. Rietveld, A profile refinement method for nuclear and magnetic structures, J. Appl. Crystallogr. 2 (1969) 65–71.

Chapter 5 Graphene-Enabled Ni_3C/Ni Composites with High Strength and Toughness

5.1 Background and motivation

A joint enhancement of strength and toughness is a vital requirement for next generation structural materials. Unfortunately, this pursuit often falls into a compromise between hardness versus ductility [1]. Such a dilemma originates from the fact that the size of the plastic deformation zone in front of the crack tip, which works to dissipate local stress, is inversely proportional to the yield strength [2]. Moreover, in most engineering materials, once fracture is initiated, cracks propagate rapidly without any shielding behind the crack tip [3]. The wisdom of Nature negates this conflict by constructing materials with a hierarchical architecture, all while utilizing only limited materials and nontoxic processes [4]. A common example is nacre or mother-of-pearl. As one of the most well-known natural armors, nacre is endowed by a brick-and-mortar structure composited with aragonite (a mineral form of $CaCO_3$) platelets and biopolymer [5]. Acting as the major load-bearers, aragonite platelets (the bricks) with 5-10 μm in length and 0.5 μm in thickness are constructed by nanocrystals [5]. The biopolymer (the mortar) with only several nanometers in thickness closely binds the aragonite platelets together [6]. Such a complex structure enables multiple extrinsic toughening mechanisms at different length-scales, leading to an outstanding combination of strength and toughness that is hardly seen in engineered materials. The layer-by-layer architecture redirects the crack growth into a tortuous path, effectively consuming fracture energy via extending the crack length and reducing stress concentration [7]. In addition, mineral bridges shield the crack opening [8] while bio-polymer layers dissipate fracture energy [9]. In the meantime, surface nanoasperities interlock the aragonite platelets, preventing large-scale delamination [10]. While entirely mimicking the reinforcing multitude of these scale levels is difficult, the hierarchical architecture may hold the key of suppressing the dilemma between strength and toughness, and therefore, many researchers have gained inspiration from these bio-designs for new composite materials. Similar to nacre, ceramic composites with additional soft phases like polymers or metals have shown that brittle ceramic materials can be converted into tough materials via architecture designing [11–18]. Bioinspired polymer composites with added hard ceramic platelets exhibited high strength, outperforming most engineering polymers, while retaining ductility [19–23]. These studies are nothing short of remarkable; the toughness of such composites was magnitudes higher than the simple mixture of constituents. However, the intrinsically low ductility of ceramics and low strength of polymers limit the overall potential mechanical performance. Moreover, weak bonding between hard phases and soft phases may also lead to interface delamination. Therefore, it can be expected that cloning nacre's architecture with stronger constituents such as metals in engineered composites is a more promising as well as more challenging task.

Previously, ceramics and intermetallic compounds have been used as hard phases in constructing metal-based composites with brick-and-mortar structure which exhibited notable mechanical properties [24–27]. Recently, graphene, a single layer of carbon atoms with sp^2 bonds, is considered an ideal reinforcing agent for metal matrix composites because of its 2D morphology, ultra-high elastic modulus of 1 TPa, and high strength of 140 GPa [28]. So far, graphene has been composited with metals such as Al, Cu, and Ni, for the construction of laminated structures [29–34]. However, the agglomeration and degradation of graphene sheets, as well as the poor bonding between graphene and the metal matrix or unexpected reactions, resulted in a much lower than expected reinforcement efficiency. Therefore, unlocking the true potential of graphene in metals is still unresolved. An alternative approach is to utilize the unique morphological features of graphene, inducing interfacial reactions to form nacre-like brick-and-mortar architecture in composites [29]. Ni and Ni alloys are widely used in different applications, especially in high temperature, extreme environments such as combustion engines or turbine blades due to their outstanding mechanical performance and stability [35]. Considering the strategical significance of developing new Ni alloys with superior properties, several studies have attempted to composite graphene with Ni, but the high solubility of carbon in Ni and the tendency of forming coarse Ni_3C particles [36] led to electrochemical deposition [32], spark plasma sintering [33], and/or laser sintering [34] the only methods to sinter Ni/graphene composites.

The obtained composites, although exhibiting superior hardness, are unlikely to be mass produced. Therefore, the question remains: can we fabricate graphene-enabled, high-performance Ni matrix composites with nacre-like brick-and-mortar structure via feasible and scalable procedures?

Here, a graphene-derived Ni/Ni_3C composite with a characteristic nacre-like, brick-and-mortar architecture was fabricated by conventional powder metallurgy. Ni powders were homogeneously coated with graphene by shear mixing and freeze drying. At high temperature, carbon dissolved into Ni, facilitating the sintering process. Subsequently, part of the carbon atoms reacted with Ni, forming Ni_3C second phase particles along grain boundaries. The Ni_3C second phase particles were deformable and aligned into thin, long stripes, forming a brick-and-mortar structure via cold rolling. Another portion of carbon remained in the Ni matrix as interstitial solid solution atoms. The Ni_3C platelets served as major load-bearers and strengthened the composite, while the Ni matrix ensured ductility. Because of the confluence of strengthening and toughening mechanisms, the fabricated composite exhibited a 73 % improvement of strength and only a 28 % compromise of ductility, leading to a notable enhancement of toughness. The 2D material-enabled powder processing can be applied to different materials combinations, creating possibilities for new metal matrix composites.

5.2 Experimental methods

Fabrication of graphene-derived Ni/Ni_3C composites

Graphite and Ni powders were purchased from Sigma-Aldrich Company without further purification. Graphene was prepared using the shear mixing method. Specifically, 1.5 g of graphite powders with purity of 99.9 % were added into 200 mL H_2O and then shear mixed at 3000 rpm at room temperature for 1 h by a Silverson L5M-A shear mixer. Subsequently, the suspension stood for 2 h and the large particles deposited at the bottom were filtrated for reuse. The upper transparent liquid contained about 0.09 to 0.12 g graphene. 5 g Ni powders with 99 % purity were then shear mixed with the graphene sheets for 2 h. After shear mixing, the Ni/graphene powders were collected and lyophilized for 6 h. The obtained powders were compressed in a round mold with a diameter of 25 mm at 80 MPa and then sintered at 1450 ℃ for 1 h with the protection of Ar. After sintering, the coin was rolled at room temperature with a reduction rate of 80 %. For comparison, four reference samples were fabricated. For the first reference sample, a pure nickel plate (99% purity) was purchased from ESPI Metal and cold rolled with the same thickness reduction rate as used for the Ni/Ni_3C composite plates. For the second reference sample, Ni powders were shear-mixed, freeze dried, compressed, and sintered without adding graphene. The sample was cold rolled with the same thickness reduction rate as used for the Ni/Ni_3C composite plates. For the third and fourth reference samples, Ni powders were composited with 4 wt.% and 6 wt.% graphene, respectively, and hybrid powders were then compressed and sintered under the same conditions.

Material and mechanical characterizations

Tensile testing was carried out on an Admet eXpert 2600 tensile universal testing machine with an extension speed of 0.06 mm/min. Strain was measured using the Vic-2D digital image correlation system from Correlated Solutions with one photo every two seconds. Specimens for tensile tests were prepared in dog-bone shape. *In situ* tensile tests and 3-point bending tests were carried out on a MTI Instrument SEMtester 1000 Tensile Stage. Nanoindentation tests were carried out using a MicroMaterials Vantage nanoindenter with a load of 200 mN and 10 mN. The nanoindenter was a diamond Berkovich tip whose shape function was carefully calibrated. The elastic modulus of the diamond tip was 1140 GPa and the Poisson's ratio was 0.07. XRD patterns were obtained using PANalytical X'Pert Pro MPD equipped with Cu Kα radiation (λ = 0.15406 nm). Microstructure of the specimens was characterized with a FEI Quanta 650 SEM with an EDS detector, a FEI TITAN G2 aberration corrected scanning TEM (STEM)/high resolution TEM (HRTEM). TEM and STEM specimens for cross sectional imaging were cut using a Helios dual beam focused ion beam (FIB). APT experiments were carried on a LEAP5000XS.

Numerical simulations

Finite element simulation was performed on ANSYS student edition. The model size was 25 × 25 × 125 (W × H × L) μm. The constituent particle size was determined based on the SEM images, ranging from 20-70 μm in length and approximately 2-3 μm in thickness, with a standard width of 5 μm. The volume fraction of the constituent particles in the model was 10 %. Boundary conditions were assigned as fixed support at one end and distributed face load applied at the other. Loading was a ramped load uniformly over 30 s to maximum of 0.375 N (600 MPa) along positive x direction. The unit cell of Ni_3C ($R\bar{3}c$ space group, a = 4.553Å and c = 12.92Å) was constructed via density functional theory (DFT) using Cambridge Serial Total Energy Package (CASTEP). The generalized gradient approximation (GGA-PBE) was selected to describe the exchange and correlation energy. The Broyden–Fletcher–Goldfarb–Shanno (BFGS) minimizer was used to perform cell optimization, and the convergence tolerance of total energy was set to be 1×10^{-6} eV/atom.

5.3 Synthesis of graphene-enabled Ni/Ni_3C composites

5.3.1 Fabrication of graphene/Ni powders

Shear mixing was employed to produce few layered graphene and coat the graphene sheets on Ni particles simultaneously, largely improving the production efficiency. Specifically, 1.5 g graphite was dispersed in 200 mL dilute water and shear mixed at 3000 rpm for 1 h. The relationships between the shear mixing rate, duration, and the amount of graphene productivity were thoroughly studied by K. R. Paton et al. [37]. After shear mixing, the coarse, undefoliated graphite powders were subsided and removed, leaving few-layered graphene in the liquid. Under the current conditions, the weight of the fabricated graphene from 1.5 g graphite was about 0.09-0.12 g. The obtained graphene sheets exhibited thin, flexible morphology (Fig. 5-1a) with an almost intact crystal structure (Fig. 5-1b and c).

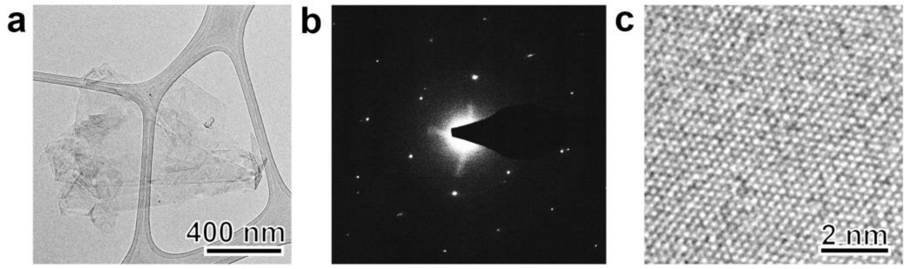

Fig. 5-1 Graphene sheets produced by shear mixing. a. TEM image of the graphene from shear mixing. b. SAED pattern of the graphene sheet. c. HRTEM image of the graphene sheet, showing intact crystal structure.

Without further treatment, the graphene-containing suspension was shear mixed with 5 g Ni powders with irregular shape for 2 hours, corresponding to about 2 % in weight percentage (wt.) and about 10 % in atomic percentage (at.) of carbon. Subsequently, the Ni/graphene powders were freeze dried for 6 hours. After these procedures, scanning electron microscopy (SEM) observation showed that the graphene sheets were closely coated over the Ni powders without noticeable aggregation (Fig. 5-2a). Both shear mixing and freeze drying are critical for homogeneously coating graphene on Ni powders. Without shear mixing, graphene sheets were loosely attached on the Ni powders and could not permeate into the small gaps or crevices on the particle surface (Fig. 5-2b). Without freeze drying, graphene sheets agglomerated into coarse graphite particles (Fig. 5-2c). The method can be feasibly grafted to other materials and may find more applications in various fields. Transmission electron microscopy (TEM) inspection unveiled that the graphene had closely coated the Ni powders without free space (Fig. 5-2d). The thickness of the graphene coating layer ranged from 10 to 15 nm, equaling to 20-30 atomic layers. An in situ heating observation revealed that the graphene sheets gradually dissolved into the Ni particle even without any compression (Fig. 5-2e), indicative of a very intimate bonding between graphene and Ni. Ni powders with 4 wt.% and 6 wt.% graphene were also prepared as references.

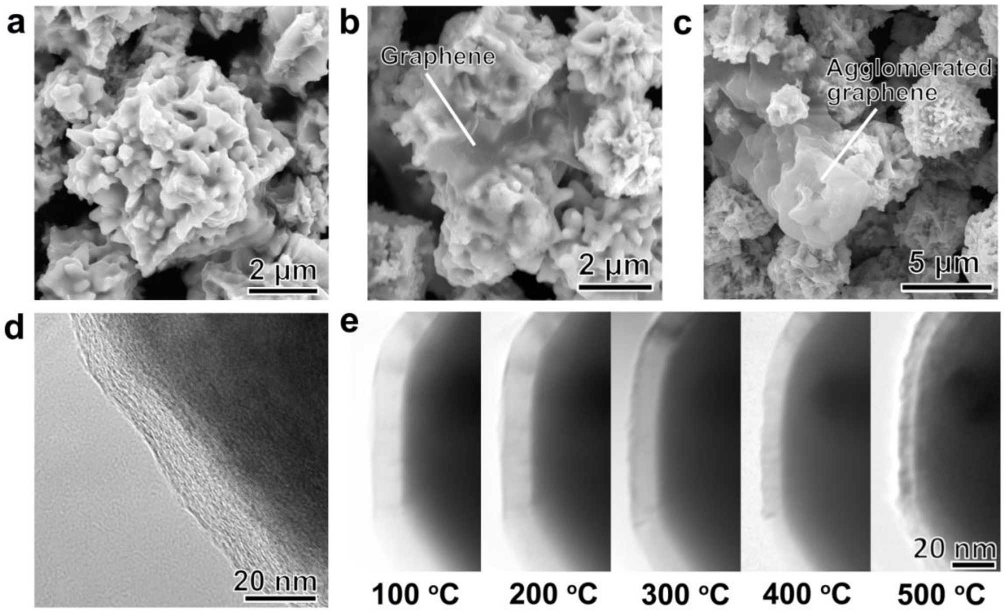

Fig. 5-2 Ni/graphene powders after shear mixing and freeze drying. a. SEM image of Ni/graphene powders, showing no noticeable aggregation of graphene sheets. b. Without shear mixing, graphene sheets were loosely wrapped on Ni particles. c. Without freeze drying, graphene agglomerated, forming graphite particles. d. TEM image of the surface of a Ni/graphene powder, showing that few layered graphene closely coated around the Ni particle. e. *In situ* heating observation of a Ni/graphene powder. Graphene gradually dissolved into Ni with increasing temperature.

5.3.2 Microstructure of graphene-enabled Ni/Ni_3C composite

The Ni particles with 2 wt.% graphene produced by shear mixing and freeze drying were compressed in a round mold with 25 mm in diameter to a pressure of 80 MPa and then sintered at 1450 ℃ under the protection of Argon, slightly lower than the melt point of Ni (1455 ℃). After sintering, the Ni/graphene powders were melted together, showing no evidence of pulverization or fracture (Fig. 5-3a inset). After chemical etching, the Ni/graphene powder derived ingot exhibited clean, well defined grain boundaries, indicative of the formation of grain boundary precipitates (Fig. 5-3a). Ni powders without graphene, with 4 wt.% of graphene, and with 6 wt.% of graphene were also compressed, sintered under the same condition as references. The Ni powder derived ingot displayed no obvious grain boundaries after chemical etching (Fig. 5-3b). Sintering enabled the Ni powders with 4 wt.% graphene to form a coin which was broken into pieces after minor deformation, indicative of weak bonding between particles (Fig. 5-3c). The Ni powders with 6 wt.% of graphene could not be sintered together (Fig. 5-3d). Close-up inspection of the sintered sample with 4 wt.% graphene showed a discontinuous microstructure with isolated particles. Energy dispersive X-ray spectroscopy (EDS) carbon map uncovered that carbon segregated on the particle surfaces. According to the Ni-C phase diagram, the highest solubility of carbon in nickel is 2.7 at.%, and the eutectic reaction point is located at 10 at.% of carbon [36], which corresponds to about 2 wt.%. When 4 wt.% graphene (or 20 at.%) was composited with Ni, some carbon remained on the Ni particle surfaces even part of the Ni powders melted. The excessive carbon left on the Ni particle surfaces prohibited the sintering of Ni powders.

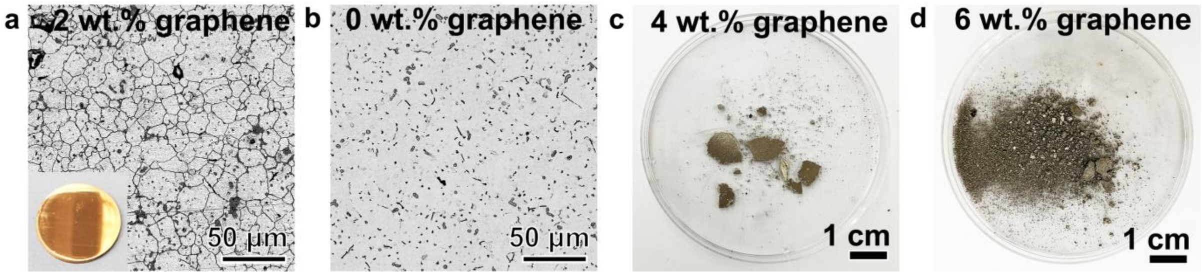

Fig. 5-3 Ni powders with different concentrations of graphene after sintering. a. Ni/2 wt.% graphene. b. Ni. c. Ni/4 wt.% graphene. d. Ni/6 wt.% graphene.

Cold rolling with a 40 % deformation reduction in thickness was first applied on the sintered coins. The grain boundary precipitates were broken into long, thin stripes, which gradually aligned along the rolling direction during deformation. After the deformation reduction in thickness was increased to 80 %, the boundary precipitates were aligned in a parallel fashion, forming a brick-and-mortar architecture (Fig. 5-4a) (RD: rolling direction; TD: transverse direction; ND: normal direction). The fracture surface also exhibited a laminated feature with elongated dimples (Fig. 5-4b) which had the same shape as the second phase particles in Fig. 5-4a. TEM inspection unveiled large second phase particles embedded within the matrix (Fig. 5-4c). The dislocation density within the second phase particles was lower than that of the Ni matrix. Also, the grain size and shape of the Ni matrix were different near and beyond the second phase particles. Close-up inspection of the Ni matrix exhibited stripe-like grains with a thickness ranging from 100 to 300 nm, a typical cold rolled microstructure (Fig. 5-4d). On the contrary, Ni grains near the large second phase particle were smaller in size with an equiaxed morphology (Fig. 5-4e). The difference in grain size and shape may derive from higher deformation energy, which may stimulate dynamic recrystallization. High resolution TEM (HRTEM) imaging of the boundary showed no noticeable defects, such as voids or cracks (Fig. 5-4f), indicating that the cold deformation did not break the bonding between the precipitates and the matrix. Instead, there was an amorphous transition zone between Ni matrix and the second phase particles, suggesting that the second phase particles precipitated out from the Ni matrix.

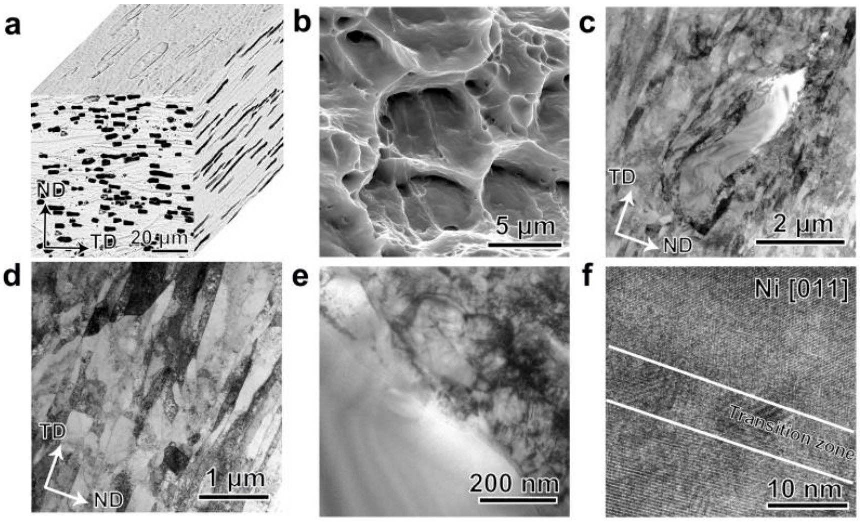

Fig. 5-4 Microstructure of the graphene-enabled Ni/Ni_3C composite. a. SEM image of cold rolled Ni/Ni_3C composite, showing brick-and-mortar structures. b. Fracture surface of Ni/Ni_3C composite, showing laminated structure constructed by elongated dimples. c. Low magnification TEM image, showing large second phase particle embedded in the Ni matrix. d. After cold rolling, Ni grains were deformed into long stripes with the thickness ranging from 100-300 nm. e. Close-up observation of the Ni/Ni_3C boundary. f. HRTEM image of the interface between Ni and a second phase particle, revealing a transition zone.

A critical question arises: what is the second phase particle? The X-ray diffraction (XRD) spectrum of the Ni/graphene derived composite exhibited a weak peak at about 43 °(Fig. 5-5a and b) which was similar to the Ni_3C (002) peak illustrated in ref. [36]. In order to determine the composition of the second phase particles, EDS analysis and HRTEM observation were employed. EDS spectra showed the existence of Ni and carbon with a Ni/C ratio about 3:1 (Fig. 5-5c). Therefore, we can likely assume that the second phase particle is Ni_3C.

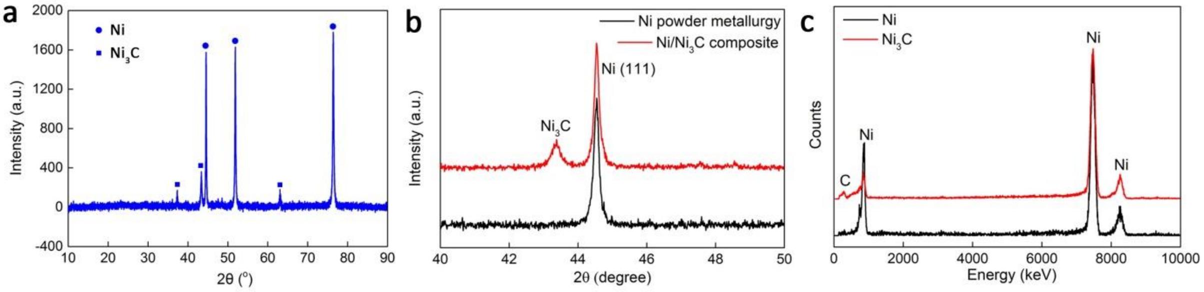

Fig. 5-5 XRD and EDS spectra of Ni/Ni_3C composite and Ni produced by powder metallurgy. a. Comprehensive XRD spectrum of Ni/Ni_3C composite. b. XRD spectra of Ni/Ni_3C composite and Ni produced by powder metallurgy from 40° to 50°. c. EDS spectra of Ni_3C and Ni matrix in Ni/Ni_3C composite.

Ni_3C is a stable nickel/carbon component below 1000 ℃. It has an hcp structure with a lattice parameter of a=0.26 nm and c=0.43 nm. The unit cell of Ni_3C plotted by Materials Studios is shown in Fig. 5-6a, in which Ni and C atoms arranged layer-by-layer. According to the crystal structure, on the [-110] plane of the Ni_3C particle, Ni atoms should exhibit visual distances of 0.23 nm and 0.26 nm (Fig. 5-6a) under HRTEM. The HRTEM image (Fig. 5-6b) and corresponding fast Fourier transform (FFT) pattern (Fig. 5-6c) exactly matched the calculation. Therefore, by coupling the results from XRD, EDS and HRTEM, the large second phase particles are conclusively determined to be Ni_3C. A close [01-1]//[-110] orientation relation between Ni and Ni_3C can be derived from Fig. 5-4f, which may lead to the weak XRD peaks. Armed with solid experimental results, we can conclude the formation mechanism of the nacre-like Ni/Ni_3C composite with brick-and-mortar structure. As illustrated in Fig. 5-6d, Ni powders were closely wrapped by graphene after shear mixing and freeze drying. The graphene sheets dissolved into the Ni matrix and precipitated out as Ni_3C in the sintering and cooling. The Ni_3C second phase particles were broken and elongated into long strips during cold deformation, forming the brick-and-mortar structure.

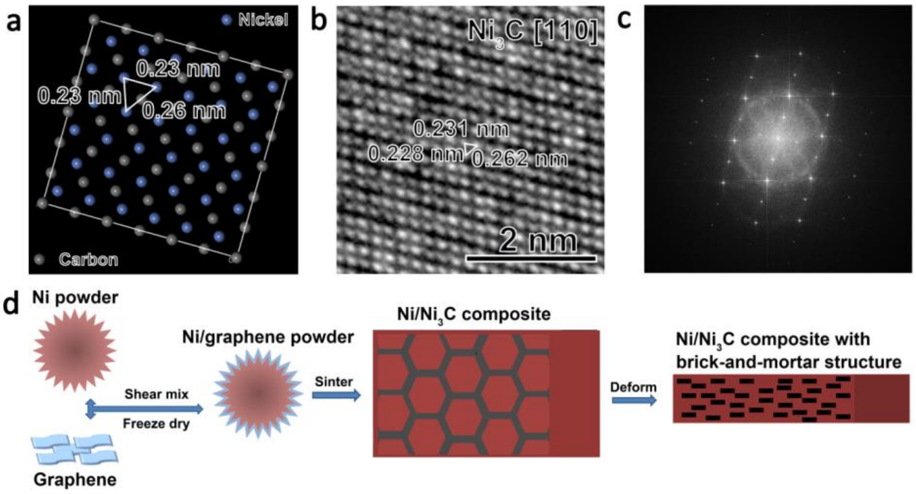

Fig. 5-6 Crystal structure of Ni_3C. a. Ni_3C crystal on [-110] plane. b. HRTEM image of the [-110] plane of Ni_3C particle, showing identical atomic arrangement as in the (a). c. FFT pattern of the [-110] plane. d. Schematic illustration of the formation of Ni/Ni_3C composite with brick-and-mortar structure.

5.3.3 Mechanical performance of the Ni/Ni_3C composite

Encouragingly, such graphene derived Ni/Ni_3C composite with brick-and-mortar structure exhibited outstanding mechanical performance. The tensile specimens were fabricated into a dog-bone shape with a sample size demonstrated in Fig. 5-7a. Tensile tests were carried out at a strain rate of 0.06 mm/min. The strain was measured by Correlated Solution's Vic-2D digital image correlation system with one photo every two seconds. Three tests were conducted on each group of samples. In a typical tensile test, the Ni/Ni_3C composite showed a yield strength of 774 GPa and an ultimate tensile strength of 1095 GPa (Fig. 5-7a). The strength is comparable to the strongest Ni based alloys [38]. Intriguingly, although the strength had an obvious improvement, the ductility only exhibited a minor decrease. The Ni/Ni_3C composite has a joint enhancement of mechanical properties: a 73 % improvement of strength, a 6 % increase on Young's modulus, and an 82.3 % enhancement of hardness with only a 28 % comprise to ductility (Fig. 5-7b). Such outstanding combination between strength and ductility resulted in a 44 % increase of toughness (the area under the strength/strain curve) than the pure Ni reference sample, indicating that the nacre-like, brick-and-mortar architecture effectively mitigated the conflict between strength and toughness. So far, a large amount of bio-inspired, nacre-like composites including ceramic based (diamond marks in Fig. 5-7c) [11–18], polymer based (round marks in Fig. 5-7c) [19–

23], and metal based (square marks in Fig. 5-7c) [24–27,29–34] composites have been developed. Freeze-casting has been widely used to construct laminated ceramic composites [11–13]; polymer crosslinking, on the other hand, is the primary route to fabricate layer-by-layer architectured polymer-based composites [20,21]; compressing sintering, powder processing, electrochemical deposition and laser sintering have been employed to synthesize nacre-like metal-based composites [29-34]. The soft phases (polymers and metals) with a volume fraction ranging from 5 % to 40 % in the nacre-like ceramic composites effectively improved the ductility of the composites, with a tradeoff of reduction in the characteristically high strength of ceramics (diamond marks in Fig. 5-7c). The hard phase (mainly ceramic flakes) in nacre-like polymer-based composites prohibited the decoiling of polymer chains, which notably enhanced the strength of the polymer matrixes (round marks in Fig. 5-7c). In the nacre-like metal-based composites, the volume fraction of metal matrix, which is normally considered as the soft phase, is often over 70 %. Hard phases with platelet-like morphology, such as graphene, ceramics, and intermetallic compounds, were homogeneously dispersed in the metal matrixes, facilitating a joint enhancement of strength and toughness (square marks in Fig. 5-7c). Due to the intrinsically high strength of Ni and the constructed brick-and-mortar architecture, the graphene enabled Ni/Ni_3C composite outperformed most other nacre-like composites in terms of the combination of yield strength and ductility (star mark in Fig. 5-7c).

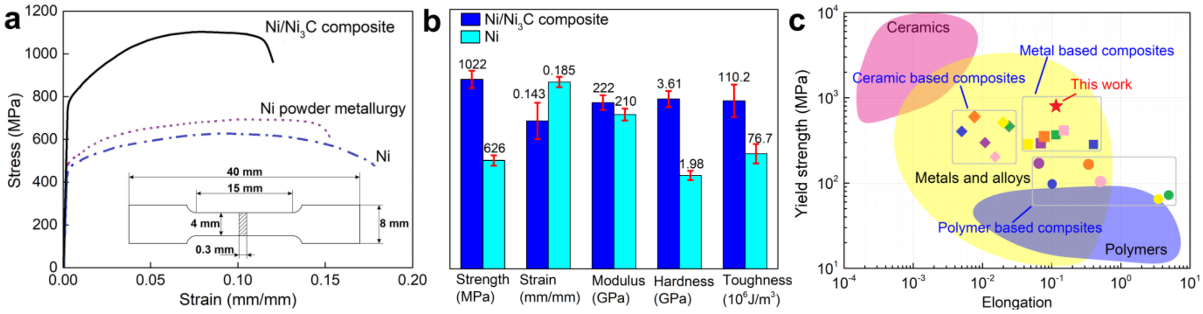

Fig. 5-7 Mechanical properties of graphene-enabled Ni/Ni_3C composite with brick-and-mortar structure. a. Tensile stress-strain curves of Ni, Ni produced by powder metallurgy, and Ni/Ni_3C composite (inset is the size of tensile specimen). b. Comparative bar chart of mechanical properties of Ni and Ni/Ni_3C composite. c. Elongation vs. yield strength plot showing that the as-fabricated Ni/Ni_3C composite had an outstanding combination between strength and ductility (mechanical properties of nacre-like composites were derived from ref. [11-27, 29-34]).

5.4 Stiffening, strengthening, and toughening mechanisms of the Ni/Ni_3C composite

5.4.1 Stiffening mechanisms of the Ni/Ni_3C composite

It is important to understand the stiffening, strengthening, and toughening mechanisms of the graphene derived Ni/Ni_3C composite. The Young's modulus of the composite was slightly higher than pure Ni (Fig. 5-7b). Apparently, the enhancement of Young's modulus derives from the Ni_3C platelets. A volume fraction of 13.3 % of the Ni_3C platelets was calculated from five low-magnification SEM images on ND/TD and ND/RD planes, respectively. Low-load nanoindentation tests were carried out to identify the mechanical properties of the Ni_3C platelets. As shown in a typical nanoindentation displacement-load curve, the Ni_3C platelets exhibited higher hardness and reduced modulus (Fig. 5-8a). On average, the Ni_3C platelet has a hardness of 6.5 GPa (3.4 GPa higher than that of Ni matrix) and an elastic modulus of 364 GPa (154 GPa higher than Ni). The hardness (Fig. 5-8b) and reduced modulus (Fig. 5-8c) maps derived from nanoindentations exhibited an alternating hard-soft-hard structure with the hard part as the Ni_3C platelets. Due to the linear nature of elastic deformation and the intimate bonding between Ni matrix and Ni_3C platelets, the maximum enhancement of Young's modulus can be estimated by the rule of mixtures below:

$$E = E_1 v_1 + E_2 v_2 \qquad (1)$$

where E is the modulus of the composite, E_1 is the modulus of Ni matrix (210 GPa), v_1 is the volume fraction of Ni (86.7 %), E_2 is the modulus of Ni_3C platelets (364 GPa), v_2 is the volume fraction of Ni_3C platelets (13.3 %). The upper limit of Young's modulus of the composite was calculated to be 230.5 GPa. The lower limit of modulus enhancement can be calculated by the equation:

$$E = \left[\frac{v_1}{E_1} + \frac{v_2}{E_2}\right]^{-1} \qquad (2)$$

The lower limit of modulus was calculated to be 220.97 GPa, which is close to the average value of Young's modulus obtained from tensile tests (222 GPa).

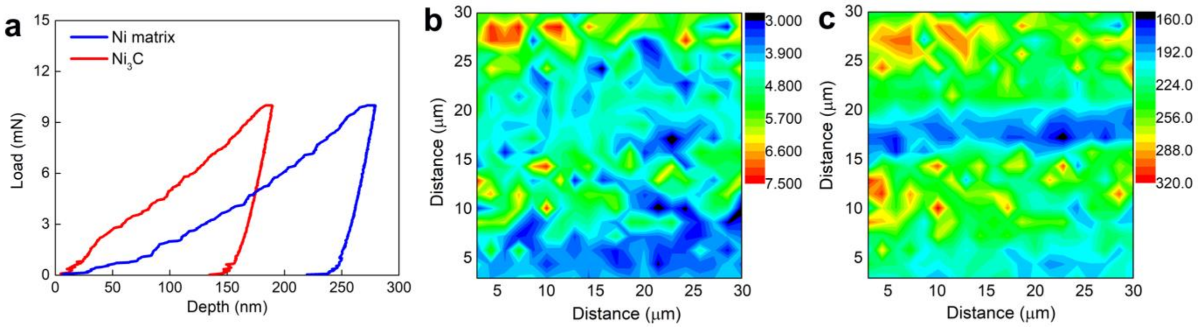

Fig. 5-8 Stiffening mechanism of graphene derived Ni/Ni$_3$C composite with brick-and-mortar structure. a. Nanoindentation load-displacement curves of Ni and Ni$_3$C platelet. b. Hardness map derived from nanoindentation tests. c. Reduced modulus map derived from nanoindentation tests.

5.4.2 Strengthening mechanisms of the Ni/Ni$_3$C composite

Subsequently, we attempted to unveil the strengthening mechanisms of the graphene enabled Ni/Ni$_3$C composite. According to the tensile stress-strain curves in Fig. 5-7a, the yield strength of Ni/Ni$_3$C composite had a 288 MPa improvement comparing with that of Ni sample produced by powder metallurgy (from 492 MPa to 774 MPa). Apparently, the Ni$_3$C platelets indeed contributed to the improvement of yield strength. Based on the experimental results, a finite element model (FEM) was constructed (Fig. 5-9). When a tensile stress of 600 MPa was exerted along the x-axis, the FEM simulation showed a high concentration of stress on the platelets, indicating that the platelets acted as the load-bearers and effectively strengthened the composite. The strengthening effect from Ni$_3$C platelets can be validated by the rule of mixtures because we can assume that the Ni$_3$C platelets deformed synchronously with the Ni matrix during elastic deformation. Based on the tensile test results, the Ni/Ni$_3$C composite started yielding at a strain of about 0.35 %. If we assume the Ni$_3$C platelets were brittle and break at the yield point, and the yield strength of the Ni matrix (σ_y) was 492 MPa, the improved yield strength of the composite (σ_{TS}) was then calculated by the equation:

$$\sigma_{TS} = \sigma_y \nu_1 + \varepsilon E_2 \nu_2 \qquad (3)$$

where ε is the strain at yield point (0.35 %). The yield strength of the composite due to Ni$_3$C platelets was calculated to be 661.4 MPa, which was lower than the experimental results.

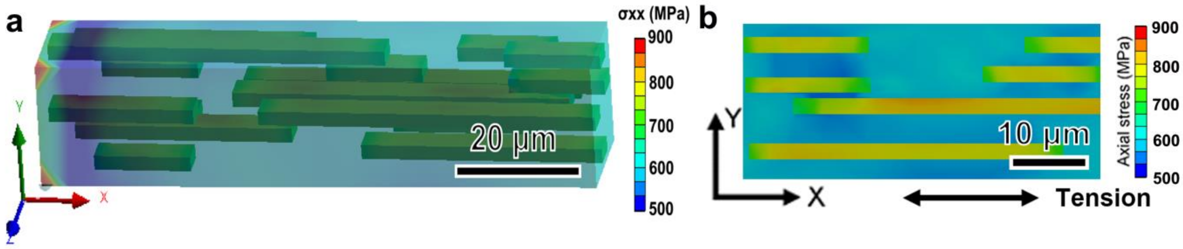

Fig. 5-9 Finite element simulation of the Ni/Ni$_3$C composite under tension. a. 3D FEA model of Ni/Ni$_3$C composite. b. 2D close-up view of the FEA model.

The hardness derived from nanoindentation on the Ni sample produced by powder metallurgy was about 2.2 GPa, which was lower than that of the Ni matrix in the Ni/Ni$_3$C composite (Fig. 5-10a). Therefore, the Ni matrix should be strengthened by other mechanisms. The second source of strengthening may derive from the grain boundaries, i.e. the grain size. The grain boundaries acted as pinning points to impede dislocation propagation. The relationship between grain size and strength can be demonstrated by Hall-Patch equation [39,40]:

$$\sigma_y = \sigma_0 + \frac{k_y}{\sqrt{d}} \qquad (4)$$

where σ_y is the yield strength, $\sigma_0$is a materials constant for the starting stress for dislocation movement, k_y is the strengthening coefficient, and d is the grain size. Therefore, the change of the yield strength due to the reduction of grain size should be:

$$\Delta\sigma_{gb} = \frac{k_y}{\sqrt{d_1}} - \frac{k_y}{\sqrt{d_2}} \qquad (5)$$

Based on TEM inspections (Fig. 5-10b and Fig. 5-10c), the average grain size along the normal direction of the Ni/Ni$_3$C composite was 198 nm (d_1) and that of the Ni sample produced by powder metallurgy was 543 nm (d_2). The finer grain size after adding graphene may originate from the formation of second phase particles, which can prohibit recrystallization and grain growth. The k_y was measured to be 4.9 MPa mm$^{1/2}$ [40]. Thusly, the yield strength enhancement derived from grain boundaries was 138.3 MPa. The grain refinement of the Ni matrix in the Ni/Ni$_3$C composite may be due to the similarity of lattice parameters between Ni and graphene. The lattice parameter of graphene on [002] plane is 0.246 nm while the atom distance of Ni along (110) direction is 0.248 nm. Such similarity of lattice parameters may induce strong heterogeneous nucleation at high temperature annealing, leading to smaller grains.

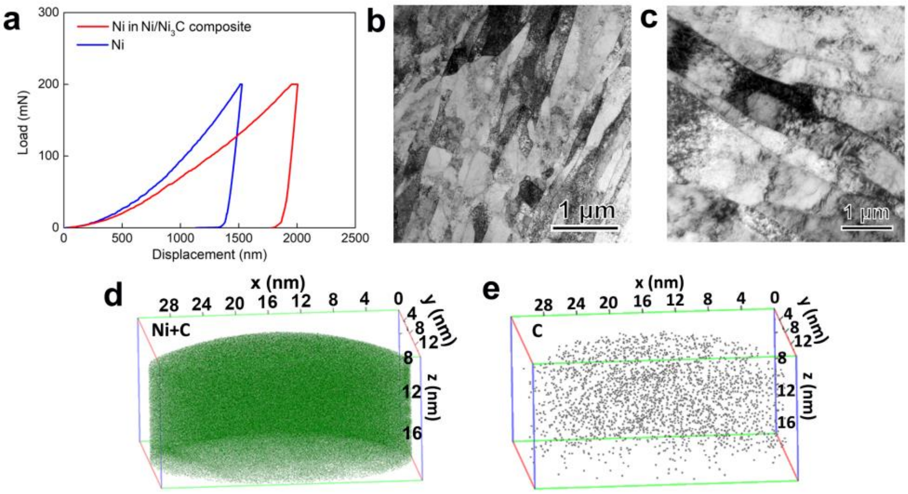

Fig. 5-10 Strengthening mechanisms of Ni matrix in Ni/Ni$_3$C composite. a. Nanoindentations on Ni in Ni/Ni$_3$C composite and Ni produced by powder metallurgy. b. TEM inspection of Ni/Ni$_3$C composite after 80 % reduction in thickness in cold rolling. c. TEM inspection of Ni produced by powder metallurgy after 80 % reduction in thickness in cold rolling. d. APT map of Ni and C atom distribution. f. APT map of C atom distribution.

Because the deformation was the same for all the samples, so the remaining mechanisms were precipitate strengthening and solution atom strengthening. A rational hypothesis is that carbon dissolved into the Ni matrix and then precipitated out as atom clusters and/or second phase particles, which pinned the migration of dislocations and strengthened the Ni matrix. A direct evidence of the precipitates should be the weak secondary patterns that appear in selected area electron diffraction (SAED) patterns. However, the SAED pattern of the Ni matrix along both [011] and [112] directions showed no other patterns except for the Ni, eliminating the possibility of nano-sized precipitates or atom clusters. Thusly, solid solution strengthening had the highest likelihood for improving the yield strength. Fig. 5-10d and e are atom probe tomography (APT) maps, showing homogeneously dispersed carbon atoms in the Ni matrix. The atomic percentage of carbon in Ni matrix was about 1 at.%. The strengthening effect of interstitial solution atoms originates from the pinning of dislocation due to lattice distortion. The strength contribution can be expressed as (2):

$$\Delta\sigma_{ss} = kc \qquad (6)$$

where k is a parameter related to shear modulus and lattice distortion, c is the concentration of interstitial solution atoms. For body centered cubic (BCC) metals, such as Fe, carbon atoms can generate a nonsymmetrical stress field, which strongly interacts with dislocations, leading to a large k of 5G (G is the shear modulus). However, the smaller lattice distortion and symmetric stress field stemmed from carbon interstitial atoms in face centered cubic (FCC) Ni have much weaker pinning effects on dislocations, making the k only G/10 (2). The shear modulus of Ni is 72 GPa and the concentration of carbon was 1 at. % based on the ATP result. The theoretical yield strength enhancement contributed by carbon interstitial atoms was calculated to be 72 MPa. Therefore, the Ni/Ni_3C composite is triply strengthened by Ni_3C platelets, grain boundaries, and carbon interstitial solution atoms. The theoretical improvement of yield strength was calculated to be:

$$\sigma_{TS} = (\sigma_y + \Delta\sigma_{gb} + \Delta\sigma_{ss})\nu_1 + \varepsilon E_2 \nu_2 = 778.3\ MPa \qquad (7)$$

which was close to the experimentally derived improvement of yield strength.

5.4.3 Toughening mechanisms of the Ni/Ni_3C composite

In engineering alloys, the increase of strength derived from interstitial atoms and second phase particles usually tradeoff with the reduction in ductility. Especially large, brittle carbides often introduce defects which may become the source of cracks. However, the graphene derived Ni/Ni_3C composite exhibited an obvious plastic deformation stage and a higher static toughness than the pure Ni (Fig. 5-7a). An *in situ* tensile test was carried out under SEM to unveil the influence of Ni_3C platelets on crack formation and propagation during deformation. A speckled coating created by a mix of conductive silver glue and carbon black was coated on the sample to trace the evolution of strain via digital image correlation. A small notch was also made on the sample edge. As shown in Fig. 5-11a, no apparent strain concentration was found at a low displacement of 0.05 mm. With an increase of the exerted load, the crack started at the artificial notch. The crack propagated along 45 ^{o} against the loading direction, a typical fracture of ductile metals. Therefore, the Ni_3C platelets likely did not act as the fracture source and stimulate cracking. Close-up observation of the crack initiation near the artificial notch showed that multiple small cracks appeared before the major crack propagated (Fig. 5-11b), indicating that in addition to the intrinsic toughening mechanisms, such as fine grain size and parallelly aligned grain orientation, the brick-and-mortar structure may introduce extrinsic toughening mechanisms to further improve the toughness.

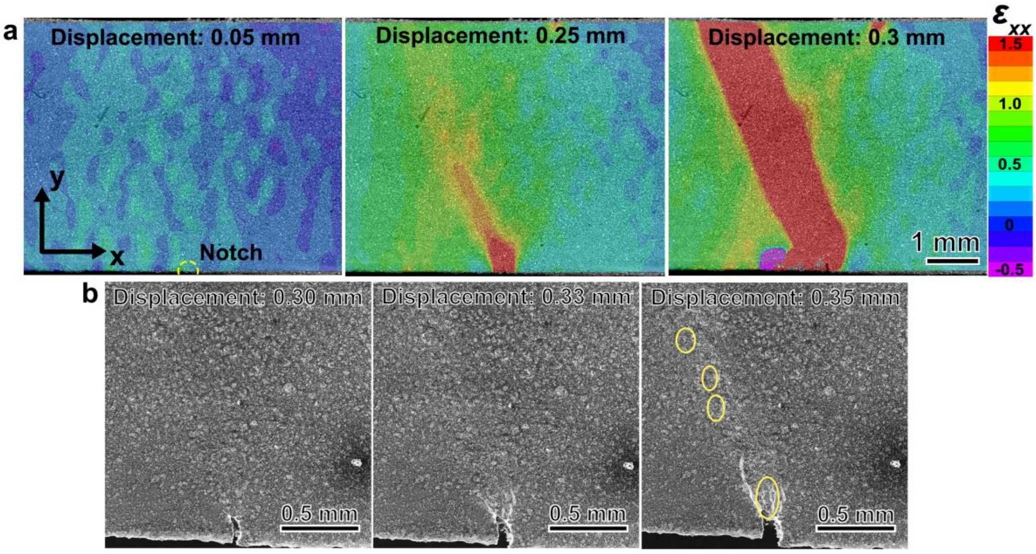

Fig. 5-11 ***In situ* tensile test of graphene-derived Ni/Ni$_3$C composite.** a. *In situ* tensile test with DIC strain map. b. Close-up observation of the crack initiation at the artificial notch.

To reveal the possible extrinsic toughening mechanisms, an *in situ* three-point bending test was carried out (Fig. 5-12a). Although an artificial notch was made, the crack initiated at a large deflection, indicative of outstanding ductility. After the crack initiated, instead of propagating perpendicular towards another side of the three-point bending plate, the crack was gradually deviated to be parallel to the three-point bending sample length direction by the parallelly aligned Ni$_3$C platelets (Fig. 5-12a), which shifted the crack mode, leading to lower effective stress around the crack tip and higher difficulty for crack opening. Moreover, the interlacing Ni$_3$C platelets resulted in a zig-zag morphology of crack edges and formation of small cracks near the primary crack in both in-plane and out-of-plane, which inevitably elongated the crack length. The energy required to propagate the crack, W_s, is related to the crack length:[29]

$$W_s = 2ab\gamma \qquad (7)$$

where a is the crack length, b is the out-of-plane thickness of the solid material, and γ is the sum of surface energy (γ_s) and energy related to plastic deformation (γ_p). Apparently, the longer the crack length is, the higher the toughness. In addition to the crack deflection, metal bridges appeared behind the crack tip and the layer-by-layer structure blunted the crack tip, which further prohibited the crack opening and propagating (Fig. 5-12a). Thusly, the Ni_3C/Ni brick-and-mortar structure indeed contributed to the improvement of toughness. Worth mentioning is that the inspection of the chemically etched sample unveiled that the Ni_3C platelets in fact deformed with the Ni matrix (Fig. 5-12b). This result demonstrated a critical truth that the Ni_3C platelets are ductile; it can deform with the matrix without inducing notable cracks. It answered two essential questions: 1. why the Ni_3C grain boundary precipitates formed the brick-and-mortar structure after cold-working without introducing large defects and cracks, and 2. why the coarse Ni_3C platelets did not induce fracture during deformation.

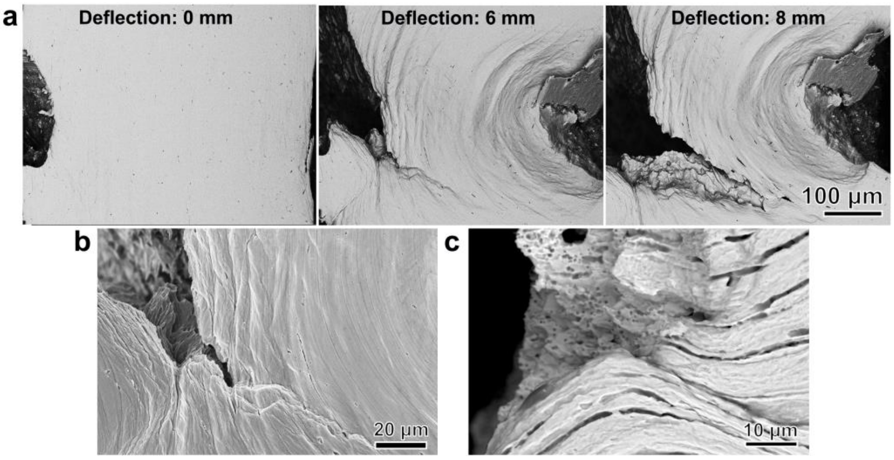

Fig. 5-12 *In situ* three-point bending test of graphene-derived Ni/Ni_3C composite. a. *In situ* three-point bending test under SEM. b. Close-up inspection of the crack propagation of three-point bending Ni/Ni_3C sample before chemical etching. c. After chemical etching.

5.5 Conclusions

In summary, a prototypical graphene derived Ni/Ni_3C composite with nacre-like, brick-and-mortar structure was developed. Graphene closely wrapped the Ni powders via shear mixing and freeze-drying procedures. The Ni/graphene powders were compressed and sintered at 1450 ℃, forming Ni_3C at the grain boundary area. The Ni_3C platelets were deformable. They were rolled into long stripes during the cold deformation, leading to the formation of a brick-and-mortar structure. Additional carbon atoms were dissolved into the Ni matrix and existed as interstitial solution atoms. The Ni_3C platelets not only acted as the load-bearers, but also redirected the crack. The small grains and interstitial solution atoms prohibited the dislocation propagation and enhanced the Ni matrix. In total, the confluence of multiple strengthening and toughening mechanisms enabled a 73 % increase on strength and a 6 % increase on Young's modulus, while only 28 % comprise on ductility, leading to a 44 % improvement of toughness. This strategy presents a new promise for the design and synthesis of new graphene-enabled metal matrix composites with exceptionally high mechanical robustness for a variety of applications.

References

[1] R.O. Ritchie, The conflicts between strength and toughness, Nat. Mater. 10 (2011) 817–822.

[2] T. L. Anderson, *Fracture Mechanics: Fundamentals and Applications, Third Edition (3rd Edition)* (Taylor & Francis Group, 2005).

[3] M.E. Launey, R.O. Ritchie, On the fracture toughness of advanced materials, Adv. Mater. 21 (2009) 2103–2110.

[4] U.G.K. Wegst, H. Bai, E. Saiz, A.P. Tomsia, R.O. Ritchie, Bioinspired structural materials, Nat. Mater. 14 (2014) 23–36.

[5] X. Li, W.C. Chang, Y.J. Chao, R. Wang, M. Chang, Nanoscale structural and mechanical characterization of a natural nanocomposite material: The shell of red abalone, Nano Lett. 4 (2004) 613–617.

[6] Z.H. Xu, Y. Yang, Z. Huang, X. Li, Elastic modulus of biopolymer matrix in nacre measured using coupled atomic force microscopy bending and inverse finite element techniques, Mater. Sci. Eng. C. 31 (2011) 1852–1856.

[7] R. Z. Wang, Z. Suo, A. G. Evans, N. Yao, I. A. Aksay, Deformation mechanisms in nacre. J. Mater. Res. 16 (2001) 2485–2493.

[8] A.Y.M. Lin, P.Y. Chen, M.A. Meyers, The growth of nacre in the abalone shell, Acta

Biomater. 4 (2008) 131–138.

[9] Z. Huang, Z. Pan, H. Li, Q. Wei, X. Li, Hidden energy dissipation mechanism in nacre, J. Mater. Res. 29 (2014) 1573–1578.

[10] A.Y.-M Lin, M.A. Meyers, Interfacial shear strength in abalone nacre, J. Mech. Behav. Biomed. Mater. 2 (2009) 607–612.

[11] M.E. Launey, E. Munch, D.H. Alsem, H.B. Barth, E. Saiz, A.P. Tomsia, R.O. Ritchie, Designing highly toughened hybrid composites through nature-inspired hierarchical complexity, Acta Mater. 57 (2009) 2919–2932.

[12] E. Munch, M. E. Launey, D. H. Alsem, E. Saiz, A. P. Tomsia, R. O. Ritchie, Tough, bio-inspired hybrid materials. Science 322 (2008) 1516 –1520.

[13] F. Bouville, E. Maire, S. Meille, B. Van De Moortèle, A.J. Stevenson, S. Deville, Strong, tough and stiff bioinspired ceramics from brittle constituents, Nat. Mater. 13 (2014) 508–514.

[14] M. Grossman, F. Bouville, F. Erni, K. Masania, R. Libanori, A.R. Studart, Mineral nano-interconnectivity stiffens and toughens nacre-like composite materials, Adv. Mater. 29 (2017) 1605039.

[15] R.P. Wilkerson, B. Gludovatz, J. Watts, A.P. Tomsia, G.E. Hilmas, R.O. Ritchie, A novel approach to developing biomimetic (“nacre-like”) metal-compliant-phase (nickel–alumina) ceramics through coextrusion, 28 (2016) 10061–10067.

[16] H. Bai, F. Walsh, B. Gludovatz, B. Delattre, C. Huang, Y. Chen, A.P. Tomsia, R.O. Ritchie, Bioinspired hydroxyapatite/poly(methyl methacrylate) composite with a nacre-mimetic architecture by a bidirectional freezing method, Adv. Mater. 28 (2016) 50–56.

[17] A. Dreyer, A. Feld, A. Kornowski, E.D. Yilmaz, H. Noei, A. Meyer, T. Krekeler, C. Jiao, A. Stierle, V. Abetz, H. Weller, G.A. Schneider, Organically linked iron oxide nanoparticle supercrystals with exceptional isotropic mechanical properties, Nat. Mater. 15 (2016) 522–528.

[18] M.E. Launey, E. Munch, D.H. Alsem, E. Saiz, A.P. Tomsia, R.O. Ritchie, A novel biomimetic approach to the design of high-performance ceramic-metal composites., J. R. Soc. Interface. 7 (2010) 741–753.

[19] L.J. Bonderer, A.R. Studart, L.J. Gauckler, Bioinspired design and assembly of platelet reinforced polymer films, Science 319 (2008) 1069–1073.

[20] S. Seo, D.W. Lee, J.S. Ahn, K. Cunha, E. Filippidi, S.W. Ju, E. Shin, B.-S. Kim, Z.A. Levine, R.D. Lins, J.N. Israelachvili, J.H. Waite, M.T. Valentine, J.E. Shea, B.K. Ahn, Significant performance enhancement of polymer resins by bioinspired dynamic bonding, Adv. Mater. 29 (2017) 1703026.

[21] W. Cui, M. Li, J. Liu, B. Wang, C. Zhang, L. Jiang, Q. Cheng, A strong integrated strength and toughness artificial nacre based on dopamine cross-linked graphene oxide. *ACS Nano* 8 (2014) 9511–9517.

[22] J.M. Malho, P. Laaksonen, A. Walther, O. Ikkala, M.B. Linder, Facile method for stiff, tough, and strong nanocomposites by direct exfoliation of multilayered graphene into native nanocellulose matrix, Biomacromolecules. 13 (2012) 1093–1099.

[23] J. Wang, J. Qiao, J. Wang, Y. Zhu, L. Jiang, Bioinspired Hierarchical Alumina–Graphene Oxide–Poly(vinyl alcohol) Artificial Nacre with Optimized Strength and Toughness, ACS Appl. Mater. Interfaces 7 (2015) 9281–9286.

[24] M. Konieczny, Mechanical properties and deformation behavior of laminated Ni-(Ni_2Al_3+$NiAl_3$) and Ni-(Ni_3Al+NiAl) composites, Mater. Sci. Eng. A. 586 (2013) 11–18.

[25] M. Konieczny, Microstructural characterisation and mechanical response of laminated Ni-intermetallic composites synthesised using Ni sheets and Al foils, Mater. Charact. 70 (2012) 117–124.

[26] A. Dutta, S.A. Tekalur, Synthetic staggered architecture composites, Mater. Des. 46 (2013) 802–808.

[27] F.M. Heim, Y. Zhang, X. Li, Uniting strength and Toughness of Al Matrix Composites with Coordinated Al_3Ni and Al_3Ti Reinforcements, Adv. Eng. Mater. 20 (2017) 1700605.

[28] C. Lee, X. Wei, J.W. Kysar, J. Hone, Measurement of the elastic properties and intrinsic strength of monolayer graphene, Science 321 (2008) 385–388.

[29] Y. Zhang, X. Li, Bioinspired, graphene/Al_2O_3 doubly reinforced aluminum composites with high strength and toughness, Nano Lett. 17 (2017) 6907–6915.

[30] Z. Li, Q. Guo, Z. Li, G. Fan, D.-B. Xiong, Y. Su, J. Zhang, D. Zhang, Enhanced mechanical properties of graphene (reduced graphene oxide)/aluminum composites with a bioinspired nanolaminated structure, Nano Lett. 15 (2015) 8077–8083.

[31] M. Cao, D.B. Xiong, Z. Tan, G. Ji, B. Amin-Ahmadi, Q. Guo, G. Fan, C. Guo, Z. Li, D. Zhang, Aligning graphene in bulk copper: Nacre-inspired nanolaminated architecture coupled with in-situ processing for enhanced mechanical properties and high electrical conductivity, Carbon 117 (2017) 65–74.

[32] Z. Ren, N. Meng, K. Shehzad, Y. Xu, S. Qu, B. Yu, J. K. Luo, Mechanical properties of nickel-graphene composites synthesized by electrochemical deposition. Nanotechnology 26 (2015) 65706.

[33] T. Borkar, H. Mohseni, J. Hwang, T.W. Scharf, J.S. Tiley, S.H. Hong, R. Banerjee, Excellent strength-ductility combination in nickel-graphite nanoplatelet (GNP/Ni) nanocomposites, J. Alloys Compd. 646 (2015) 135–144.

[34] Z. Hu, G. Tong, D. Lin, Q. Nian, J. Shao, Y. Hu, M. Saei, S. Jin, G.J. Cheng, Laser sintered graphene nickel nanocomposites, J. Mater. Process. Technol. 231 (2016) 143–150.

[35] P. Zhu, J.C.M. Li, C.T. Liu, Adiabatic temperature of combustion synthesis of Al-Ni systems, Mater. Sci. Eng. A. 357 (2003) 248–257.

[36] V.K. Portnoi, A.V. Leonov, S.N. Mudretsova, S.A. Fedotov, Formation of nickel carbide in the course of deformation treatment of Ni-C mixtures, Phys. Met. Metallogr. 109 (2010) 153–161.

[37] K. R. Paton *et al.*, Scalable production of large quantities of defect-free few-layer graphene by shear exfoliation in liquids. Nat. Mater. 13 (2014) 624–630.

[38] Product Handbook of Product Handbook of High-Performance Nickel Alloys (Special Metals, a PCC Company).

[39] E.O. Hall, The deformation and ageing of mild steel: III Discussion of results, Proc. Phys. Soc. London Sect. B. 64 (1951) 747–753.

[40] R.W. Armstrong, Hall–Petch description of nanopolycrystalline Cu, Ni and Al strength levels and strain rate sensitivities, Philos. Mag. 96 (2016) 3097–3108.

Chapter 6 Summary, Impact, and Outlook

6.1 Summary

Since the groundbreaking discovery, graphene, the single-layered carbon with sp^2 bonds, is considered to be a game-changer of various fields because of its superior mechanical, electronic, and thermal properties. However, after years of intensive studies, most of graphene-based products are still at a conceptual level. In addition to the difficulties of massive production and long-term preservation, how to efficiently and effectively exploit graphene remains challenging. In this dissertation, graphene was employed in Li-S batteries and metal matrix composites, aiming to explore graphene applications in energy storage and energy-saving structures.

In Chapter 1, a thorough literature review of graphene applications in Li-S batteries and metal matrix composites was provided. It has been demonstrated that graphene interacts with sulfur and polysulfides physically and chemically, buffering the volume fluctuation induced by the S/Li_2S redox and immobilizing the dissolved polysulfides. Recent studies also indicate that graphene can stabilize Li anodes and prevent the growth of Li dendrites. For metal matrix composites, single-layered graphene can impede the propagation of dislocations and mobilization of grain boundaries, leading to substantial strengthening effect. Moreover, graphene sheets have grain refining effect in some metals. However, the graphene sheets are often defective and tend to agglomerate, which severely decreased the reinforcing efficiency of graphene. Three research tasks and corresponding research objectives were designed according to the state-of-the-art research.

In Chapter 2, graphene was incorporated with low-cost, biomass-derived porous carbon for high-performance Li-S battery cathodes. Banana peels with naturally porous structures were successfully converted into conductive carbon scaffolds. Annealing $Ni(NO_3)_2$ treated ABP created nanopores and graphene/Ni nanoparticles simultaneously on the cell walls of ABP. The hierarchically porous ABP/Ni/graphene architecture accommodated the volume change during the charge/discharge cycling, suppressed the formation of passive layer, mitigated dissolution of polysulfides, and shortened the pathway of ion transfer. Moreover, the highly conductive Ni nanoparticles and graphene further enhanced electron transfer, ensuring low internal resistance and high coulombic efficiency. In another work, the recycled paper was creatively composited with graphene oxide sheets by a capillary method. The obtained recycled paper/graphene oxide hybrid was converted into APC/graphene scaffold. The graphene film encapsulated sulfur nanoparticles, increasing the sulfur loading and electrode's conductivity as well as preventing the vaporization of sulfur. The APC/graphene/S composite was used as a free-standing cathode to construct Li-S batteries, which exhibited a superior lifespan, excellent capacity retention rate and outstanding rate ability. The porous APC/graphene/S architecture accommodated the volume change induced by the transformation between sulfur and polysulfides. The graphene film entrapped and encapsulated polysulfides and facilitated electron/ion transfer. The banana-peel and recycled paper derived Li-S batteries present a new promise for the design and fabrication of high-performance energy storage devices while reducing material waste.

In Chapter 3, the mechanisms of Li anode induced Li-S battery failure were unveiled and the methods for preventing Li anode malfunction were developed. It was found that stripping/plating of mossy Li whiskers continuously produced SEI flotsams and dead Li particles on the anode surface. These passive deposits, together with sulfur and Li_2S, were repeatedly compressed by the growth of mossy Li, densifying into a compact crust. The formed passive crust blocked the charge transfer pathway for the lithium underneath, leading to the lithium anode failure. The formation mechanism of mossy Li was then studied. Upon discharging, the boundaries of the SEI grains created a pathway for etching, leading to collapse along the squares and the formation of irregularly shaped pits. In the following charge process, mossy Li whiskers grew from the bottom of the pits. Therefore, the formation of mossy Li is closely related to the inhomogeneous etching of the anode surface. When studying lithium plating in practical batteries, the stripping process cannot be ignored. The findings and proposed mechanisms are expected to improve the understanding of the failure mechanisms in other long life-span Li metal based batteries. To slow down the growth of mossy Li, two methods were employed. A porous conductive APC interlayer was placed between the Li anode and separator to redistribute Li ions, promoting the homogeneous deposition of Li during electrochemical reactions and enhancing the lifespan. ALA, a common food supplement, was combined with GO to form a stronger artificial SEI, which effectively prevented the growth of mossy Li, leading to high specific capacitance and low capacity decay. The ALA/GO composite is promising for overcoming the challenges of Li dendrite growth and polysulfide shuttling.

In Chapter 4, the reaction between graphene oxide and Al was used to fabricate graphene/Al_2O_3/Al composites with superior mechanical properties. During high-temperature sintering, oxygen on GO sheets reacted with Al, forming Al_2O_3 nanoparticles along with the interfaces. The Al_2O_3 nanoparticles strengthened the composite by pining dislocations and refining grains. The nacre-like laminated structure toughened the composite via elongating crack length and blunt crack tip. Moreover, the Al_2O_3 nanoasperities and metal Al bridges jointly prevented large-scale delamination of the layers, further delaying catastrophic fracture. Compared with pure aluminum, the obtained composite exhibited a 210% improvement in hardness, a 223% increase in ultimate strength, a 67% enhancement in Young’s modulus, and a 30% rise in toughness. The toughness value exceeded its individual constituents and their simple mixture. This smart manufacturing strategy can be grafted to other metallic materials such as Mg, Ti, Cu, and Zn. The design principles create new opportunities for developing bio-inspired materials to achieve superior mechanical performance for applications in an extensive range of fields.

In Chapter 5, Ni/Ni_3C composites with nacre-like, brick-and-mortar structure were fabricated by stimulating the reaction between Ni and graphene. Graphene closely wrapped the Ni powders via shear mixing and freeze-drying. The Ni/graphene powders were compressed and then sintered at 1450 ℃, forming Ni_3C at the grain boundaries. The Ni_3C platelets were deformable. They were rolled into long stripes during the cold deformation, leading to the formation of a brick-and-mortar structure. Additional carbon atoms were dissolved into the Ni matrix as interstitial solution atoms. The Ni_3C platelets not only acted as the load-bearers, but also redirected the crack. The small grains and interstitial solution atoms prohibited the dislocation propagation and enhanced the Ni matrix. In total, the confluence of multiple strengthening and toughening mechanisms enabled a 73 % increase on strength and a 6 % increase on Young’s modulus, while only 28 % comprise on ductility, leading to a 44 % improvement of toughness. This strategy presents a new promise for the design and synthesis of new graphene-enabled metal matrix composites with exceptionally high mechanical robustness for a variety of applications.

This dissertation demonstrated effective applications of graphene in Li-S batteries and metal matrix composites. To transform wastes into wealth, graphene sheets were composited with biomass-derived porous carbon, forming high-energy Li-S battery cathodes. To overcome the growth of mossy Li, graphene oxide was combined with polymers, forming stronger artificial SEI. To enhance the strength and toughness of metal matrix composites, interfacial reactions between graphene and metals were exploited, forming composites with nacre-like microstructure. In summary, graphene can serve as a game changer for energy storage and energy saving if being used smartly and effectively.

6.2 Outlook

While this dissertation explored effective graphene applications in Li-S batteries and Al and Ni-based metal matrix composites, two research directions are promising and need to be explored.

6.3.1 Graphene-enabled high-energy density Li-S batteries

Although previous studies have depicted a promising solution to overcome the Li-S battery challenges, graphene and its derivatives also have their disadvantages. Scientifically, the conductivity of graphene is often compromised by the functional groups and heteroatoms on/in graphene, which are critical for the polysulfide immobilization. Therefore, it is difficult to achieve simultaneously high conductivity and high polysulfides absorption by using graphene frameworks alone. In addition, the bonding energy between polysulfides and functionalized/doped graphene is weaker than that between polysulfides and metal oxides, metal nitrides, or metal sulfides. Practically, graphene and GO are not low-cost materials at the current stage considering the time and material to make them. Moreover, graphene sheets tend to aggregate, thus special storage and transportation methods are needed. In order to fabricate graphene based Li-S batteries, the following three directions are worth exploring.

1) Fundamentally understand the interactions between graphene, functional groups, heteroatoms and sulfur, polysulfides. Although several studies have focused on the interactions and made notable progress, but it is far beyond a comprehensive understanding, especially at quantitative level. If quantitative and statistic conclusions are obtained from theoretical and experimental studies, we can optimize the amount of functional groups/heteroatoms and sulfur/carbon ratio, largely improving the utilization efficiency of sulfur and graphene;

2) Explore high-performance, low-cost graphene composites. Graphene based composites for Li-S battery cathodes have shown unparalleled advantages comparing with sole graphene frameworks. However, most of current studies on the composites are based on trial-and-error trials. Advanced computational methods, such as machine learning, should help us to find the best recipe.

3) Extend the applications of graphene and its derivatives to separator, binder, electrolyte, and anode. Graphene and its derivatives should find applications in other components in Li-S batteries. Achieving outstanding performance requires a holistic improvement of every individual component in the battery and graphene has the great potential to enhance the function and properties of separator, binder, electrolyte, and anode.

6.3.2 2D material-enabled advanced metal matrix composites

Previous research demonstrated that graphene-activated metal powders can be used for the fabrication of high-performance metal matrix composites with nacre-like microstructure, showing a new approach to develop 2D material-enabled advanced alloys and metal matrix composites. 2D materials can be homogeneously coated onto the metal powders with intimate bonding. Interfacial reactions are expected to occur during powder processing and sintering, forming new microstructures. More importantly, the 2D material activated metal powders have the potential to be used in additive manufacturing, creating possibilities for designing new materials. The successful development of nacre-like metal matrix composites from 2D material activated metal powders opens a new pathway towards next-generation structural materials with high strength and toughness. Considering the unlimited combinations between metals/alloys and 2D materials, as well as the possibility of multiple integrations, such as doubly coating two types of 2D materials on metal powders, numerous new materials can be designed and developed.